UNIVERSITY OF OKLAHOMA

GRADUATE COLLEGE

SEARCH FOR THIRD GENERATION VECTOR-LIKE LEPTONS WITH THE

ATLAS DETECTOR

A DISSERTATION

SUBMITTED TO THE GRADUATE FACULTY

in partial fulfillment of the requirements for the

Degree of

DOCTOR OF PHILOSOPHY

By

JOSEPH MUSE
Norman, Oklahoma
2022

SEARCH FOR THIRD GENERATION VECTOR-LIKE LEPTONS WITH THE
ATLAS DETECTOR

A DISSERTATION APPROVED FOR THE
HOMER L. DODGE DEPARTMENT OF PHYSICS AND ASTRONOMY

BY THE COMMITTEE CONSISTING OF

Dr. Phillip Gutierrez, Chair

Dr. Brad Abbott

Dr. Kuver Sinha

Dr. Karen Leighly

Dr. Keri Kornelson

Acknowledgements

I would like to thank my advisor Phil Gutierrez, who was always supportive of all the projects I wanted to take on. Your willingness to let me make my own mistakes and try any far-fetched idea I had was always accompanied by thoughtful guidance. This work wouldn't have been possible without you, and I truly appreciate everything you've done for me.

I would also like to acknowledge my advising committee: Kuver Sinha, who taught me everything I know about particle physics. Karen Leighly, who cultured my interest in machine learning. Keri Kornelson, who was supportive, positive and was courteous enough to never demoralize a silly physicist with tests of mathematical acumen. Last, but certainly not least: Brad Abbott. I consider you a mentor but more importantly, a friend. I will always appreciate your honesty, physics insight and advice about whatever was on my mind.

I also need to acknowledge the rest of my OU HEP family. To the OU HEP support staff: Horst Severini, Chris Walker and Chad Cunningham for your support in facilitating my research. To the rest of the experimental OU HEP group: Mike Strauss, John Stupak and Pat Skubic. Without each of you, the group would be a shell of what it is today.

To Marija Marjanovic, I run a risk of missing something if I try to list all of the things I couldn't have done without you. Instead, I just want to say how truly grateful I am for all of your help, guidance and support. You are a great physicist, mentor and friend. Thank you for everything.

To my friends at Argonne: Vallary Bhopatkar, Tim Cundiff, Manoj Jadhav, Evan Van de Wall and Binbin Dong. It was a true pleasure to work with all of you and I appreciate all of your support and knowledge. I'll never forget our late nights at FTBF.

To Jessica Metcalfe, it was an honor working on pixels with you. Your knowledge and guidance allowed me to develop a skillset that I will carry with me for the rest of my career. I will always appreciate the trust you put in me to take on big projects and the support to succeed.

To my OU physics friends: Joseph Lambert, Nick Reynolds Tran, Ryan O'Toole, Daniel Vagie and Daniel Wilbern; I wouldn't have finished without each of you. Joseph, thank you for the countless beers and great memories. Nick, thank you for being an incredible person and friend. Ryan, you were my first friend in Oklahoma and I will never forget smoke-filled evenings at Louies. Daniel Vagie, you may be the nicest person I've ever met and I am proud to call you my friend. Daniel Wilbern, this analysis would be nothing without you. I'll miss our cathartic complaining about literally everything.

To my family: my parents- Jerry and Cindy- and my sister- Alyse. Without your love and support, this wouldn't have been possible. You always believed that I could do anything and always encouraged me. I love you all more than I can justify with words. And to the rest of my family: Antonio, Ailce and Ingrid for providing an escape with your warmth and always accepting me with open arms.

And to Dr. Karen Castillioni, you may have gotten here first but I would never have gotten here without you. Your constant words of encouragement and putting with me at my most intolerable is a testament to how you're truly the most amazing person I've ever met. I love you.

Table of Contents

List of Tables

List of Figures

Abstract

The Standard Model of particle physics provides a concise description of the building blocks of our universe in terms of fundamental particles and their interactions. It is an extremely successful theory, providing a plethora of predictions that precisely match experimental observation. In 2012, the Higgs boson was observed at CERN and was the last particle predicted by the Standard Model that had yet-to-be discovered. While this added further credibility to the theory, the Standard Model appears incomplete. Notably, it only accounts for 5% of the energy density of the universe (the rest being "dark matter" and "dark energy"), it cannot resolve the gravitational force with quantum theory, it does not explain the origin of neutrino masses and cannot account for matter/anti-matter asymmetry. The most plausible explanation is that the theory is an approximation and new physics remains.

Vector-like leptons are well-motivated by a number of theories that seek to provide closure on the Standard Model. They are a simple addition to the Standard Model and can help to resolve a number of discrepancies without disturbing precisely measured observables. This thesis presents a search for vector-like leptons that preferentially couple to τ leptons. The search was performed using proton-proton collision data from the Large Hadron Collider collected by the ATLAS experiment from 2015 to 2018 at center-of-mass energy of $\sqrt{s} = 13$ TeV, corresponding to an integrated luminosity of 139 fb^{-1}. Final states of various lepton multiplicities were considered to isolate the vector-like lepton signal against Standard Model and instrumental background. The major backgrounds mimicking the signal are from WZ, ZZ, $t\bar{t} + Z$ production and from mis-identified leptons. A number of boosted decision trees were used to improve rejection power against background where the signal was measured

using a binned-likelihood estimator. No excess relative to the Standard Model was observed.

Exclusion limits were placed on vector-like leptons in the mass range of 130 to 898 GeV.

Chapter 1

Introduction

For the past 100 years, our understanding of the fundamental composition of our universe has been evolving. From J. J. Thomson's discovery of the electron through the development of quantum mechanics up to the present day, our understanding has been converging towards a model that encompasses the structure of all known elementary particles and their interactions. This model, the Standard Model of particles and particle interactions (SM), has been extremely successful in both its predictions as well as its precision. In 2012, the final particle predicted by the SM that had not been observed was discovered at CERN; the Higgs Boson [1, 2]. Despite its successes, the SM is unfortunately incomplete. Notably, it only accounts for 5% of the energy density of the universe (the rest being "dark matter" and "dark energy"), it cannot resolve gravitational force with quantum theory, it does not explain the origin of neutrino masses and cannot account for matter/anti-matter asymmetry. The most plausible explanation is that the theory is a low-energy approximation and that higher energy, Beyond the Standard Model (BSM) physics is unaccounted for.

This thesis presents a search for an extension to the SM in the form of a "vector-like lepton" using data collected by the ATLAS detector. This chapter will discuss the SM and the theory behind vector-like leptons. Chapter 2 will introduce the ATLAS detector. Chapter 3 will discuss reconstructed physics objects used for the analysis. Chapter 4 lists the data and simulated samples used in the analysis. Chapter 5 details the analysis strategy. Chapter 6 defines analysis regions used to search for vector-like leptons. Chapter 7 will introduce physics background estimation. Chapter 8 lists the systematic uncertainties included in the statistical

analysis. Chapter 9 describes the statistical analysis and results. Finally, Chapter 10 will interpret the results from this thesis.

1.1 The Standard Model

Four fundamental forces govern the interactions of the universe. The familiar gravitational force is best described by General Relativity (GR), which dictates that spacetime is a dynamic entity under the influence of energy and mass densities. The force of gravity is the result of geodesic motion along curved spacetime. Special Relativity is a localized approximation of GR, where spacetime is assumed flat (analogous to how the Earth appears flat at human scales despite the well-known and never-disputed observation of its curvature from space).

The remaining three forces: the electromagnetic, the weak and the strong nuclear forces are described by Quantum Field Theory (QFT). QFT extends quantum mechanics to the relativistic regime by introducing a flat four-dimensional Minkowski spacetime, where spacetime curvature and gravity are considered negligible at microscopic scale. In this formulation, fundamental particles and interactions are viewed as quantized, relativistic fields and observable particles are *on-shell*[1] excitations of these fields.

The equations of motion for a quantum field satisfy the Euler-Lagrange equation:

$$\partial_\mu \left(\frac{\partial \mathcal{L}}{\partial(\partial_\mu \phi)} \right) - \frac{\partial \mathcal{L}}{\partial \phi} = 0 \tag{1.1}$$

where $\mathcal{L}$ is the Lagrangian density, ϕ is the field and μ[2] is the spacetime index ($\mu = \{0, 1, 2, 3\}$). The Lagrangian must be invariant to physical transformations. For instance, rotations

---

[1]On-shell refers to conservation of the stress-energy tensor where a particle's mass-energy relationship has solutions of a hyperboloid shell.

[2]Einstein convention is implied, where summation occurs over repeated indices.

and translations through spacetime must preserve the physics of the system. Further, any transformation that leaves the system invariant corresponds to a conservation law, as described by Noether's theorem [3]. Examples of Noether's theorem are the conservation of angular momentum with rotation and the conservation of energy and momentum through spacetime translations. In general, physics is symmetric with respect to the Poincaré group, which includes Lorentz transformations, rotations and translations.

The SM is a QFT which is invariant under the local gauge transformation of $SU(3)_C \otimes SU(2)_L \otimes U(1)_Y$ [4, 5]. Quantum chromodynamics (QCD) is the theory of strong interactions between quarks and gluons and is described by the $SU(3)_C$ gauge group. The unified electroweak theory, composed of the weak interaction and quantum electrodynamics (QED) is described by the $SU(2)_L \otimes U(1)_Y$ gauge group. The Higgs mechanism is responsible for generating the mass of elementary particles.

1.1.1 Elementary Particles

There are two types of fundamental particles in the SM: *bosons* and *fermions*. Bosons are particles which obey Bose-Einstein statistics and have integer[3] spin quantum numbers. Fermions obey Fermi-Dirac statistics and have half-integer spin quantum numbers. *Gauge bosons* are "carriers" of the fundamental forces, the *Higgs boson* generates mass in the SM and fermions are "matter particles" which interact with each other by exchanging gauge bosons. Fermions are further categorized into *leptons* and *quarks*, where the former have QCD quantum numbers and the latter do not. For every particle in the SM, there exists an *anti-particle* with opposite electric charge and parity (CP). The particle content of the SM is

---

[3]In units of $\hbar$.

shown in Figure 1.1.
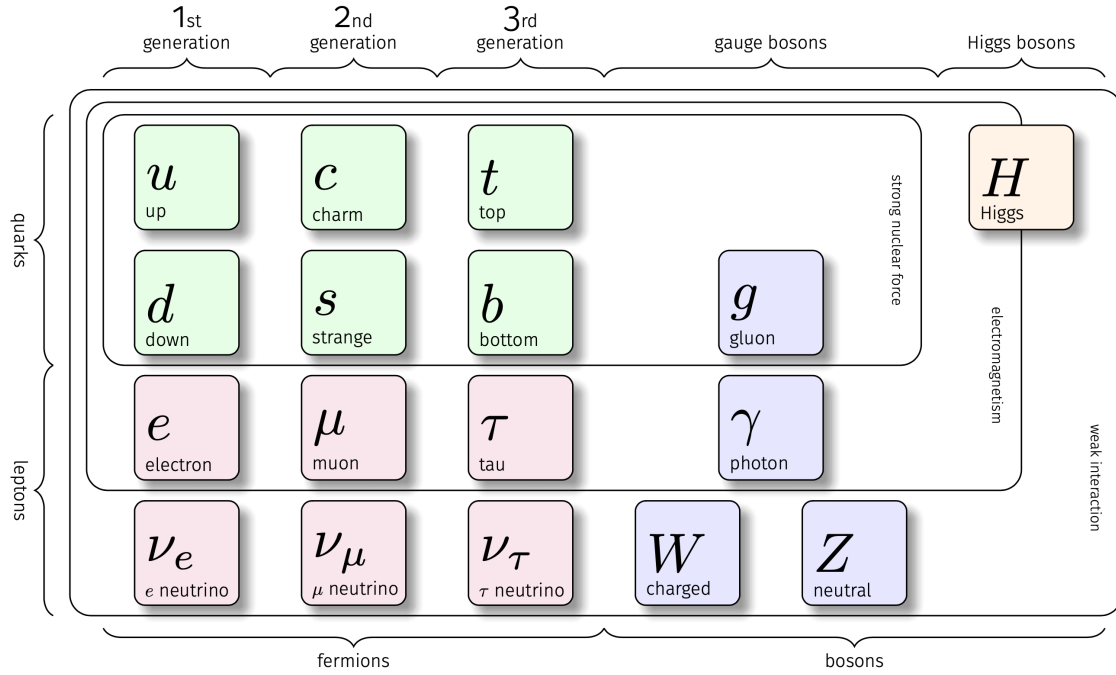
Figure 1.1: Particle content of the SM. Gauge bosons are carriers of fundamental forces and the Higgs boson generates mass. Fermions are matter particles and are divided into quarks and leptons, where the former have QCD quantum numbers.

Fermions   Fermions in the SM are represented as a Dirac spinor, which is an irreducible representation of the Poincaré group. The Dirac spinor is composed of *left-handed* and *right-handed* components:

$$\Psi_{\mathrm{D}} = \begin{pmatrix} \psi_{\mathrm{L}} \\ \psi_{\mathrm{R}} \end{pmatrix} \tag{1.2}$$

where Ψ_{D} is the Dirac spinor and $\psi_{\mathrm{L/R}}$ are the left and right-handed components. The two-component group structure of fermions implies the SM is a chiral theory and is most evident in its representation in $\mathrm{SU(2)_L}$, where a generic SM fermion has the structure:

$$\mathrm{SU(2)_L}: \quad \psi_\mathrm{L} = \begin{pmatrix} \psi_\mathrm{1,L} \\ \psi_\mathrm{2,L} \end{pmatrix}, \quad \psi_\mathrm{R} = \psi_\mathrm{R}$$

In this representation, the left-handed $\mathrm{SU(2)_L}$ doublet transforms differently than the right-handed $\mathrm{SU(2)_L}$ singlet. The weak interaction subsequently treats the left and right-handed components in a unique manner. Table 1.1 summarizes SM fermions.

Leptons are fermions which do not have QCD quantum numbers. There are three *generations* of leptons which share identical quantum numbers but have different masses. Each generation consists of a charged[4] and neutral lepton (neutrino), which are rotated into one another by the $\mathrm{SU(2)_L} \otimes \mathrm{U(1)_Y}$ electroweak gauge group. The first generation of leptons is the familiar electron (e) and the electron-neutrino (ν_e). The second generation is the muon (μ), which is identical to the electron but with a mass that is approximately 207 times larger [6], and the muon-neutrino (ν_μ). The third generation is the tau lepton (τ), which is also identical to the electron but with a mass that is approximately 3477 times larger [6], and the tau-neutrino (ν_τ). Neutrinos are massless in the SM since they do not have a right-handed component and do not obtain mass through the Higgs mechanism (Section 1.1.3). However, it has been observed that neutrinos are massive, concluding the SM is incomplete. The $\mathrm{SU(2)_L}$ structure for leptons is given below, where i runs over all three generations:

$$\mathrm{SU(2)_L}: \quad L_{i,\mathrm{L}} = \begin{pmatrix} \nu_{i,\mathrm{L}} \\ l_{i,\mathrm{L}} \end{pmatrix}, \quad L_{i,\mathrm{R}} = l_{i,\mathrm{R}}$$

Quarks are fermions with QCD quantum numbers. Like leptons, there are three generations of quarks. Each generation consists of charged "up-type" and "down-type" quarks, which are rotated into one another by the $\mathrm{SU(2)_L} \otimes \mathrm{U(1)_Y}$ electroweak gauge group. The first generation

---

[4]Charge refers to electric charge, which is the quantum number associated with QED

of quarks is the up (u) and down (d) quarks. The second generation is the charm (c) and strange (s) quarks and the third generation is the top (t) and bottom (b) quarks. Every quark is massive in the SM since each has left and right-handed components. As quarks have QCD quantum numbers, they cannot exist in a free state due to *QCD color confinement* (Section 1.1.4). The SU(2)$_{\mathrm{L}}$ structure for quarks is given below, where i runs over all three generations:

$$\mathrm{SU(2)_L}: \quad Q_{i,\mathrm{L}} = \begin{pmatrix} u_{i,\mathrm{L}} \\ d_{i,\mathrm{L}} \end{pmatrix}, \quad Q_{i,\mathrm{R}} = u_{i,\mathrm{R}}, \quad d_{i,\mathrm{R}}$$

Bosons Bosons in the SM are integer-spin particles. Gauge bosons are force-carrying spin-1 *vector bosons* and the Higgs is a spin-0 *scalar boson*. Both vector and scalar bosons are irreducible representations of the Poincaré group.

The gauge boson associated with QED is the massless photon (γ). There are three gauge bosons associated with the weak interaction: the neutral Z boson and two charged $W^{\pm}$ bosons. Both the Z and $W^{\pm}$ bosons are massive. The gauge bosons associated with QCD are eight massless gluons (g). The Higgs boson (H) exists as a condensate in the SM, effectively breaking the symmetry of vacuum (Section 1.1.3). Interaction with the Higgs field is the mechanism where particles of the SM obtain mass. Table 1.2 summarizes SM bosons.

1.1.2 Electroweak Interaction

The electroweak interaction is a unified representation of the weak interaction and QED consisting of the SU(2)$_{\mathrm{L}}$ ⊗ U(1)$_{\mathrm{Y}}$ electroweak gauge group. The SM is massless prior to electroweak symmetry breaking (Section 1.1.3). The massless electroweak Lagrangian is

Fermion	Type	Generation			Interaction		
		1	2	3	QED	Weak	QCD
Leptons	Charged	e 0.511 MeV	μ 105.7 MeV	τ 1.8 GeV	X	X	
	Neutral	ν_e ?	ν_μ ?	ν_τ ?		X	
Quarks	Up	u 2.16 MeV	c 1.27 GeV	t 172.4 GeV	X	X	X
	Down	d 4.67 MeV	s 93 MeV	b 4.18 GeV	X	X	X

Table 1.1: Summary of fermions in the SM. Leptons and quarks are shown, categorized into charged and neutral leptons and up and down-type quarks. Below each species is the measured mass, where the mass of neutrinos is currently unknown. The "X" indicates the fermion has quantum numbers for the corresponding interaction. Mass values are taken from [6].

written as:

$$\mathcal{L}_{\text{EW}} = \bar{\Psi}i\gamma^\mu D_\mu \Psi - \frac{1}{4}W_i^{\mu\nu}W_{\mu\nu}^i - \frac{1}{4}B^{\mu\nu}B_{\mu\nu} \tag{1.3}$$

where Ψ is the Dirac spinor fermion field (Equation 1.2), W^i is the three-component ($i = \{1, 2, 3\}$) *weak isospin* gauge field associated with $\text{SU}(2)_{\text{L}}$ and B is the *hypercharge* gauge field associated with $\text{U}(1)_{\text{Y}}$. The indices μ and ν are spacetime indices ($\mu, \nu = \{0, 1, 2, 3\}$).

Spin	Boson		Mass [GeV]	Multiplicity	Interaction
Spin-0	Higgs	H	125.10	1	
Spin-1	Photon	γ	0	1	QED
	Z	Z	91.1876	1	Weak
	W	$W^{\pm}$	80.379	2	Weak
	Gluon	g	0	8	QCD

Table 1.2: Summary of bosons in the SM. Scalar (spin-0) and vector (spin-1) bosons are shown. Included with each boson is the measured mass, multiplicity and associated interaction. Mass values are taken from [6].

The *field strength tensors* ($W_i^{\mu\nu}$, $B^{\mu\nu}$) can be expanded for comparison:

$$W_i^{\mu\nu} = \partial^\nu W_i^\mu - \partial^\mu W_i^\nu - g_W \epsilon_{ijk} W_\mu^i W_\nu^i, \tag{1.4}$$

$$B^{\mu\nu} = \partial^\nu B^\mu - \partial^\mu B^\nu \tag{1.5}$$

The extra term in Equation 1.4 relative to Equation 1.5 is a consequence of the non-Abelian nature of the $SU(2)_L$ group and gives rise to weak isospin gauge boson self-interactions.

Embedded in the covariant derivative (D_μ in Equation 1.3) are the generators for the $SU(2)_L$ and $U(1)_Y$ gauge groups. Eigenvalues of the generators correspond to quantum numbers associated with the interaction. The covariant derivative is defined as:

$$D_\mu = \partial_\mu - ig'\frac{Y}{2}B_\mu - ig_W t^i W_\mu^i \tag{1.6}$$

where t^i are the three generators for $SU(2)_L$ and Y is the generator for $U(1)_Y$. The g' and

g_W parameters are the coupling strengths of the B and W fields. Given the generators, the fermion fields are invariant to gauge transformations of the form:

$$\psi_L \rightarrow [1 - ig_W t^i \alpha]\psi_L \tag{1.7}$$

$$\psi_{L,R} \rightarrow [1 - ig'Y\alpha]\psi_{L,R} \tag{1.8}$$

with α given as an arbitrary phase. In Equation 1.7, only left-handed fermions transform under $SU(2)_L$. In Equation 1.8, both right and left-handed fermions transform under $U(1)_Y$.

The physical gauge fields associated with the weak interaction (Z, $W^\pm$) and QED (γ) are linear combinations of the massless B and W fields. These combinations are the result of electroweak symmetry breaking (Section 1.1.3), such that:

$$\gamma = B\cos\theta_W + W^3\sin\theta_W \tag{1.9}$$

$$Z = -B\sin\theta_W + W^3\cos\theta_W \tag{1.10}$$

$$W^+ = \frac{1}{\sqrt{2}}(W^1 - iW^2) \tag{1.11}$$

$$W^- = \frac{1}{\sqrt{2}}(W^1 + iW^2) \tag{1.12}$$

where θ_W is the empirically determined weak-mixing angle. From this, the electric charge can be derived from the Gell-Mann-Nishijima relation [7, 8]:

$$q = T^3 + \frac{Y}{2} \tag{1.13}$$

where Y is the hypercharge and T_3 is the third component of weak isospin, which are eigenvalues of the associated generators. This relation allows the electric charge for each

particle in the SM to be defined, given their hypercharge and weak isospin quantum numbers. Table 1.3 shows the quantum numbers for SM fermions and bosons.

	Field	Isospin (T^3)	Hypercharge (Y)	Electric Charge (q)
Fermions	ν_L	$\frac{1}{2}$	-1	0
	e_L	$-\frac{1}{2}$	-1	-1
	u_L	$\frac{1}{2}$	$\frac{1}{3}$	$\frac{2}{3}$
	d_L	$-\frac{1}{2}$	$\frac{1}{3}$	$-\frac{1}{3}$
	e_R	0	-2	-1
	u_R	0	$\frac{4}{3}$	$\frac{2}{3}$
	d_R	0	$-\frac{2}{3}$	$-\frac{1}{3}$
Bosons	γ	0	0	0
	$W^\pm$	± 1	0	± 1
	Z	0	0	0
	g	0	0	0
	H	$-\frac{1}{2}$	1	0

Table 1.3: Quantum numbers associated with SM particles [6]. All three generations of fermions share quantum numbers and only the first generation is shown for brevity.

Neutral currents involving the physical Z and γ bosons, preserve the *flavor*[5] of fermions involved in the interaction. However, *charged currents* involving the $W^\pm$ bosons is flavor-

---

[5]Flavor refers to the species of fermion, distinguished by generation and quantum numbers (6 flavors for leptons and 6 for quarks).

changing. Specifically, mass and flavor eigenstates for quarks can be mixed through the unitary CKM matrix [9, 10], which can only occur through interactions with the $W^\pm$ boson. Further, the $W^\pm$ boson rotates the charged and neutral left-handed leptons and up and down left-handed quarks into one another.

1.1.3 Electroweak Symmetry Breaking

The Lagrangian presented in Equation 1.3 is massless, implying SM fermions and gauge bosons are also massless. However, mass associated with these particles is empirically determined. Adding mass terms of the form $m\bar{\Psi}\Psi$ would break SU(2)$_\text{L}$ gauge invariance. *Electroweak symmetry breaking* (EWSB), or the *Higgs mechanism*, is introduced to address this glaring issue [11, 12, 13].

Consider the Higgs field as a scalar (spin-0) SU(2)$_\text{L}$ doublet:

$$\Phi = \begin{pmatrix} \phi^+ \\ \phi^0 \end{pmatrix} \tag{1.14}$$

where ϕ^+ is a charged component and ϕ^0 is a neutral component, both of which are complex. The Lagrangian for Higgs can be written as:

$$\mathcal{L}_{\text{Higgs}} = |D_\mu \Phi|^2 \underbrace{-\mu^2|\Phi|^2 - \lambda|\Phi|^4}_{-V(\Phi)} \tag{1.15}$$

where D_μ is the covariant derivative defined in Equation 1.6 and $V(\Phi)$ is the field potential. The symmetry of the electroweak interaction is preserved when $\mu^2 > 0$ since the potential would have a single minima. The symmetry is spontaneously broken when $\mu^2 < 0$. In the case of broken symmetry, the Higgs field has an infinite set of non-zero minima or *vacuum*

expectation values (v) such that:

$$< \Phi^\dagger \Phi >= \frac{v^2}{2} = -\frac{\mu^2}{2\lambda} \tag{1.16}$$

The choice of vacuum state from the set of infinite possibilities, in turn, spontaneously breaks the symmetry of electroweak interaction. The Higgs potential for a non-zero v is illustrated in Figure 1.2.
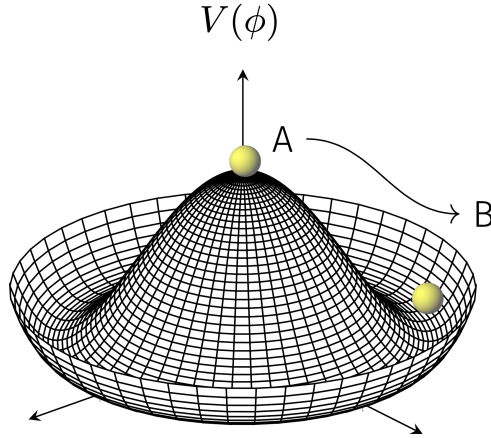
Figure 1.2: The Higgs potential for a non-zero v. The point at zero (A) is not the minimum of the potential. The minima of the potential is an infinite set of non-zero values (B). Therefore, the vacuum or ground state is also non-zero and the choice of ground state is spontaneous symmetry breaking.

Expanding ϕ^0 around the chosen vacuum state introduces a massive scalar and three massless *Goldstone bosons* [14]. The Goldstone bosons are absorbed by the $W^\pm$ and Z bosons and introduces both a mass and longitudinal polarization mode [15]. This is made explicit by utilizing the *unitary gauge* where the Higgs doublet becomes:

$$\Phi = \frac{1}{\sqrt{2}} \begin{pmatrix} 0 \\ v + h \end{pmatrix} \tag{1.17}$$

12

where h is introduced as the physical Higgs boson. Expanding the first term in Equation 1.15:

$$
\begin{aligned}
|D_\mu\Phi|^2 =& \frac{1}{2}(\partial_\mu h)(\partial^\mu h) + \frac{1}{8}g_W^2(W_\mu^1 + iW_\mu^2)(W^{1\mu} - iW^{2\mu})(v+h)^2 \\
&+ \frac{1}{8}(g_W W_\mu^3 - g'B_\mu)(g_W W^{3\mu} - g'B^\mu)(v+h)^2
\end{aligned}
\tag{1.18}
$$

The mass of the physical $W^\pm$ can be defined by comparing Equation 1.18 with Equations 1.11 and 1.12, such that:

$$
m_W = \frac{1}{2}g_W v
\tag{1.19}
$$

The physical Z and γ bosons can be written in matrix form using Equations 1.9, 1.10 and 1.18:

$$
\frac{1}{8}v^2 \begin{pmatrix} \gamma & Z \end{pmatrix} \begin{pmatrix} 0 & 0 \\ 0 & g_W^2 + g'^2 \end{pmatrix} \begin{pmatrix} \gamma \\ Z \end{pmatrix}
\tag{1.20}
$$

where the masses can be easily defined as:

$$
m_\gamma = 0
\tag{1.21}
$$

$$
m_Z = \frac{1}{2}v\sqrt{g_W^2 + g'^2}
\tag{1.22}
$$

Due to the $\mathrm{SU(2)_L}$ doublet structure of the Higgs field, it is also possible to introduce a coupling term with SM fermions. This term couples left and right-handed fermions and is called a *Yukawa interaction*:

$$
\mathcal{L}_{\mathrm{Yukawa}} = g_f[\bar\psi_R(\Phi^\dagger\psi_L) + (\bar\psi_L\Phi)\psi_R]
\tag{1.23}
$$

where the Yukawa coupling is proportional to the fermion mass and is defined as:

$$
g_f = \sqrt{2}\frac{m_f}{v}
\tag{1.24}
$$

The Yukawa couplings for each fermion are not explicitly predicted by the SM and are left as free parameters. Therefore, the Yukawa couplings (and fermion masses) are empirically determined from precision measurements. Introduction of the Higgs does not allow a mass term for neutrinos due to the absence of right-handed components. The masses of neutrinos are predicted to be exactly zero by the SM.

1.1.4 Quantum Chromodynamics

QCD is associated with the non-Abelian $SU(3)_C$ gauge group. The only fermions which contain QCD quantum numbers are quarks, where massless gluons act as force carriers. The Lagrangian for QCD is defined as:

$$\mathcal{L}_{\mathrm{QCD}} = \bar{Q}(i\gamma^{\mu}D_{\mu})Q - \frac{1}{4}G_a^{\mu\nu}G_{a\mu\nu} \tag{1.25}$$

where Q represents the quark fields and G_a corresponds to the eight gluon fields such that $a = \{1,..,8\}$.

The generators of the $SU(3)_C$ gauge group are presented by introducing the covariant derivative:

$$D_{\mu} = \partial_{\mu} - ig_S T^a G_{\mu}^a \tag{1.26}$$

where T^a are the eight $SU(3)_C$ gauge group generators. The quantum numbers for QCD are three *colors*[6]: red, green, blue. Each quark is charged with exactly one color or anti-color and gluons are charged with color-neutral quantum states of color/anti-color pairs.

The field strength tensor for gluons:

---

[6]Color in this context is purely nomenclature and does not correspond to the traditional definition.

$$G_{\mu\nu}^a = \partial_\mu G_\nu^a - \partial_\nu G_\mu^a - g_S f^{abc} G_\mu^b G_\nu^c \tag{1.27}$$

contains a non-Abelian term: $g_S f^{abc} G_\mu^b G_\nu^c$. This indicates gluons are self-coupling and contain color charge. The gluon field strength increases as the distance between two quarks increases, therefore, quarks cannot appear as free particles (*confinement*). Quarks only exist in color-neutral bound states called *hadrons*.

An important phenomenological and experimental aspect of confinement is associated to QCD observables in proton-proton collisions. The energy required to maintain a free quark is less favorable than the spontaneous production of an associated anti-quark from vacuum. When quarks are generated, they quickly undergo *hadronization* and become collimated showers of hadrons, or *jets*. These collimated showers contain both the original hadronized quark as well as other hadronization products from gluon radiations. This makes individual quark and gluon identification at proton-proton colliders extremely difficult.

1.1.5 Proton-Proton Collisions

Physics processes generated through collisions of protons are studied in this thesis. Protons are hadrons comprised of one d and two u quarks (*valance quarks*). Gluon exchange between valance quarks produce quark/anti-quark pairs, or *sea quarks*. The proton is a composite particle where valance quarks, sea quarks and gluons each carry a portion of the total proton momentum. Collectively, quarks and gluons embedded within a hadron are referred to as *partons*.

Consider an arbitrary interaction between colliding protons:

$$p_1 + p_2 \rightarrow A + B \tag{1.28}$$

the *cross-section* for this arbitrary process can be written as:

$$\sigma^{p_1 p_2 \to AB} = \int_0^1 \int_0^1 dx_1 dx_2 \sum_{a,b} f_{a/p_1}(x_1, \mu_F^2) f_{b/p_2}(x_2, \mu_F^2) \times [\hat{\sigma} + \alpha_s(\mu_R^2)\hat{\sigma}_1 + ...]_{ab \to AB} \quad (1.29)$$

where a, b are partons, μ_F^2 is the *factorization scale*, μ_R^2 is the *renormalization scale*, α_s is the strong coupling constant[7] and $f_{j/p_i}(x_i)$ is the *parton distribution function* (PDF) [16].

The strong coupling constant is dependent on the momentum transfer scale Q^2. At large scales where $Q^2 >> \mu_R^2$, $\alpha_s << 1$ and QCD processes can be calculated perturbatively. The expression in brackets ([...]) from Equation 1.29 refers to perturbative expansion of the cross-section, where higher order QCD processes are calculated, such as gluon radiations. The *order* of the expansion is the number of higher order terms included in the calculation and affects the precision.

The PDF is a probability distribution function describing the probability to find a parton of type j with momentum fraction x_i at momentum transfer scale Q^2. The factorization scale is the momentum transfer scale that separates large Q^2 hard-scattering processes from small Q^2 soft-scattering processes. Hard-scattering processes are associated with large momentum transfer and soft-scattering occurs from proton remnants left over from hard-scattering process. Typically, the renormalization and factorization scales are set such that $\mu_R = \mu_F$.

Figure 1.3 shows the probability for a parton with momentum fraction x, to interact at the momentum transfer scale Q^2. The example shown is from the MSTW08 PDF set for $Q^2 = 10$ GeV^2 (left) and $Q^2 = 10^4$ GeV^2 (right).

---

[7]$\alpha_s = \frac{g_S^2}{4\pi}$, where g_S is the coupling constant given in Equation 1.26.
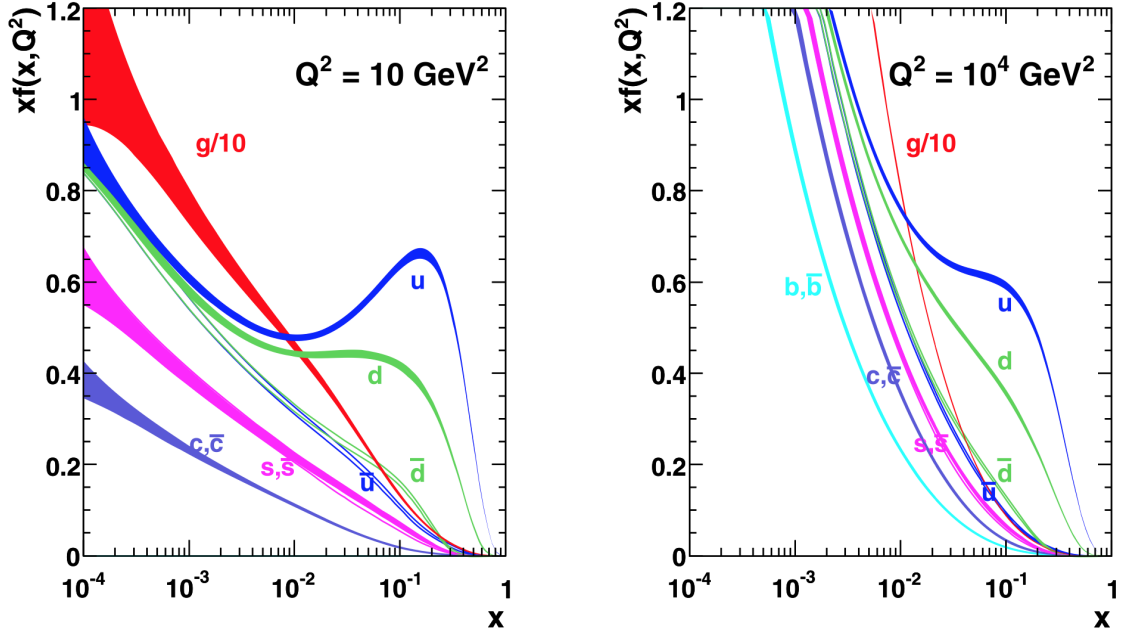
Figure 1.3: MSTW08 PDF set for $Q^2 = 10$ GeV^2 (left) and $Q^2 = 10^4$ GeV^2 (right) [17].

1.2 Vector-like Leptons

The SM is a chiral theory (Section 1.1.1) where left and right-handed fermions do not transform identically under the SU(2)$_L$ gauge group. The SM does not forbid inclusion of fermions with left and right-handed components transforming identically. In fact, their presence could explain notable discrepancies between observation and SM prediction. Such a particle could still decouple at energy scales higher than the electroweak scale due to its ability to generate a mass term independent of EWSB. Mass terms that are not a result of EWSB negate the need for large Yukawa couplings which could strain precisely measured observables [18, 19, 20].

A fermion whose left and right-handed components transform in the same way is referred to as *vector-like*. This thesis considers the specific case of a vector-like lepton (VLL) SU(2)$_L$ doublet. The SU(2)$_L$ structure of SM leptons and VLLs can be written as:

17

$$\mathbf{SM} \quad L_{Li} = \begin{pmatrix} \nu_{Li} \\ e_{Li} \end{pmatrix}, \qquad L_{Ri} = e_{Ri}$$

$$\mathbf{VLL} \quad L'_L = \begin{pmatrix} \nu'_L \\ e'_L \end{pmatrix}, \quad L'_R = \begin{pmatrix} \nu'_R \\ e'_R \end{pmatrix}$$

where i is for each generation of SM lepton (e, μ, τ) and L' represents the VLL, where only one generation is assumed.

The Yukawa terms in the Lagrangian are then amended to include terms associated with the VLL:

$$\mathcal{L}_{\text{Yukawa}} = g_{Li}(\bar{L}_{Li}\Phi)L_{Ri} + \epsilon\bar{L}'_L\Phi L_{Ri} + m_{L'}\bar{L}'_L L'_R + \text{h.c.} \tag{1.30}$$

where g_{Li} is the SM Yukawa coupling, Φ is the Higgs doublet, ϵ is the Yukawa coupling between SM leptons and VLL, and $M_{L'}$ is the mass term from left and right-handed gauge invariant VLL coupling.

This Lagrangian implies a mass matrix with off-diagonal terms:

$$\begin{pmatrix} \bar{L}_{Li} & \bar{L}'_L \end{pmatrix} \begin{pmatrix} g_{Li}v & 0 \\ \epsilon v & m_{L'} \end{pmatrix} \begin{pmatrix} L_{Ri} \\ L'_R \end{pmatrix} = \bar{\ell}_L \mathcal{M} \ell_R \tag{1.31}$$

The mass matrix can be diagonalized by a unitary change of basis to define mass eigenstates as the physical leptons. In the case of SM leptons, the mass and flavor eigenstates are the same since the SM lepton mass matrix is diagonal. Off-diagonal terms, however, do occur for quarks and as a proposed mechanism to generate the observed neutrino mass (CKM and

PMNS [21] matrices, respectively). For SM leptons, diagonal rotations from the mass and flavor bases yield a universality between the three generations.

Charged-lepton flavor conservation is the result of a diagonal SM lepton mass matrix. The weak interaction and QED do not mix lepton generations and preserve charged-lepton flavor. Further, the coupling constants for the weak interaction and QED are independent of lepton generation and is referred to as *lepton universality*. The observation of *charged-lepton flavor violation* or *lepton non-universality* would indicate significant deviations from the SM.

VLLs have been proposed in a number of BSM theories. An example is Supersymmetry (SUSY), which offers a solution to quadratically divergent SM quantum corrections to the Higgs mass (*hierarchy problem*). They are also a simple, model-independent extension to the SM and are a viable solution to recent anomalies observed, such as strains on SM lepton universality predictions [22, 23] and the muon $g - 2$ anomaly [24].

This thesis considers the case of a VLL coupling preferentially to the SM τ lepton, in part due to relatively unconstrained charged-lepton flavor violation measurements compared to electrons and muons [19, 20]. The VLL considered is an $SU(2)_L$ doublet, given as:

$$L'_{L,R} = \begin{pmatrix} \nu' \\ \tau' \end{pmatrix} \tag{1.32}$$

with a mass matrix for SM τ and τ':

$$\mathcal{M}_\tau = \begin{pmatrix} g_\tau v & 0 \\ \epsilon v & m_{\tau'} \end{pmatrix} \tag{1.33}$$

The masses for τ' and τ are therefore:

$$M_{\tau'} = m_{\tau'}(1 + \epsilon^2 v^2/2m_{\tau'}^2 + ...), \tag{1.34}$$

19

$$M_\tau = g_\tau v(1 + \epsilon^2 v^2 / 2m_{\tau'}^2 + ...) \tag{1.35}$$

where the VLL component masses are degenerate to first order, $M_{\tau'} = M_{\nu'}$, and $\epsilon = 0.04$ to impose decay lengths on the centimeter scale. The Feynman diagrams for VLL production and decay are shown in Figure 1.4.
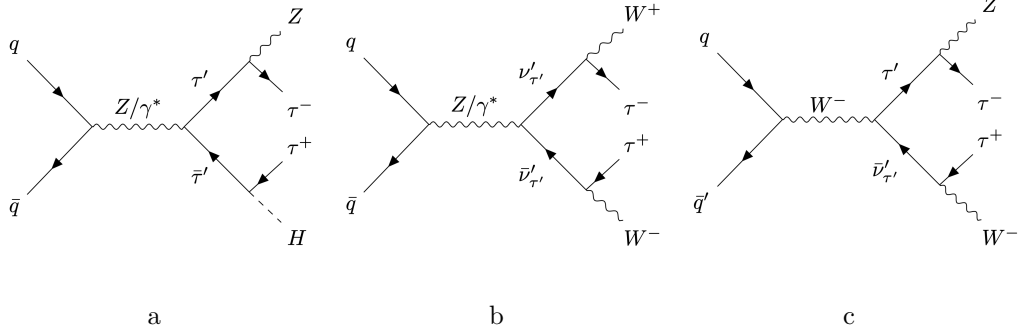
Figure 1.4: Feynman diagrams for τ' and ν' production and decay. (a) Pair-production of τ'. (b) Pair-production of ν'. (c) Production of τ' and ν'

Production of τ' and ν' in proton-proton collisions occurs either through pair-production or $\tau'\nu'$ production:

$$pp \to \tau'\bar{\tau}' \tag{1.36}$$

$$pp \to \nu'\bar{\nu}' \tag{1.37}$$

$$pp \to \tau'\bar{\nu}' \tag{1.38}$$

The decay modes for τ' and ν' include a SM τ and either $W^\pm$, Z or h. Defining $r_X = m_X^2 / M_{\tau'}^2$ for $X = W^\pm, Z, h$ and

$$g_{\tau\nu'}^{W^\pm} = -\epsilon m_{W^\pm} / M_{\tau'} \tag{1.39}$$

$$g_{\tau\tau'}^{Z} = -\epsilon m_Z / \sqrt{2} M_{\tau'} \tag{1.40}$$

20

$$y^h_{\tau\tau'} = -\epsilon/\sqrt{2} \tag{1.41}$$

the decay widths for τ' and ν' are:

$$\Gamma(\tau' \to W^\pm \nu) = 0 \tag{1.42}$$

$$\Gamma(\tau' \to Z\tau) = \frac{M_{\tau'}}{32\pi}(1 - r_Z^2)(2 + 1/r_Z)|g^Z_{\tau\tau'}|^2 \tag{1.43}$$

$$\Gamma(\tau' \to h\tau) = \frac{M_{\tau'}}{32\pi}(1 - r_h^2)|y^h_{\tau\tau'}|^2 \tag{1.44}$$

$$\Gamma(\nu' \to W^\pm \tau) = \frac{M_{\tau'}}{32\pi}(1 - r_{W^\pm}^2)(2 + 1/r_{W^\pm})|g^{W^\pm}_{\tau\nu'}|^2 \tag{1.45}$$

The parameter ϵ cancels when considering the branching ratios. For large τ' mass, the branching ratios for the τ' decays asymptotically approach:

$$\mathrm{BR}(\tau' \to W^\pm \nu) : \mathrm{BR}(\tau' \to Z\tau) : \mathrm{BR}(\tau' \to h\tau) = 0 : 1 : 1 \tag{1.46}$$

and ν' decays exclusively to $W^\pm$:

$$\mathrm{BR}(\nu' \to W^\pm \tau) = 1 \tag{1.47}$$

Figure 1.5 shows the production cross-section of τ' and ν', as well as the branching ratios of τ' as a function of τ' mass. The production cross sections are calculated at next-to-leading order (NLO) in QCD, where the dominant production mode is $\tau'\nu'$ production by a factor of 2-3.

Beginning in Chapter 3, a search for this particular model of VLLs using data collected by the ATLAS detector will be described. A previous set of searches performed with the CMS detector serve as a point of comparison for the analysis presented in this thesis. These searches excluded VLL masses up to 790 GeV [25] using 77.4 fb^{-1} of integrated luminosity and up to 1045 GeV [26] using 138 fb^{-1} at $\sqrt{s} = 13$ TeV.
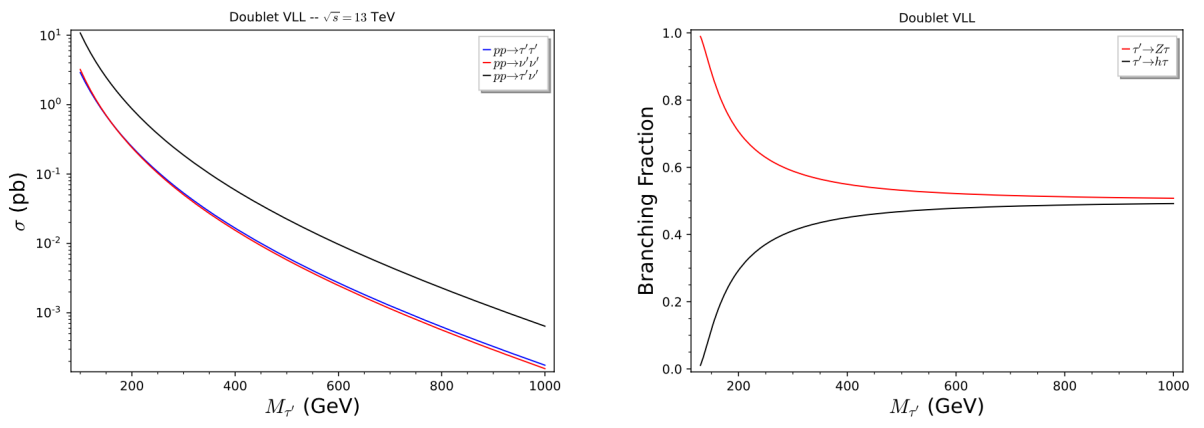
Figure 1.5: Production cross-sections at NLO in QCD for VLL as a function of

τ' mass (left). Branching ratios of τ' decay modes as a function of mass (right).

Chapter 2

Experimental Apparatus

The ATLAS detector is a large general-purpose particle detector designed to record the results of proton-proton collisions at the Large Hadron Collider (LHC). The LHC is located along the French-Swiss border near Geneva, Switzerland and is operated by CERN. The decay products from proton-proton collisions are used to probe fundamental particle physics at the TeV scale. The physics analysis results presented in this thesis were recorded during LHC Run 2 which ran from 2015-2018.

2.1   The Large Hadron Collider

The LHC [27] is the largest and most powerful particle accelerator ever built. It is an underground, circular, two-ring synchrotron with diameter of approximately 27 km located at CERN near Geneva, Switzerland. The LHC began physics runs in 2008 with a center-of-mass energy of 8 TeV, where LHC Run 1 concluded in 2013. LHC Run 2 began in 2015 and lasted until 2018, where the center-of-mass energy increased to 13 TeV.

The LHC accelerates two beams of hadrons (two beams of protons or two beams of heavy ions), where they are collided at one of four interaction points. At each of these interactions points, there is a large detector designed for a particular physics goal. ATLAS (**A** **T**oroidal **L**HC **A**pparatu**S**) [28] and CMS (**C**ompact **M**uon **S**olenoid) [29] are general-purpose experiments designed to probe both SM and BSM physics. ALICE (**A** **L**arge **I**on **C**ollider **E**xperiment) [30] is designed to study quark-gluon plasmas and LHCb (**LHC-b**eauty) [31] is designed to study B-hadron physics.

2.1.1 The Machine
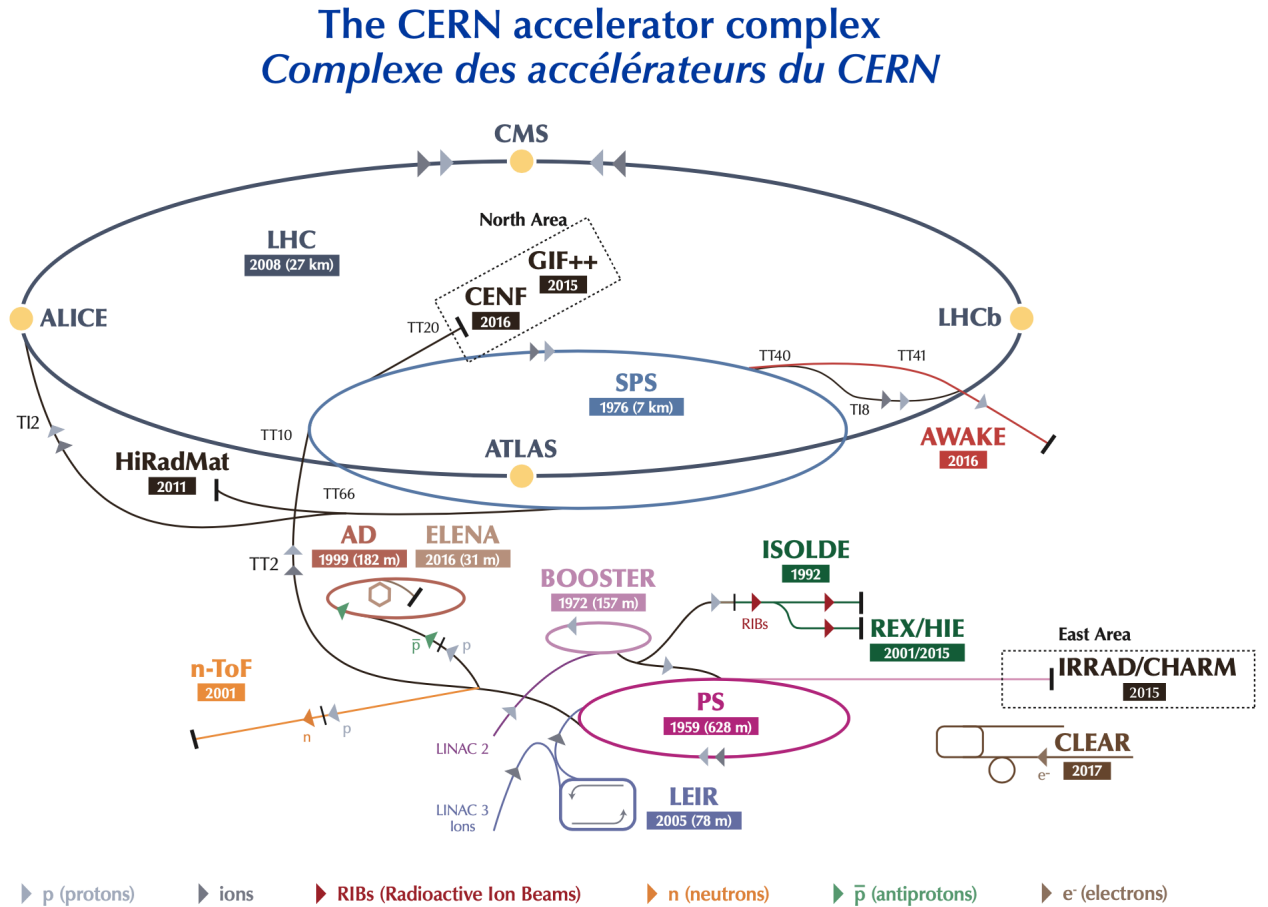
Figure 2.1: CERN Accelerator Complex [32].

The LHC is part of the CERN accelerator complex shown in Figure 2.1. The source of the proton beam is a bottle of hydrogen, where its electrons are stripped by a strong electric field, producing protons. The protons are accelerated in LINAC2 to 50 MeV and then injected into the Proton Synchrotron Booster (PSB) followed by the Proton Synchrotron (PS), where

they are accelerated to 1.4 GeV and 25 GeV, respectively. From the PS, protons are further accelerated to 450 GeV in the Super Proton Synchrotron (SPS) and then injected into the LHC, where they reach their maximum energy of 6.5 TeV.

Protons are sent in *bunches* along the LHC accomplished by superconducting radio frequency cavities which use powerful oscillating electric fields on the order of 2 MV. There are upwards of 2808 bunches spaced by 25 nanoseconds in time (40 MHz), with each bunch containing 10^{11} protons. Superconducting dipole magnets are used to steer and bend the beam. The magnets are made of a niobium-titanium (Nb-Ti) alloy and are cooled to a temperature of 1.9 K using super-fluid helium. At this temperature, the dipole magnets are capable of producing a magnetic field of 8.4 T. Quadrupole and higher order magnets are used to focus the beam near the interaction points.

2.1.2 Luminosity and Pile-up

The ability of a particle accelerator to produce interactions is quantified by the *instantaneous luminosity*. The luminosity is inherently a quantity that depends on properties of the beam. Assuming a Gaussian beam profile, the instantaneous luminosity can be written as:

$$\mathcal{L} = f \frac{n_b^2}{4\pi \sigma_x \sigma y} \tag{2.1}$$

where f is the bunch crossing frequency, n_b is the number of protons in each beam (assumed the same) and $\sigma_{x,y}$ are the beam widths in the transverse directions.

The instantaneous luminosity can also be expressed in terms of event production such that:

$$\mathcal{L} = \frac{1}{\sigma} \frac{dN}{dt} \tag{2.2}$$

where $\frac{dN}{dt}$ is the rate of produced events and σ is the *cross-section*, which is related to the probability of the interaction and is a function of the center-of-mass energy of the accelerator ($\sqrt{s}$). For a fixed center-of-mass energy, the total or *integrated luminosity*, is the time-integral of the instantaneous luminosity:

$$L = \int \mathcal{L} dt \tag{2.3}$$

measured in inverse barns (1 b = 10^{-8} m^2).

The total amount of integrated luminosity delivered to ATLAS during LHC Run 2 was 156 fb^{-1}, as measured by the LUCID-2 detector [33]. Due in part to detector warm up latencies, the total integrated luminosity recorded by ATLAS is less than the amount delivered and amounted to 147 fb^{-1}. The final integrated luminosity for use in physics analysis with stable beam conditions was 139 fb^{-1}. The luminosity is shown cumulatively for the full LHC Run 2 period in Figure 2.2.
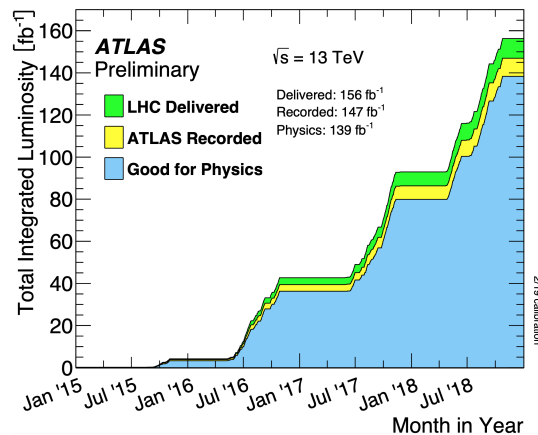
Figure 2.2: The cumulative integrated luminosity delivered during LHC Run 2 given in green. The cumulative integrated luminosity recorded by ATLAS given in yellow. The cumulative integrated luminosity for use in physics analysis given in blue [34].

26

Luminosity is directly proportional to the number of proton-proton interactions per bunch-crossing. This is beneficial in the sense that more interactions result in more available data in a shorter period of time. However, processes that yield interesting physics do not occur with every interaction. So-called "soft-scattering" processes are low momentum transfer interactions which can interfere with data-taking and create sub-optimal conditions for detector operations. The presence of soft-scattering background processes is referred to as *pile-up* and will be referred to at various points in this thesis.

The number of pile-up events can be quantified as:

$$\mu = \frac{L\sigma_{\mathrm{inelastic}}}{n_b f} \tag{2.4}$$

where $\sigma_{\mathrm{inelastic}}$ is the inelastic cross-section for proton-proton interactions. Figure 2.3 shows the average number of interactions per bunch crossing ($< \mu >$) for the LHC Run 2 data taking period which was approximately 34 [34].
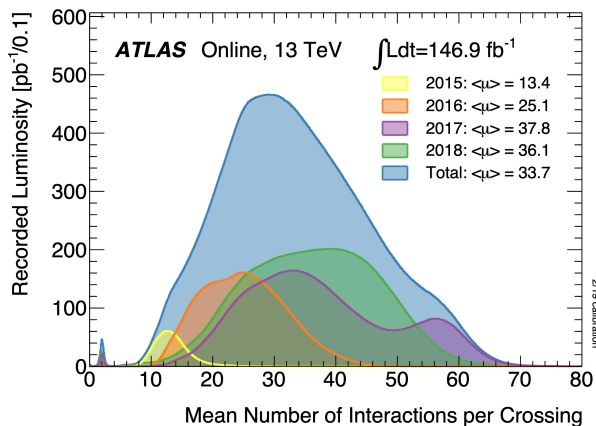
Figure 2.3: Average pile-up interactions per year for LHC Run 2 [34].

2.2 The ATLAS Detector

The ATLAS detector [28] is designed to record interactions from proton-proton collisions at the LHC. The physics program at ATLAS is robust and includes precision SM measurements as well as BSM searches. It is the largest detector of its kind ever built and is one of two general purpose detectors at the LHC (the other being CMS).

ATLAS is a cylindrical detector 44 m in length and 25 m in height, with "barrel" and "end-cap" components. The barrel portion of the detector is coaxial with the interaction point and the end-cap portions are comprised of two forward disk-shaped regions. This design allows almost full 4π solid angle coverage. Figure 2.4 shows a schematic of the detector and its various sub-detector systems.
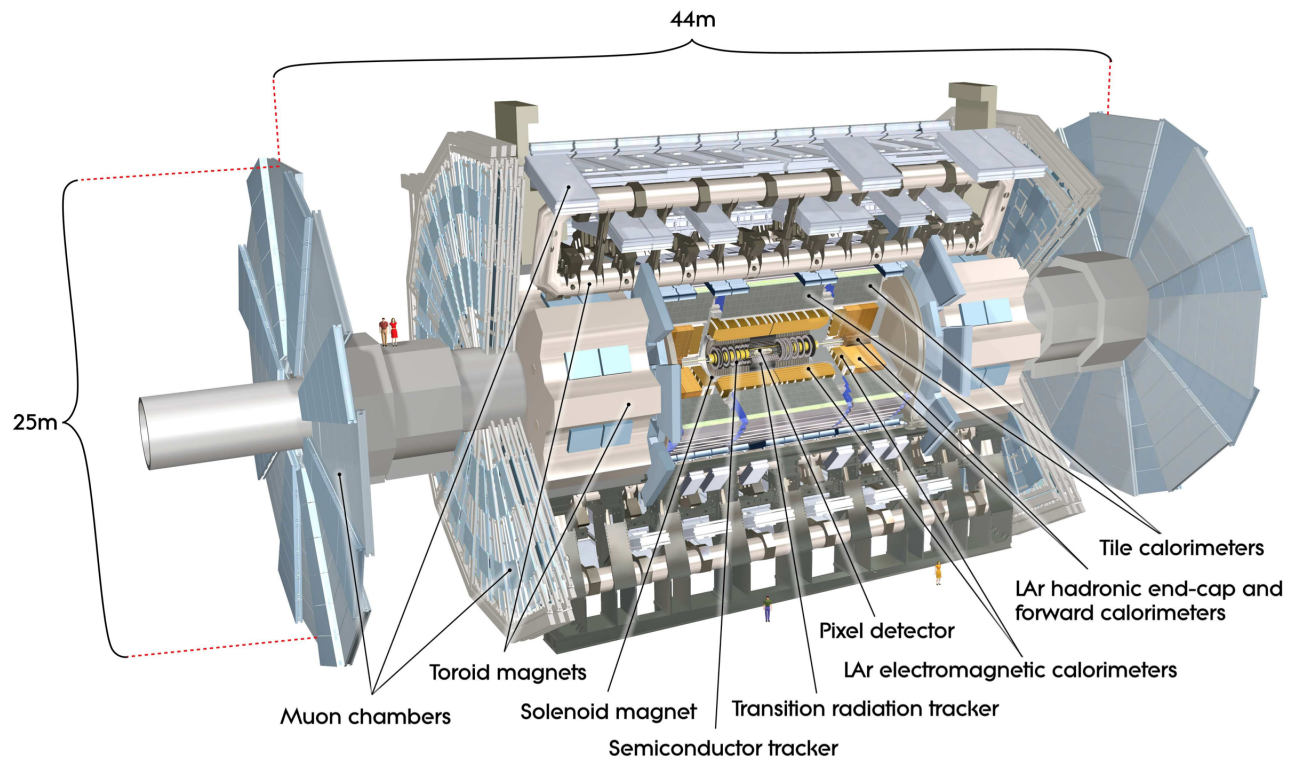
Figure 2.4: The ATLAS Detector [28].

ATLAS studies proton-proton collisions by reconstructing the four-momenta of decay products. ATLAS has four main sub-detector systems, each of which contributes a specific measurement to the overall reconstruction process. The sub-detector components will be described in more detail in the forthcoming sections, but an overview is given below:

- The **Inner Tracker** is the innermost layer of the ATLAS detector and is comprised of high granularity tracking detectors. It is responsible for recording the trajectory of charged particles and infers momentum by using a solenoidal magnetic field. The inner tracker is also responsible for reconstructing the interaction vertex.

- The **Calorimeter System** surrounds the inner tracker and is responsible for measuring the energy of particles. There are two calorimeter systems: the electromagnetic and the hadronic. The former measures energy deposits of charged particles and photons, and the latter measures energy deposits of hadrons.

- The **Muon Spectrometer** is a tracking system that provides a secondary measurement of muons, which transverse the majority of the detector without being absorbed.

- The **Magnet System** provides magnetic fields used for the measurement of charged particle momentum and electric charge. There are two magnet systems, the first is a 2 T solenoid magnet that surrounds the inner tracker and the second is a toroid magnet that surrounds the muon spectrometer. The toroidal magnet system varies between 0.5 and 1 T.

The coordinate system of ATLAS is defined relative to the interaction point (or LHC bunch-crossing point), which is taken as the origin. The z-axis points along the direction

of the beam-line, the x-axis is defined towards the center of the LHC ring and the y-axis is straight upward. Particles measured by ATLAS are relativistic, thus the coordinate system is best described in the $\eta - \phi$ plane, where η is the *pseudorapidity*[1] and ϕ is the azimuthal angle along the direction of the beam-line. The polar angle perpendicular to the beam-line (θ) is related to η, such that:

$$\eta = -\ln\left(\tan\frac{\theta}{2}\right) \tag{2.5}$$

The angular separation between two objects in the $\eta - \phi$ plane is:

$$\Delta R = \sqrt{(\Delta\eta)^2 + (\Delta\phi)^2} \tag{2.6}$$

The momentum of particles transverse to the beam-line (p_T) is a Lorentz-invariant quantity. The transverse component of the initial proton-proton interaction is approximately zero. Therefore, the initial p_T of any given event is also approximately zero by momentum conservation. As ATLAS is designed to reconstruct energy and momentum of particles that are a result of these interactions, it should naively be expected that the total reconstructed p_T of events is also approximately zero. However, many events have substantial "missing energy" due to the presence of neutrinos which escape the detector without interaction or absorption. Therefore, the *missing transverse energy* (E_T^{miss}) is another useful quantity that will be used extensively in this thesis.

2.2.1 Inner Tracker

The ATLAS inner tracker (IT) [35] consists of three sub-detector systems: the pixel detector (PD), the semiconductor tracker (SCT) and the transition radiation detector (TRT). The IT

---

[1]In the relativistic or massless limit $\eta \approx y$, where y is the *rapidity* and differences in y are Lorentz invariant.

begins approximately 3 cm from the beam-line and extends to 1.1 m while providing full 2π coverage in ϕ. Along the beam-line it provides $|\eta|$ coverage up to 2.5. A cross-section of the IT is shown in Figure 2.5.
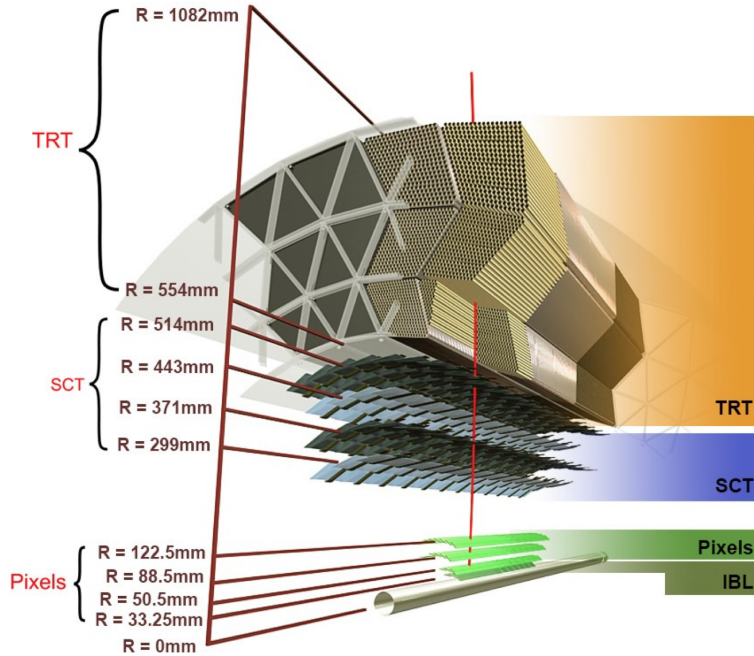
Figure 2.5: ATLAS inner tracker with sub-detector systems: pixel detector, semiconductor tracker, transition radiation tracker (in order of increasing radial distance from beam-line) [36].

Each of these sub-detector systems are designed to provide information for measurement of charged particle trajectory and momentum. The IT is surrounded by a solenoid magnet. The magnetic field produced by the solenoid provides a measurement of charged particle momentum [37], where the momentum of a charged particle is proportional to its radius of curvature in a known magnetic field. The transverse momentum resolution provided by the inner tracker is:

$$\frac{\sigma_{p_T}}{p_T} = a p_T \oplus b \tag{2.7}$$

31

where a was measured as 0.0048 and b as 0.16 using cosmic ray data [38]. The resolution deteriorates as a function of increasing p_T. As the p_T increases, the radius of curvature also increases leading to stiffer curves. This makes it intrinsically more difficult to precisely determine the momentum.

In addition to trajectory and momentum measurements for individual particles, the IT is responsible for reconstructing interaction vertices. This is important in two main ways. First, it allows precise measurement of secondary vertices which are the result of unstable particles decaying away from the primary vertex, such as for τ leptons and B-hadrons, which aids in their identification. Second, it allows for the primary hard-scatter vertex to be decoupled from secondary pile-up vertices. This helps to negate background processes from unrelated interactions. The important quantities for vertex determination are the longitudinal and transverse *impact parameters*, z_0 and d_0, where the impact parameter resolutions are 80 and 20 μm respectively for tracks above 10 GeV [39].

Pixel Detector   The PD is composed of n-in-n silicon-crystal as the active material. A reversed-bias is applied across the sensor, which has a two-fold effect. First, a charge-depleted region is created which allows unique charge carriers to be produced upon ionization from transversing charged particles. Second, the bias sweeps ionized charge towards readout electrodes. The crystal is segmented into *pixels*, which allows readout with high granularity.

Pixel detectors are built into *modules*, which consists of multiple pixels that share data readout and power. There are 1,744 modules with 47,232 pixels resulting in over 80 million readout channels. The pixel dimension, or *pitch*, is 50×400 μm in the $r - z$ plane where r is the radial direction from the beam-line and z is the direction along the beam-line. The

resolution of the detector is 14×115 μm in the $r - z$ plane, which is derived by considering charge-sharing between neighboring pixels. There are three barrel layers and three end-cap layers in both forward regions.

Insertable b-Layer   Prior to LHC Run 2, a fourth layer was inserted into the PD as the innermost layer to the beam-line, called the insertable b-layer (IBL) [36]. The pixel technology was improved relative to the original PD design, including introduction of so-called 3D sensors. These sensors allow operation at lower bias voltage, have an intrinsically shorter drift length and are radiation-hard.

The pitch of IBL pixels is smaller than the original PD at 50×250 μm in the $r - z$ plane. These modules are also capable of operating at up to fluences of 5×10^{15} n_{eq}/cm^2 non-ionizing energy loss, where n_{eq}/cm^2 is neutron radiation-equivalent flux. Addition of the IBL improved impact parameter resolution by 40% [39].

Semiconductor Tracker   The SCT is another silicon-based tracking system surrounding the PD. The principle of operation is the same as pixels, but with a larger pitch. This increase of pitch is necessary to increase the number of measurement points needed for track reconstruction while minimizing costs of the entire IT. The density of tracks decreases with radial distance from the interaction point, which maintains the practicality of the design.

The SCT is comprised of 4,088 double-sided p-in-n silicon-crystal modules with an 80 μm pitch in the $r - z$ plane, totaling 768 readout strips per module. The sensors on the top and bottom are rotated by 40 mrad relative to each other to improve resolution. There are four barrel layers and nine end-cap layers in each forward region, yielding a total of 6.3 million readout channels. The resolution in r is 17 μm and 580 μm in z.

Transition Radiation Tracker The final radial layer of the IT is the TRT, which is a collection of 298,304 straw tubes. The tubes are filled with a gas mixture of 70% Xe, 27% CO_2 and 3% O_2. As a charged particle transverses the gas, ionized electrons are collected by a gold-plated tungsten wire where they are processed for readout. The resolution in the $r - \phi$ plane is 130 μm, which is significantly lower than the semiconductor trackers closest to the beam-line. However, the TRT provides 36 hits per track, which allows for a meaningful measurement when combined with the PD and SCT.

The TRT also provides a method of particle identification between electrons and charged pions. X-rays are produced when relativistic charged particles cross between boundaries of materials with different dielectric constants. This effect is larger for electrons, which means more radiation emissions are produced for electrons than for pions.

2.2.2 Calorimeters

Calorimeters are used in ATLAS to measure the energy of particles produced in proton-proton interactions. The calorimeters are placed after the IT (and also after the solenoid magnet). ATLAS uses *sampling* calorimeters which means that only a fraction of incident energy is absorbed, however, this provides granularity in the $\eta - \phi$ plane. This design utilizes a dense *absorbing material* which creates showers of secondary particles that are readout in the *active material*. The energy of the incident particle is measured by counting the constituents of the shower. The design of the ATLAS calorimeters is such that the incident particle is completely stopped before exiting the detector. This provides a robust energy measurement and also works to reduce the amount of E_T^{miss}, which is important to infer the presence of neutrinos. Figure 2.6 shows a schematic of the ATLAS calorimeter system.
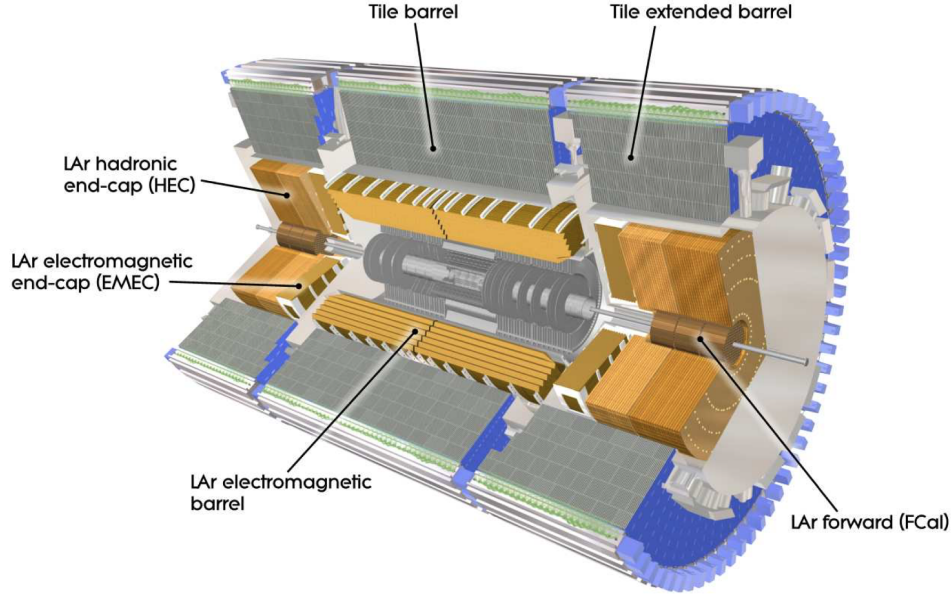
Figure 2.6: The ATLAS Calorimeter System with the electromagnetic and hadronic calorimeters [28].

ATLAS employs two types of calorimeters, designed to measure the energy deposits of different types of particles. The electromagnetic calorimeter (ECAL) measures the energy of electrons and photons, where the hadronic calorimeter (HCAL) measures the energy of hadrons (and also hadronically decaying τ leptons). Calorimeters are typically designed based on the *radiation length* (X_0) or the *nuclear interaction length* (λ) of the material. For the ECAL, the defining quantity is X_0, which is the length that a high energy electron can transverse the material before its energy decreases by $1/e$ of its original energy. For the HCAL, the defining quantity is λ, which is the mean length transversed by a hadron before an inelastic nuclear interaction.

Electromagnetic Calorimeter   The ATLAS ECAL [40] surrounds the IT and solenoid magnet, where it covers the area of $|\eta| < 3.2$, including the barrel and end-cap regions. The

active material is liquid argon (LAr) and the absorber material is lead. Electrons and photons initiate electromagnetic showers in the lead material and the showering particles ionize the LAr, where they are read out with the help of an electric field.

The ECAL has a distinctive accordion shape enabling full ϕ coverage. However, there exists a crack region in η $(1.37 < |\eta| < 1.52)$ which has a degraded performance. Electrons in this area were removed in the analysis described in this thesis. The ECAL consists of three layers with a total number of radiation lengths corresponding to 24 X_0. The three layers have decreasing granularity as a function of radial distance from the beam-line, where the first layer provides the most robust energy measurement. The second layer is designed to contain the majority of shower products not absorbed in the first layer, and the third layer acts as a containment layer.

The energy resolution of the ECAL is estimated to be:

$$\frac{\sigma_E}{E} = \frac{0.10}{\sqrt{E}} \oplus c \tag{2.8}$$

where 0.10 is a stochastic value accounting for shower fluctuations and inefficiencies in energy deposition. c, is measured to be less than 2% and accounts for errors in shower containment and energy loss [41].

Hadronic Calorimeter The ATLAS HCAL [42, 43] surrounds the ECAL and consists of the barrel region with $|\eta| < 1.7$, the end-cap from $|\eta| = 1.7$ to $|\eta| = 3.2$ and the forward region from $|\eta| = 3.1$ to $|\eta| = 4.9$. The active material in the barrel are scintillating titles and the absorber material is steel. In the end-cap and forward region, the active material is LAr and the absorbing material is copper in the end-cap and copper/tungsten in the forward region. Hadrons initiate hadronic showers in the absorbing material and the showering particles

ionize the active material, where they are read out. The HCAL consists of three longitudinal layers with a total number of nuclear interaction lengths corresponding to 10 λ.

The energy resolution of the HCAL is estimated to be:

$$\frac{\sigma_E}{E} = \frac{0.52}{\sqrt{E}} \oplus 0.057 \tag{2.9}$$

where the resolution is degraded relative to the ECAL [44]. The main reason for degraded energy resolution performance is low energy nuclear processes, which are typically not reconstructed and yield a significant energy loss. Another culprit is the fact that hadronic showers typically contain an electromagnetic component, which respond differently than the hadronic component in the HCAL.

2.2.3 Muon System

The Muon Spectrometer (MS) [45] is a standalone detector surrounding the calorimeters. It is designed to provide a secondary measurement of the position and momentum of muons, complementary to the IT. Muons are *Minimum Ionizing Particles* (MIPs), which transverse the detector volume without being absorbed and are important decay products for both SM and BSM processes. Therefore, a secondary measurement for muons is advantageous.

The MS is an extremely large detector equipped with its own toroidal magnetic field for momentum measurements, which is 0.5 and 1 T in the end-caps and barrel, respectively [37]. The MS is comprised of gaseous tracking detectors due to its size, which extends to a radius of 11 m and covers the an area of $|\eta| < 2.7$. There are four sub-detector systems: the Monitored Drift Tubes (MDTs), the Cathode Strip Chambers (CSCs), the Resistive Plate Chambers (RPCs) and the Thin Gap Chambers (TGCs). A schematic of the MS is shown in

Figure 2.7.
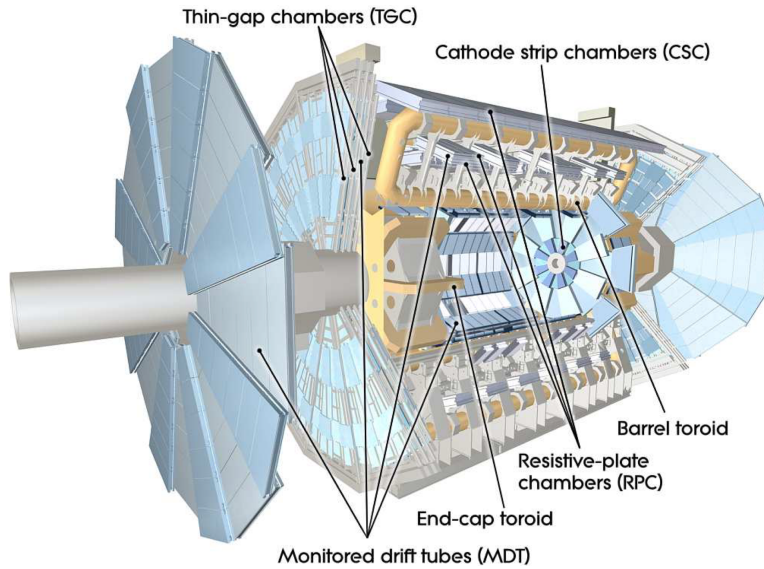
Figure 2.7: ATLAS Muon System with sub-detector systems: the Monitored Drift Tubes, the Cathode Strip Chambers, the Resistive Plate Chambers and the Thin Gap Chambers [28].

The MDTs and CSCs are high precision tracking detectors, where MDTs are used in the barrel region ($|\eta| < 2.7$) and CSCs in the forward region ($2.0 < |\eta| < 2.7$]). The MDTs are gas tubes with a central high voltage wire for charge collection. CSCs are also gas tubes but with multiple high voltage wires for segmented readout capability. The CSCs are used in the forward region, where the readout rate is high and precision readout is required.

The RPCs and TGCs are lower precision tracking detectors compared with the MDTs and CSCs. However, they are designed with a faster readout capability and are used for μ triggering (described in Section 2.2.4). RPCs are used in the barrel region ($|\eta| < 1.05$) and TGCs are used in the end-cap ($1.05 < |\eta| < 2.4$). RPCs are gaseous tracking detectors utilizing two resistive plates for charge collection. TGCs operate similarly to CSCs but with a smaller space between wires which helps to achieve time resolution and high-rate capabilities

necessary for triggering.

2.2.4 Trigger System

The proton collision rate at the LHC is 40 MHz, which corresponds to 50-60 TB of available data every second when taking into account all available information from the ATLAS detector systems. This amount of data comes with obvious problems of feasibility in terms of available bandwidth and disk storage. Fortunately, only a subset of collision data is useful for physics, as most information is the result of low momentum transfer soft-interactions. In order to select events that are of physics interest, effectively cutting bandwidth down to a manageable rate, a trigger system is used to pre-select events for reconstruction and storage. There are two independent trigger systems in ATLAS: the hardware-based first level (L1) and the software-based high level triggers (HLT) [46]. The trigger system for ATLAS is shown schematically in Figure 2.8.

The L1 trigger uses information from the ECAL and MS, which provide signals to offline hardware for signal processing. The offline hardware requires a latency of 2.5 μs to avoid dead-time from subsequent collisions. The ECAL and MS L1 trigger systems process events independently by searching for *regions of interest* (RoIs). The calorimeter defines RoIs based on energy deposit clusters in the ECAL. The MS defines RoIs based on track multiplicities. If a RoI is found, the full event information is sent to the HLT for further processing, otherwise the event is discarded. The L1 trigger system reduces the bandwidth from 40 MHz to 80 kHz.

The HLT trigger system is a farm of CPU cores which reconstruct objects passed from the L1 trigger to make finer decisions regarding event selection. Information from all sub-detector systems is used where events can be selected based on event topology, including isolation and
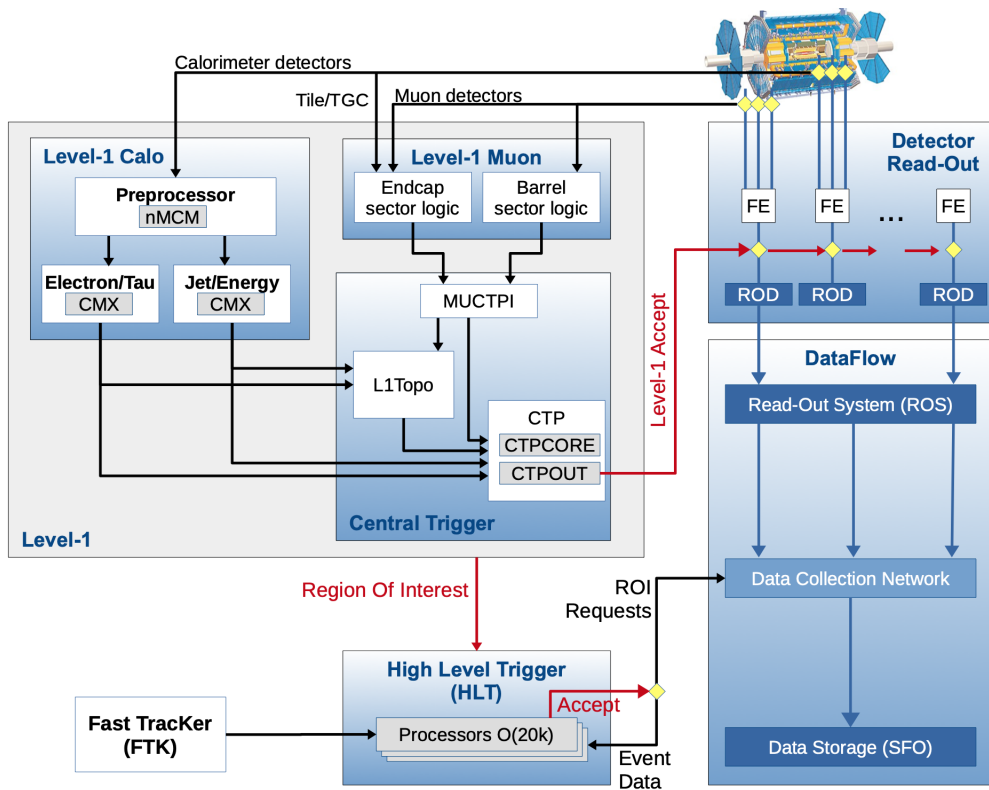
Figure 2.8: ATLAS Trigger System [46].

momentum requirements. Events are sent offline for further processing if it passes the criteria of at least one HLT trigger. The HLT trigger menu is specific for the run year and is meant to select events based on detector conditions, and for specific calibration and analysis purposes. The bandwidth is reduced to 1 kHz after the HLT trigger. *Pre-scales* can be applied to the L1 or HLT triggers to ensure the bandwidth is kept to 1 kHz, where only a fraction of events are kept.

Chapter 3

Physics Object Definitions

Physics objects are reconstructed utilizing raw hit information from the ATLAS sub-detectors. The reconstructed objects are typically identified with a level of confidence in terms of selecting *prompt* objects and rejecting *non-prompt* objects. Prompt objects are those which originate from the primary interaction and non-prompt objects originate from pile-up, hadron decays or are mis-identified. This manifests itself as a choice in *working point*, which is generally defined in terms of true particle selection efficiency and false particle background selection efficiency. Working points overlap such that "tighter" working points are a subset of "looser" ones. The choice depends on the needs of the analysis and this chapter will discuss those used for this thesis. In particular, the reconstruction of individual particle tracks and vertices, topological calorimeter clusters, electrons, muons, jets, hadronically decaying taus and missing transverse momentum will be introduced.

3.1 Tracks and Vertices

A *track* is the trajectory of a particle through a detector. ATLAS performs track reconstruction through an algorithmic process, beginning with raw hits from the PD and SCT [47]. Charge deposited into silicon layers can be distributed across multiple pixels or strips, which provides information about the angle of trajectory through the detector volume. Figure 3.1 shows a representation of a particle with a trajectory across two layers of silicon, given by the blue arrow. The readout electrodes are shown in green and the relative amount of collected charge on each electrode is shown as the red bar. In the electrode with the larger red bar,

more charge was deposited and is directly proportional to the area of silicon the particle transversed. Adjacent pixels or strips are combined into *clusters*.
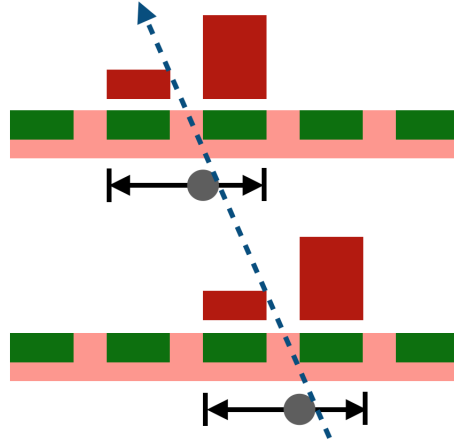
Figure 3.1: Clustering of hits in adjacent silicon electrodes based on collected charge. See the text for more information.

Clusters form the basis of 3D *space-points*, which are defined by utilizing charge information from adjacent pixels and hits on both sides of strip modules to infer the three-dimensional particle track. Sets of three individual space-points across layers are grouped to form *track seeds*. Seeds are used for the curvature measurement needed to infer the particle momentum. Space-points in adjacent layers are then added to track seeds to form *track candidates*. Incorporating additional space-points into a track candidate utilizes a combinatorial Kalman filter [48]. Multiple track candidates are possible as multiple additional space-points may be compatible with the original track candidate.

In order to distinguish multiple potential track candidates, an ambiguity solver is employed and issues each track candidate a probability score. A χ^2 fit is also utilized to provide additional information regarding the significance of the fitted track. Clusters can only be

assigned to a maximum of two track candidates and a track candidate can not have more than two shared clusters. Tracks are also rejected if the track p_T is less than 400 MeV or has less than seven clusters assigned. Once the track candidates have been identified by assigned probability and χ^2, the track is extended by adding space-points from the TRT.

Track candidates are then extrapolated towards the beam-line to reconstruct the impact parameters. The transverse impact parameter (d_0) is measured relative to the beam-line in the transverse direction. The longitudinal impact parameter (z_0) represents the distance along the beam-line between d_0 and the primary vertex (once defined) or the *beam spot* (prior to primary vertex determination). The beam spot is estimated by a likelihood fit to the spatial distribution of multiple primary vertices. This is done every 10 minutes during detector calibration by using a dedicated data stream [49]. The beam spot serves as a reference point for impact parameter determination. Tracks that are consistent with impact parameter requirements are kept, while those that are inconsistent are discarded. The requirements are such that $|d_0| < 2.0$ mm and $|z_0\sin\theta| < 3.0$ mm.

Final track candidates are those that are not discarded from the aforementioned algorithmic approach including resolution of ambiguities. These are then subject to a high-resolution fit using all available information. Interaction vertices are defined from final track candidates using *vertex finding* and *vertex fitting* [49]. In vertex finding, all tracks with similar impact parameter measurements are used to define vertex seed positions. An iterative χ^2 minimization step is then performed and after each iteration, tracks are assigned a score based on their compatibility with the vertex. The vertex position is then recalculated by using the score assigned to tracks. After the minimization step is complete, tracks that are incompatible by more than seven standard deviations are assigned a new vertex and the process begins again.

The primary vertex is defined as the vertex with the highest sum of transverse momenta squared $(\sum p_T^2)$ and at least two tracks.

3.2 Topological Calorimeter Clusters

Energy deposition in the calorimeter system is typically spread across multiple calorimeter cells. Individual cells are clustered together to reconstruct energy deposition from prompt objects. ATLAS uses the *topo-cluster* algorithm [50] to group calorimeter cells into topologically-connected clusters or *topo-clusters*.

The algorithm uses the signal-to-noise significance, defined as:

$$\zeta = \frac{E_{\text{cell}}}{< E_{\text{cell}}^{\text{noise}} >} \tag{3.1}$$

where E_{cell} is the energy deposited in the cell and $< E_{\text{cell}}^{\text{noise}} >$ is the average noise in the cell. First, *Cluster seeds* are formed from all cells with $\zeta > 4$. Adjacent cells, both in the same layer and neighboring layers, are added to the cluster if $\zeta > 2$. This process is repeated until all adjacent cells with $\zeta > 2$ are added to the cluster. Finally, all adjacent cells with $\zeta > 0$ are added to the cluster. If clusters are merged after this process, they are split if significant local maxima exist. The result of the topo-cluster algorithm is shown for a simulated di-jet event in Figure 3.2.

3.3 Electrons

Electrons are reconstructed by matching topo-clusters in the ECAL with tracks reconstructed in the ID [51]. However, given the high probability of bremsstrahlung, a specialized Gaussian-sum filter track-finding algorithm [52] is used for electrons to account for energy losses with
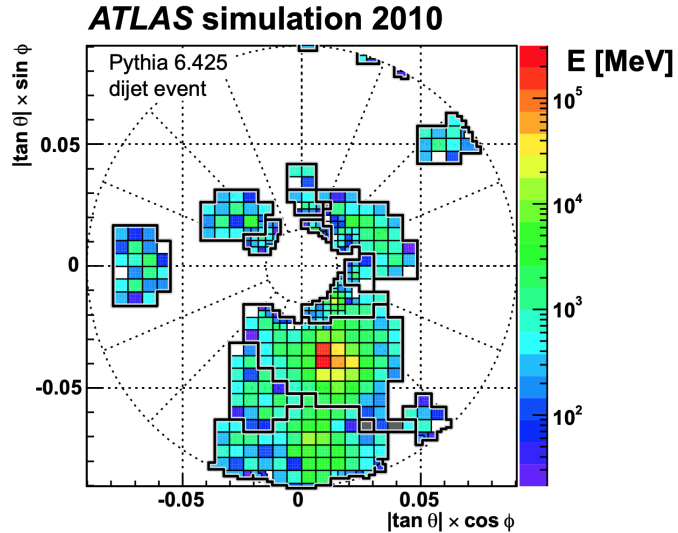
Figure 3.2: Result of the topo-cluster algorithm for a simulated di-jet event. The energy deposition is shown in the z-axis and reconstructed clusters are outlined in grey lines [50].

interaction in ID material.

Once electrons are reconstructed, the energy scale is calibrated to correspond to the original e energy. First, the relative energy response of individual ECAL layers are adjusted in data to match the relative response in simulation. A multivariate analysis technique is then used to calculate the energy of e, which is trained using simulated events without pile-up and is applied to both simulated and data events. The algorithm is designed to optimize the energy resolution and minimize effects from energy loss in front of the ECAL. The input variables are related to shower development in the ECAL. The ratio of the reconstructed momentum from the ID to the energy deposited in the ECAL is then utilized to correct for localized irregularities in calorimeter cell response using $Z \rightarrow e^+e^-$ events. Finally, scale factors are applied to data to correct for residual mis-calibration between data and simulation. Additional scale factors are applied to simulation to account for differences in

energy resolution between data and simulation.

Identification working points are defined using a likelihood discriminant technique which is able to discriminate prompt electrons from converted photons, hadrons and electrons originating from hadronic decays. Information from the calorimeter shower shape, the energy-to-momentum ratio and compatibility between the shower shape and reconstructed e track, are all considered in the discriminant. Three working points with increasing background rejection power are defined: `loose`, `medium` and `tight`. The average true (background) e efficiencies are 93% (0.5%), 88% (0.2%) and 80% (0.1%), respectively[1].

Isolation criteria is also imposed on e candidates to further separate prompt electrons from background electrons and is particularly important in a high pile-up environment. The calorimeter-based variable, E_T^{cone20}, is defined as the sum of transverse energy in all topo-clusters inside a cone of radius $\Delta R = 0.2$, with the e energy subtracted. The tracker-based variable, $p_T^{\mathrm{varcone30}}$, is the sum of tracks with $p_T > 1$ GeV in a cone of size $\Delta R = \min(10/p_T, 0.3)$, excluding the electron track. Isolation working points are defined using cuts on E_T^{cone20} and $p_T^{\mathrm{varcone30}}$. The `Gradient` working point is designed to maximize prompt e efficiency by varying cuts across the p_T spectrum. The `HighPtCaloOnly`, `Loose` and `Tight` working points have fixed cuts. The `HighPtCaloOnly` working point is designed to maximize background rejection at large E_T, where the `Tight` working point provides a greater background rejection compared with `Loose`. Figure 3.3 shows the true e identification and isolation reconstruction efficiencies for the various working points measured in $Z \to e^+e^-$ events.

This thesis defines two types of e candidates. Signal electrons (referred to as "tight") are

---

[1]Background efficiency is the percentage of background objects selected by the working point.
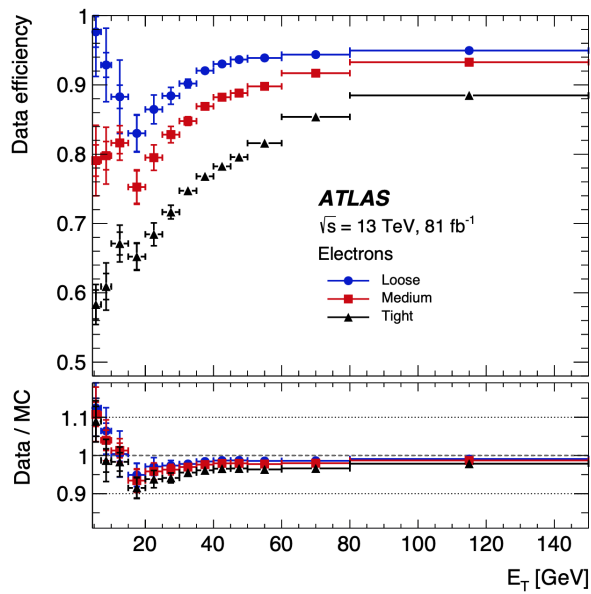
a
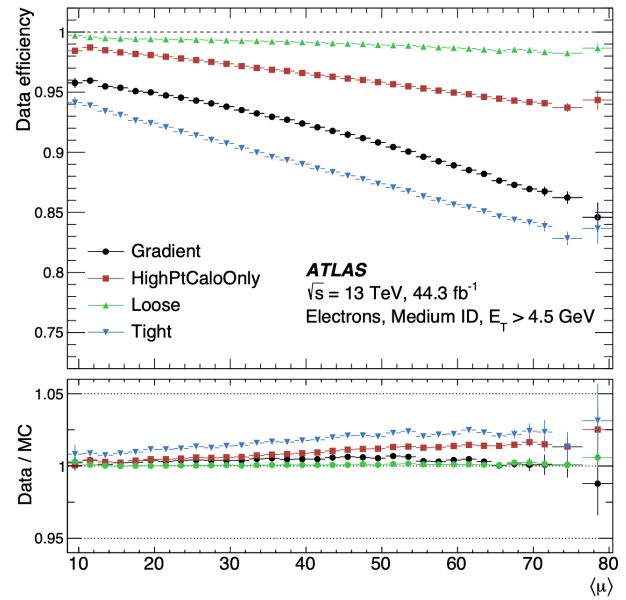
b

Figure 3.3: (a) True e reconstruction efficiency as a function of E_T for all available likelihood-based identification working points. (b) True e reconstruction efficiency as a function of $< \mu >$ for `Medium` identification electrons, with all available isolation working points [51].

those selected for the nominal analysis. Background electrons (referred to as "loose") have a less constraining cut than signal electrons and are used to estimate the fake e contribution (Chapter 7)[2]. Signal electrons in this thesis are selected with the `Tight` identification working point. The analysis presented in this thesis targets events with boosted topology where electrons are less separated, therefore the `Loose` isolation working point is chosen ($E_T^{\text{cone20}}/p_T < 0.2$ and $p_T^{\text{varcone30}}/p_T < 0.15$). Background electrons are the same as signal electrons except for either an inverted identification or isolation working point. The inverted identification working point is `Loose` and inverted isolation working point is `!Loose`[3].

e candidates in this thesis are selected with $p_T > 30$ GeV and $|\eta| < 2.47$, excluding the transition region between the barrel and end-cap ECAL ($1.37 < |\eta| < 1.52$). To ensure electrons originate from the primary vertex, requirements are placed on the transverse and longitudinal impact parameters such that $|d_0(\sigma)| < 5.0$ and $|z_0 \sin \theta| < 0.5$ mm, where $d_0(\sigma)$ is the d_0 significance. The electron selection criteria is given in Table 3.1.

3.4   Muons

Muons are reconstructed independently in the ID and the MS [53]. Tracks in the ID are reconstructed as described in Section 3.1. In the MS, hits are grouped individually in the sub-detector systems prior to global combination. μ candidates must first be triggered in the TGC or RPC and hits are combined. A straight-line fit is then performed with hits in the MDT. Lastly, a fit in the $\eta - \phi$ plane is used to combine hits in the CSC. Track seeds

---

[2] "Tight" and "loose" in this context follow field-centric nomenclature and distinguish between objects selected for analysis and those used for the study of fakes. A "tight" signal object does not necessarily have the same definition as the `Tight` working point. Rather, a chosen working point is used to **define** a "tight" signal object.

[3]Borrowing from the language of programming operators, where ! = "not"

Requirement	Signal Electrons (Tight)	Background Electrons (Loose)
Identification	`Tight`	`Loose`
		`or`
Isolation	`Loose`	`!Loose`
p_T	> 30 GeV	
$|\eta|$	< 2.47 with crack veto $1.37 < |\eta| < 1.52$	
$|d_0(\sigma)|$	< 5	
$|z_0 \sin\theta|$	< 0.5 mm	

Table 3.1: e selection for the analysis presented in this thesis.

are chosen starting with middle layers where trigger hits are available and then moving to the remaining MS layers. Segments in the sub-detector systems are combined into track candidates using a global χ^2 fit. Once candidates tracks in the ID and MS are resolved, global μ candidates can be defined using available information:

- *Combined muons (CB):* μ candidates are built from track information in both the ID and MS. A global re-fitting procedure is performed to match candidate tracks, where tracks can either be extrapolated from the MS to the ID, or from the ID to the MS.

- *Segment-tagged muons (ST):* μ candidates are extrapolated from the ID to the MS, where hits only exist in one layer of the MS. This is typically used in low p_T events or in areas of poor acceptance.

- *Calorimeter-tagged muons (CT):* μ candidates with tracks from the ID matched to a calorimeter deposit. This is typically used to compensate in regions with inactive

material.

- *Extrapolated muons (ME):* μ candidates with a reconstructed MS track, but poorly reconstructed tracks in the ID. This is typically used to extend the acceptance into regions not covered by the ID.

The momentum scale and resolution are corrected in simulation to match data. A likelihood template fit extracts information regarding the mis-match between simulation and data using the invariant mass spectra of $Z \to \mu^+\mu^-$ and $J/\psi \to \mu^+\mu^-$ events. Both momentum scale and momentum smearing corrections are obtained separately in the ID and MS and are applied to simulation.

Identification working points are designed to select prompt muons from hadronic decays. A discriminating procedure uses information from charge and momentum ratios in the ID and MS, and the χ^2 of combined tracks from the ID and MS. The working points derived using this procedure are:

- `Medium`: Uses CB and ME μ candidates. Designed to minimize uncertainties and is the default working point in ATLAS. The average true (background) μ efficiency is 96.1% (0.17%).

- `Loose`: Uses any μ candidate type. CT and ST muons are added to the `Medium` selection in the $|\eta| < 0.1$ region. Designed to maximize the reconstruction efficiency of muons. The average true (background) μ efficiency is 98% (0.76%).

- `Tight`: Uses CB muons with at least two hits in the MS while satisfying the `Medium` working point. Designed to maximize purity of muons with a trade-off in efficiency.

The average true (background) μ efficiency is 91.8% (0.11%).

- **High-p_T**: Uses CB muons that pass the `Medium` working point. Candidates must have at least three tracks in the MS and $p_T > 100$ GeV. Improves high p_T resolution with a trade-off in efficiency. The average true (background) μ efficiency is 80.4% (0.13%).

Isolation criteria is also imposed on μ candidates to further separate prompt muons from background muons and is particularly important in a high pile-up environment. Working points are defined by considering the momentum of the μ candidate in the ID. The ID-based variable, $p_T^{\text{varcone30}}$, is the sum of tracks with $p_T > 1$ GeV in a cone of size $\Delta R = \min(10/p_T, 0.3)$, excluding the μ track. Working point definitions are similar to those of electrons (Section 3.3). Figure 3.4 shows the identification and isolation reconstruction efficiencies for true muons.

The thesis defines two types of μ candidates. Signal muons (referred to as "tight") are those selected for the nominal analysis. Background muons (referred to as "loose") have a less constraining cut and are used to estimate the fake μ contribution (Chapter 7). Signal muons in this thesis are selected with the `Medium` identification working point for $p_T < 300$ GeV and the `High-$p_T$` identification working point for $p_T > 300$ GeV. μ candidates are also required to satisfy the `Tight` isolation working point ($p_T^{\text{varcone30}}/p_T < 0.06$). Background muons are the same as signal muons, with the isolation working point inverted to `!Tight`.

μ candidates in this thesis are selected with $p_T > 30$ GeV and $|\eta| < 2.5$. To ensure muons originate from the primary vertex, requirements are placed on the transverse and longitudinal impact parameters such that ($|d_0(\sigma)| < 3.0$ and $|z_0 \sin\theta| < 0.5$ mm. The μ selection criteria is given in Table 3.2.
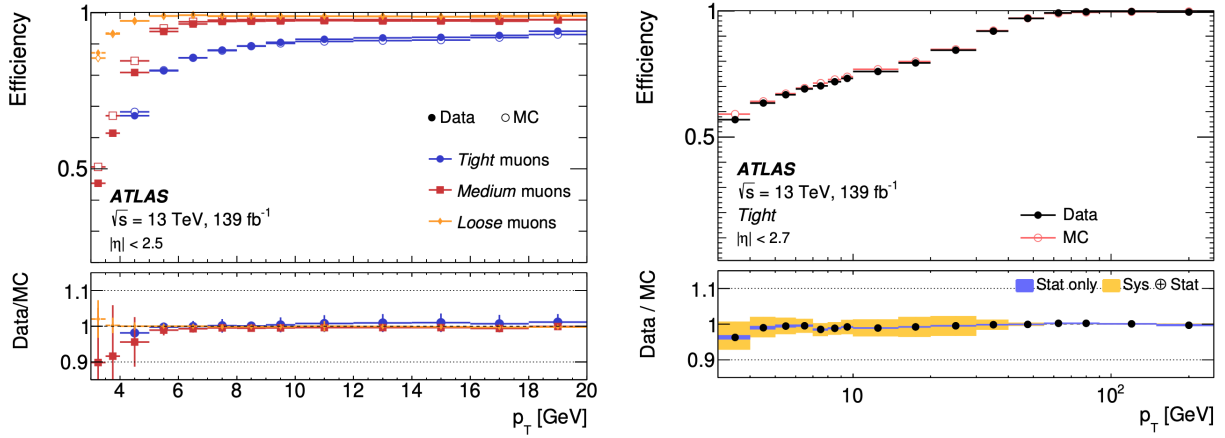
Figure 3.4: (a) True μ reconstruction efficiency as a function of p_T for all available identification working points in $J/\psi \to \mu^+\mu^-$ events. (b) True μ reconstruction efficiency as a function of p_T for the `Tight` isolation working point in $Z \to \mu^+\mu^-$ events [53].

Requirement	Signal Muons (Tight)	Background Muons (Loose)
Identification		Medium (High-p_T> 300 GeV)
Isolation	Tight	!Tight
p_T		> 30 GeV
$|\eta|$		< 2.5
$|d_0(\sigma)|$		< 3
$|z_0 \sin\theta|$		< 0.5 mm

Table 3.2: μ selection for the analysis presented in this thesis.

3.5 Jets

Reconstruction of hadronic jets in the ATLAS detector makes use of the *Particle Flow* algorithm [54]. Particle flow utilizes both track and topo-cluster information to separate charged and neutral particles. Tracks are selected according to Section 3.1 and are matched to topo-clusters introduced in Section 3.2. All topo-clusters and tracks within a cone of $\Delta R = 0.2$ of each other are subtracted. This is to remove tracks and energy depositions associated with single charged particles.
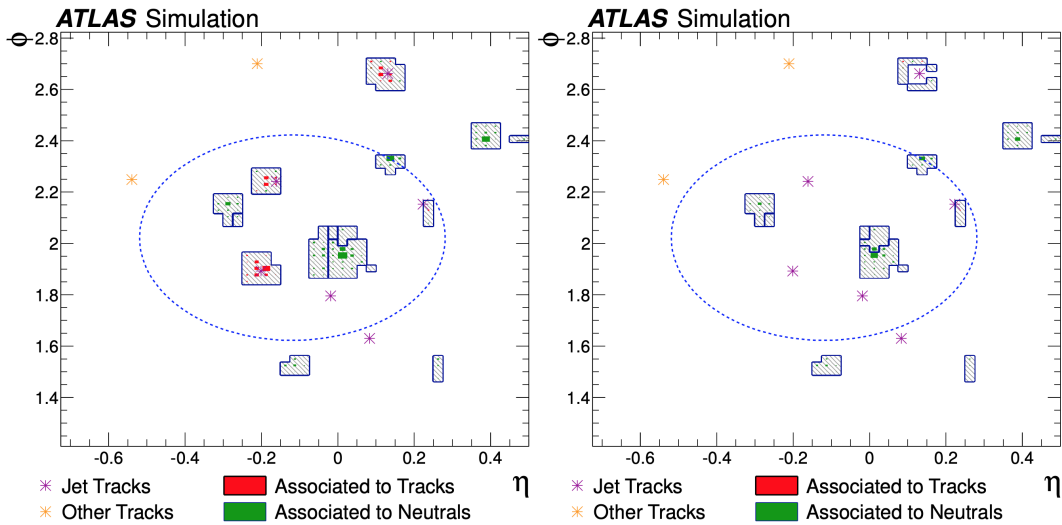
Figure 3.5: Energy subtraction for particle flow jets. Topo-clusters are shown in the blue boxes and tracks are shown with asterisks. The blue eclipse corresponds to a simulated truth jet. On the left, all topo-clusters are shown. On the right, topo-clusters remaining after track subtraction are shown [54].

The remaining topo-clusters, and remaining tracks consistent with the primary vertex ($|z_0 \sin\theta| < 2.0$ mm), are used as input to the anti-k_t algorithm [55]. Anti-k_t is an iterative cone algorithm that clusters objects together to form jets. Two distance parameters are

calculated to form clusters:

$$d_{ij} = \min\left(\frac{1}{k_{ti}^2}, \frac{1}{k_{tj}^2}\right)\frac{\Delta_{ij}}{R^2}, \tag{3.2}$$

$$d_{iB} = \frac{1}{k_{ti}^2} \tag{3.3}$$

where i and j are indices for input objects (tracks and topo-clusters) and $\Delta_{ij}^2 = (\gamma_i - \gamma_j)^2 + (\phi_i - \phi_j)^2$, with γ_i and ϕ_i as the rapidity and azimuthal angle of object i, respectively. k_{ti} is the transverse momentum of object i, and R is the distance parameter which defines the radius of the resulting jet, taken to be 0.4 for ATLAS reconstruction.

In each step of the iterative process, the distances between all objects are calculated. If the distance between object i and the beam-spot (d_{iB}) is the smallest distance, object i is taken as a jet and is removed from the algorithm. Otherwise, if the smallest distance calculated is between object i and j (d_{ij}), these are merged and the process is repeated until no clusters and tracks are left.

Reconstructed jets require an energy calibration step to negate detector effects that can alter the true energy scale or *Jet Energy Scale* (JES) [56]. Detector effects that contribute include energy leakage, non-uniformity of calorimeter response and pile-up. First, the four-momentum of the jet candidate is re-calculated to point towards the primary vertex, rather than the beam spot (without changing the energy). Next, excess energy due to the presence of pile-up is removed by using an area-based correction to the jet candidate p_T. Residual pile-up effects not removed from the last step are accounted for by correcting jet candidate p_T as a function of both μ and the number of primary vertices. After pile-up corrections, the four-momentum of the jet candidate in data is corrected to the simulated JES. The jet candidate is further calibrated by removing flavor dependence and energy leakage effects.

The final step, is an "in situ" calibration of data to simulation using reference objects such as Z bosons, photons and calibrated jets.

To further reject pile-up, the *jet-vertex-tagger* (JVT) is employed [57]. The JVT works by comparing tracks associated with the jet candidate. Specifically, it compares the sum of track p_T associated with the primary vertex to the sum of track p_T associated with any vertex. This thesis uses the `Medium` JVT working point which corresponds to an efficiency of 92%.

Hadrons containing b-quarks (b-jets) can be tagged due to the long lifetime of b-quarks before hadronization. The majority of b-jets have a decay length on the order of millimeters, where the secondary vertex associated with the decay can be decoupled from the primary vertex. ATLAS uses low-level algorithms to identify b-jet properties [58]. Two impact parameter-based algorithms (IP2D and IP3D) use the large impact parameters of b-jets as input. The secondary vertex-finding algorithm (SV1) reconstructs this vertex. A third low-level algorithm is used to reconstruct the full b-jet decay chain using topological jet variables (JetFitter). These low-level algorithms are fed into a multivariate, deep feed-forward neural network (DL1). Figure 3.6 shows the unit-normalized distributions of simulated b-jets, c-jets and light flavor jets as a function of the DL1 output. Several working points are derived, which correspond to a b-tagging efficiency of 60%, 70%, 77% or 85% as measured in $t\bar{t}$ simulated events. This thesis uses the 77% efficiency working point which corresponds to rejection factors[4] of approximately 134, 6 and 22 for light-quark and gluon jets, c-jets and hadronically-decaying τ leptons, respectively.

Jet candidates in this thesis are selected with $p_T > 20$ GeV and $|\eta| < 2.5$. Jet candidates are also selected with the `Medium` JVT working point applied (JVT > 0.2 for $p_T < 60, |\eta| <$

---

[4]Rejection factors are the reciprocal of background efficiency.
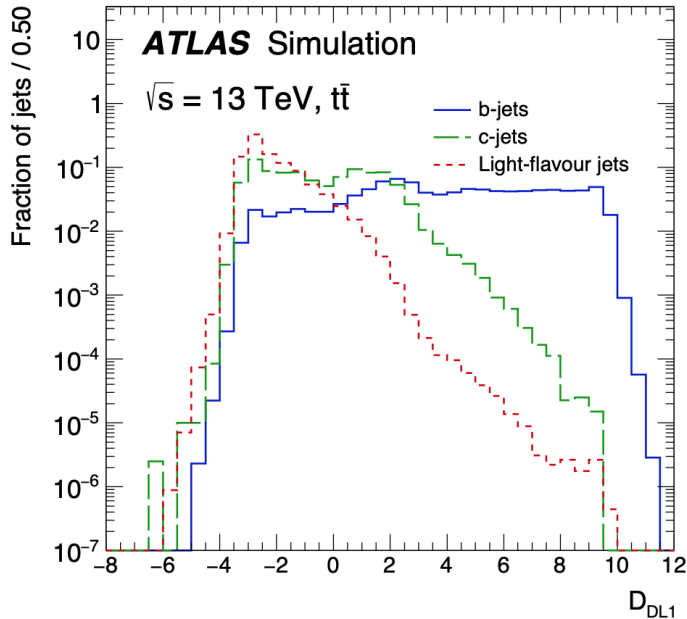
Figure 3.6: Unit-normalized distributions of simulated b-jets, c-jets and light flavor jets as a function of the DL1 output [58].

2.4). b-tagged jet candidates are selected with the 77% efficiency working point. The jet selection criteria is given in Table 3.3.

Requirement	Jets
p_T	> 20 GeV
$|\eta|$	< 2.5
JVT	Medium
b-tag	77%

Table 3.3: Jet selection for the analysis presented in this thesis.

3.6 Hadronic Taus

Tau leptons are unique compared to other charged leptons in that they have hadronic decay modes, which occur about 65% of the time [6]. This thesis considers only τ decays into the hadronic final state (τ_{had}) containing a tau neutrino ν_τ and hadrons. Since ν_τ is lost in the detector volume, only hadronic decay products consisting of charged and neutral pions are visible and are denoted by $\tau_{\text{had-vis}}$. Of the possible τ_{had} decays, 72% contain one charged pion (referred to as 1-prong) and 22% contain three charged pions (referred to as 3-prong) in the final state.

Taus have a mean lifetime of 290.3 fs, which results in a boosted decay length of a few milimeters. This decay length typically occurs before the first layer of the ID such that taus can only be measured indirectly. ATLAS is inefficient at identifying leptonically decaying taus since their signature closely resembles that of a prompt e or μ. Instead, ATLAS utilizes dedicated reconstruction and identification algorithms to tag τ_{had} decays [59].

Jets originating from τ_{had} decays (τ-jets) contain one or three charged tracks inside a cone of $\Delta R < 0.2$ and a relatively void cone of $\Delta R < 0.4$, referred to as the *core cone* and *isolation cone*, respectively. QCD jets however, tend towards a larger number of tracks within a larger cone. The difference in jet structure between τ and QCD jets is illustrated in Figure 3.7.
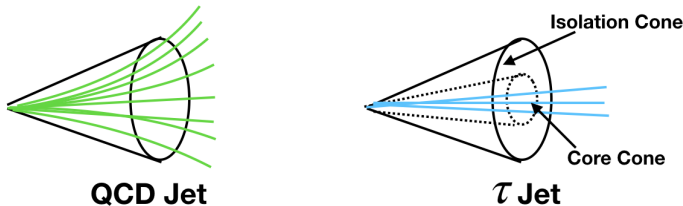
Figure 3.7: Illustration between the difference in QCD and τ-jet cones.

QCD jets can be initiated by either hadronization of quarks or gluons. Quark-initiated jets tend to be more narrow and contain less particles than those jets initiated by gluons. This implies the probability for a quark or a gluon-initiated jet to be reconstructed as a τ-jet differ. As a consequence, the background rejection efficiencies for mis-identified quark and gluon-initiated τ-jets are unique and must be taken into consideration when estimating the fake background composition, as described in Chapter 7.

$\tau_{\text{had-vis}}$ candidates are selected from jets reconstructed through the process outlined in Section 3.5. Reconstructed jets are required to have $p_T > 10$ GeV and $|\eta| < 2.5$. Once the candidate jet is chosen, associated tracks are then used to identify the *tau vertex* (TV). Tracks associated to the TV must have $p_T > 1$ GeV and belong to the core cone region ($\Delta R < 0.2$).

True $\tau_{\text{had-vis}}$ candidates are identified by utilizing a dedicated Recurrent Neural Network (RNN) [60], which is a multivariate analysis technique trained on multi-jet and $Z \to \tau^+ \tau^-$ simulation events to discriminate against QCD jets. There are independent RNNs for 1 and 3-prong $\tau_{\text{had-vis}}$ candidates due to their differing signatures in the detector. From the RNN output, working points are defined with increasing background rejection power. The working points are given in Table 3.4 and the distributions of background rejection power as a function of true $\tau_{\text{had-vis}}$ efficiency is shown in Figure 3.8.

There is also a multivariate analysis technique used to separate 1-prong $\tau_{\text{had-vis}}$ from electrons, which uses a Boosted Decision Tree (BDT) rather than an RNN and is trained on $Z \to e^+ e^-$ events. This thesis uses the `Tight` working point, where the true $\tau_{\text{had-vis}}$ efficiency is 95% and the background rejection power is on the order of 10^2.

The thesis defines two types of $\tau_{\text{had-vis}}$ candidates. Signal taus (referred to as "tight") are those selected for the nominal analysis. Background taus (referred to as "loose") have

Working Point	$\tau_{\text{had-vis}}$ Efficiency		Background Rejection	
	1-prong	3-prong	1-prong	3-prong
Tight	60%	45%	70	700
Medium	75%	60%	35	240
Loose	85%	75%	21	90
Very Loose	95%	95%	9.9	16

Table 3.4: Working points for RNN-based $\tau_{\text{had-vis}}$ identification against QCD jets. The 1 and 3-prong $\tau_{\text{had-vis}}$ efficiencies and background rejection powers are given.
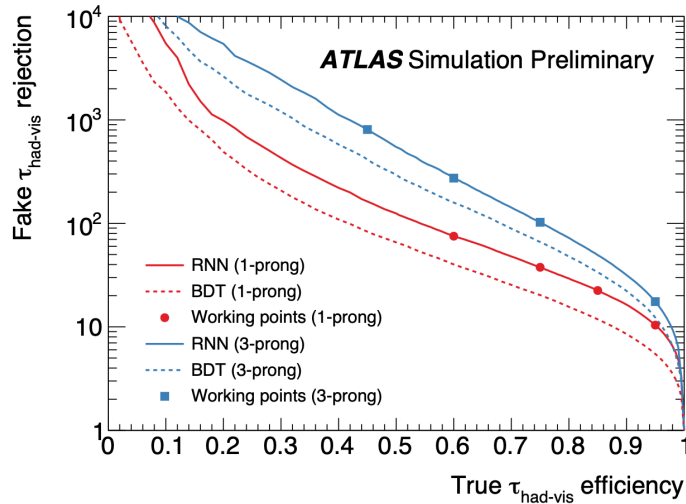
Figure 3.8: Background rejection as a function of signal efficiency for the output RNN used to discriminate $\tau_{\text{had-vis}}$ from QCD jets. The working points are defined with increasing background rejection power: Very Loose, Loose, Medium and Tight. Overlaid is a previous iteration of $\tau_{\text{had-vis}}$ identification utilizing a BDT [60].

a less constraining cut than signal taus and are used to estimate the fake tau contribution (Chapter 7). Signal taus in this analysis are selected with the `Medium` RNN identification working point to discriminate against jets. Background taus are the same as signal taus except with the working point inverted to `Very Loose` but `!Medium`. For both background taus, a cut is placed on the output RNN score (> 0.05) in order to reject against gluon-initiated jets which tend to dominate at low scores.

$\tau_{\text{had-vis}}$ candidates are selected with $p_T > 20$ GeV and $|\eta| < 2.47$, excluding the transition region between the barrel and end-cap ECAL ($1.37 < |\eta| < 1.52$). $\tau_{\text{had-vis}}$ are also required to be either 1 or 3-prong and have a total charge of ± 1. Additionally $\tau_{\text{had-vis}}$ candidates must pass the `Tight` BDT working point to reject against electrons. The $\tau_{\text{had-vis}}$ selection criteria is given in Table 3.5.

Requirement	Signal Taus (Tight)	Background Taus (Loose)
QCD Jet RNN	`Medium`	`VeryLoose!Medium`
e BDT	`Tight`	
p_T	> 20 GeV	
$|\eta|$	< 2.47 with crack veto $1.37 < |\eta| < 1.52$	
Charge	± 1	
Prongs	1 or 3	
RNN Score	> 0.01	

Table 3.5: $\tau_{\text{had-vis}}$ selection for the analysis presented in this thesis.

3.7 Missing Transverse Momentum

Proton-proton collision kinematics at the LHC are such that the total p_T of the system prior to collision is approximately zero. According to momentum conservation, the total p_T of all decay products should also be approximately zero. Any momentum imbalance indicates either the presence of SM neutrinos or new physics with non-interacting particles. Therefore, this momentum imbalance, called missing transverse momentum (E_T^{miss}) is an important quantity.

Reconstructing E_T^{miss} requires the calculation of a so-called *hard-term*, which is the momenta of fully reconstructed objects and a *soft-term*, which is the total momenta of reconstructed tracks originating from the primary vertex but unassociated to any reconstructed object [61, 62]. E_T^{miss} is a vector quantity, but for the purposes of this thesis, the magnitude will be taken such that $E_T^{\text{miss}} = |\mathbf{E_T^{\text{miss}}}|$.

$\mathbf{E_T^{\text{miss}}}$ is calculated as

$$\mathbf{E_T^{\text{miss}}} = \mathbf{p_T^{\text{hard}}} + \mathbf{p_T^{\text{soft}}} \tag{3.4}$$

where the hard-term is defined as:

$$\mathbf{p_T^{\text{hard}}} = -\sum \mathbf{p_T^e} - \sum \mathbf{p_T^\gamma} - \sum \mathbf{p_T^{\tau_{\text{had-vis}}}} - \sum \mathbf{p_T^\mu} - \sum \mathbf{p_T^{\text{jets}}} \tag{3.5}$$

and the soft-term is defined as:

$$\mathbf{p_T^{\text{soft}}} = -\sum \mathbf{p_T^{\text{tracks}}} \tag{3.6}$$

The hard-term is always calculated first using the reconstructed p_T of electron, photon, $\tau_{\text{had-vis}}$, muon and jet candidates, in order. Reconstructed particles that overlap with those already used in the calculation are removed. Once the hard-term is calculated, the soft-term

is then included. The use of the soft term is motivated by improved performance in E_T^{miss} reconstruction in a high pile-up environment.

Chapter 4

Data and MC Samples

This chapter describes the proton-proton collision dataset as well as simulated Monte Carlo (MC) signal and background samples used for this thesis. The dataset is comprised of proton-proton collisions recorded by the ATLAS detector at a center-of-mass energy $\sqrt{s} = 13$ TeV. The data was recorded during LHC Run 2 from 2015 until 2018 with a total integrated luminosity of 139 fb^{-1}.

Simulated samples are comprised of the MC16a (corresponding to the 2015-2016 dataset), MC16d (corresponding to the 2017 dataset) and MC16e (corresponding to the 2018 dataset) MC campaigns. Generated MC backgrounds event were simulated through the entire ATLAS detector [63] using the `GEANT4` [64] simulation package. Signal samples were simulated using a fast simulation based on parametrization of the ATLAS ECAL and HCAL and `GEANT4` for the rest of the detector systems [65]. Physics objects in simulated events were then reconstructed in the same way as the data. Corrections to simulated events are applied to match data for particle selection efficiencies, energy resolutions and energy scales. Simulated events are also normalized to their production cross-sections, as calculated by theory expectations.

Pile-up is simulated in MC samples with minimum-bias interactions generated using `PYTHIA` 8.186 [66] with the A2 tune [67] and overlaid onto hard-scatter events. A variable number of additional interactions are generated, where samples are re-weighted to match the distribution of the mean number of interactions observed in data ($< \mu >$).

4.1 Data Samples

Data collected during 2015, 2016, 2017, and 2018 are used in this thesis, which yields a total integrated luminosity of 139 fb^{-1}. The uncertainty in the combined 2015–2018 integrated luminosity measurement is 1.7% [68], obtained using the LUCID-2 detector [69].

The data utilized in this analysis corresponds to *luminosity blocks* (LB) compiled in the *good run lists* (GRL) [70]. LBs contained in the GRLs have data with similar data-taking conditions, including stable beam and favorable sub-detector operations.

4.1.1 Simulated Signal Samples

VLL signal samples were generated with matrix element calculation at leading-order (LO) using `MadGraph5_aMC@NLO` v2.6.2 [71], interfaced to `PYTHIA` 8.212 [72] for parton showering and hadronization with the A14 tune [73]. The NNPDF2.3LO [74] parton distribution function (PDF) was used.

Signal samples were generated for 10 values of $M_{\tau'}$: 130, 200, 300, 400, 500, 600, 700, 800, 900, and 1000 GeV. The lowest mass point of 130 GeV is chosen to ensure on-shell Higgs decays from τ'. The Yukawa coupling parameter between SM τ and τ' was set to $\epsilon = 0.04$. Samples were generated at LO but scaled to next-to-leading-order (NLO) in QCD. The LO and NLO production cross-sections calculated at generator level are given in Table 4.1.

The signal samples were generated according to final state lepton multiplicity. Specifically, multiplicities of *light leptons* ℓ (e and μ) and τ_{had} are considered and are collectively referred to as "leptons". Leptonic τ decays are kept in the sample, but are not counted towards multiplicity. There are three such generated samples corresponding to 2 leptons, 3 leptons

and 4 leptons, as shown in Table 4.2. The light leptons and τ_{had} in these samples were required to have $p_T > 18$ GeV and $|\eta| < 2.8$. The filter efficiency of segmenting signal events in this manner is given in Table 4.3.

Mass [GeV]	σ_{LO} [fb]	σ_{NLO} [fb]
130	4903.1	6504.0
200	1044.3	1359.2
300	228.72	,291.19
400	72.66	90.75
500	28.268	34.522
600	12.398	14.889
700	5.9046	6.986
800	2.9912	3.478
900	1.5798	1.813
1000	0.8654	0.975

Table 4.1: Production cross-sections for VLL as a function of mass.

Each signal sample contains events of the six possible final states in approximately correct proportion according to the relative production cross-sections of $\tau'\tau'$, $\tau'\nu'_\tau$ and $\nu'_\tau\nu'_\tau$ and branching ratios of $\tau' \to Z\tau$ and $\tau' \to h\tau$. In order to correct for small differences between theory and generator calculation, a scale factor is applied to each signal MC event. The scale factor was derived using MC truth-particle information by comparing the ratio of theory-predicted luminosity with the luminosity represented in the sample, as well as the theory-predicted branching ratio with the final state yield observed in the sample. The scale

66

	2 e/μ	3 e/μ	4+ e/μ
0 τ	2 lep	3 lep	
1 τ	3 lep		
2+ τ		4 lep	

Table 4.2: Signal sample splitting according to final state lepton multiplicity.

Mass [GeV]	2 lep	3 lep	4 lep
130	0.027	0.045	0.027
200	0.041	0.067	0.040
300	0.054	0.088	0.048
400	0.060	0.100	0.053
500	0.063	0.106	0.059
600	0.065	0.111	0.062
700	0.065	0.115	0.065
800	0.066	0.116	0.067
900	0.067	0.120	0.069
1000	0.068	0.123	0.070

Table 4.3: Generator filter efficiency of each signal sample.

factors are given in Table 4.4.

Decay mode	130 [GeV]	200	300	400	500	600	700	800	900	1000
$ZZ\tau\tau$	1.137	1.0658	1.0528	1.0454	1.0448	1.0459	1.0449	1.0419	1.043	1.0437
$ZW\tau\tau$	1.1191	1.063	1.051	1.0476	1.0449	1.044	1.0448	1.046	1.0453	1.0467
$Zh\tau\tau$	0.7957	1.021	1.033	1.033	1.0358	1.0382	1.038	1.0367	1.0396	1.0402
$hh\tau\tau$	0.556	0.9788	1.0128	1.0213	1.0265	1.0314	1.0323	1.032	1.0343	1.0372
$Wh\tau\tau$	0.7826	1.018	1.0308	1.0346	1.0368	1.0363	1.0365	1.0409	1.0416	1.0421
$WW\tau\tau$	1.1023	1.0597	1.0515	1.0459	1.0449	1.0417	1.0448	1.0449	1.0476	1.0482

Table 4.4: Signal MC scale factors used to correct for the relative proportion of the final states in the samples. The values of the six weights are given for the ten mass points studied in this thesis.

4.2 Background Samples

There are two primary sources of backgrounds which were accounted for in this analysis. The first are reducible backgrounds from either mis-identified leptons or from charge mis-identification. The second are irreducible backgrounds, which are prompt backgrounds originating from physics processes that have final states similar to the signal.

The mis-identified (fake) background is estimated using the data-driven *fake factor* method. A data-driven method is used rather than MC simulation as the majority of fake leptons are mis-identified jets. Large uncertainties from QCD simulation result in inadequate fake estimation. The treatment of fakes is described in Section 7.

Charge mis-identification is due to bremsstrahlung in the ID. Since muons rarely undergo

bremsstrahlung, charge mis-identification is only considered for electrons. There are two main mechanisms that can result in charge mis-identification. The first is when a radiated γ pair-produces e^+e^- and calorimeter deposits are erroneously matched to a pair-produced e with opposite charge. The second case is where the radiated γ does not pair-produce, and the calorimeter deposit is matched to a track with ill-defined curvature. Charge mis-identification is addressed by applying scale factors to reconstructed electrons, which are calculated using a data-driven approach [75].

Prompt backgrounds are estimated from MC simulation. The background processes considered are V+jets[1], VV, VVV and top quark production. Processes are normalized to their theory production cross-sections. Reconstructed light leptons and hadronic taus selected in the analysis are truth-matched in order to neglect mis-identified leptons present in MC simulation. Truth matching is described in Section 4.3. The following sections will describe generation of simulated backgrounds used in this thesis. The full list of MC samples is given in Table 4.5.

4.2.1 V+jets Backgrounds

The production of V+jets processes was simulated with the `SHERPA` 2.2.1 [76] generator. Matrix elements were calculated at NLO for up to two partons, and LO for up to four partons using the `Comix` [77] and `OpenLoops` [78, 79, 80] libraries.

The `SHERPA` parton shower [81] based on Catani–Seymour dipole factorization and the cluster hadronization model [82] was used. The NNPDF3.0NNLO PDF [83] set was used along with a dedicated set of tuned parton-shower parameters developed by the `SHERPA`

---

[1]V is a generic label for weak vector bosons such that $V = W, Z$.

authors.

The NLO matrix elements for a given jet multiplicity were matched to the parton shower using a color-exact variant of the MC@NLO algorithm [84]. Different jet multiplicities were then merged into an inclusive sample using an improved CKKW matching procedure [85, 86] which was extended to NLO accuracy using the MEPS@NLO prescription [87].

4.2.2 VV Backgrounds

Samples of diboson final states (VV) were simulated with either the `SHERPA` v2.2.1 or v2.2.2 generator depending on the process, including off-shell effects and Higgs boson contributions. Fully leptonic final states and semileptonic final states, where one boson decays leptonically and the other hadronically, were generated using matrix elements calculated at NLO in QCD for up to one additional parton and at LO for up to three additional parton emissions. Samples for the loop-induced processes, $gg \to VV$, were generated at LO for up to one additional parton emission for both the cases of fully leptonic and semileptonic final states.

The matrix element calculations were matched and merged with the `SHERPA` parton shower based on Catani–Seymour dipole factorization using the MEPS@NLO prescription. The virtual QCD corrections were provided by the `OpenLoops` library. The NNPDF3.0NNLO PDF set was used.

Uncertainties from higher orders in QCD (extra radiation) were evaluated [88] using seven variations of the QCD factorization and renormalization scales in matrix elements by factors of 0.5 and 2, avoiding variations in opposite directions. Uncertainties in the nominal PDF set were evaluated using 100 replica variations. Additionally, the results were cross-checked using the central values of the CR14nnlo [89] and MMHT2014 NNLO [90] PDF sets. The

effect of the uncertainty in the strong coupling constant, α_s, was assessed by variations of ± 0.001. Treatment of uncertainties will be discussed in more detail in Chapter 8.

4.2.3 VVV Backgrounds

The production of triboson (VVV) events was simulated with the `SHERPA` generator using factorized gauge-boson decays. Matrix elements were calculated at NLO for the inclusive process and at LO for up to two additional parton emissions.

The matrix element calculations were matched and merged with the `SHERPA` parton shower based on Catani–Seymour dipole factorization using the MEPS@NLO prescription. The virtual QCD corrections were provided by the `OpenLoops` library. The NNPDF3.0NNLO PDF set was used.

4.2.4 Top Backgrounds

Top quark processes involving single-top, $t\bar{t}$ and $t\bar{t} + h$ production was modeled using the `Powheg-Box` v2 [91, 92, 93] generator. Matrix elements were calculated at NLO in the strong coupling constant, α_s, with the NNPDF3.0NNLO PDF set. The h_{damp} parameter, which controls the matrix element and parton showering matching in `POWHEG` and was set to $1.5 \times m_{\mathrm{top}}$ for $t\bar{t}$ production, where the mass of the top quark (m_{top}) is taken as 172.5 GeV. [94]. The events were interfaced with `PYTHIA` v8.230 [72] using the A14 tune [73] and the NNPDF2.3LO PDF set. The decays of bottom and charm hadrons were simulated using the `EVTGEN` v1.6.0 program [95].

$t\bar{t} + V$ and $t\bar{t}t\bar{t}$ production was modeled using the `MadGraph5_aMC@NLO` v2.3.3 generator. Matrix elements were calculated at NLO in the strong coupling constant, α_s, with the

NNPDF3.0NNLO PDF set. Top quarks were decayed at LO using `MADSPIN` [96, 97] to preserve spin correlations. The events were interfaced with `PYTHIA v8.210` for the parton shower and hadronization, using the A14 set of tuned parameters and the NNPDF2.3LO PDF set. The decays of bottom and charm hadrons were simulated using the `EVTGEN` v1.6.0 program. For $t\bar{t} + V$, the functional form of the renormalization and factorization scales was set to the default of $0.5 \times \sum_i \sqrt{m_i^2 + p_{\mathrm{T},i}^2}$, where the sum runs over all the particles generated from the matrix element calculation.

The impact of using a different parton shower and hadronization model was evaluated for $t\bar{t} + Z$. Additional samples were generated with the `SHERPA` v2.2.0 generator at LO accuracy, using the MEPS@NLO set-up with up to one additional parton for the $t\bar{t} + ll$ sample and two additional partons for the others. A dynamic renormalization scale was used and is defined similarly to that of the nominal $t\bar{t} + W$ samples. The default `SHERPA` v2.2.0 parton shower was used along with the NNPDF3.0NNLO PDF set.

Uncertainties for $t\bar{t} + Z$ from higher orders in QCD (extra radiation) were evaluated by simultaneously varying the renormalization and factorization scales by factors of 2.0 and 0.5. Uncertainties $t\bar{t} + Z$ in the PDFs were evaluated using the 100 replicas of the NNPDF3.0NNLO PDF set. Treatment of uncertainties will be discussed in more detail in Chapter 8.

Other top processes with negligible effect on the analysis are outlined in Table 4.5.

Process	Event Generator	Showering	Matrix Element	PDF	Usage
Signal	Madgraph	Pythia	LO	NNPDF2.3LO	signal
$Z \to ll$	Sherpa 2.2.1	Sherpa	NNLO	NNPDF3.0NNLO	both
$W \to ll$	Sherpa 2.2.1	Sherpa	NNLO	NNPDF3.0NNLO	fakes
VV (lep)	Sherpa 2.2.2	Sherpa	NLO	NNPDF3.0NNLO	both
VV (semi-lep)	Sherpa 2.2.1	Sherpa	NLO	NNPDF3.0NNLO	both
VVV	Sherpa 2.2.2	Sherpa	NLO	NNPDF3.0NNLO	both
t	PowhegBox v2	Pythia8	NLO	NNPDF3.0NNLO	both
$t\bar{t}$	PowhegBox v2	Pythia8	NLO	NNPDF3.0NNLO	both
$t\bar{t} + WW$	AMC@NLO	Pythia8	LO	NNPDF3.0NNLO	both
$t\bar{t} + H$	PowhegBox v2	Pythia8	NLO	NNPDF30ME	both
$t\bar{t} + V$	AMC@NLO	Pythia8	NLO	MEN30NLO	both
ttt	AMC@NLO	Pythia8	NLO	NNPDF2.3LO	both
$t\bar{t}t\bar{t}$	AMC@NLO	Pythia8	NLO	NNPDF2.3LO	both

Table 4.5: Summary of MC samples used in the analysis.

4.3 Truth Matching Prompt Leptons

This thesis relies on *truth-matching* of reconstructed leptons to their true identification at generator-level. The primary purpose is to correctly handle the inclusion of fake leptons (Chapter 7). For prompt backgrounds, leptons in the analysis must be truth-matched with the nominal reconstruction requirements. For fake backgrounds, truth-matched leptons with a relaxed nominal reconstruction requirement are subtracted from data in order to avoid double-counting. Those leptons with nominal reconstruction requirements are referred to as "tight" and those with a relaxed requirement are "loose". The exact definitions for each object was introduced in Chapter 3.

Chapter 5

Analysis Strategy

This thesis describes a search for vector-like leptons (VLL), which were introduced in Section 1.2. The goal is to observe a signal consistent with VLLs, where the signal manifests itself through kinematic and topological properties of decays into SM particles. The ATLAS detector is used to reconstruct SM decay products, which are selected through reconstruction definitions consistent with maximal signal selection efficiency. The definition of SM objects selected for this analysis were given in Chapter 3.

In performing a search for a particular physics process, one designs a statistical analysis such that hypothesis testing can be performed. A hypothesis is typically excluded if the observed p-value is below a pre-defined threshold. In high energy physics, it is common to convert the p-value into an equivalent significance, Z. In a counting experiment with only statistical errors considered, the significance is defined as: [98, 99]:

$$Z = \sqrt{2[(S+B)\ln(1+S/B) - S]} \tag{5.1}$$

where S and B are the expected signal and background events, respectively. The total number of expected signal and background events are estimated from simulation, or from data-driven background estimation techniques. If the signal and background distributions are binned into a histogram, a significance distribution can be calculated bin-by-bin. The significance is related to the inconsistency of a random variable and the background-only hypothesis, therefore a common strategy is to maximize the distribution of Z[1].

This thesis utilizes a multivariate technique called a *boosted decision tree* (BDT). BDTs

---

[1]In many cases, it is assumed that $S << B$ and Z can be approximated as $S/\sqrt{B}$

take distributions of variables as input and classifies events as either signal or background in a supervised training procedure. The output is a score (*BDT score*) which is a function of the level of confidence that a given event is signal or background. A BDT is chosen as it is able to define regions with maximal Z.

5.1 Classification of Events

The search for VLLs is performed using events categorized into several final states differing in lepton multiplicity. Specifically, final states are categorized into seven regions based on the number of light leptons (two, three and four or more) and hadronic taus (one and two or more). The two ℓ regions are further split into regions of same sign or opposite sign electric charge (SS or OS) and same or opposite flavor (SF or OF).

The lepton multiplicity final states are designed for sensitivity to the $\tau'\nu_\tau'$ production mode, which has a production cross-section that is two to three times that of τ' or ν_τ' pair-production (Figure 1.5). The relative contribution of each production mode for the seven lepton multiplicity final states is shown in Figure. 5.1. The origin of signal events in the seven final states with relative fractions of $\tau'\nu_\tau'$, $\tau'\tau'$ and $\nu_\tau'\nu_\tau'$ production are:

$\geq 4\ell, \geq 0\tau$ (64%, 26%, 10%)	Leptonic Z, W decays with at least one leptonic τ decay.
$3\ell, \geq 1\tau$ (64%, 27%, 9%)	Leptonic Z decay with either a leptonic W or τ decay.
$2\ell, \geq 2\tau$ (57%, 35%, 8%)	Leptonic Z decay with hadronic W and τ decays. $Z \to \tau\tau$ with leptonic W and τ.
2ℓ SSOF, 1τ (67%, 26%, 7%)	Hadronic Z and τ with leptonic W and τ.
2ℓ SSSF, 1τ (67%, 26%, 7%)	Hadronic Z and τ with leptonic W and τ.
2ℓ OSOF, 1τ (55%, 38%, 7%)	Leptonic Z and leptonic τ or W with lost lepton from Z. Hadronic Z and leptonic τ and W.
2ℓ OSSF, 1τ (57%, 36%, 7%)	Leptonic Z and leptonic τ with hadronic W and τ with lost lepton from Z. Hadronic Z and leptonic τ and W.
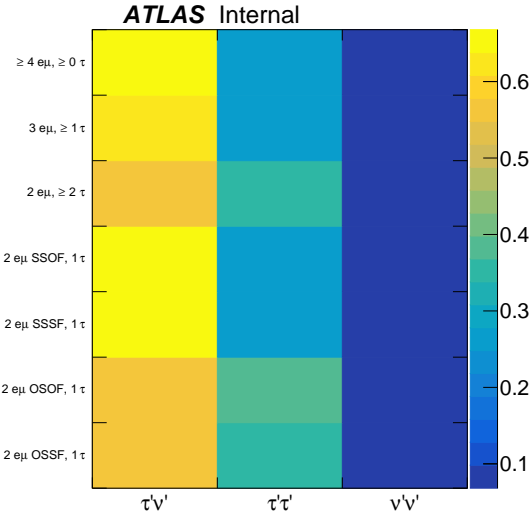
Figure 5.1: Relative contributions of τ' and ν'_τ production modes for each lepton multiplicity final state.

Figures 5.2-5.5 show the distributions of selected kinematic and topological variables in each of the lepton multiplicity final states. Estimated background contributions are shown as a stacked histogram, where signal corresponding to τ' masses of 800, 900 and 1000 GeV are

overlaid. The significance of each distribution is given in the bottom plot. The distributions of missing transverse momentum (E_T^{miss}), the number of jets (N_j), the transverse momentum of the leading τ ($p_T(\tau_{\text{lead}})$) and the invariant mass of the ℓ and τ_{had} system ($M_{\ell\tau}$) are shown.

In order to promote a statistically significant result, a discriminating variable between signal and background should be chosen. This variable should provide discrimination power between signal and background while containing regions of physically observable yields. The distributions shown in Figures 5.2-5.5 do provide discrimination power, however, the signal yield is typically much smaller than background and would not be observable. Kinematic and topological information embedded in the lepton multiplicity states can be used in conjunction to provide a robust discriminant through a BDT. This discriminant provides maximal separability and significance such that signal yields are observable relative to background predictions.

5.2   Boosted Decision Trees

Decision trees work as binary discriminators of events based on input variable cuts, where an individual tree is referred to as a *weak classifier*. Figure 5.6 shows an example decision tree and equivalent parameter space. Input data begins at the *root node* where it is split into successive *branch nodes* based on cuts which are optimized to separate signal and background. Each branch node continues the process using a different cut until events land on a *leaf or termination node*, where they are classified as either signal or background.

Weak classifiers are trained by maximizing a criterion function to determine the best split at each node [100, 101, 102]. Assuming weighted events with weight W_i, the *purity* of the
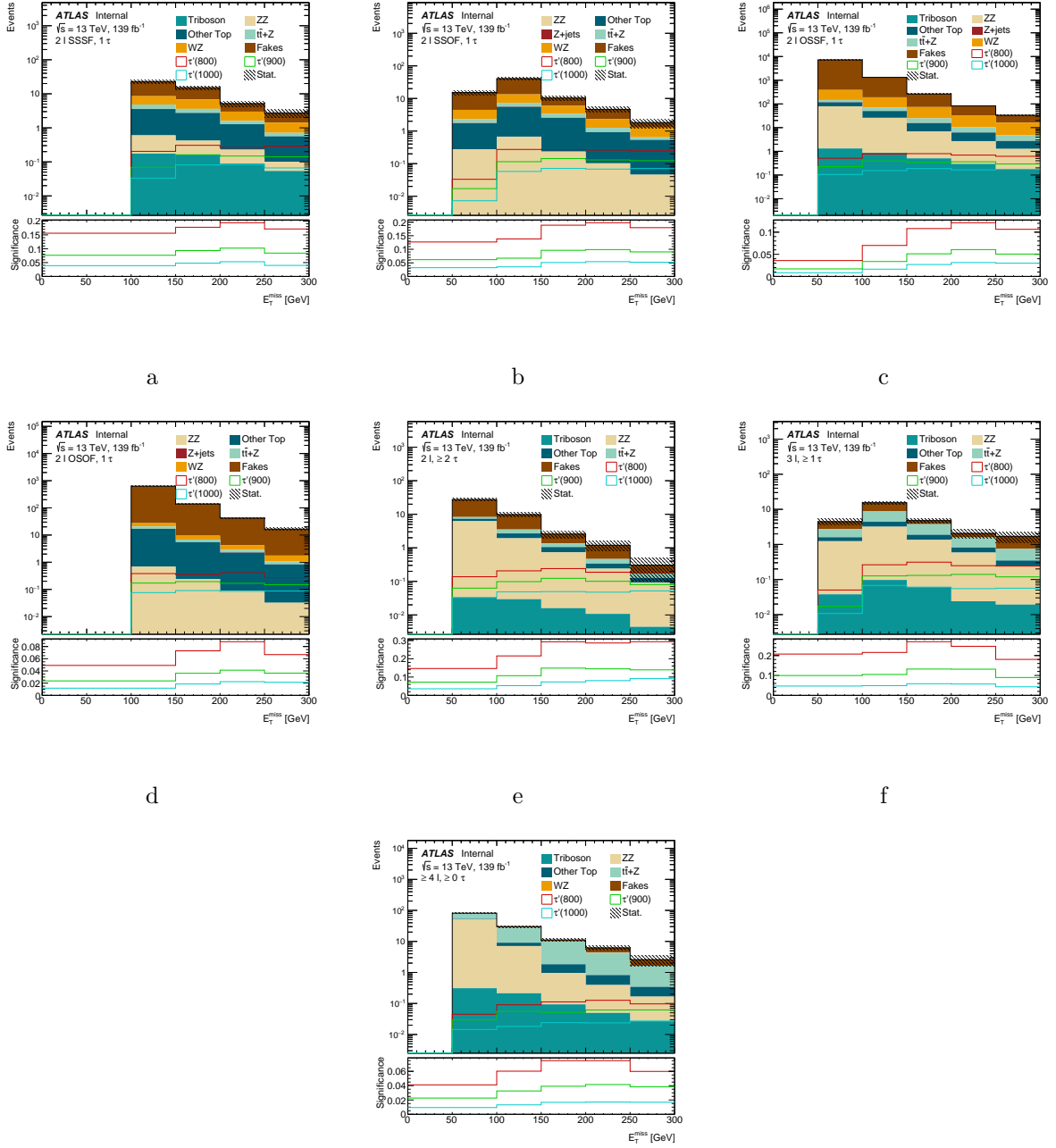
Figure 5.2: Distributions for background and signal (τ' masses of 800, 900 and 1000 GeV) in the top plot and significance in the bottom plot for the missing transverse momentum (E_T^{miss}) variable. "Stat." in the legend refers to statistical uncertainty. (a) 2ℓ SSSF, 1τ (b) 2ℓ SSOF, 1τ (c) 2ℓ OSSF, 1τ (d) 2ℓ OSOF, 1τ (e) $2\ell, \geq 2\tau$ (f) $3\ell, \geq 1\tau$ (g) $\geq 4\ell, \geq 0\tau$

79
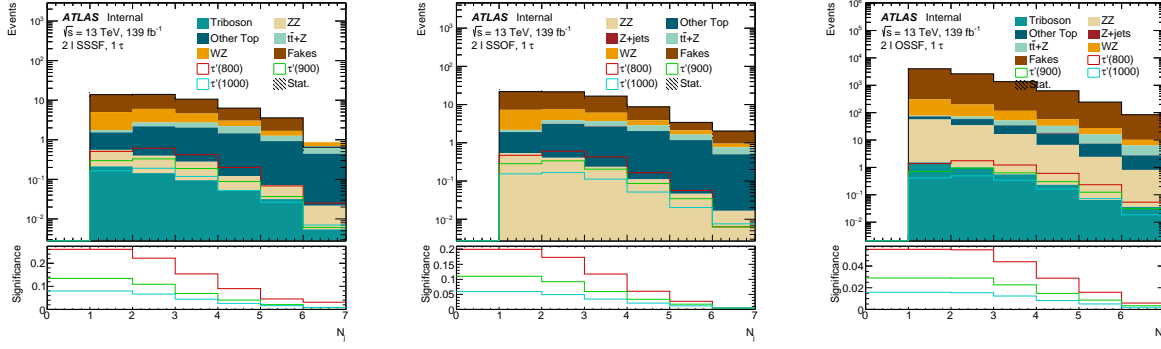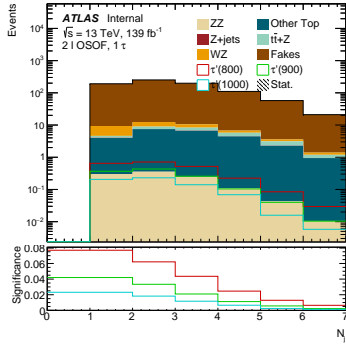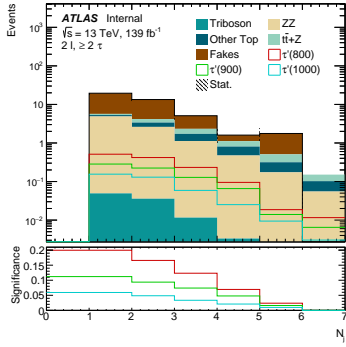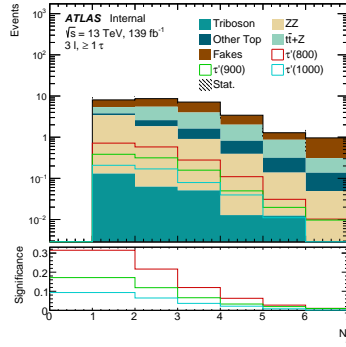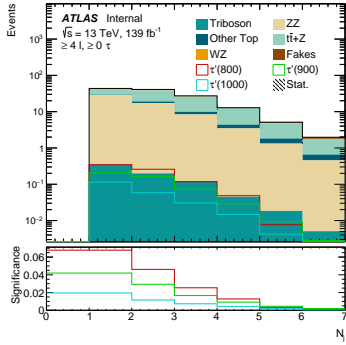
Figure 5.3: Distributions for background and signal (τ' masses of 800, 900 and 1000 GeV) in the top plot and significance in the bottom plot for the number of jets (N_j) variable. "Stat." in the legend refers to statistical uncertainty. (a) 2ℓ SSSF, 1τ (b) 2ℓ SSOF, 1τ (c) 2ℓ OSSF, 1τ (d) 2ℓ OSOF, 1τ (e) $2\ell, \geq 2\tau$ (f) $3\ell, \geq 1\tau$ (g) $\geq 4\ell, \geq 0\tau$

80
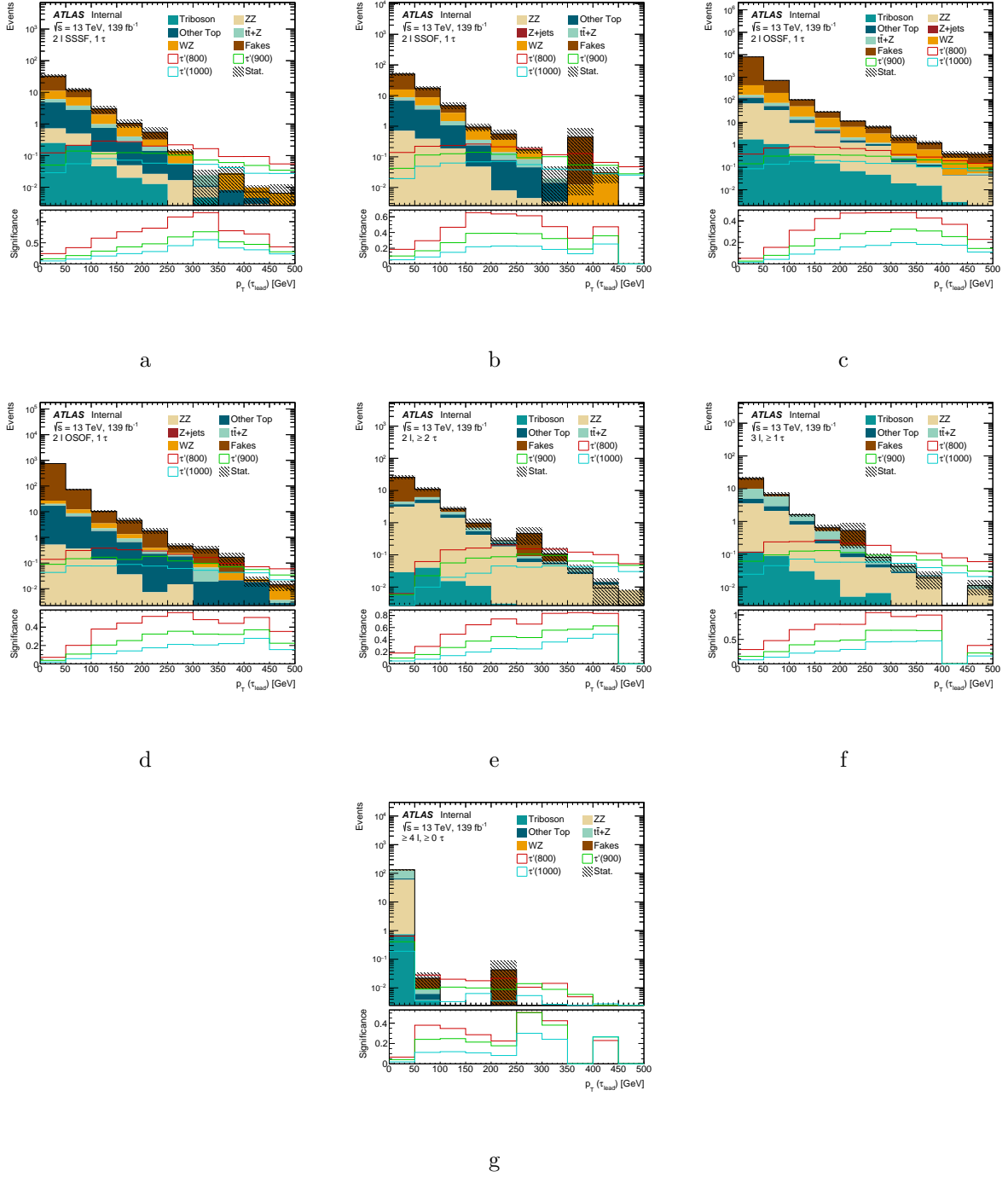
Figure 5.4: Distributions for background and signal (τ' masses of 800, 900 and 1000 GeV) in the top plot and significance in the bottom plot for the transverse momentum of the leading tau ($p_T(\tau_{\text{lead}})$) variable. "Stat." in the legend refers to statistical uncertainty. (a) 2ℓ SSSF, 1τ (b) 2ℓ SSOF, 1τ (c) 2ℓ OSSF, 1τ (d) 2ℓ OSOF, 1τ (e) $2\ell, \geq 2\tau$ (f) $3\ell, \geq 1\tau$ (g) $\geq 4\ell, \geq 0\tau$

81
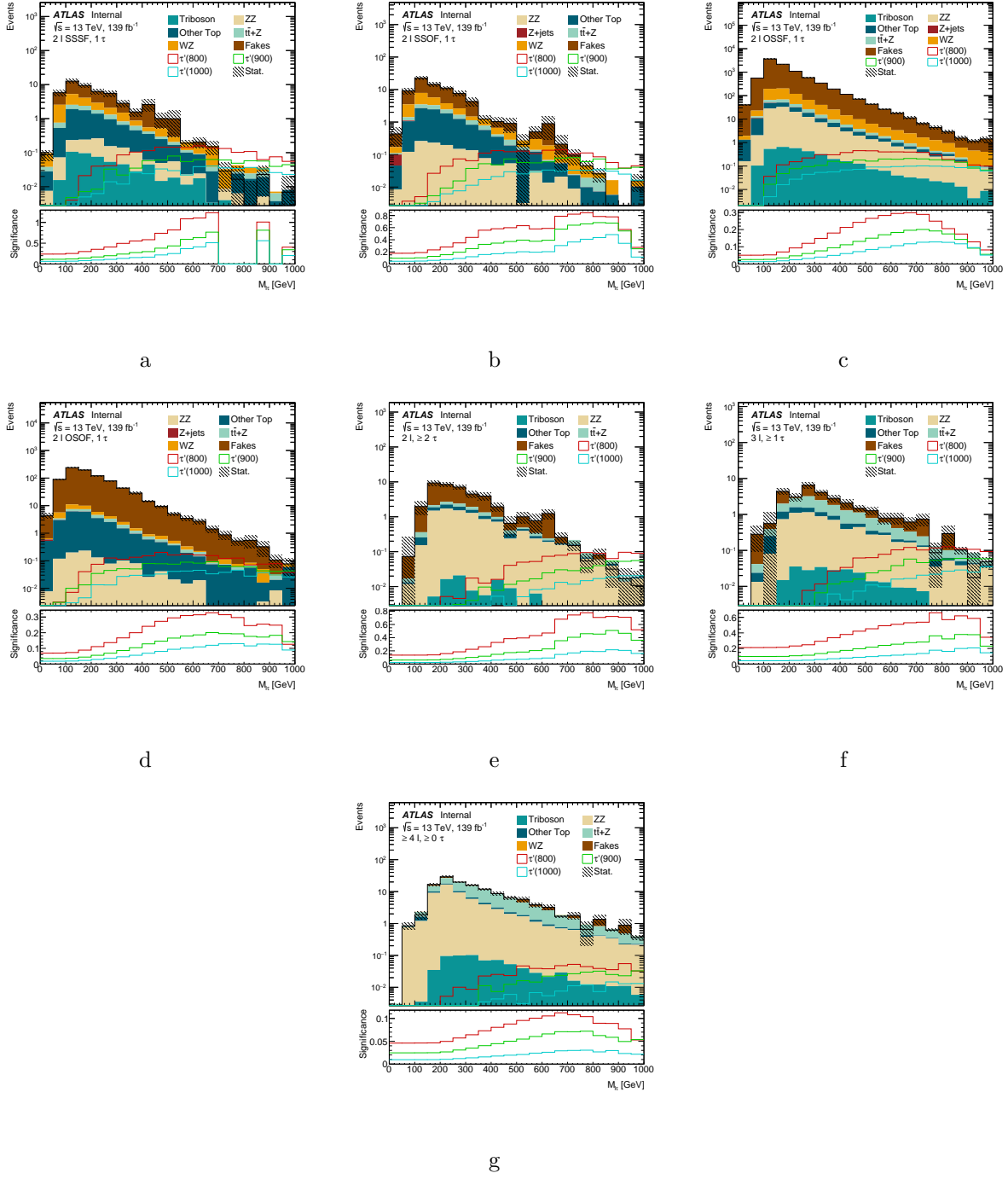
Figure 5.5: Distributions for background and signal (τ' masses of 800, 900 and 1000 GeV) in the top plot and significance in the bottom plot for the invariant mass of ℓ and τ system ($M_{l\tau}$). "Stat." in the legend refers to statistical uncertainty. (a) 2ℓ SSSF, 1τ (b) 2ℓ SSOF, 1τ (c) 2ℓ OSSF, 1τ (d) 2ℓ OSOF, 1τ (e) $2\ell, \geq 2\tau$ (f) $3\ell, \geq 1\tau$ (g) $\geq 4\ell, \geq 0\tau$
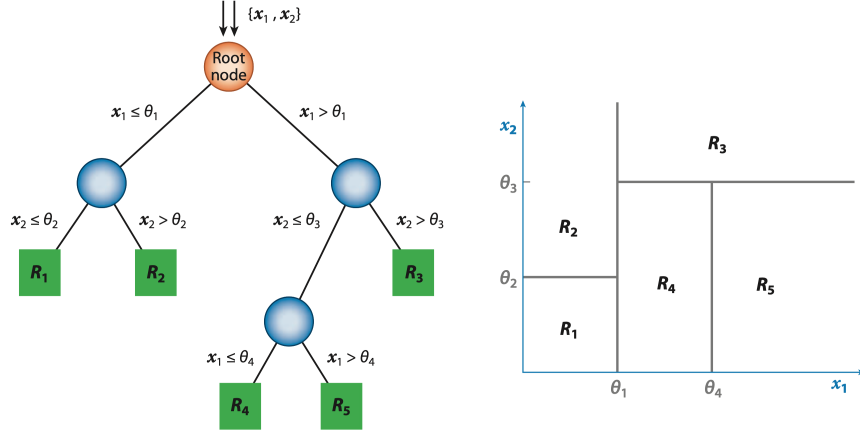
Figure 5.6: Example decision tree with two input variables, x_1 and x_2. The full dataset is given to a root note, where subsequent splits are made by imposing cuts θ_i, on the inputs. R_i are the termination (leaf) notes. The figure on the right shows the equivalent representation in parameter space [100].

sample in a given node can be written as:

$$p(i) = \frac{\sum_i W_i}{\sum_n W_n} \tag{5.2}$$

where i is runs over signal or background, such that $i = S, B$ and the index n runs over every event in the node. The *Gini Impurity* is the probability of incorrectly classifying a random event and is defined as:

$$\text{Gini} = \sum_i p(i)(1 - p(i)) \tag{5.3}$$

When determining the appropriate split from a "mother" node into two "daughter" nodes, one maximizes the criterion function:

$$\text{Criterion} = \text{Gini}_{\text{mother}} - \text{Gini}_{\text{daughter,1}} - \text{Gini}_{\text{daughter,2}} \tag{5.4}$$

where the purity of the node determines if events classified into the node are labeled as signal or background (typically by a threshold value). Branch splitting is terminated into leaves

after a specified number of splits. In principle, the split can occur until each training event is classified into its own leaf. However, this typically results in a situation where the tree learns statistical fluctuation in the data, which is referred to as *overtraining*.

Boosting is a process which uses an ensemble of weak classifiers to improve classification performance by successively training multiple trees on weaknesses of the last. Each tree is considered a weak classifier in this case. In boosting algorithms, misclassification errors are used to train a subsequent tree in an effort to improve overall performance.

Consider a set of data, $\{x_i, y_i\}_{i=1}^{n}$, where x_i are the data points whose targets y_i, are known binary labels for background or signal. Now consider a decision function $G(x)$, which is a predictive model for each data point. Estimating the form of $G(x)$ can be done using a boosting algorithm. The `AdaBoost` algorithm [103] estimates $G(x)$ by first minimizing the weighted sum error for misclassified points:

$$\text{err}_t = \sum_{\substack{i=1 \\ \hat{y}_i \neq y_i}}^{n} w_{i,t} / \sum_{i=1}^{n} w_{i,t} \tag{5.5}$$

where $w_{i,t}$ is the ith event's weight for the tth boosting iteration and $\hat{y}_i$ is the ith event's predicted classification. When $t = 1$, the event weights are the nominal weights given to the algorithm and are updated after each iteration such that:

$$w_{i,t+1} = w_{i,t} e^{-y_i \alpha_t \hat{y}_{i,t}} \tag{5.6}$$

where,

$$\alpha_t = \frac{1}{2} \ln \left(\frac{1 - \text{err}_t}{\text{err}_t} \right) + \ln(K - 1) \tag{5.7}$$

The $\ln(K - 1)$ term ensures the weight is updated when $(1 - \text{err}_t) > 1/K$. This thesis uses the `SAMME` algorithm, where $K = 3$ [104]. The final functional form of $G(x)$ is taken as a

weighted superposition of weak classifiers in the training procedure such that:

$$G(x) = \sum_t \alpha_t G_t(x) \tag{5.8}$$

Events that are classified as background in a weak classifier are scored as -1 and those as signal are scored as 1, where $G_t(x) = \{-1, +1\}$. $G(x)$ is the signal and background discriminating BDT score distribution used in this thesis and also runs from -1 to 1.

5.2.1 Training Strategy

This thesis utilizes the `AdaBoost` algorithm housed in the `SciKit Learn` package [105]. A total of seven BDTs were trained, one for each lepton multiplicity final state defined in Section 5.1. Event weights are used in the training, where events with negative weights are excluded to avoid issues with stability.

K-folds cross validation separates the dataset into K-equal randomized partitions. The BDT is trained K times (which yields effectively K BDTs), where for each training iteration one of the partitions is used as a *testing set* and the remaining K-1 combine to build a *training set*. This method guarantees that each partition is used as the testing set once, which helps to mitigate training and scoring biases. This thesis uses K = 5 and is illustrated in Figure 5.7.

The trained BDT is then applied to events to classify them as signal or background for use in the analysis. A BDT from a particular fold is only applied to those events that were used as the testing set. This ensures that biases are minimized by only applying a BDT to events that were not used for training.

Training is performed on a combined signal sample using mass points, $M_{\tau'} = 800$, 900 and 1000 GeV. The samples were added without scaling for differences in production cross-section.
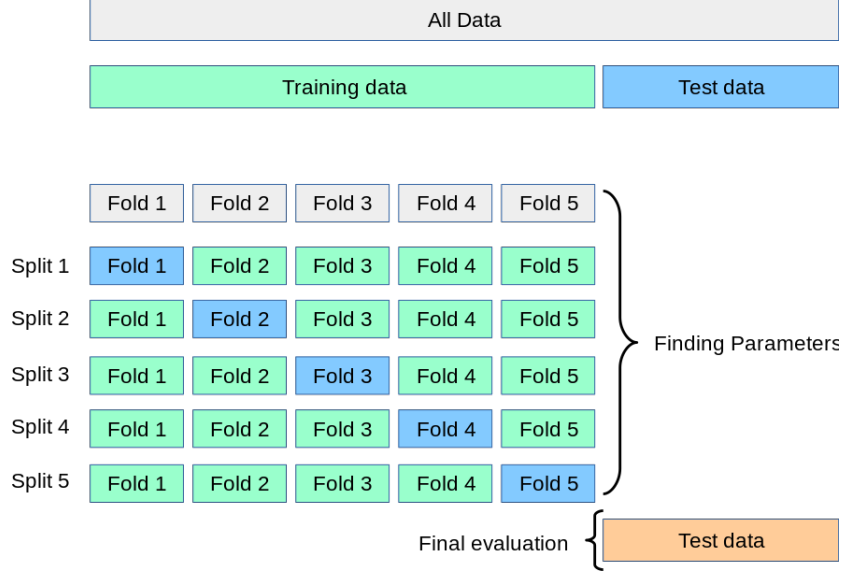
Figure 5.7: Illustration of K-folds cross validation with 5 folds. The dataset is split into five equal, random partitions, where for each iteration one fold is used as the testing set [105].

Thus, the shapes of the distributions are added while avoiding scaling biases that would favor those mass points with a higher cross-section. These mass points are chosen to maximize the signal efficiency in the high mass regions. Distributions on the lower end of the mass spectrum generally have a large signal significance and are excluded from training.

Another motivation for excluding lower mass points is to avoid training biases resulting from differences in kinematic distributions. Therefore, mass points with comparable kinematics are trained together. This is shown in Figure. 5.8, which gives the E_T^{miss} distributions for the low mass and high mass signal, inclusive in lepton multiplicity.

5.2.2 Training Regions

In order to yield a better separation between signal and background, a cut on E_T^{miss} was made prior to training for each lepton multiplicity region, as shown in Figure 5.9. The cut value was
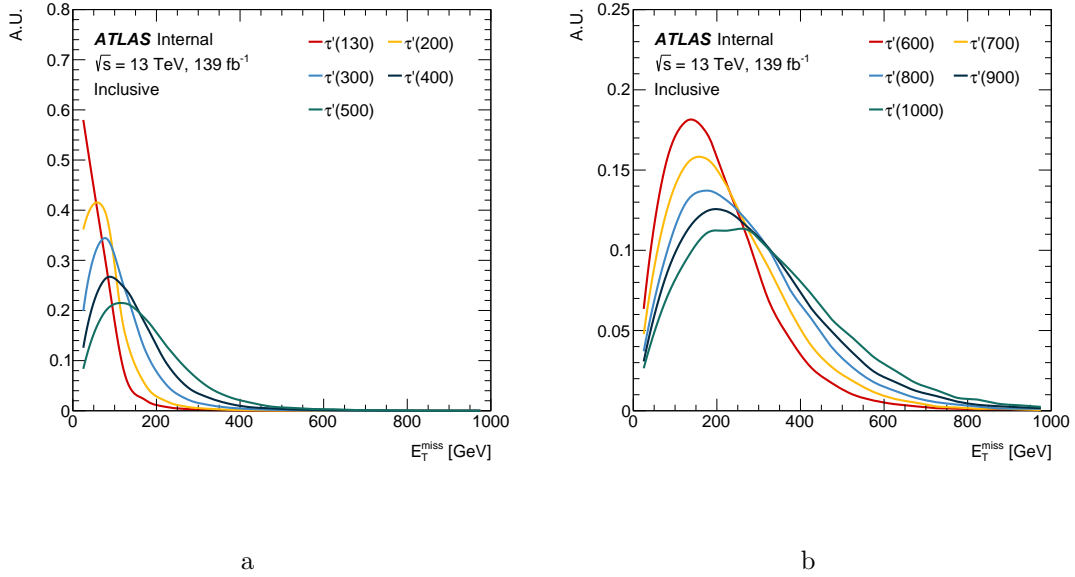
Figure 5.8: E_T^{miss} distributions for signal mass points used in this thesis. The distributions are inclusive in final state lepton multiplicity. (a) $M_{\tau'} = 130\text{-}500$ GeV. (b) $M_{\tau'} = 600\text{-}1000$ GeV.

determined by comparing the unit-normalized distributions of signal and background. This helps to reduce the number of background events in the training sample as they statistically dominate over signal and can lead to overtraining and biases. A cut was also placed such that every event had at least one jet, which further reduced background events while maintaining signal significance. One BDT is trained for each lepton multiplicity final state described in Section 5.1. The definition of the BDT training regions is given in Table 5.1.

The BDT score distributions for the seven lepton multiplicity final states are shown in Figure 5.10. These distributions are from optimized BDT algorithms and the training has been validated using performance metrics. Optimization will be described in Section 5.2.3 and performance metrics in Section 5.2.4. Comparing with Figures 5.2-5.5, the signal significance is much larger and the separation of signal and background is much more robust in the BDT
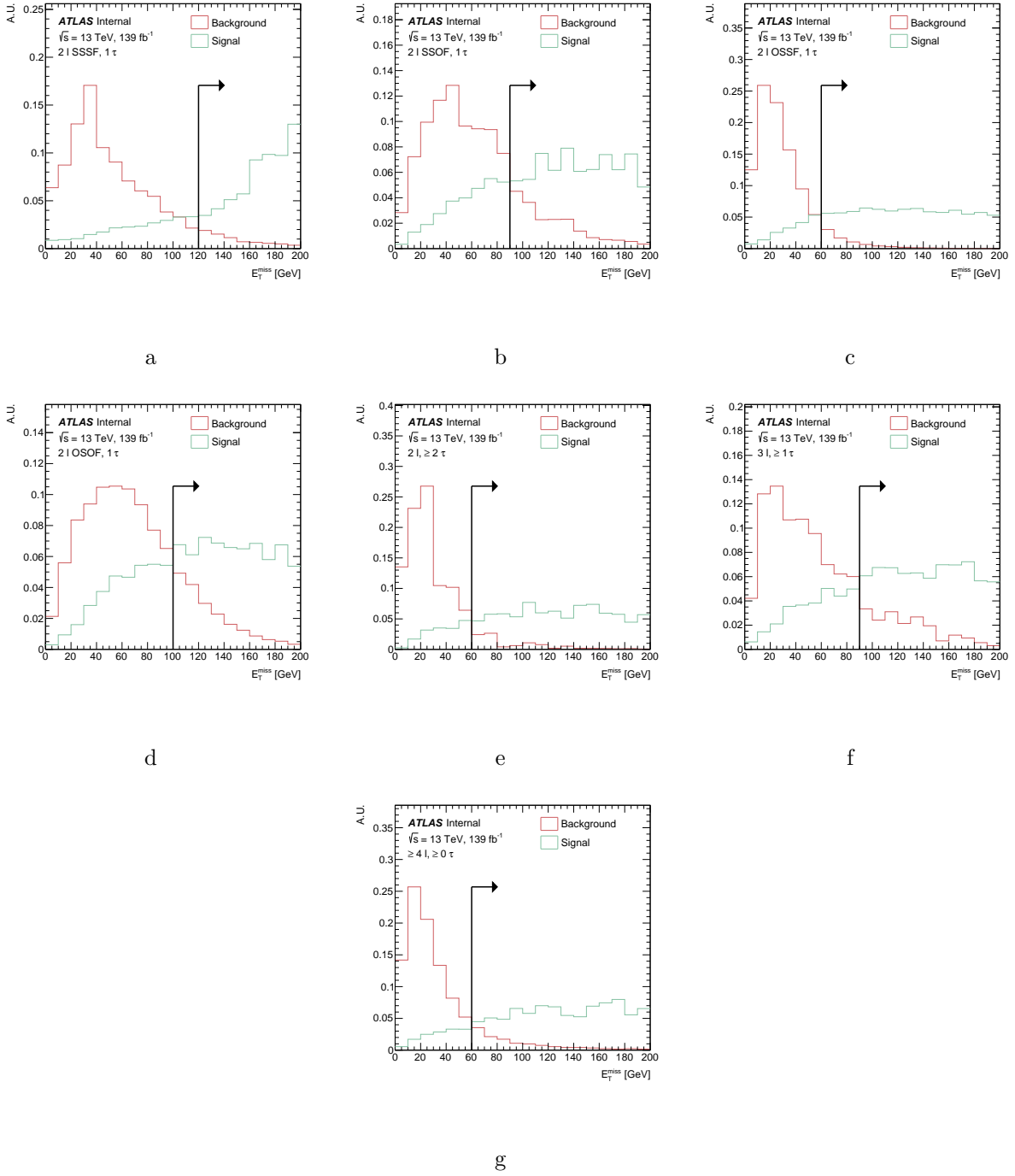
Figure 5.9: Unit-normalized E_T^{miss} distributions for various lepton multiplicity regions. The arrows indicate the E_T^{miss} cut placed before BDT training. These distributions contain events with at least one jet. (a) 2ℓ SSSF, 1τ (b) 2ℓ SSOF, 1τ (c) 2ℓ OSSF, 1τ (d) 2ℓ OSOF, 1τ (e) $2\ell, \geq 2\tau$ (f) $3\ell, \geq 1\tau$ (g) $\geq 4\ell, \geq 0\tau$

	2ℓ					3ℓ	4ℓ
N_ℓ	2	2	2	2	2	3	≥ 4
S/F	SSSF	SSOF	OSSF	OSOF			
N_τ	1	1	1	1	≥ 2	≥ 1	≥ 0
N_j	> 0	> 0	> 0	> 0	> 0	> 0	> 0
E_T^{miss} [GeV]	≥ 120	≥ 90	≥ 60	≥ 100	≥ 60	≥ 90	≥ 60

Table 5.1: Training region definitions for the BDTs used in this thesis. One BDT is trained for each lepton multiplicity final state.

score. These distributions will be the basis for analysis region definitions, which will be defined in Chapter 6.

5.2.3 BDT Optimization

Hyperparameter Optimization *Hyperparameters* define aspects of the BDT algorithm and are related to the desired complexity of the model. The hyperparameters used in this thesis are listed below [105].

- **Maximum Tree Depth:** controls the maximum number of higher level nodes that a tree can achieve. The complexity of the model increases with the tree depth.

- **Maximum Features Per Split:** the maximum number of variables to consider at each split. This parameter controls the complexity of the model, which can be problematic when the dimensionality of the input is much larger than the statistics of the training samples.
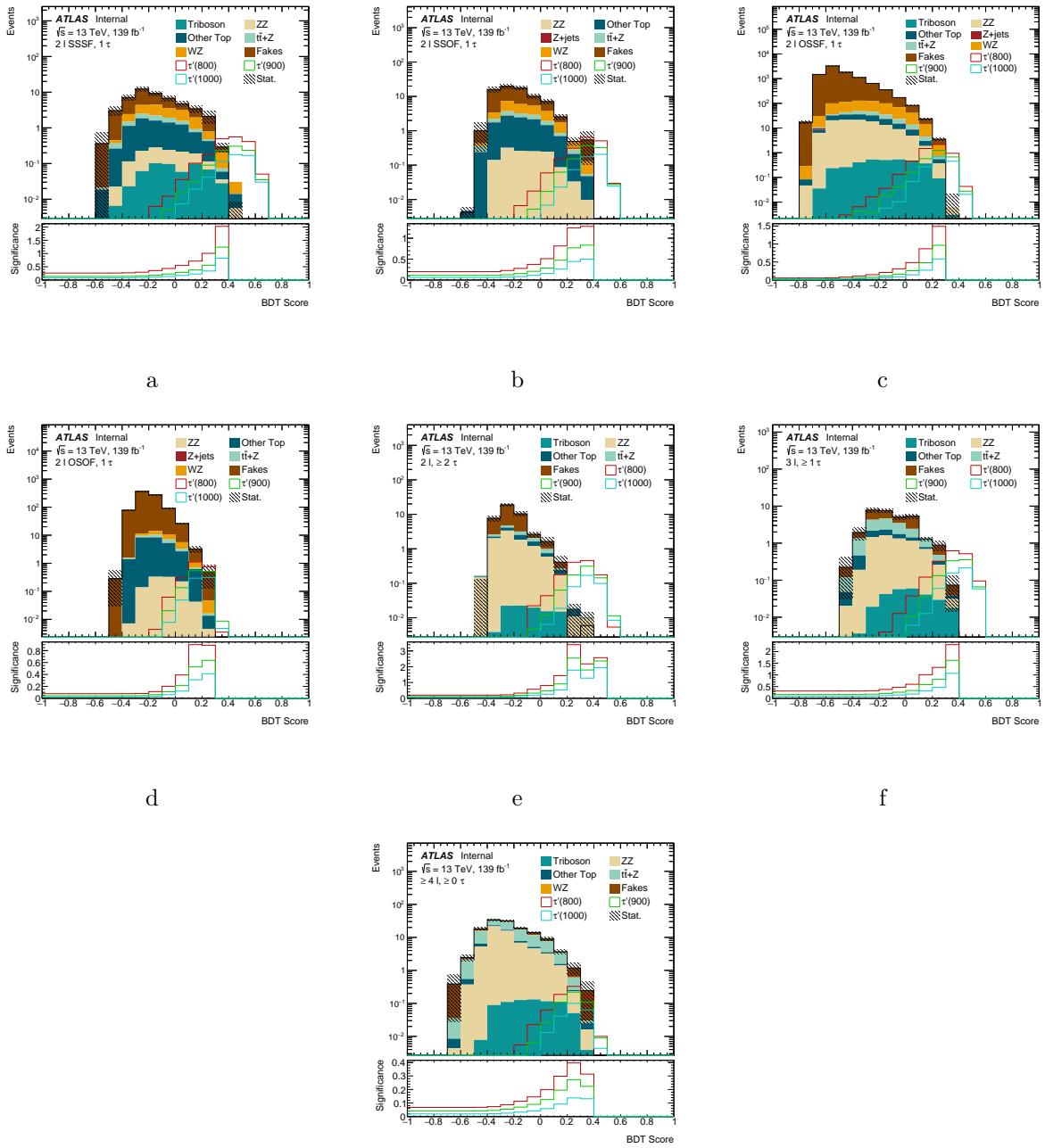
Figure 5.10: BDT score distributions for (a) 2ℓ SSSF, 1τ (b) 2ℓ SSOF, 1τ (c) 2ℓ OSSF, 1τ (d) 2ℓ OSOF, 1τ (e) $2\ell, \geq 2\tau$ (f) $3\ell, \geq 1\tau$ (g) $\geq 4\ell, \geq 0\tau$. "Stat." in the legend refers to statistical uncertainty.

- **Minimum Samples Per Leaf:** the minimum of weighted samples that must be in each leaf node per split. Nodes will be created according to the maximum tree depth so long as the minimum number of samples in each node is satisfied. A higher number of minimum samples per leaf decreases the complexity of the model and a lower number of minimum samples per leaf increases the probability of overtraining the model.

- **Minimum Samples Per Split:** the minimum of weighted samples that must be in a node to allow that node to be split. If the node contains less events than this parameter, the node will terminate and no further splitting will occur. This is to ensure the dimensionality of the model is contained by the statistics of the input.

- **Number of Estimators:** the number of iterations allowed in the boosting algorithm. The larger the number of estimators, the more complex the model.

- **Learning Rate:** a weight that is applied to each classifier at each step of the boosting algorithm.

A grid search of possible values of hyperparameters was conducted for each BDT in order to optimize the algorithm performance for the region in question. For each iteration of hyperparameter space, a 5-folds cross validation was utilized in order to minimize biases when choosing training and testing sets from data. After scanning the possible values of hyperparameters, the set with the largest average AUC score (Section 5.2.4) was chosen as the nominal set for a given BDT. These values are reported in Table 5.2.

Input Variable Optimization In total, there are 34 variables which are used as possible input to the BDTs. The following variable list is not inclusive for each trained BDT as each

region has a subset of variables that are chosen after variable optimization.

E_T^{miss}	The missing transverse momentum in the event.
$\mathbb{S}(E_T^{\mathrm{miss}})$	The missing transverse momentum significance in the event.
L_T	The scalar sum of $\ell\, p_T$ in the event.
$L_T + E_T^{\mathrm{miss}}$	The scalar sum of $\ell\, p_T$ and E_T^{miss} in the event.
$L_T + p_T(\tau)$	The scalar sum of $\ell\, p_T$ and sum of $\tau_{\mathrm{had}}\, p_T$ in the event.
$p_T(\ell_1)$	The leading $\ell\, p_T$ in the event.
$p_T(\ell_2)$	The sub-leading $\ell\, p_T$ in the event.
$p_T(j_1)$	The leading jet p_T in the event.
$p_T(\tau_1)$	The leading $\tau_{\mathrm{had}}\, p_T$ in the event.
N_j	The number of jets in the event.
N_b	The number of b-jets in the event.
H_T	The scalar sum of jet p_T in the event.
$L_T + H_T$	The scalar sum of $\ell\, p_T$ and sum of jet p_T in the event.
$M_{\ell\ell}$	The invariant mass of all light leptons in the event.
$M_{\ell\tau}$	The invariant mass of all light leptons and taus in the event.
$M_{\ell j}$	The invariant mass of all light leptons and jets in the event.
M_{jj}	The invariant mass of all jets in the event.
$M_{j\tau}$	The invariant mass of all jets and taus in the event.
M_T	The transverse mass of the leading ℓ in the event.
M_{OSSF}	The invariant mass the opposite sign same flavor pair of light leptons closest to the Z mass in the event.
$\Delta\phi(j_1 E_T^{\mathrm{miss}})$	$\Delta\phi$ between E_T^{miss} and the leading jet in p_T in the event.
$\Delta\phi(\ell_1 E_T^{\mathrm{miss}})$	$\Delta\phi$ between E_T^{miss} and the leading ℓ in p_T in the event.
$\Delta\phi(\ell_1 \ell_2)$	$\Delta\phi$ between the leading and sub-leading ℓ in p_T in the event.
$\Delta\phi(\ell_1 j_1)$	$\Delta\phi$ between the leading ℓ and leading jet in p_T in the event.
$\Delta\phi(\tau_1 E_T^{\mathrm{miss}})$	$\Delta\phi$ between E_T^{miss} and the leading τ_{had} in p_T in the event.
$\Delta\phi(\ell_1 \tau_1)$	$\Delta\phi$ between the leading ℓ and leading τ_{had} in p_T in the event.
$\Delta\phi(j_1 \tau_1)$	$\Delta\phi$ between the leading jet and leading τ_{had} in p_T in the event.
$\Delta R(j_1 E_T^{\mathrm{miss}})$	ΔR between E_T^{miss} and the leading jet in p_T in the event.
$\Delta R(\ell_1 E_T^{\mathrm{miss}})$	ΔR between E_T^{miss} and the leading ℓ in p_T in the event.
$\Delta R(\ell_1 \ell_2)$	ΔR between the leading and sub-leading ℓ in p_T in the event.
$\Delta R(\ell_1 j_1)$	ΔR between the leading ℓ and leading jet in p_T in the event.
$\Delta R(\tau_1 E_T^{\mathrm{miss}})$	ΔR between E_T^{miss} and the leading τ_{had} in p_T in the event.
$\Delta R(\ell_1 \tau_1)$	ΔR between the leading ℓ and leading τ_{had} in p_T in the event.
$\Delta R(j_1 \tau_1)$	ΔR between the leading jet and leading τ_{had} in p_T in the event.

Hyperparameter	2ℓ					3ℓ	4ℓ
	SSSF	SSOF	OSSF	OSOF			
Maximum Tree Depth	7	5	11	11	11	15	13
Maximum Features	60%	80%	80%	100%	80%	80%	100%
Minimum Samples Per Split	60%	80%	20%	80%	20%	80%	60%
Minimum Samples Per Leaf	5%	5%	5%	5%	20%	5%	5%
Number of Estimators	500	1000	1000	1500	1000	1000	1500
Learning Rate	0.2	0.2	0.2	0.4	0.2	0.2	0.2

Table 5.2: Optimized hyperparameters used for the BDT trainings.

After the hyperparameter values have been optimized, the list of input variables for each BDT was optimized. This was done by training the BDT using the optimized hyperparameter values and removing the lowest ranked variable. The process is repeated until the variable list contains one variable. Ranking is done by counting the number of nodes for which a particular variable is used as the cut variable across all weak classifiers. The AUC score (Section 5.2.4) was calculated as a function of the number of variables and the input variable list was chosen at the point where the AUC score decreases by at least 0.02%. A decrease in AUC score was found to correspond to a roughly 5% decrease in signal significance. The optimized list of input variables for each BDT is reported in Table 5.2.3, which also includes the variable ranking. Variables without a ranking value were excluded as input for the corresponding BDT after optimization. Appendix A provided results on a study performed to assess the effect of the number of variables on the overall result of the analysis.

Variables that are selected in the optimization are only kept for BDT training if the χ^2

p-value between the data and background distributions is greater than 0.05. The post-fit background distributions are used, with normalization factors for $t\bar{t}+Z$, WZ and ZZ applied (derived in Chapter 9). The input variable distributions are shown in Appendix B.

5.2.4 Performance Metrics

Overtraining In order to verify the BDT did not train on statistical fluctuations of the training set, a testing set was used to validate training performance. The BDT scores follow a probability distribution function, thus, a well-trained classifier is able to classify events in the training and testing sets with equal probability. The χ^2 test was applied to both the signal and background BDT score distributions to calculate the probability that both the testing and training sets were drawn from the same distribution. The normalized distributions of the testing and training sets for both background and signal are shown in Figure 5.11 where the χ^2 p-value is at least 0.05 for all cases (shown in parenthesis below the lepton multiplicity label). The distributions are cumulative across each fold.

ROC-AUC A *receiver operating characteristic* (ROC) curve is generated by calculating the false positive and true positive rates for various decision boundaries. The use of these curves is three-fold. First, they give a metric for the performance of the classifier which is proportional to the *area under the curve* (AUC). Second, they allow adjustment of the decision boundary to address the problem at hand and either maximize efficiencies or minimize false positive and false negative errors. Lastly, they can indicate overtraining issues as a training and testing set should have a similar curve if training has been done properly. The ROC curves of the testing and training sets are shown in Figure 5.12.

Variable	2ℓ					3ℓ	4ℓ
	SSSF	SSOF	OSSF	OSOF			
E_T^{miss}	4	7	4	21	5	8	6
$\mathbb{S}(E_T^{\mathrm{miss}})$	20	5	14	24	9	24	7
L_T	27	32			32		23
$L_T + E_T^{\mathrm{miss}}$	3	3	2	2	23	4	1
$L_T + p_T(\tau)$	22	22		26			
$p_T(l_1)$	19	4			30	5	12
$p_T(l_2)$	23	15		18			
$p_T(j_1)$	15	19	10	12	22	19	18
$p_T(\tau_1)$	1	1	1	1	2	2	
N_j	21	14	28	23	26		22
N_b	26	26	21	22	29	20	16
H_T		28		28	33	21	13
$L_T + H_T$		12	3	14			
M_{ll}	18	10	25	20	10	22	
$M_{l\tau}$	2	2	5	3	1	1	5
M_{lj}		11	26	11	27	14	14
M_{jj}	7	21	24	15	1	12	8
$M_{j\tau}$	28	31	15	9	6	18	2
M_T	16	23	16	18	8	17	11
$M_{lE_T^{\mathrm{miss}}}$	8						
M_{OSSF}			22		7	6	17
$\Delta\phi(j_1 E_T^{\mathrm{miss}})$				27	21		4
$\Delta\phi(l_1 E_T^{\mathrm{miss}})$	9	16	20	8	20	10	10
$\Delta\phi(l_1 l_2)$	13	13	18	16	28	13	3
$\Delta\phi(l_1 j_1)$	25	17	13	17	13	25	9
$\Delta\phi(\tau_1 E_T^{\mathrm{miss}})$	5	6	6	13	3	3	
$\Delta\phi(l_1 \tau_1)$		25	19		19	16	
$\Delta\phi(j_1 \tau_1)$	17	20	27	29	24		
$\Delta R(j_1 E_T^{\mathrm{miss}})$	24	18	23	10	31		20
$\Delta R(l_1 E_T^{\mathrm{miss}})$	12	29	11	19	17	11	21
$\Delta R(l_1 l_2)$	6	24	7	7	15		19
$\Delta R(l_1 j_1)$	29		8	4	11		15
$\Delta R(\tau_1 E_T^{\mathrm{miss}})$	14	27	9	5	12	9	
$\Delta R(l_1 \tau_1)$	10	8	12	6	16	15	
$\Delta R(j_1 \tau_1)$	11	9	17	25	25	23	

Table 5.3: Variable rankings for variables used as input for BDTs. Variables which do not have a ranking are not included in the corresponding BDT. The list is creating using an optimization procedure by assessing the AUC score after removal of the variable.
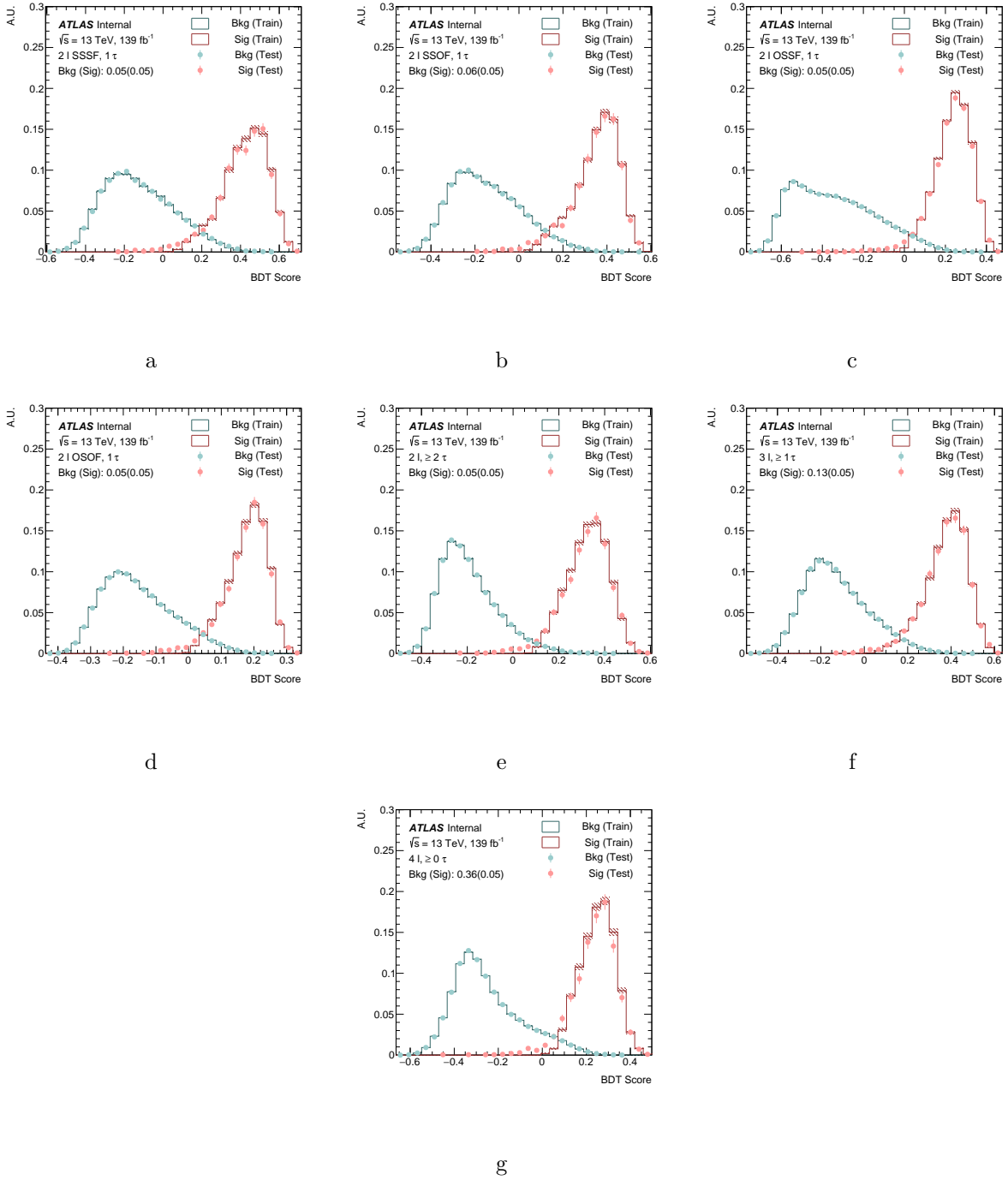
Figure 5.11: The normalized distributions of the cumulative testing and training sets for both background and signal. The χ^2 probability is given in parenthesis below the lepton multiplicity label. (a) 2ℓ SSSF, 1τ (b) 2ℓ SSOF, 1τ (c) 2ℓ OSSF, 1τ (d) 2ℓ OSOF, 1τ (e) $2\ell, \geq 2\tau$ (f) $3\ell, \geq 1\tau$ (g) $\geq 4\ell, \geq 0\tau$

96
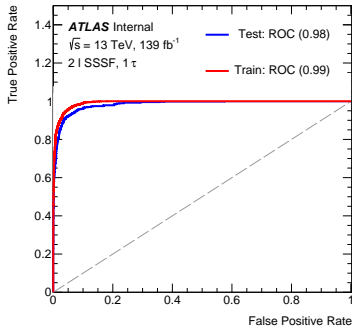
a
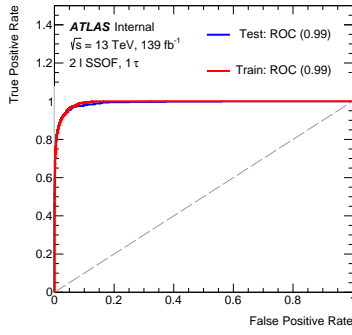
b
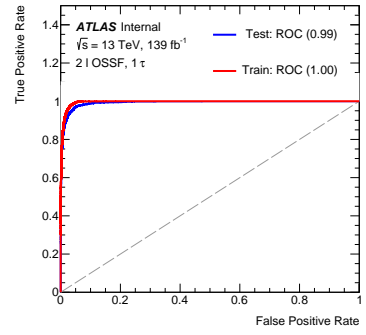
c
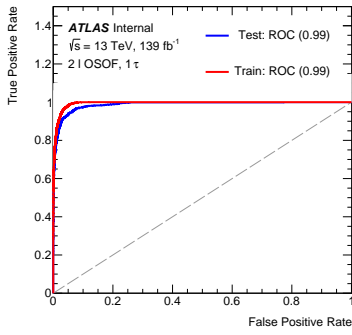
d
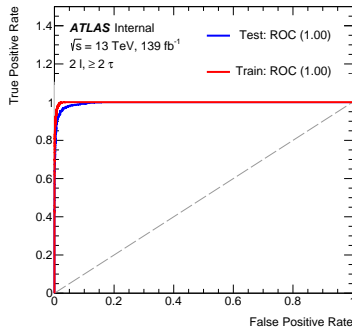
e
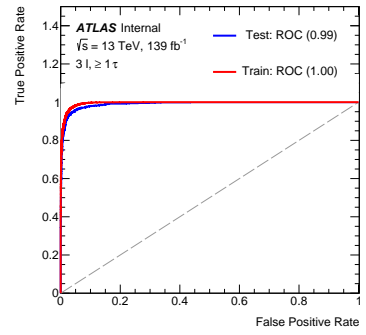
f
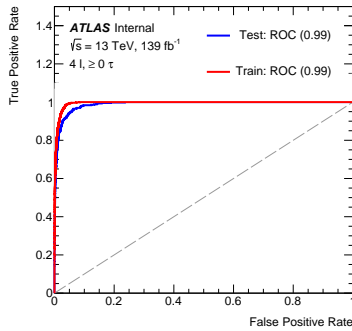
g

Figure 5.12: The ROC curves of the cumulative testing and training sets. The values in parenthesis in the legend are the calculated AUC scores and the dashed curve is considered random guessing. (a) 2ℓ SSSF, 1τ (b) 2ℓ SSOF, 1τ (c) 2ℓ OSSF, 1τ (d) 2ℓ OSOF, 1τ (e) $2\ell, \geq 2\tau$ (f) $3\ell, \geq 1\tau$ (g) $\geq 4\ell, \geq 0\tau$

Chapter 6

Analysis Regions and Event Selection

Events from proton-proton collisions are categorized into *analysis regions*. The analysis regions refer to *control regions* (CRs), *validation regions* (VRs) and *signal regions* (SRs). CRs are used to fit dominant background normalizations for further extrapolation to VRs and SRs. This extrapolation is to ensure background yields are consistent with the SM in regions of phase space probed by the analysis, which are typically low statistics regions that may be poorly modeled. CRs are also used to constrain systematic uncertainties. VRs are used to validate background estimations and CR extrapolations. SRs are used for hypothesis testing and are designed to maximize the significance.

The analysis region definitions presented in this chapter are derived based on the strategy outlined in Chapter 5. Events are separated based on the lepton multiplicity of final states and are fitted with a trained BDT. The BDT score in each lepton multiplicity final state is used to define various analysis regions and also as the discriminating variable in the statistical analysis.

Background processes are those that can mimic the VLL signal by having a similar final state, of which there are two types: irreducible prompt backgrounds which are modeled by MC simulation and the mis-modeled (fake) lepton background which is estimated using a data-driven technique. The prompt backgrounds relevant for this analysis are Z+jets, diboson (ZZ and WZ), triboson and top (split into $t\bar{t} + Z$ and an inclusive sample). The fake background contains contributions from mis-identified electrons, muons and hadronic taus which are combined into an inclusive sample. The background modeling will be described in

more detail in Chapter 7.

The CRs target dominant backgrounds in the SRs, which for this thesis are observed to be WZ, ZZ, $t\bar{t} + Z$ and fake hadronic taus. VRs are defined for each of the backgrounds targeted by CRs. There is also a VR for each SR, taken as the inverted BDT score. This is done in order to validate background predictions and fake estimates. Figure 6.1 shows the various SR and CR's as a function of ℓ and τ_{had} multiplicity. In total, there are seven SRs and four CRs defined for this thesis.
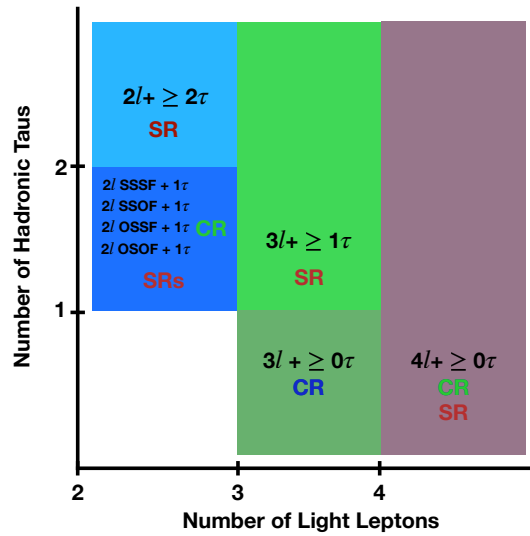
Figure 6.1: SRs and CRs as a function of ℓ and τ_{had} multiplicity.

This chapter will detail the selection criteria for analysis regions used in this thesis, where Table 6.1 provides an overview.

6.1 Triggers

Events must satisfy triggers corresponding to two light leptons. Triggers of this type are chosen as each lepton multiplicity state targeted in the analysis contains at least two light

	CRs				SRs							VRs									
	$t\bar{t}$+Z CR	WZ CR	ZZ CR	Fake τ_{had} CR	2ℓ SR					3ℓ SR	4ℓ SR	$t\bar{t}$+Z VR	WZ VR	ZZ VR	2ℓ VR					3ℓ VR	4ℓ VR
N_ℓ	≥ 4	3	≥ 4	2	2	2	2	2	2	3	≥ 4	3	2	3	2	2	2	2	2	3	≥ 4
S/F				OSSF	SSSF	SSOF	OSSF	OSOF					SSOF		SSSF	SSOF	OSSF	OSOF			
N_τ	≥ 0	0	≥ 0	1	1	1	1	1	≥ 2	≥ 1	≥ 0	≥ 1	1	≥ 1	1	1	1	1	≥ 2	≥ 1	≥ 0
N_j	> 0	> 0	> 0	> 0	> 0	> 0	> 0	> 0	> 0	> 0	> 0	> 0	> 0	> 0	> 0	> 0	> 0	> 0	> 0	> 0	> 0
N_b	> 0	0	0									> 0	0	0							
E_T^{miss} [GeV]	≥ 60	≥ 90	< 60	≥ 60	≥ 120	≥ 90	≥ 60	≥ 100	≥ 60	≥ 90	≥ 60				≥ 120	≥ 90	≥ 60	≥ 100	≥ 60	≥ 90	≥ 60
BDT Score	< 0.08	≥ 0.08	< 0.08	< −0.15	≥ 0.15	≥ 0.1	≥ 0.1	≥ 0.1	≥ −0.11	≥ 0.08	≥ 0.08	< 0.08	< 0.15	< 0.08	< 0.15	< 0.1	< 0.1	< 0.1	< −0.11	< 0.08	< 0.08
																	≥ 0.15				

Table 6.1: Analysis regions used in this thesis. CRs and VRs associated with a particular background are explicitly labeled. Other VRs not associated with a particular background are for general validation of the associated lepton multiplicity SR. The difference between these SR and VRs is the BDT score cut.

leptons. The triggers are either di-electron (ee), di-muon ($\mu\mu$) or electron+muon ($e\mu$). None of the triggers used in the analysis are pre-scaled and both objects that fired the trigger must be matched to a reconstructed particle. Table 6.1 shows the triggers used, as well as their threshold p_T for the data-taking year.

6.2 Signal Regions

Each SR has a corresponding BDT which is trained according to Chapter 5. These regions are defined by ℓ and τ_{had} final state multiplicities. In addition, the same kinematic and topological pre-selection requirements for the BDT training regions are used to define SRs. However, SRs are further selected by imposing a BDT score cut to isolate regions with large signal significance. SRs are initially *blinded* from data, where data is omitted and only the signal and background predictions are used. This is maintained until background contributions are understood through careful study of the CRs and VRs, which are left unblinded in order to

Trigger	p_T threshold [GeV]			
	2015	2016	2017	2018
di-electron (ee)	12	17	17	17
di-muon ($\mu\mu$)	18,8	22,8	22,8	22,8
electron+muon ($e\mu$)	17,14	17,14	17,14	17,14

Table 6.2: Triggers used to select events. The triggers are either di-electron (ee), di-muon ($\mu\mu$) or electron+muon ($e\mu$). The p_T thresholds are shown for each trigger. For di-muon and electron+muon triggers, the first threshold corresponds to the leading light lepton p_T, where the second corresponds to the sub-leading light lepton p_T.

validate against data in regions with low expected signal contamination. Table 6.3 outlines the selection cuts used to define SRs. In total, there are 7 SRs used in the analysis. The SRs will be introduced in terms of the ℓ multiplicity.

In the 2ℓ SRs, events are categorized according to electric charge and lepton flavor states for the pair of two light leptons. Events with exactly one τ_{had} are grouped according to whether the light leptons have the same electric charge (SS), opposite electric charge (OS), same flavor (SF) or opposite flavor (OF). All events with at least two hadronic taus are contained within a single SR.

In the 3ℓ and 4ℓ SRs, events with exactly three light leptons must also have at least one τ_{had}. In events with at least four light leptons, there is no explicit cut on the number of final state hadronic taus.

	2ℓ SRs					3ℓ SR	4ℓ SR
N_ℓ	2	2	2	2	2	3	≥ 4
S/F	SSSF	SSOF	OSSF	OSOF			
N_τ	1	1	1	1	≥ 2	≥ 1	≥ 0
N_j	> 0	> 0	> 0	> 0	> 0	> 0	> 0
E_T^{miss} [GeV]	≥ 120	≥ 90	≥ 60	≥ 100	≥ 60	≥ 90	≥ 60
BDT Score	≥ 0.15	≥ 0.1	≥ 0.1	≥ 0.1	≥ -0.11	≥ 0.08	≥ 0.08

Table 6.3: SR definitions used in this thesis.

The signal region definitions are given explicitly below:

- **2ℓ SRs:**

  – **SSSF:** The first SR is the case of exactly two same sign, same flavor light leptons and exactly one reconstructed τ_{had}. Cuts are imposed such that N_j is greater than 0, E_T^{miss} is greater than 120 GeV and the BDT score is greater than 0.15.

  – **SSOF:** The second SR is the case of exactly two same sign, opposite flavor light leptons and exactly one reconstructed τ_{had}. Cuts are imposed such that N_j is greater than 0, E_T^{miss} is greater than 120 GeV and the BDT score is greater than 0.1.

  – **OSSF:** The third SR is the case of exactly two opposite sign, same flavor light leptons and exactly one reconstructed τ_{had}. Cuts are imposed such that N_j is greater than 0, E_T^{miss} is greater than 60 GeV and the BDT score is greater than 0.1.

– **OSOF:** The fourth SR is the case of exactly two opposite sign, opposite flavor light leptons and exactly one reconstructed τ_{had}. Cuts are imposed such that N_j is greater than 0, E_T^{miss} is greater than 100 GeV and the BDT score is greater than 0.1.

– **Inclusive:** The fifth SR is the case of exactly light leptons of any sign and any flavor and at least two reconstructed hadronic taus. Cuts are imposed such that N_j is greater than 0, E_T^{miss} is greater than 60 GeV and the BDT score is greater than -0.11.

- **3ℓ SR:**

  – The sixth SR is the case of exactly three light leptons and at least one reconstructed τ_{had}. Cuts are imposed such that N_j is greater than 0, E_T^{miss} is greater than 90 GeV and the BDT score is greater than 0.08.

- **4ℓ SR:**

  – The seventh SR is the case of at least four light leptons and any number of reconstructed hadronic taus. Cuts are imposed such that N_j is greater than 0, E_T^{miss} is greater than 60 GeV and the BDT score is greater than 0.08.

Figure 6.2 shows the SRs with all contributing backgrounds prior to the statistical analysis fitting procedure. Signal mass point distributions corresponding to $M_{\tau'} = 800$, 900 and 1000 GeV are also shown.
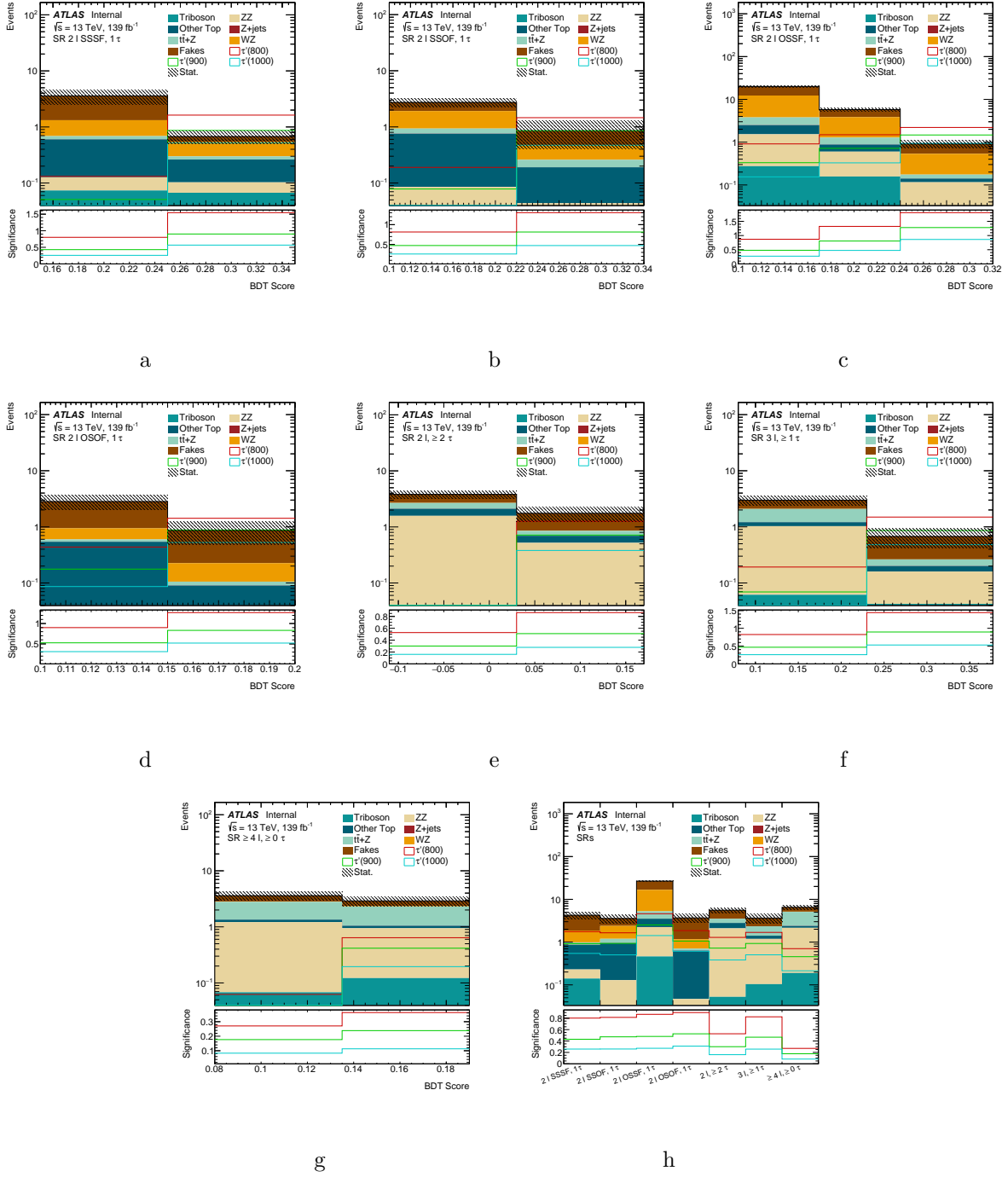
Figure 6.2: Pre-fit BDT score distributions for the SRs used in this thesis. The bottom plots show the signal significance. "Stat." in the legend refers to statistical uncertainty. (a) 2ℓ SSSF, 1τ (b) 2ℓ SSOF, 1τ (c) 2ℓ OSSF, 1τ (d) 2ℓ OSOF, 1τ (e) $2\ell, \geq 2\tau$ (f) $3\ell, \geq 1\tau$ (g) $\geq 4\ell, \geq 0\tau$ (h) Total signal and background yield in each SR.

6.3   Control Regions

CRs are defined by maximizing a particular background processes. In this thesis, CRs are used for two purposes: constraint of the uncertainty in the origin of fake hadronic taus and normalization of dominant prompt background processes.

The estimation of fake hadronic taus (Chapter 7.6) is dependent on the type of jet mis-identified as a τ_{had}. The SRs defined in Section 6.2 are dominated by fake taus originating from light flavor (LF) jets which are hadronizations of u, d, s quarks or heavy flavor (HF) jets which are hadronizations of b or c quarks. The relative contributions from LF or HF is taken explicitly in the fake estimation. However, the SRs contain a sub-dominant component of fake taus originating from gluon or pile-up jets, typically less than 20%. A systematic uncertainty is introduced for this contribution and its effect in the analysis regions constrained by the hypothesis testing fitting procedure (Chapter 9). The 2ℓ OSSF, 1τ BDT score distribution was found to contain a large contribution of gluon and pile-up-initiated fake hadronic taus at very low BDT scores. This region was taken as the CR to constrain the systematic uncertainty. Figure 6.3a shows the fake τ_{had} composition in the SRs as taken from MC simulation. Figure 6.3b shows the composition of fake τ_{had} in the 2ℓ OSSF, 1τ BDT score distribution. The region to the left of the red line is taken as the CR, where the gluon and pile-up fraction begins to deviate from the SRs.

The dominant prompt backgrounds in this analysis are WZ, ZZ and $t\bar{t} + Z$ production. The normalization factors calculated in these regions are applied to the corresponding backgrounds in SRs and VRs. These regions utilize trained BDTs (Chapter 5) that have the same ℓ multiplicity. Table 6.4 outlines the selection cuts used to define these regions which
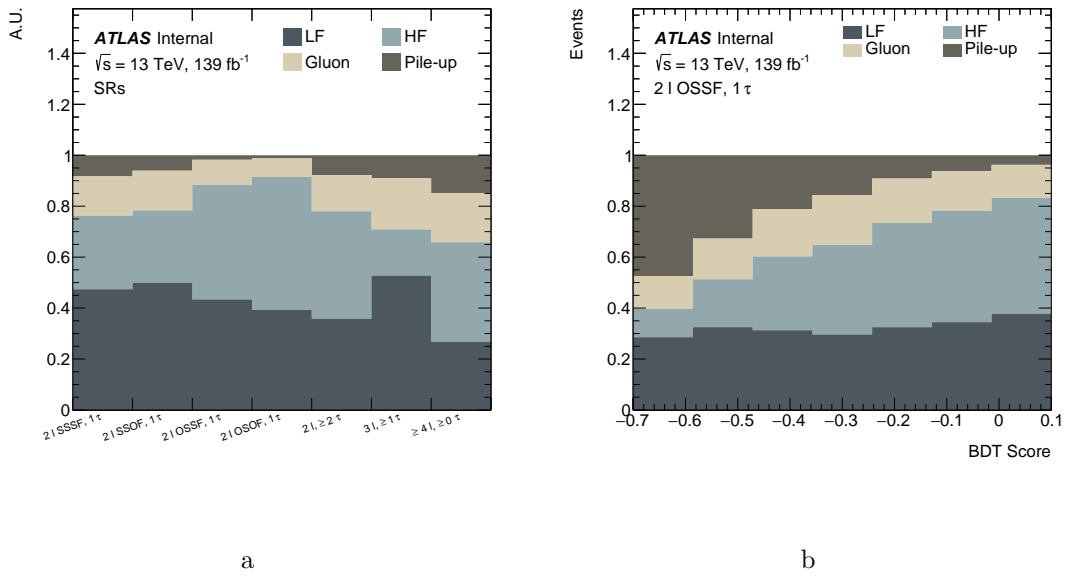
Figure 6.3: (a) Composition of fake τ_{had} in the SRs as taken from MC simulation. The majority of regions have a collective gluon and pile-up contribution less than 20%. (b) Composition in the BDT score of the 2ℓ OSSF, 1τ region. The CR is taken to the left of the red line where the gluon and pile-up fraction begins to deviate from the SRs.

differ from the SRs by either the number of hadronic taus or the BDT score cut. In total, there are four CRs used in the analysis. CR definitions are given explicitly below:

	$t\bar{t}$+Z CR	WZ CR	ZZ CR	Fake τ_{had} CR
N_ℓ	≥ 4	3	≥ 4	2
S/F				OSSF
N_τ	≥ 0	0	≥ 0	1
N_j	> 0	> 0	> 0	> 0
N_b	> 0	0	0	
E_T^{miss} [GeV]	≥ 60	≥ 90	< 60	≥ 60
BDT Score	< 0.08	≥ 0.08	< 0.08	< -0.15

Table 6.4: CR definitions used in this thesis.

- **Background Normalization CRs:**

  – **$t\bar{t} + Z$ CR:** The first CR is used to normalize the combined background coming from $t\bar{t} + Z$, which has at least four light leptons and any number of hadronic taus. Cuts are imposed such that N_j is greater than 0, N_b is greater than 0, E_T^{miss} is greater than 60 GeV and the BDT score is less than 0.08.

  – **WZ CR:** The second CR is used to normalize the background coming from WZ, which has exactly three light leptons and exactly zero hadronic taus. Cuts are imposed such that N_j is greater than 0, N_b is exactly 0, E_T^{miss} is greater than 90 GeV and the BDT score is greater than 0.08.

  – **ZZ CR:** The third CR is used to normalize the background coming from ZZ,

107

which has at least four light leptons and any number of hadronic taus. Cuts are imposed such that N_j is greater than 0, N_b is exactly 0, E_T^{miss} is greater than 60 GeV and the BDT score is less than 0.08.

- **Fake τ_{had} CR:** The fourth CR is used to constrain the uncertainty in composition of fake hadronic taus originating from gluon and pile-up jets, which has exactly two opposite sign, same flavor light leptons and exactly one reconstructed τ_{had}. Cuts are imposed such that N_j is greater than 0, E_T^{miss} is greater than 60 GeV and the BDT score is less than -0.15.

Figure 6.4 shows the CRs with all contributing backgrounds prior to the statistical analysis fitting procedure. Signal mass point distributions corresponding to $M_{\tau'} = 800$, 900 and 1000 GeV are also shown.

6.4 Validation Regions

Validation regions are used in this thesis to verify the background modeling. There are three VRs that correspond to the background normalizations targeted by CRs detailed in Section 6.3. Additionally, there are seven additional VRs that do not address a particular background, rather, are used to check overall background modeling for the various ℓ and τ_{had} multiplicity states. They are defined with the same cuts as the SRs, trained with the same BDTs, but with an inverted BDT score cut. Table 6.5 outlines the selection cuts used to define these regions.

The validation region definitions are given explicitly below:

- **Background Normalization VRs:**
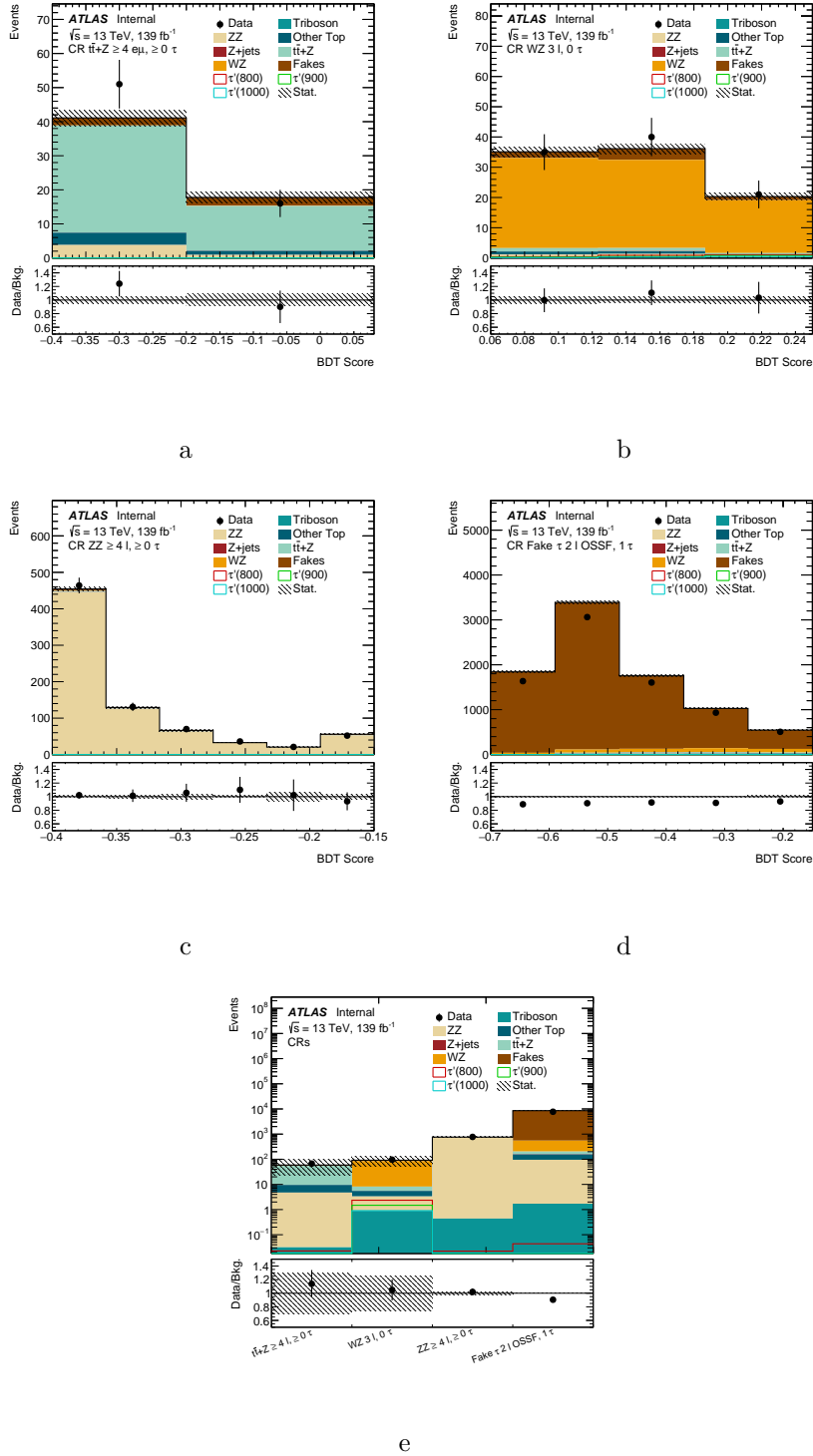
Figure 6.4: Pre-fit BDT score distributions for the CRs used in this thesis. The bottom plots show the ratio of data to the background prediction. "Stat." in the legend stands for statistical uncertainty. (a) $t\bar{t}+Z$ (b) WZ (c) ZZ (d) Fake τ_{had} (e) Total signal and background yield in each CR.

	$t\bar{t}+Z$ VR	WZ VR	ZZ VR	2ℓ VRs					3ℓ VR	4ℓ VR
N_ℓ	3	2	3	2	2	2	2	2	3	≥ 4
S/F		SSOF		SSSF	SSOF	OSSF	OSOF			
N_τ	≥ 1	1	≥ 1	1	1	1	1	≥ 2	≥ 1	≥ 0
N_j	> 0	> 0	> 0	> 0	> 0	> 0	> 0	> 0	> 0	> 0
N_b	> 0	0	0							
E_T^{miss} [GeV]				≥ 120	≥ 90	≥ 60	≥ 100	≥ 60	≥ 90	≥ 60
BDT Score	< 0.08	< 0.15	< 0.08	< 0.15	< 0.1	< 0.1	< 0.1	< -0.11	< 0.8	< 0.08
						≥ -0.15				

Table 6.5: VR definitions used in this thesis. The first three columns show the VRs for specific backgrounds targeted by CRs. The last seven columns show VRs with inverted BDT score cuts relative to SRs.

- $t\bar{t}+Z$ **VR:** The first VR is the case of exactly three light leptons and at least one reconstructed τ_{had}. Cuts are imposed such that N_j is greater than 0, N_b is greater than 0 and the BDT score is less than 0.08.

- WZ **CR:** The second VR is the case of exactly two light leptons with same sign and opposite flavor and exactly one hadronic τ_{had}. Cuts are imposed such that N_j is greater than 0, N_b is exactly 0 and the BDT score is less than 0.15.

- ZZ **CR:** The third VR is the case of exactly three light leptons and at least one reconstructed τ_{had}. Cuts are imposed such that N_j is greater than 0, N_b is exactly 0 and the BDT score is less than 0.08.

- **Inverted BDT Score VRs:**

– **SSSF:** The fourth VR is the case of exactly two same sign, same flavor light leptons and exactly one reconstructed τ_{had}. Cuts are imposed such that N_j is greater than 0, E_T^{miss} is greater than 120 GeV and the BDT score is less than 0.15.

– **SSOF:** The fifth VR is the case of exactly two same sign, opposite flavor light leptons and exactly one reconstructed τ_{had}. Cuts are imposed such that N_j is greater than 0, E_T^{miss} is greater than 120 GeV and the BDT score is less than 0.1.

– **OSSF:** The sixth VR is the case of exactly two opposite sign, same flavor light leptons and exactly one reconstructed τ_{had}. Cuts are imposed such that N_j is greater than 0, E_T^{miss} is greater than 60 GeV and the BDT score is between -0.15 and 0.1.

– **OSOF:** The seventh VR is the case of exactly two opposite sign, opposite flavor light leptons and exactly one reconstructed τ_{had}. Cuts are imposed such that N_j is greater than 0, E_T^{miss} is greater than 100 GeV and the BDT score is less than 0.1.

– **Inclusive:** The eighth VR is the case of exactly two light leptons of any sign and any flavor and at least two reconstructed hadronic taus. Cuts are imposed such that N_j is greater than 0, E_T^{miss} is greater than 60 GeV and the BDT score is less than -0.11.

– **3ℓ SRs:** The ninth VR is the case of exactly three light leptons and at least one reconstructed τ_{had}. Cuts are imposed such that N_j is greater than 0, E_T^{miss} is greater than 90 GeV and the BDT score is less than 0.08.

– **4ℓ SRs:** The tenth VR is the case of at least four light leptons and any number of reconstructed hadronic taus. Cuts are imposed such that N_j is greater than 0,

111

E_T^{miss} is greater than 60 GeV and the BDT score is less than 0.08.

Figure 6.5 shows the VRs with all contributing backgrounds prior to the statistical analysis fitting procedure. Signal mass point distributions corresponding to $M_{\tau'} = 800$, 900 and 1000 GeV are also shown.
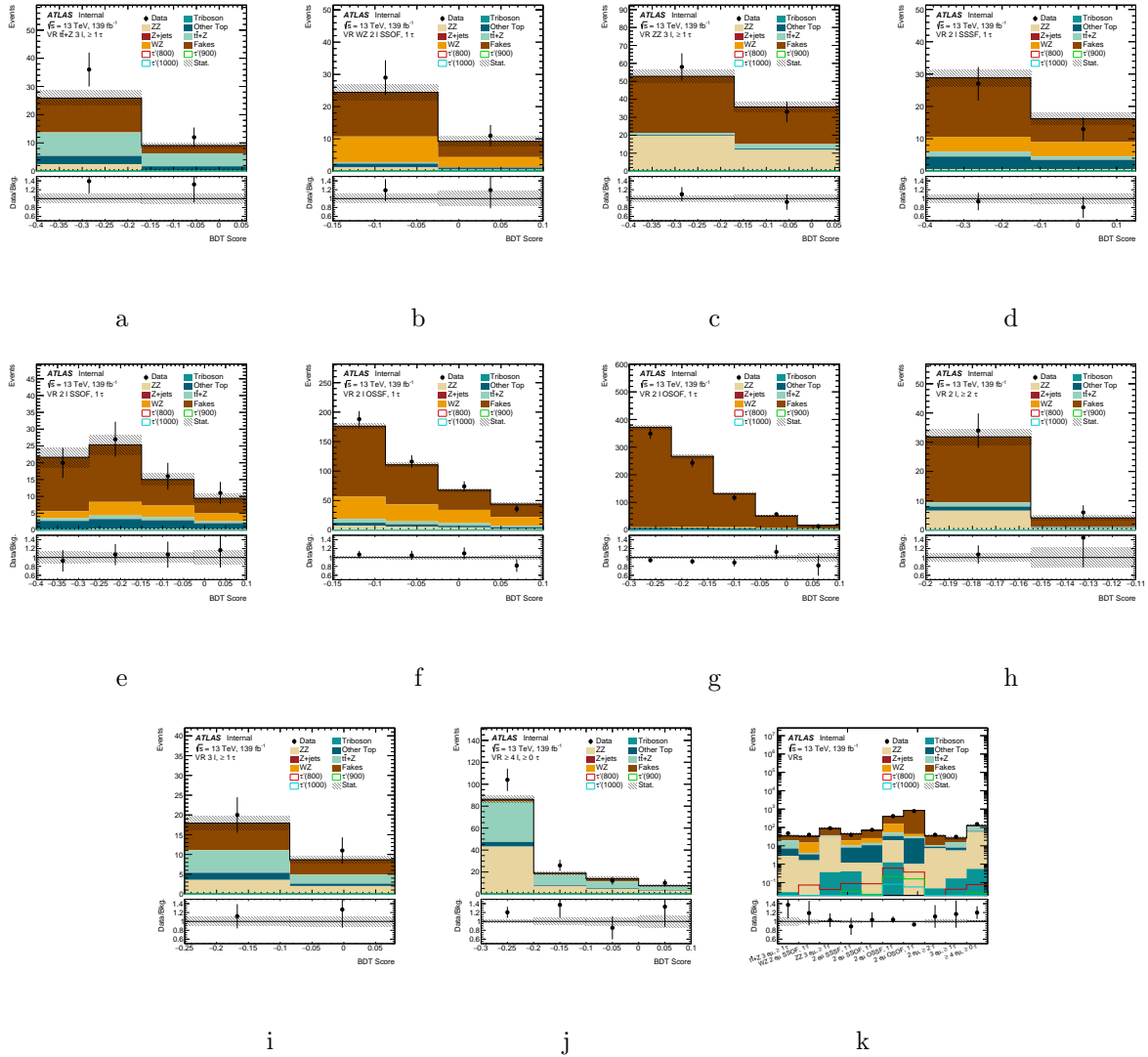
Figure 6.5: Pre-fit BDT score distributions for the VRs used in this thesis. The bottom plots show the ratio of data to the background prediction. "Stat." in the legend stands for statistical uncertainty. (a) $t\bar{t} + Z$ (b) WZ (c) ZZ (d) 2ℓ SSSF, 1τ (e) 2ℓ SSOF, 1τ (f) 2ℓ OSSF, 1τ (g) 2ℓ OSOF, 1τ (h) $2\ell, \geq 2\tau$ (i) $3\ell, \geq 1\tau$ (j) $\geq 4\ell, \geq 0\tau$ (k) Total signal and background yield in each VR

Chapter 7

Background Estimation

There are two types of backgrounds that are characterized in this thesis. Irreducible prompt backgrounds are those from physics processes with final states that closely resemble the VLL signal. The other type of background is that of mis-identified leptons (electrons, muons and hadronic taus).

The prompt background is estimated from MC simulation. For these contributions, leptons in the event must be truth-matched, as described in Section 4.3. The backgrounds contained in this set are from physics processes corresponding to WZ, ZZ, triboson, Z+jets and top quark production. The background from mis-identified electrons, muons and hadronic taus is estimated using the data-driven fake factor method.

Various studies were performed to assess the backgrounds and their agreement with SM prediction. This chapter will introduce the strategy for categorization of top quark production processes, re-weighting of the WZ background and the data-driven fake factor method for estimation of fake leptons.

7.1 Composition of Top Backgrounds

There are various background processes containing top quarks in the underlying event (Section 4.2.4), each of which has a unique production cross-section. In order to reduce the number of free parameters in the statistical analysis, namely the number of background normalization factors, negligible production modes were grouped together.

Production of $t\bar{t}$, $t\bar{t} + Z$, $t\bar{t} + H$ and $t\bar{t} + W$ were studied in detail due to significant

114

contributions in the SRs. An inclusive "Other Top" sample was defined containing t, $t\bar{t}+WW$, ttt and $t\bar{t}t\bar{t}$ production, each of which has a negligible contribution in the SRs. It is assumed grouping processes in this manner does not introduce bias due to the relatively small contribution from each constituent. For the remainder of this section WZ, ZZ, triboson, Z+jets and mis-identified lepton backgrounds are grouped into an "Other Bkg" sample to distinguish from top processes. Figure 7.1 shows the SRs (Section 6.2) split into top production modes.

Table 7.1 gives the relative breakdown of top samples for each SR. The "Other Bkg" contribution dominates in every SR. The $t\bar{t}$ sample does not contribute to any SR. The $t\bar{t}+Z$ sample has a large relative contribution between 0.13-0.42 in the 2ℓ-inc, 3ℓ and 4ℓ SRs. The $t\bar{t}+H$ sample has a relative contribution of 0.12 in the 2ℓ-inc SR. The $t\bar{t}+W$ sample is a relatively small background across all SRs, with a maximum relative contribution of 0.13 in the 2ℓ-SSOF SR. The "Other Top" contribution is less than 0.05 in every SR.

It was determined from this information that $t\bar{t}$ has a negligible contribution to the SRs and can be included in the "Other Top" inclusive sample. The $t\bar{t}+W$ sample is present in various SRs with a sub-dominant contribution, however, it is indistinguishable from $t\bar{t}$ at NLO. Since the production cross-section for $t\bar{t}+W$ is approximately 1,000 times smaller than for $t\bar{t}$, defining a unique CR for background normalization purposes is not possible. Therefore, $t\bar{t}+W$ was also included in the 'Other Top" inclusive sample.

The $t\bar{t}+H$ sample is present in various SRs with a sub-dominant contribution. However, it is difficult to decouple from $t\bar{t}+Z$ due to similar decay modes and production cross-sections. A dedicated CR for a combined sample of $t\bar{t}+H$ and $t\bar{t}+Z$ could be implemented, however, they are produced with different generators (Section 4.2.4). To avoid potential biases, the
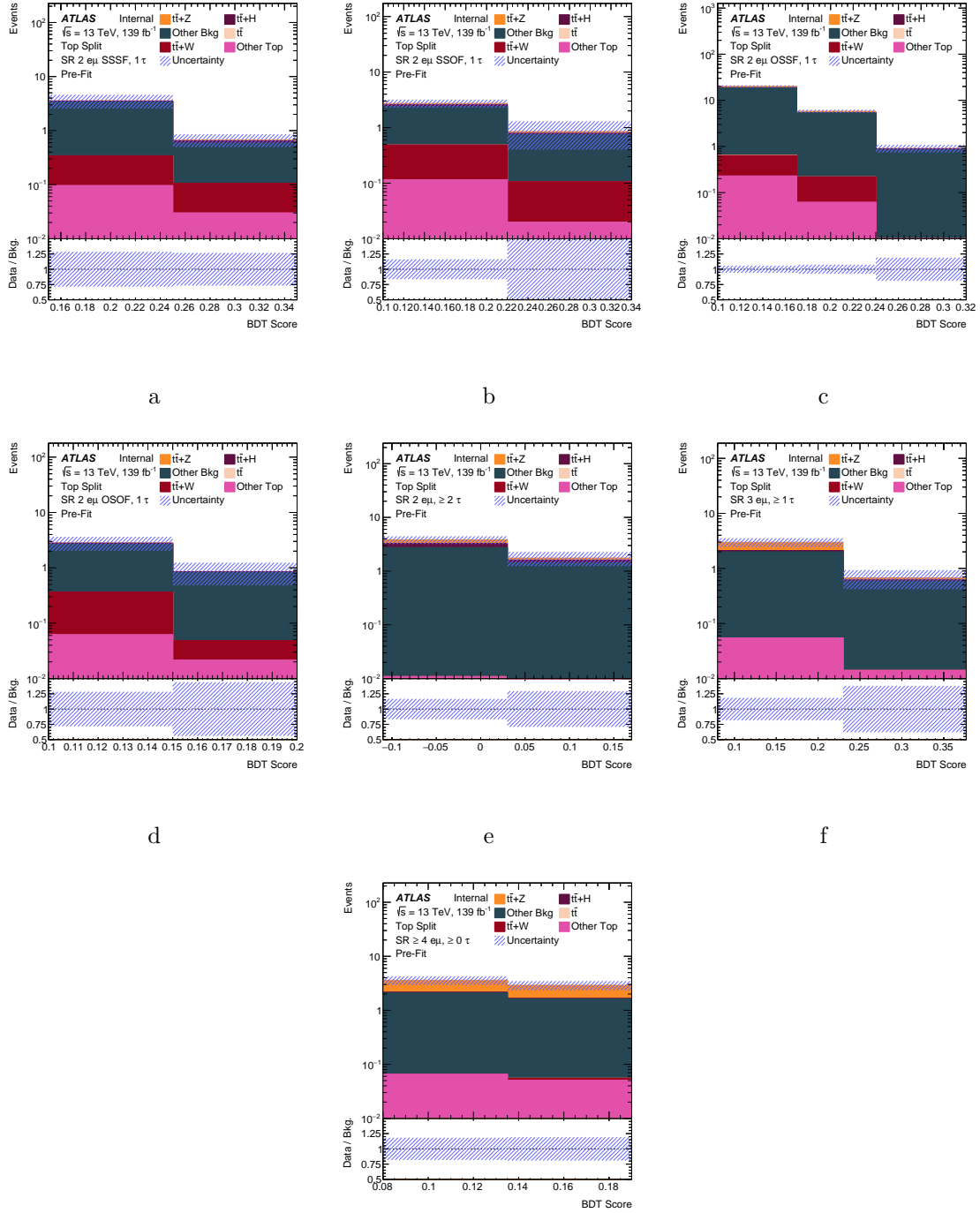
Figure 7.1: BDT score distributions for the SRs split into various top production modes. (a) 2ℓ SSSF, 1τ (b) 2ℓ SSOF, 1τ (c) 2ℓ OSSF, 1τ (d) 2ℓ OSOF, 1τ (e) 2ℓ, ≥ 2τ (f) 3ℓ, ≥ 1τ (g) ≥ 4ℓ, ≥ 0τ.

$t\bar{t} + H$ was added to the "Other Top" inclusive sample.

The $t\bar{t} + Z$ sample was kept separated from other top quark production modes since it is the dominant top production mode in four of the seven SRs. The remaining top samples were all combined into the inclusive "Other Top" sample. A dedicated CR was defined for $t\bar{t} + Z$ production for the purpose of background normalization. Production modes included in the "Other Top" sample were normalized according to theory prediction.

Background	2ℓ SRs					3ℓ SR	4ℓ SR
	SSSF	SSOF	OSSF	OSOF	2ℓ-inc		
Other Bkg	0.82	0.70	0.89	0.82	0.74	0.68	0.55
$t\bar{t}$	0	0	0	0	0	0	0
$t\bar{t} + Z$	0.03	0.07	0.06	0.02	0.13	0.25	0.42
$t\bar{t} + H$	0.04	0.06	0.02	0.05	0.12	0.04	0.02
$t\bar{t} + W$	0.08	0.13	0.02	0.09	0	0	0
Other Top	0.03	0.04	0.01	0.02	0	0.02	0.02

Table 7.1: Relative composition of various top production modes for each SR. Numbers may not add to one due to rounding.

7.2 Shape of WZ and ZZ Backgrounds

The shape of the WZ background was re-weighted to correct for mis-modeling seen when comparing data and background expectation. The mis-modeling was most prevalent in the N_j expectation and re-weighting was performed using this distribution. The CRs (Section 6.3)

for both the WZ and ZZ backgrounds were binned in N_j and the effect of re-weighting was investigated.

In the WZ background, a shift in the N_j distribution was observed. A dedicated CR ("jet re-weight WZ CR") was defined by inverting the BDT score of the WZ CR, where a similar mis-modeling is seen. The purpose of the jet re-weight WZ CR was solely for re-weighting and was not used elsewhere in the analysis. A per-bin re-weighting was performed using the jet re-weight WZ CR by taking the ratio of WZ to data. All non-WZ backgrounds were subtracted from the data yield. The weight is defined as:

$$w_b = \frac{N_b^{\text{data}} - \sum_{!WZ} N_b^{!WZ}}{N_b^{WZ}} \tag{7.1}$$

where the index b refers to the bin in the N_j distribution and $!WZ$ indicates backgrounds that are not WZ, specifically ZZ, Z+jets, $t\bar{t} + Z$, Other Top and mis-identified leptons.

Figure 7.2 shows the N_j distribution for the WZ CR and the jet re-weight WZ CR before re-weighting. Figure 7.3 shows the derived re-weighting factors as a function of N_j, and the N_j distributions for the WZ CR and the jet re-weight WZ CR after re-weighting. The χ^2 p-value for the WZ CR improves from 0.38 (Figure 7.2a) to 0.88 (Figure 7.3b) after re-weighting. This result was propagated into the analysis regions.

In the nominal ZZ CR, the N_j distribution also shows a shift. However, this shift is minimized when looking at a region with a E_T^{miss} cut more compatible with the 4ℓ SR. The "jet re-weight ZZ CR" was defined the same as the ZZ CR, but with $E_T^{\text{miss}} > 40$ GeV. Re-weighting for ZZ was not performed in order to avoid biasing the sample. Figure 7.4 shows the N_j distribution for the ZZ CR and the "jet re-weight ZZ CR" without re-weighting applied.
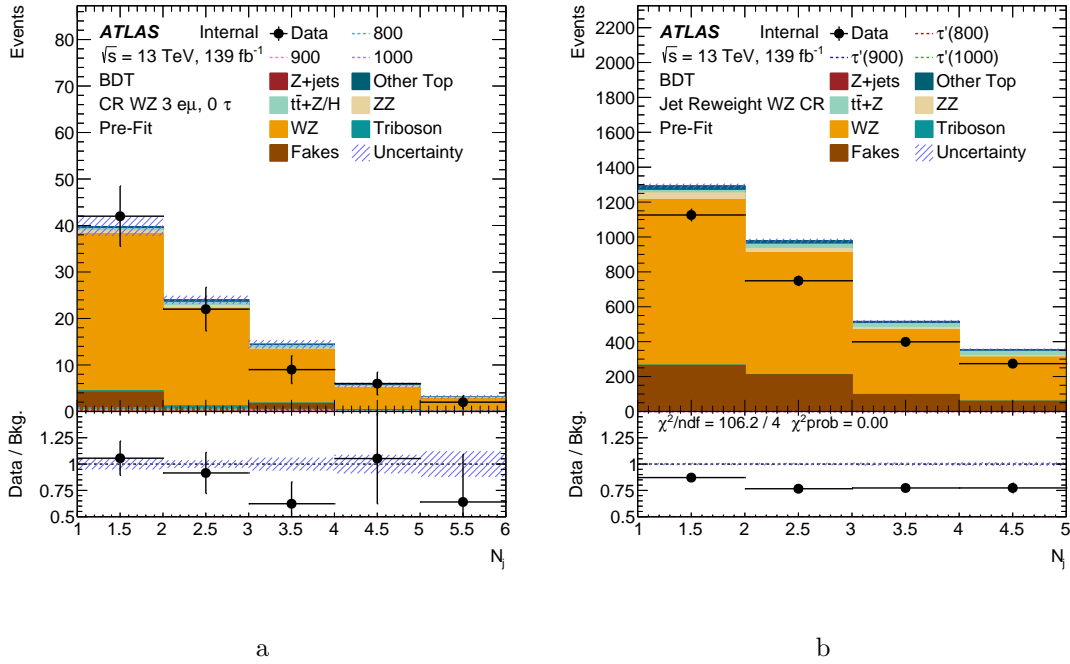
Figure 7.2: N_j distribution prior to re-weighting for (a) the WZ CR and (b) the jet re-weight WZ CR.
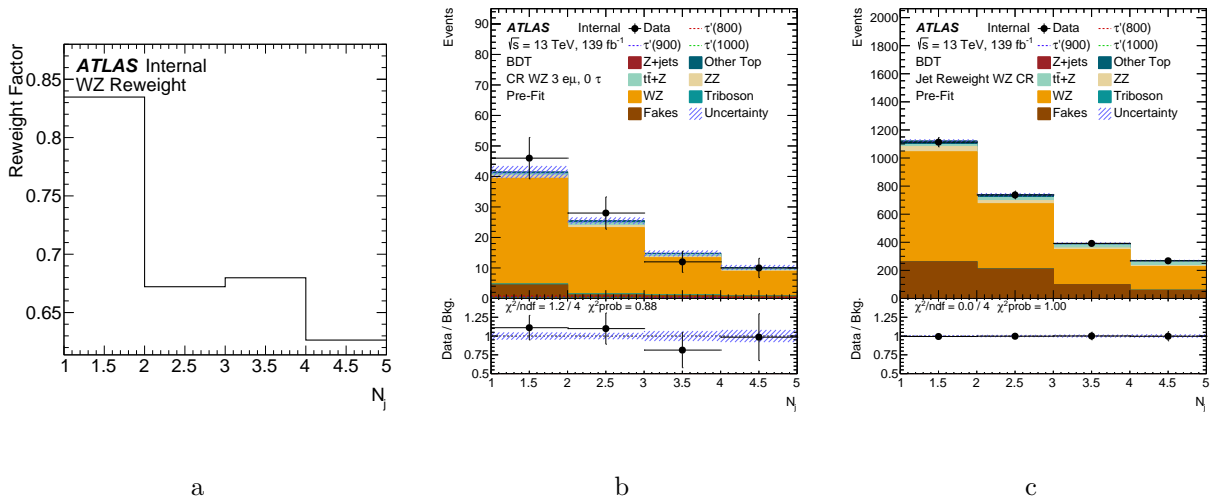
Figure 7.3: N_j distribution after re-weighting for (a) the WZ re-weighting factors (b) the WZ CR and (c) the jet re-weight WZ CR.
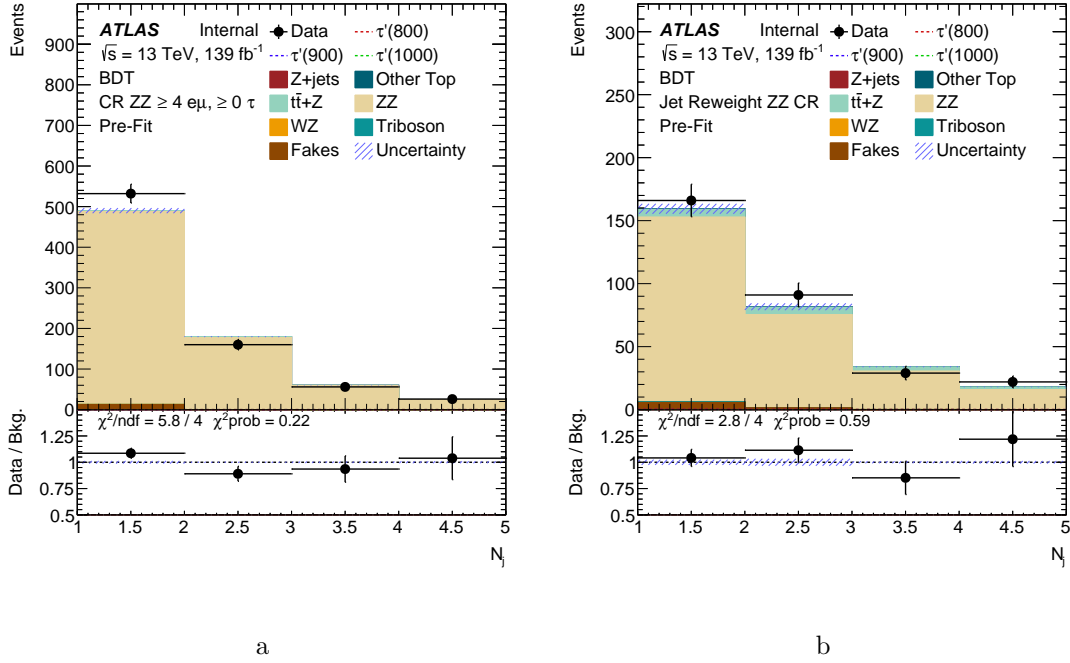
Figure 7.4: N_j distribution for (a) the nominal ZZ CR and (b) the jet re-weight ZZ CR.

7.3   Fake Factor Method

A substantial background in this thesis is the reducible background associated with mis-identified leptons. The majority of the mis-identified lepton background arises from hadronic jets that are erroneously reconstructed as prompt leptons. This so-called "fake" background is estimated using the data-driven *fake factor method* [106], where the method is employed for electrons, muons and hadronic taus. A data-driven approach is preferred as this background is difficult to simulate in MC. Fake events are rare relative to the rate of QCD events and would require an unreasonably large number of simulated events for accurate predictions.

The fake factor method performs an extrapolation from a dedicated *fake factor control region* (FFCR) to estimate the number of fakes in the analysis regions. The *fake factor* (F) is a transfer factor, which is measured in a FFCR replete with the fake object in question. F is measured using two types of objects:

- *Tight* (T): same lepton definition as the analysis regions.

- *Loose* (L): inverted lepton definition relative to the analysis regions, where "tight" leptons are a subset of "loose" leptons. "Loose" leptons are less pure in the number of true leptons compared with "tight" leptons.

The definitions of "tight" and "loose" leptons are given in Chapter 3 with the e definition in Table 3.1, the μ definition in Table 3.2 and the τ_{had} definition in Table 3.5.

The mis-identification probability for tight objects in the analysis regions is called the *fake rate* (f) and is defined as:

$$f = \frac{N_{\mathrm{T}}}{N_{\mathrm{T}} + N_{\mathrm{L}}} \tag{7.2}$$

where N_{T} are the number of fake leptons that fulfill the "tight" requirement and N_{L} are the number of fake leptons that fulfill the "loose" requirement. The fake factor is a multiplicative transfer factor which is applied to "loose" objects to estimate the number of "tight" objects that are mis-identified. The fake factor is defined as:

$$F = \frac{f}{1 - f} = \frac{N_{\mathrm{T}}}{N_{\mathrm{L}}} \tag{7.3}$$

The relationship between "loose" and "tight" objects and the FFCR and analysis regions is shown schematically in Figure 7.5.

The fake factor is dependent on the composition of the fakes. Therefore, the fake factor should be applied to analysis regions that have a similar composition as the FFCR, typically as a function of one or more kinematic variables (p_T, η, etc.). For analysis regions with one and only one lepton, the fake factor is applied as a "per-object" weight to "loose" leptons, where the number of fake leptons is estimated as:
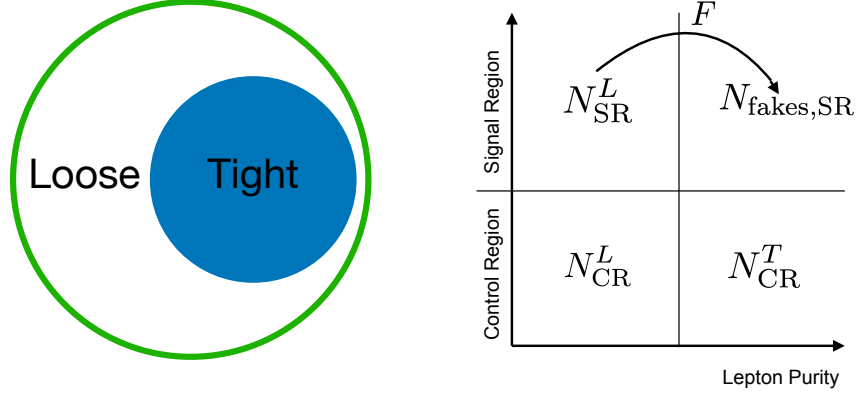
Figure 7.5: The diagram on the left illustrates how "tight" leptons are a subset of "loose" leptons. The diagram on the right shows the FFCR and analysis regions as a function of lepton purity, where "tight" leptons are more pure than "'loose". The fake factor is a transfer factor between the FFCR and analysis regions.

$$N_l^{\text{fake,SR}} = F \times \left(N_{l,\text{data}}^{\text{L,SR}} - N_{l,\text{prompt MC}}^{\text{L,SR}} \right) \tag{7.4}$$

The last term accounts for double counting true leptons which are subtracted according to MC simulation.

In order to properly account for the possibility of more than one fake lepton in an event, a "per-event" fake factor is used. Fakes from electrons, muons and hadronic taus are combined and the relative contributions are shown in Appendix C. The number of fakes can be estimated for an arbitrary number of fake leptons in the final state as:

$$N_{\text{SR}}^{\text{fake}} = \sum_{i=1}^{N^{\text{data}}} (-1)^{N_{L,i}+1} \prod_{l=1}^{N_{L,i}} F_l - \sum_{i=1}^{N^{\text{MC}}} (-1)^{N_{L,i}+1} \prod_{l=1}^{N_{L,i}} F_l \tag{7.5}$$

As an example, consider an analysis region with two final state leptons, either of which can be fake. The number of fake objects in the analysis region is then calculated as:

$$N_{\text{SR}}^{\text{fake}} \overset{l=2}{=} \left[\sum_{LT} \boxed{F_1} + \sum_{TL} \boxed{F_2} - \sum_{LL} \boxed{F_1 F_2} \right]_{\text{data}} - \left[\sum_{LT} \boxed{F_1} + \sum_{LT} \boxed{F_2} + \sum_{LL} \boxed{F_1 F_2} \right]_{\text{MC}} \quad (7.6)$$

	L_1	T_1
L_2	2 fake $-F_1 F_2$	1 fake $+F_2$
T_2	1 fake F_1	SR

7.4 Electron Fake Factor Measurement

Fake electrons arise from two main sources, where the first are mis-identified jets that are initiated by quark or gluon fragmentations and the second are real electrons whose origin is in-flight hadron decays. A QCD enriched di-jet + e region is chosen as the FFCR for the fake e background. An upper limit on E_T^{miss} is placed in order to suppress contributions from W+jets.

Pre-scaled single e triggers with relaxed isolation requirements are used. This is in order to allow adequate statistics for "loose" electrons, whose isolation requirement is inverted relative to "tight", signal electrons. Since multiple triggers can be fired for a single e in an event, the lowest pre-scale (and subsequently highest p_T threshold) trigger is used for trigger matching. The trigger list with average pre-scale is given in Table 7.2.

The e fake factor is derived in the FFCR defined below:

Trigger	Average Pre-scale	Years
HLT_e26_lhvloose_nod0_L1EM20VH	111.2	2015-2016
HLT_e28_lhvloose_nod0_L1EM20VH	367.6	2017
HLT_e28_lhvloose_nod0_L1EM22VH	384.5	2018
HLT_e60_lhvloose_nod0	32.93	2015-2018
HLT_e70_lhvloose_nod0	64.13	2018
HLT_e80_lhvloose_nod0	40.43	2018
HLT_e100_lhvloose_nod0	19.45	2015
HLT_e120_lhvloose_nod0	12.15	2016-2018
HLT_e140_lhvloose_nod0	2.637	2016-2018
HLT_e160_lhvloose_nod0	1.601	2017-2018
HLT_e200_etcut	1.0	2015
HLT_e300_etcut	1.0	2016-2018

Table 7.2: Single e triggers used in the e fake factor calculation with average pre-scale.

- Exactly one "loose" or "tight" e and exactly zero "tight" muons and "tight" hadronic taus

- $E_T^{\mathrm{miss}} < 40$ GeV

- At least two jets

- Exactly zero b-jets

The e fake factor is binned in p_T and η. Figure 7.6 shows the inclusive p_T and η distributions for "tight" and "loose" electrons in the FFCR. The plots contain the data

distributions as well as the prompt truth-matched e MC contribution, which is subtracted from data. The "tight" selection requirements yield a significantly larger truth-matched prompt e contribution than the "loose" selection requirements.

Uncertainties for the e fake factors were derived by considering the composition of fake e sources as well as MC modeling uncertainty for prompt subtraction. For each variation, the fake factor was measured independently of other variation types. The various systematics are shown in Table 7.3. The number of jets was inverted to $N_j < 2$ and the E_T^{miss} requirement was removed to account for variations in fake e composition in the FFCR. In order to assess the cross-section and luminosity uncertainties in prompt MC subtraction, the truth-matched MC contribution was scaled up and down by 10%.

Systematic	Purpose
$N_j < 2$	Composition
No E_T^{miss} requirement	Composition
MC scaled up by 10%	MC modeling
MC scaled up down 10%	MC modeling

Table 7.3: Summary of systematic variations to the e fake factor.

The largest contribution to the e fake factor uncertainty is the MC scaling uncertainty, with the exception of the jet requirement inversion at low p_T. The e fake factors and resulting variations are shown in Figure 7.7. Each individual variation is shown relative to the nominal fake factor measurement. The total uncertainty is given as the sum of statistical and systematic uncertainty added in quadrature.
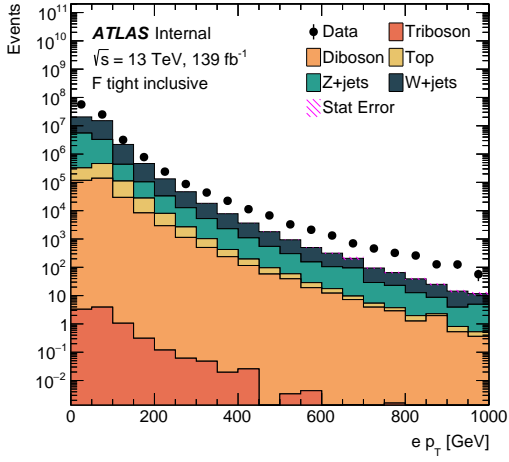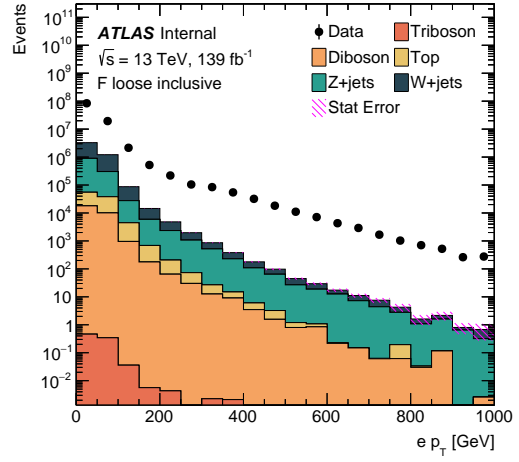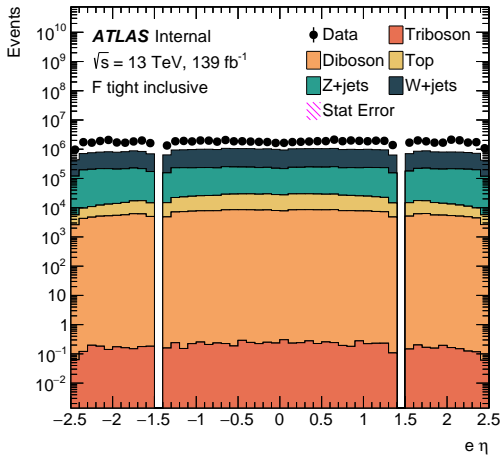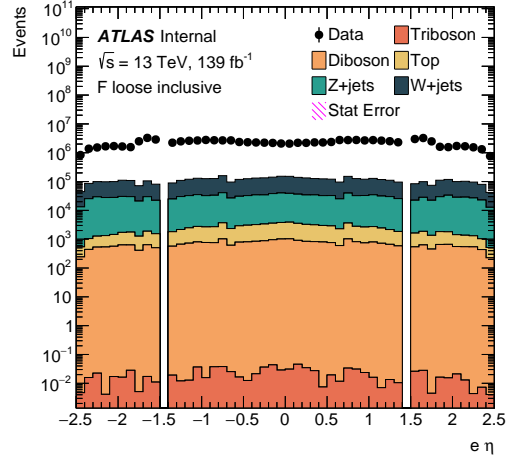
Figure 7.6: Kinematic distributions in the e FFCR. (a) p_T distribution of "tight" electrons, inclusive in η. (b) p_T distribution of "loose" electrons, inclusive in η. (c) η distribution of "tight" electrons, inclusive in p_T. (d) η distribution of "loose" electrons, inclusive in p_T.
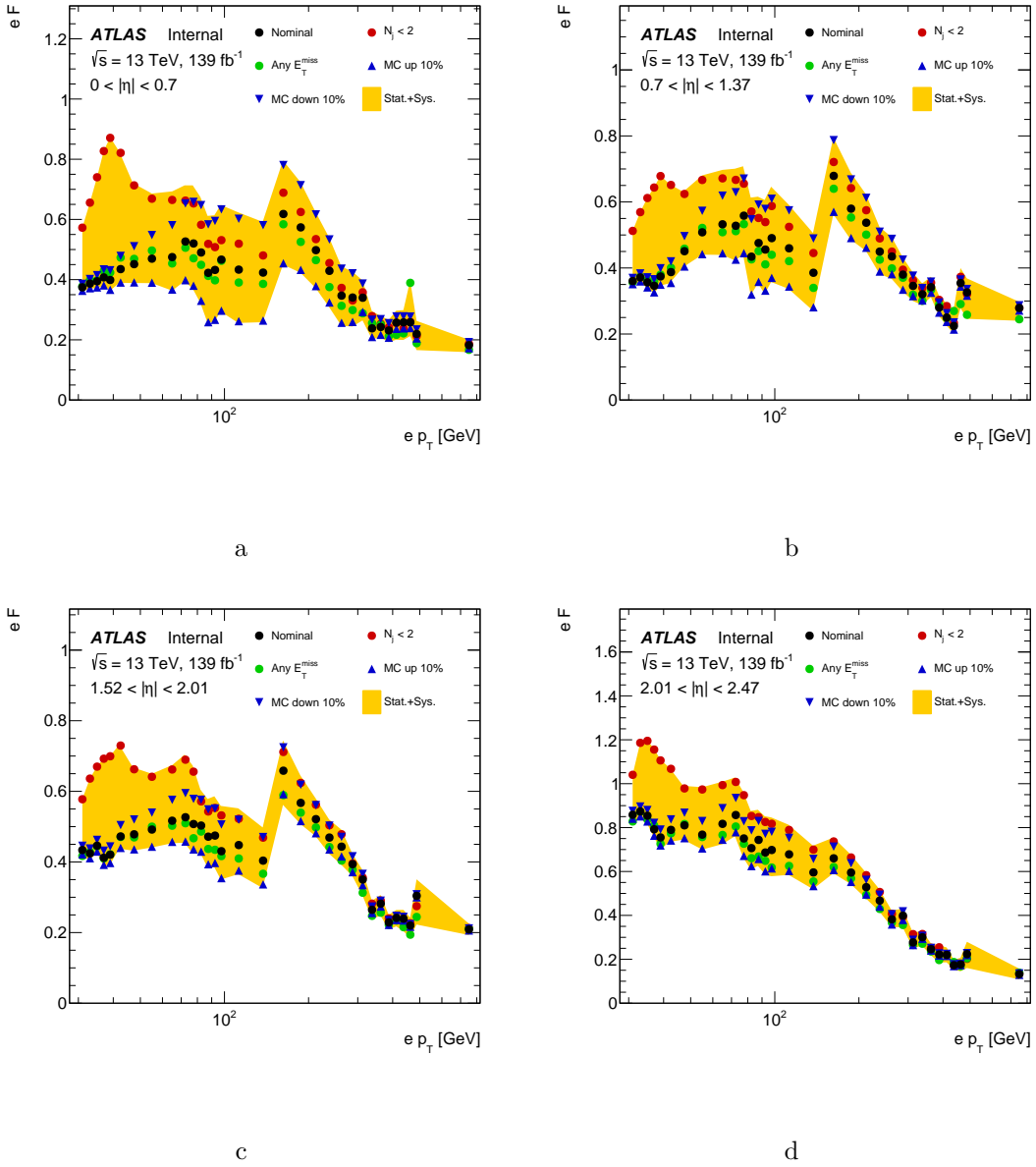
Figure 7.7: The e fake factor as a function of p_T bins with derived uncertainties split into the (a) $0 < |\eta| < 0.7$ bin, the (b) $0.7 < |\eta| < 1.37$ bin, the (c) $1.52 < |\eta| < 2.01$ bin and the (d) $2.01 < |\eta| < 2.47$ bin.

7.5   Muon Fake Factor Measurement

Fake muons mostly arise as real, non-prompt muons originating from in-flight hadron decays. A QCD-enriched di-jet region is chosen as the FFCR. The region uses a tag-and-probe technique, where the highest p_T jet acts as the *tag* and a μ candidate as the *probe*. An upper limit on E_T^{miss} is placed in order to suppress contributions from W+jets.

Pre-scaled single μ triggers with relaxed isolation requirements are used. This is in order to allow adequate statistics for "loose" muons, whose isolation requirement is inverted relative to "tight", signal muons. Since multiple triggers can be fired for a single μ in an event, the lowest pre-scale (and subsequently highest p_T threshold) trigger is used for trigger matching. The trigger list with average pre-scale is given in Table 7.4.

Trigger	Average Pre-scale	Years
HLT_mu24	49.36	2015-2018
HLT_mu50	1.0	2015-2018

Table 7.4: Single μ triggers used in the μ fake factor calculation with average pre-scale.

The μ fake factor is derived in the FFCR defined below:

- Exactly one "loose" or "tight" μ and exactly zero "tight" electrons and "tight" hadronic taus

- $E_T^{\mathrm{miss}} < 40$ GeV

- At least two jets, with the leading jet $p_T > 35$ GeV

- Exactly zero b-jets

- $\Delta\phi(\mu, j_{\text{lead}}) > 2.7$

The μ fake factor is binned in p_T and η. Figure 7.8 shows the inclusive p_T and η distributions for "tight" and "loose" muons in the FFCR. The plots contain the data distributions as well as the prompt truth-matched μ MC contribution, which is subtracted from data. The "tight" selection requirements yield a significantly larger prompt truth-matched μ contribution than the "loose" selection requirements.

Uncertainties for the μ fake factors were derived by considering the composition of fake μ sources as well as MC modeling uncertainty for prompt subtraction. For each variation, the fake factor was measured independently of other variation types. The various systematics are shown in Table 7.5. The p_T requirement for the leading jet was tightened to > 40 GeV, the E_T^{miss} requirement was removed, the E_T^{miss} requirement was tightened to < 30 GeV, the E_T^{miss} requirement was loosened to < 50 GeV, and the $\Delta\phi(\mu, j_{\text{lead}})$ requirement was varied by ± 0.1 to account for variations in fake μ composition in the FFCR. In order to assess the cross-section and luminosity uncertainties of prompt MC subtraction, the MC contribution to the fake factor was scaled up and down by 10%.

The largest contribution to the μ fake factor uncertainty is the MC scaling uncertainty. The μ fake factors and resulting variations are shown in Figure 7.9. Each individual variation is shown relative to the nominal fake factor measurement. The total uncertainty is given as the sum of statistical and systematic uncertainty added in quadrature.
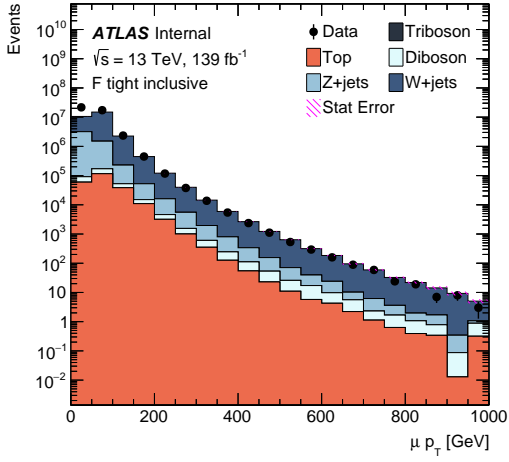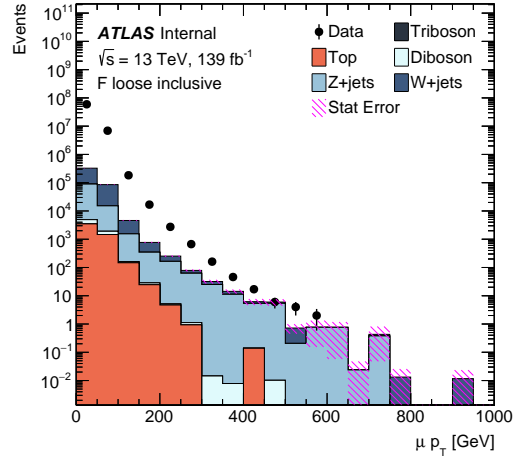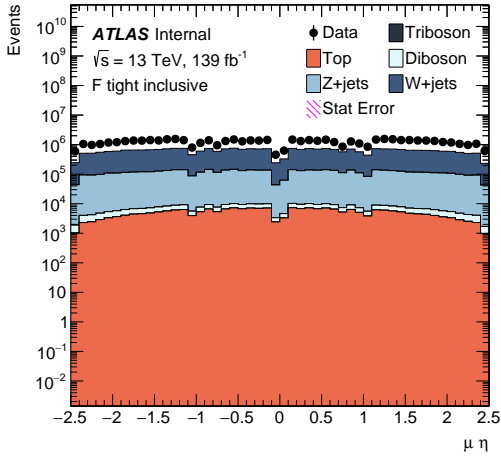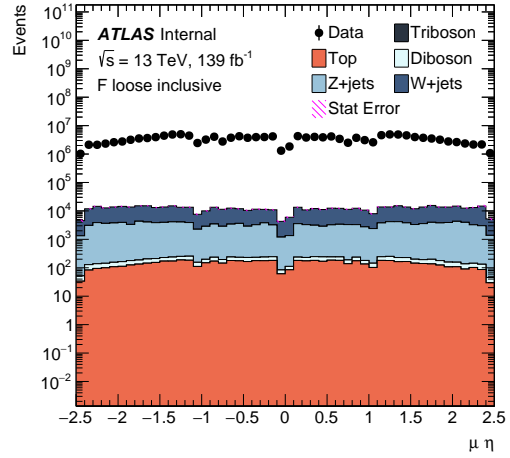
Figure 7.8: Kinematic distributions in the μ FFCR. (a) p_T distribution of "tight" muons, inclusive in η. (b) p_T distribution of "loose" muons, inclusive in η. (c) η distribution of "tight" muons, inclusive in p_T. (d) η distribution of "loose" muons, inclusive in p_T.
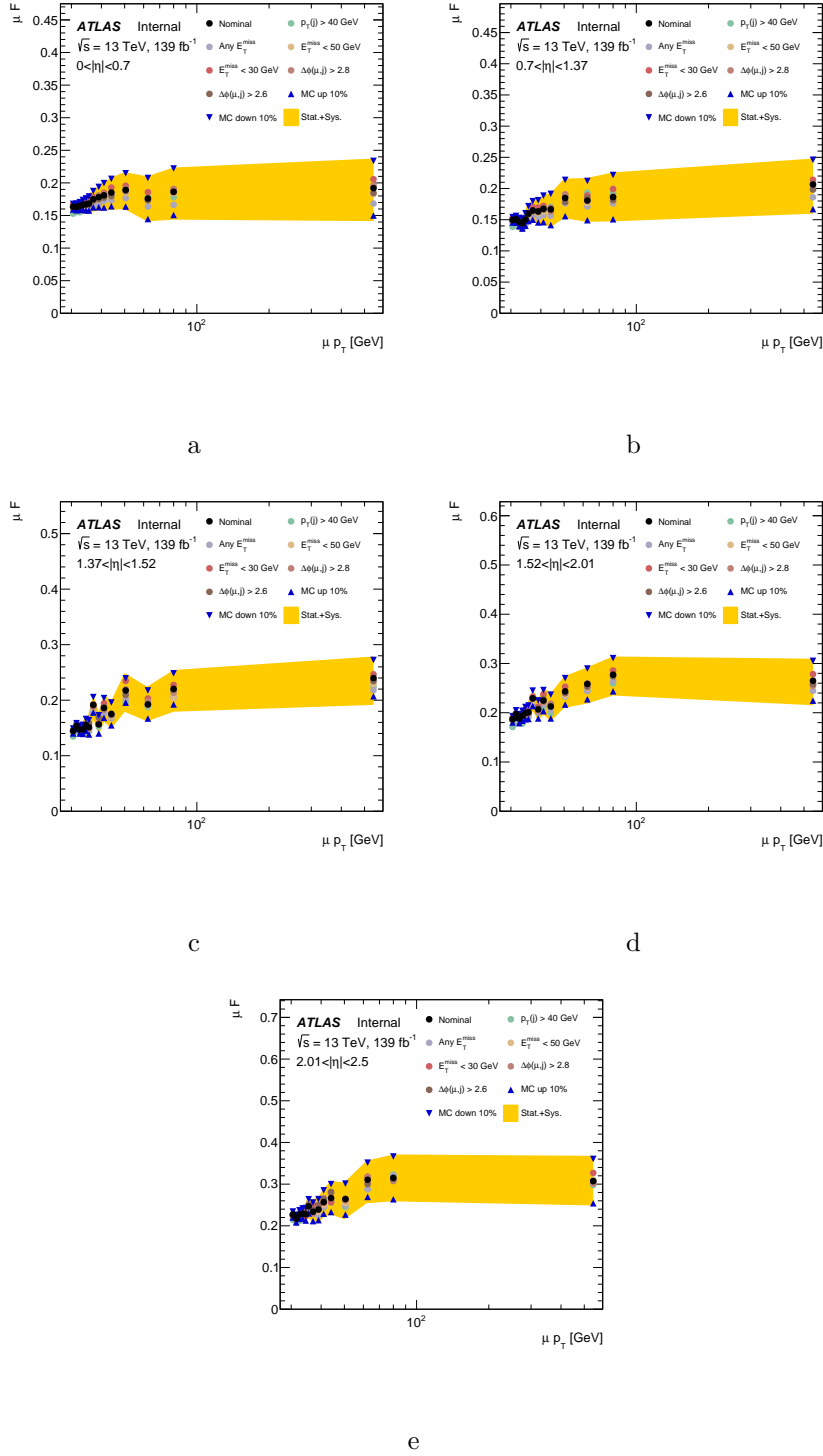
Figure 7.9: The μ fake factor as a function of p_T bins with derived uncertainties split into the (a) $0 < |\eta| < 0.7$ bin, the (b) $0.7 < |\eta| < 1.37$ bin, the (c) $1.37 < |\eta| < 1.52$ bin, the (d) $1.52 < |\eta| < 2.01$ bin and the (e) $2.01 < |\eta| < 2.47$ bin.

| Systematic	Purpose
Leading jet $p_T > 40$ GeV	Composition
No E_T^{miss} requirement	Composition
$E_T^{\text{miss}} < 50$ GeV	Composition
$E_T^{\text{miss}} < 30$ GeV	Composition
$\Delta\phi(\mu, \text{j}_{\text{lead}}) > 2.8$	Composition
$\Delta\phi(\mu, \text{j}_{\text{lead}}) > 2.6$	Composition
MC scaled up by 10%	MC modeling
MC scaled up down 10%	MC modeling

Table 7.5: Summary of systematic variations to the μ fake factor.

7.6 Fake Hadronic Tau Estimate

Fake hadronic taus are mis-identified jets that are reconstructed as hadronic taus. These mis-identified jets typically originate as quark or gluon fragmentations. Contributions from quark fragmentations can be further categorized into light flavor quark (u, d or s) hadronizations or heavy flavor quark (b, c) hadronizations. The fake factor is a function of the light and heavy flavor, and gluon composition. Therefore, the fake factor is measured in a FFCR that has comparable composition to the analysis regions. Hadronic taus are identified using an RNN that is trained separately for 1 and 3 prong due to differing topologies, which subsequently leads to non-uniform rejection power (Section 3.6). Because of this, the fake factor is binned in number of prongs in addition to kinematic variables.

In order to correctly account for differences in fake hadronic taus from light (LF) and

heavy-flavor (HF) quark origins, two unique fake factors are derived for application in the analysis regions. The two fake factor derivations will first be introduced, followed by their combined application in analysis regions. A systematic uncertainty was derived to account for the small, but non-zero gluon and pile-up contribution and will also be described in the following sections.

7.6.1 LF Fake Factor Measurement

Due to the multi-lepton final state in this analysis, it is assumed that a subset of fake hadronic taus originate as LF quark-initiated fragmentations. Therefore, a region enriched in Z+jets is chosen as one FFCRs, where $Z \to \mu\mu$. This region selects two isolated muons which allows the use of un-prescaled di-muon triggers. The trigger list is given in Table 7.6.

Trigger	Years
HLT_mu18_mu8noL1	2015
HLT_mu22_mu8noL1	2016
HLT_mu22_mu8noL1	2017-2018

Table 7.6: Di-μ triggers used in the LF fake factor calculation.

The LF fake factor is derived in the FFCR defined below:

- Exactly zero "tight" electrons, exactly two "tight" muons and exactly one "tight" or "loose" τ_{had}

- The two muons are of opposite sign with $|M_{\mu\mu} - M_Z| < 15$ GeV

- Exactly zero b-jets

133

- $E_T^{\mathrm{miss}} < 60$ GeV

The LF fake factor is binned in p_T and number of prongs. Figure 7.10 and Figure 7.11 show the inclusive p_T and η distributions for "tight" and "loose" 1 prong and 3 prong hadronic taus, respectively. The plots contain the data distributions as well as the prompt truth-matched τ_{had} MC contribution, which is subtracted from data. The "tight" selection requirements yield a significantly larger prompt τ_{had} contribution than the "loose" selection requirements. Figure 7.15 shows the fake factors as a function of p_T split by number of prongs.

7.6.2 HF Fake Factor Measurement

It was observed that a substantial portion of fake taus originate from HF quark-initiated fragmentations in analysis regions. Therefore, a region enriched in $t\bar{t}$ events is chosen as one FFCR.

The region selects two isolated light leptons, which allows the use of un-prescaled di-lepton triggers. The trigger list is given in Table 7.7.

Trigger	Years
HLT_mu18_mu8noL1	2015
HLT_mu22_mu8noL1	2016
HLT_mu22_mu8noL1	2017-2018
HLT_2e12_lhloose_L12EM10VH	2015
HLT_2e17_lhvloose_nod0	2016
HLT_2e17_lhvloose_nod0_L12EM15VHI	2017-2018

Table 7.7: Di-lepton triggers used in the HF fake factor calculation.
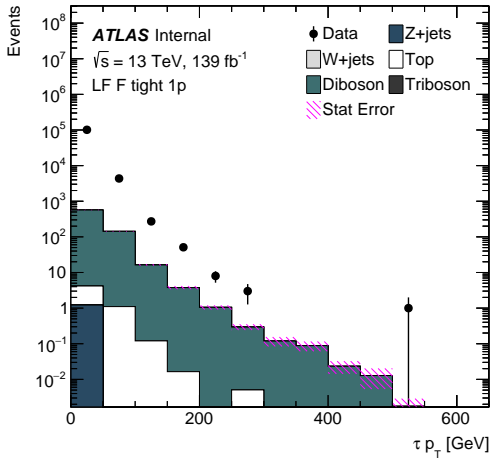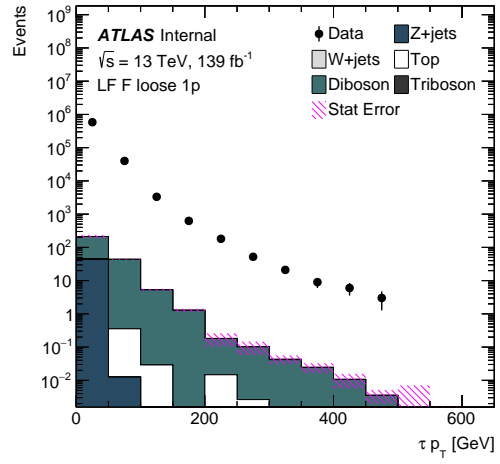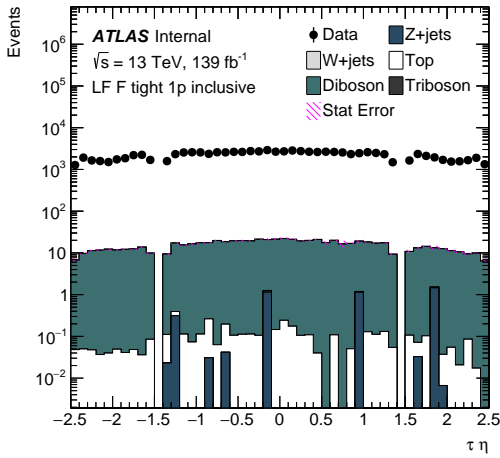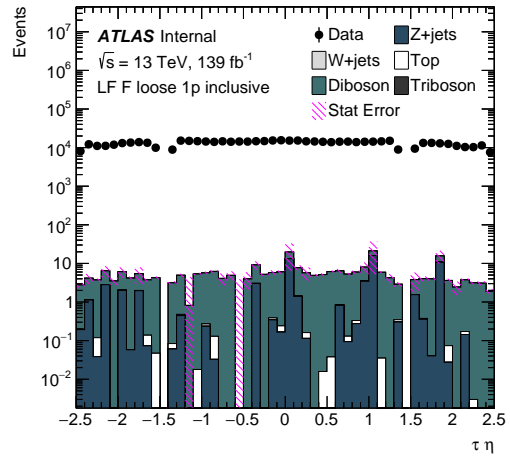
Figure 7.10: Kinematic distributions in the LF FFCR for 1 prong hadronic taus. (a) p_T distribution of "tight" hadronic taus, inclusive in η. (b) p_T distribution of "loose" hadronic taus, inclusive in η. (c) η distribution of "tight" hadronic taus, inclusive in p_T. (d) η distribution of "loose" hadronic taus, inclusive in p_T.

135
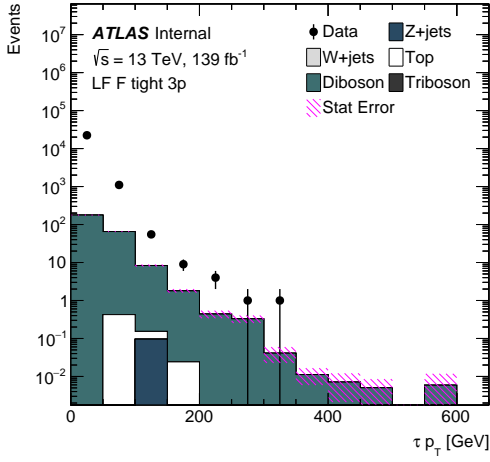
a
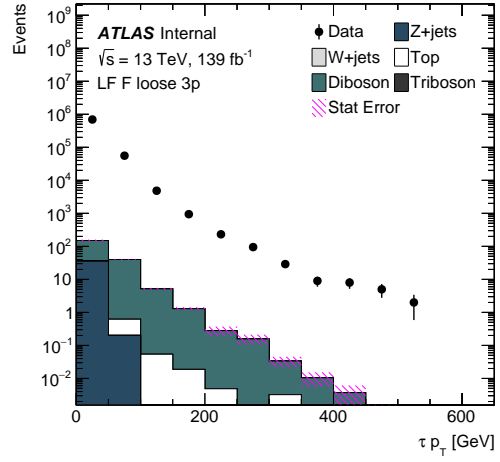
b
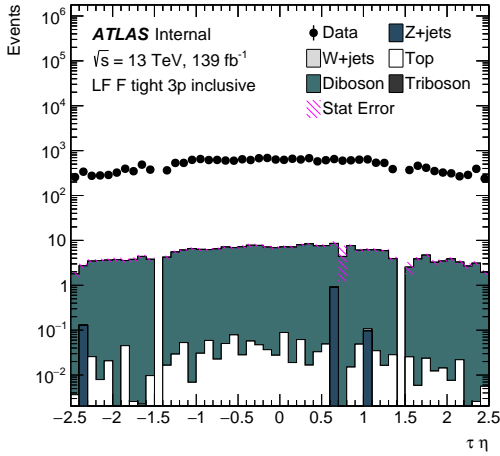
c
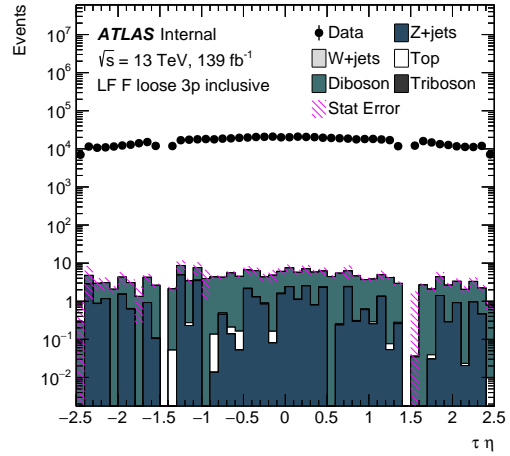
d

Figure 7.11: Kinematic distributions in the LF FFCR for 3 prong hadronic taus. (a) p_T distribution of "tight" hadronic taus, inclusive in η. (b) p_T distribution of "loose" hadronic taus, inclusive in η. (c) η distribution of "tight" hadronic taus, inclusive in p_T. (d) η distribution of "loose" hadronic taus, inclusive in p_T.

136
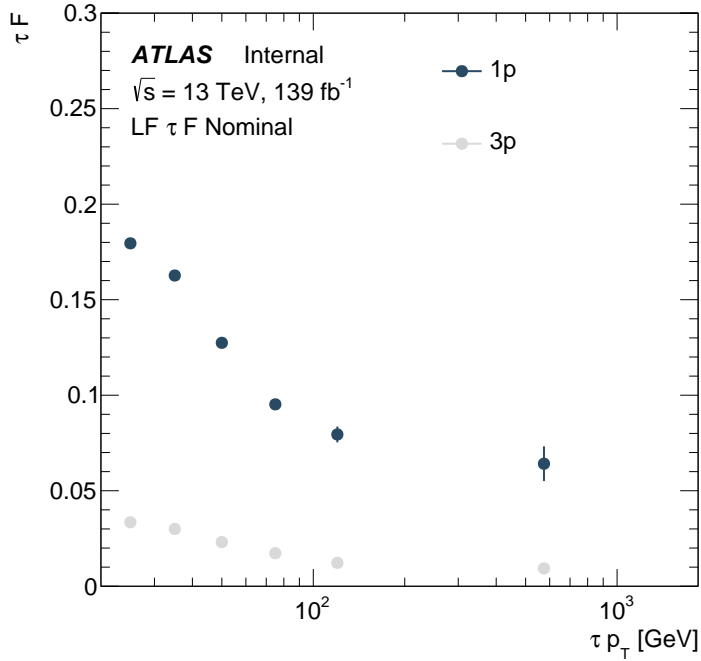
Figure 7.12: LF fake factor as a function of p_T bins split into number of prongs.

The HF fake factor is derived in the FFCR defined below:

- Exactly two "tight" light leptons and exactly one "tight" or "loose" τ_{had}

- The two light leptons are of opposite sign and same flavor with $|M_{\ell\ell} - M_Z| > 10$ GeV

- At least one b-jet

- At least two jets

The HF fake factor is binned in p_T and number of prongs. Figure 7.13 and Figure 7.14 show the inclusive p_T and η distributions for "tight" and "loose" 1 prong and 3 prong hadronic taus, respectively. The plots contain the data distributions as well as the prompt truth-matched τ_{had} MC contribution, which is subtracted from data. The "tight" selection requirements yield a significantly larger prompt τ_{had} contribution than the "loose" selection

requirements. Figure 7.15 shows the fake factors as a function of p_T split by number of prongs.

7.6.3 Application of Hadronic Tau Fake Factors

The composition of fake hadronic taus in the analysis regions can be seen as a mixture of LF and HF jets (with a small contribution from gluon and pileup-initiated jets). Figure 7.16 shows the flavor composition of fake hadronic taus split by final state lepton multiplicity, as estimated in MC simulation. Composition of the seven nominal lepton multiplicity states is shown (Chapter 5) as well as for the LF and HF FFCRs.

In order to correctly model the fake τ_{had} background, the total fake factor is taken as a weighted average of the LF and HF fake factors such that:

$$F_\tau = f_{LF}F_{LF} + f_{HF}F_{HF} \tag{7.7}$$

where $f_{LF}(f_{HF})$ is the fraction of LF (HF) contributing to the region and $F_{LF}(F_{HF})$ is the LF (HF) fake factor. The fraction of LF and HF is such that $f_{LF} + f_{HF} = 1$.

The LF and HF fractions are estimated using `HistFactory` [107]. The fitting distribution is the flavor composition (as shown in Figure 7.16). Resulting fractions used in the analysis for each lepton multiplicity state are given in Table 7.8. Due to low statistics in the SRs, the fraction was fit for each lepton multiplicity final state inclusive in BDT score (inclusive in SRs and inverted-BDT VRs).

7.6.4 Hadronic Tau Fake Factor Systematics

The fraction of LF and HF-initiated fake hadronic taus was calculated inclusive in BDT score for each lepton multiplicity final state. This was to allow adequate statistics for the fraction
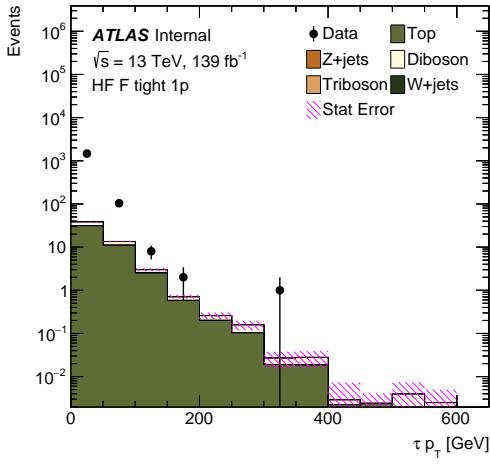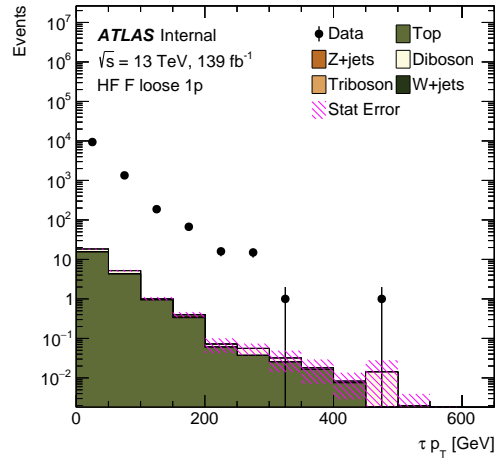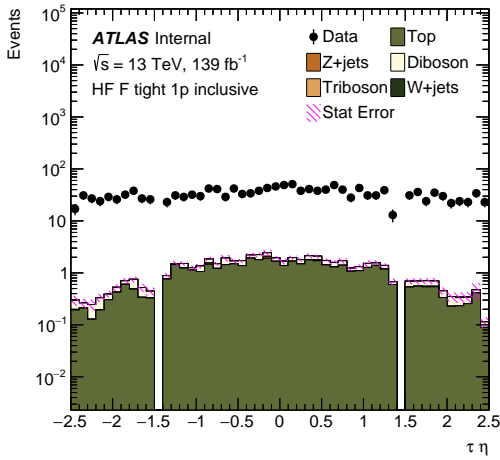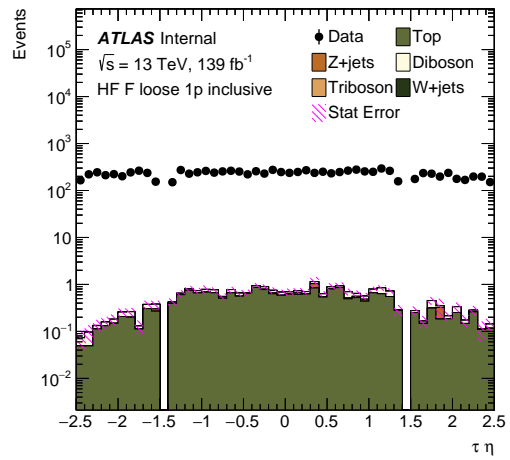
Figure 7.13: Kinematic distributions in the HF FFCR for 1 prong hadronic taus.
(a) p_T distribution of "tight" hadronic taus, inclusive in η. (b) p_T distribution of "loose" hadronic taus, inclusive in η. (c) η distribution of "tight" hadronic taus, inclusive in p_T. (d) η distribution of "loose" hadronic taus, inclusive in p_T.
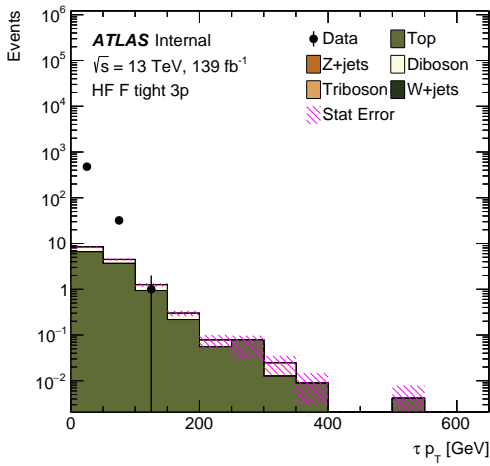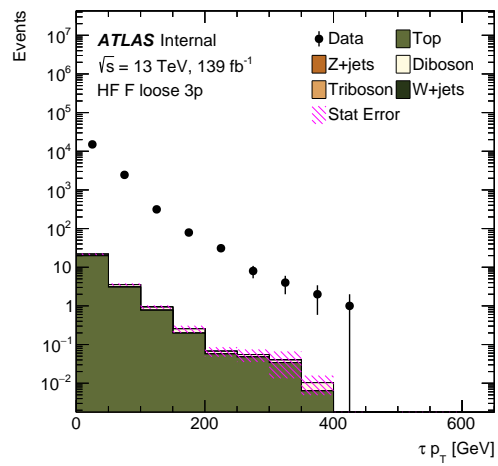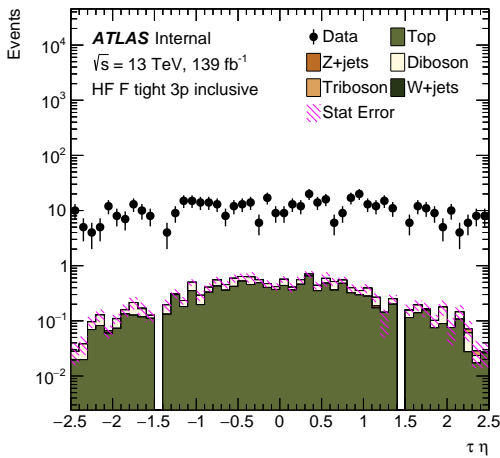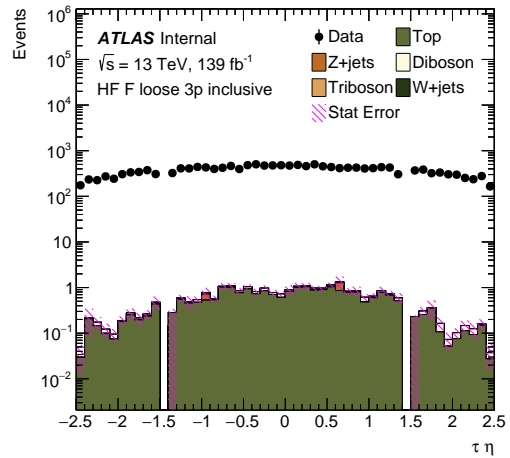
Figure 7.14: Kinematic distributions in the HF FFCR for 3 prong hadronic taus. (a) p_T distribution of "tight" hadronic taus, inclusive in η. (b) p_T distribution of "loose" hadronic taus, inclusive in η. (c) η distribution of "tight" hadronic taus, inclusive in p_T. (d) η distribution of "loose" hadronic taus, inclusive in p_T.
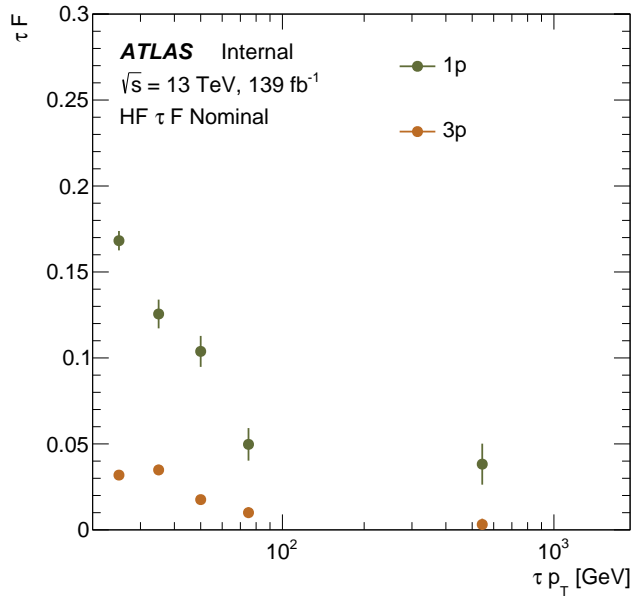
Figure 7.15: HF fake factor as a function of p_T bins split into number of prongs.
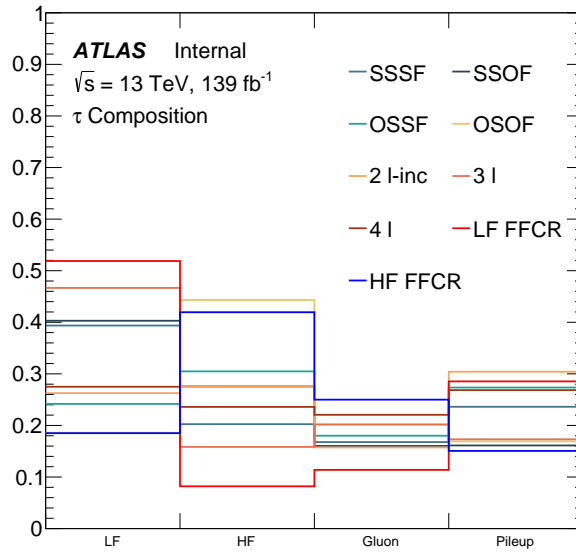
Figure 7.16: Comparison of fake τ_{had} origin for lepton multiplicity states and for the LF and HF FFCRs.

Region	f_{LF}	f_{HF}
2ℓ-SSSF	0.51	0.49
2ℓ-SSOF	0.43	0.57
2ℓ-OSSF	0.39	0.61
2ℓ-OSOF	0.23	0.77
2ℓ-inc	0.50	0.50
3ℓ	0.58	0.42
4ℓ	0.48	0.52

Table 7.8: Fraction of LF and HF used to define the final τ fake factor. The fractions are found by fitting the fraction for each contribution as a function of the fake τ_{had} origin.

fit. The inverted BDT score VRs have similar contribution to SRs in terms of LF and HF contribution, therefore a conservative systematic is introduced where f_{LF} and f_{HF} are varied from 0 to 1. This is analogous to applying either LF or HF fake factor and allowing variation to the other as an uncertainty.

To account for fake hadronic taus initiated by gluons or pile-up, a systematic uncertainty is introduced. It is assumed that gluons and pile-up are similar enough to treat together, as both are low p_T jets with a large number of soft tracks. The systematic is estimated by loosening the RNN score cut for "loose" hadronic taus from 0.01 to 0.005 (Table 3.5) in the LF FFCR. Figure 7.17 shows the composition of "loose" hadronic taus as a function of RNN score, as measured in MC simulation. Between RNN scores 0.005 and 0.01, there is a

significance number of gluon and pile-up fakes. The overall contribution with the nominal

RNN score cut is roughly 40% and increases to 65% after loosening the cut to 0.005.

a

b
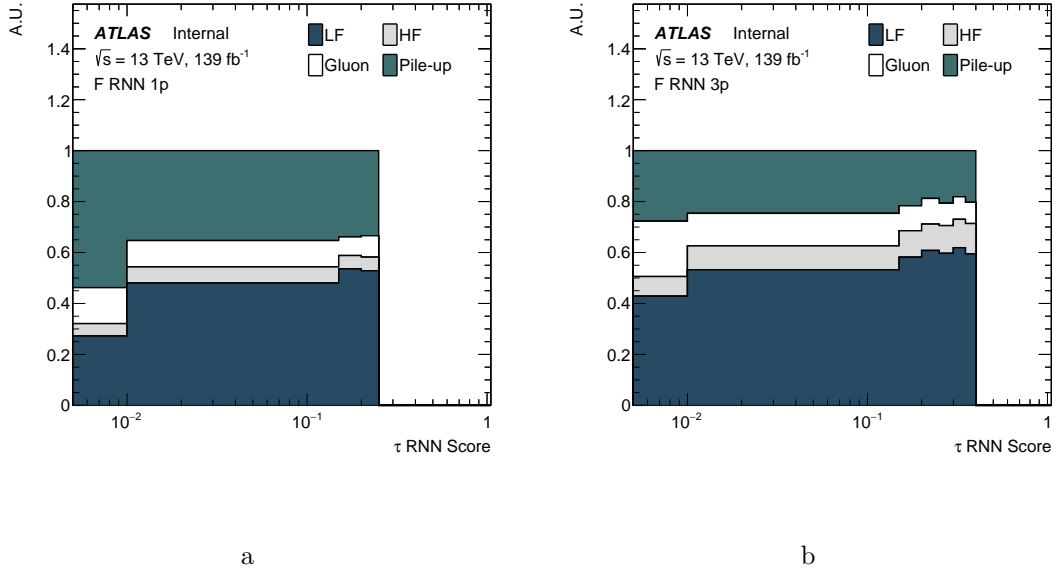
Figure 7.17: Composition of "loose" hadronic taus as a function of RNN score in the LF FFCR for (a) 1 prong and (b) 3 prong. The nominal RNN score cut for "loose" hadronic taus is 0.01.

The difference between the LF FFCR with the RNN score of "loose" taus cut at 0.005 and

0.01 is taken as an uncertainty on the fake factor. Since gluon and pile-up jets are typically

low p_T, this systematic was only imposed on fake hadronic taus with $p_T < 40$ GeV. In order

to yield an uncertainty that is not unrealistically conservative, a CR is used to constrain

the size of the variation. The fake τ_{had} CR (Section 6.3) is dominated by gluon and pile-up

jets and is used for this purpose. Figure 7.18a shows the relative contribution of fakes as a

function of fake τ_{had} p_T for the 2ℓ OSSF, 1τ lepton multiplicity region, as measured in MC

simulation. The contribution from gluon and pile-up fakes dominate at $p_T < 40$ GeV. The

fake τ_{had} composition as a function of p_T is shown for all regions in Appendix D. Figure 7.18b

shows the total number of fake hadronic taus with $p_T < 40$ GeV and $p_T > 40$ GeV in the fake τ_{had} CR.

a

b
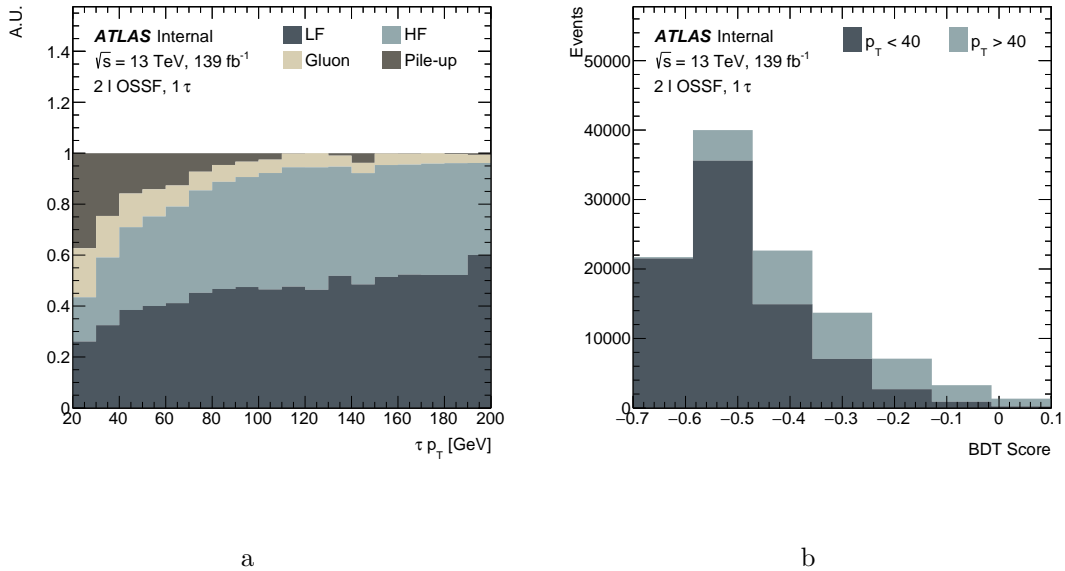
Figure 7.18: (a) The relative contribution of fakes as a function of fake τ_{had} p_T for the 2ℓ OSSF, 1τ lepton multiplicity region, as measured in MC simulation. (b) The total number of fake hadronic taus with $p_T < 40$ GeV and $p_T > 40$ GeV in the fake τ_{had} CR.

The τ_{had} fake factors are shown in Figure 7.19. The total uncertainty is given along with the LF and HF fake factors. The total statistical uncertainty for the LF and HF fake factor measurements are included in the uncertainty band. The uncertainties in the τ_{had} fake factors are taken independently for $p_T < 40$ GeV and $p_T > 40$ GeV. This is to ensure that biases in evaluating the systematics in the statistical analysis are minimized since the relative contribution of τ_{had} fake sources vary between these two p_T ranges.
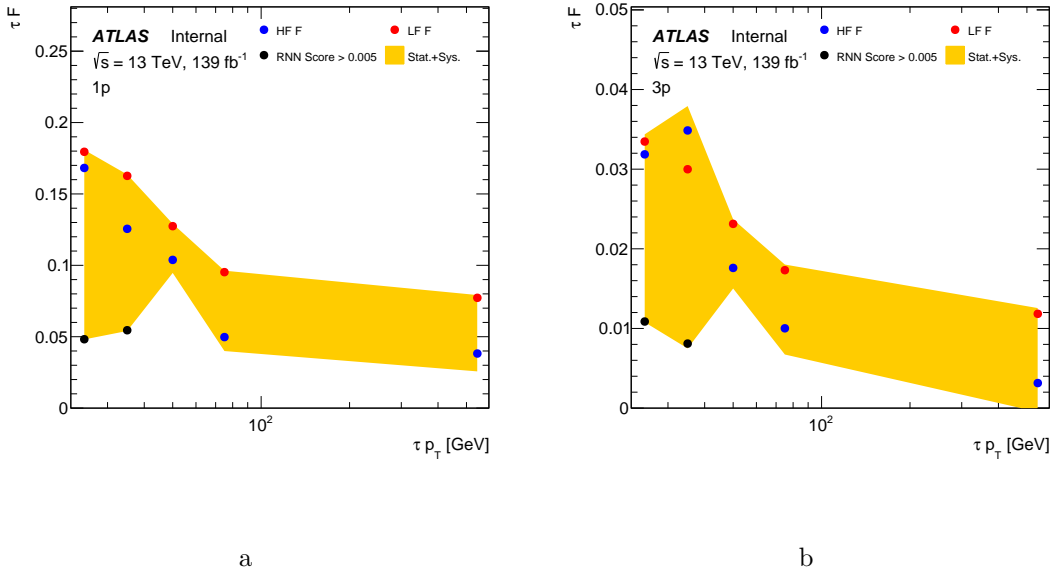
Figure 7.19: The τ_{had} fake factors for (a) 1 prong and (b) 3 prong. The total uncertainty is given along with the LF and HF fake factors. The total statistical uncertainty for the LF and HF fake factor measurements are included in the uncertainty band and are also propagated to the statistical analysis.

Chapter 8

Systematic Uncertainties

There are various sources of systematic uncertainties considered in this thesis. Systematics related to detector effects (experimental), the fake lepton estimation and the theoretical calculation of background processes (theory) are incorporated. These uncertainties affect the predicted background and signal modeling, both in terms of normalization and the shape of kinematic distributions.

Systematics are considered uncorrelated and individual systematic sources are broken into uncorrelated sub-components. An alternative would be to correlate sub-components into an envelope, however, this could lead to artificial over-constraints. Each systematic is taken as correlated between analysis regions. Systematics are assumed to follow a Gaussian distribution and are considered to be free-floating nuisance parameters in the statistical analysis. Inclusion of systematics in the statistical analysis will be described in Chapter 9.

8.1 Experimental Systematics

Systematic uncertainties resulting from the identification and reconstruction of objects considered in this thesis are taken into account. This includes identification and reconstruction uncertainties from light leptons, hadronic taus, jets, b-jets and E_T^{miss}. The uncertainty in the luminosity measurement and pile-up re-weighting scheme is also considered. A summary of the experimental systematic uncertainties is given in Table 8.1.

Systematic Uncertainty	Number of Components
Event	
Luminosity	1
Electrons	
ID and Reconstruction Efficiency	4
Energy Scale	1
Energy Resolution	1
Muons	
ID and Reconstruction Efficiency	8
Energy Scale	1
Energy Resolution	2
Momentum Scale	2
Taus	
Reconstruction	1
RNN ID	10
BDT Electron Veto	3
Tau Energy Scale	4
Jets	
Jet Energy Scale	13
Jet Energy Resolution	2
Jet Vertex	1
Heavy Flavor	5
Missing Transverse Momentum	
Soft Track Terms	3

Table 8.1: Qualitative summary of experimental systematic uncertainties considered in this thesis with the number of uncorrelated, individual components.

8.1.1 Luminosity

The estimate of integrated luminosity from the 2015-2018 LHC Run 2 dataset has an uncertainty of 1.7% [68]. This uncertainty is determined by beam-separation (*van der Meer*) scans and with information from the LUCID-2 detector [33].

8.1.2 Pile-up Re-weighting

Pile-up is modeled in simulation using zero-bias proton-proton collisions and overlaid onto simulated prompt events. The distribution of the number of interactions per bunch crossing is re-weighted to match the distribution in data. Uncertainties are provided for this re-weighting procedure as described in [108].

8.1.3 Light Leptons

Light Lepton Trigger, Identification and Reconstruction   Scale factors are derived for light lepton trigger, reconstruction and selection efficiencies in order to correct MC simulation to data [51, 53]. These scale factors are obtained in $Z \rightarrow \ell^+\ell^-$ $(\ell = \mu, e)$ *tag and probe events* as functions of lepton kinematics. In the tag and probe method, one object is selected with strict selection criteria (tag) and the other is used to measure the efficiency (probe). The uncertainties are evaluated by varying the signal selections and from including uncertainty in the estimation of backgrounds.

Lepton Momentum Scale and Resolution   The $Z \rightarrow \ell^+\ell^-$ tag and probe processes are also used to measure the light lepton momentum scale and resolution [109, 110]. Scale factors are derived in order to correct MC simulation to data. The momentum scale uncertainties

are evaluated by varying the light lepton momentum up and down by 1 σ. The resolution uncertainties are estimated using a momentum smearing technique.

8.1.4 Hadronic Taus

Tau Identification and Reconstruction Scale factors are derived for τ_{had} identification, reconstruction, QCD-jet veto and e veto efficiencies in order to correct MC simulation to data [59]. These scale factors are obtained in $Z \to \tau^+\tau^-$ tag and probe events. They are parametrized as functions of τ_{had} p_T. Electron veto efficiency scale factors are measured with $Z \to e^+e^-$ tag and probe events [59]. The uncertainties are evaluated by varying the scale factors up and down by 1 σ.

Tau Energy Scale The Tau Energy Scale (TES) correction is measured using $Z \to \tau^+\tau^-$ tag and probe events [59]. The TES is measured in both data and MC simulation, where a correction is applied to MC simulated events to match data. It is measured separately for 1 prong and 3 prong taus, as well as in the barrel and end-cap regions. The uncertainties are evaluated by varying the p_T of the τ_{had} candidate within statistical and systematic uncertainties.

8.1.5 Jets and Missing Transverse Momentum

Jet Energy Scale The JES uncertainty is a large multi-component uncertainty, where the components are derived using a variety of methods [56]. The *in-situ calibration* measures the difference in JES between data and MC simulation by exploiting the p_T balance in the central region between the jet candidate and a reference ($Z \to e^+e^-$ or photons). An *inter-calibration*

procedure is performed between a reference jet in the central region and the candidate jet in the forward region. The *single particle response* derives the uncertainty in jet calorimeter response using constituent particles and is measured in-situ as well as in test beam data. The *pile-up correction* is an uncertainty associated with JES corrections due to pile-up and is estimated by comparing p_T distributions of jet candidates in data and MC simulation. The *flavor* related systematics correct the JES due to differing calorimeter responses for light flavor and gluon jets, which generally have different showering and fragmentation properties. *Heavy flavor* systematics are corrections to the JES based on the presence of b-jets and is measured by comparing the overall reconstructed jet to constituent track p_T. The overall JES uncertainty is a function of both reconstructed jet p_T and η. Variations to the JES are propagated to the E_T^{miss} calculation. There are in total 13 JES uncertainties considered in this thesis.

Jet Energy Resolution   The uncertainty on the JER is extracted by smearing the jet energy and reapplying the object and event selections to MC simulation samples. This smearing procedure is performed according to the resolution of the calorimeter response [111].

Heavy Flavor Tagging   Heavy flavor tagging efficiency scale factors defined for b-jets, c-jets and light flavor jets are applied to jets in MC simulation [112, 113]. The phase space of possible variations due to these uncertainties is large and a principle component analysis is performed to reduce the set. This reduction preserves correlations in p_T and yields independent systematic components. Additional extrapolation uncertainties are also used: one arising from high p_T extrapolation and one from c-jet extrapolation.

Jet Vertex Tagger The uncertainty on the JVT selection is derived by varying the track and vertex parameters by ID detector resolutions.

Missing transverse momentum The uncertainties on E_T^{miss} is given in three components, where the components are measured relative to the hard-component axis. The uncertainties are derived by measuring the disagreement in data and MC simulation using p_T balance between hard and soft components [62].

8.2 Uncertainties Related to the Fake Estimate

The uncertainties presented in Section 7.3 on the fake background estimate are calculated as independent variations on the fake factor. This section summarizes the largest systematics on the fake factor calculations.

The e fake factor uncertainties include inverting the requirement on the number of jets, omitting the E_T^{miss} requirement and scaling the MC up and down by 10%. Fig. 8.1 shows the SRs where these systematics have the largest effect. These uncertainties have the largest effect in the 2ℓ-SSSF SR where the variation is $\pm 17.9\%$.

The μ fake factor uncertainties include tightening the leading jet p_T requirement to > 40 GeV, omitting the E_T^{miss} requirement, tightening the E_T^{miss} requirement to < 30 GeV, loosening the E_T^{miss} requirement to < 50 GeV, varying $\Delta\phi(\mu, \mathrm{jet_{leading}})$ requirement by ± 0.1 and scaling the MC up and down by 10%. Fig. 8.2 shows the SRs where these systematics have the largest effect. These uncertainties have the largest effect in the 2ℓ-SSOF SR where the variation is $\pm 4.3\%$.

The τ_{had} fake factor uncertainties include varying the fraction of LF and HF fake factors

a

b

c
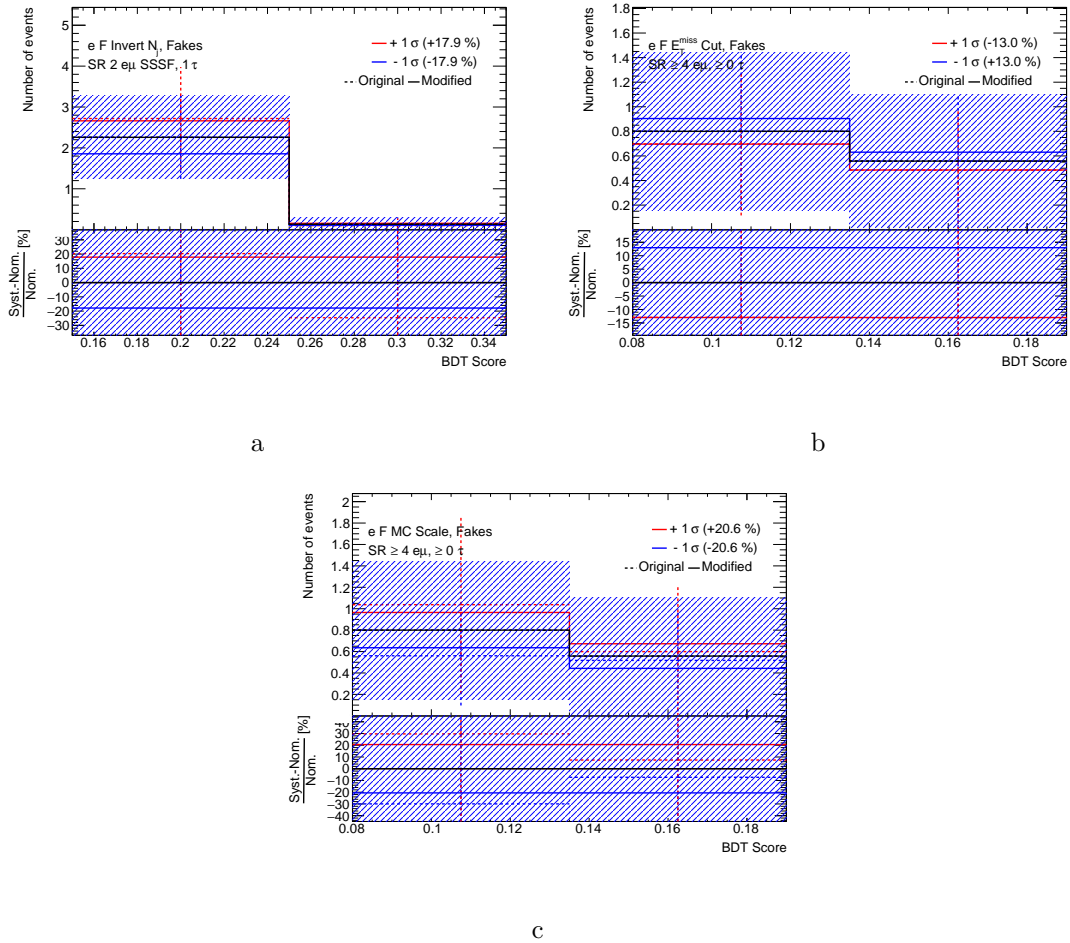
Figure 8.1: e fake factor uncertainties. (a) Inverted requirement on the number of jets. (b) Removed E_T^{miss} requirement. (c) MC scaled up and down by 10% The dashed line denotes the uncertainty before smoothing is applied, while the solid line shows the uncertainty after smoothing.
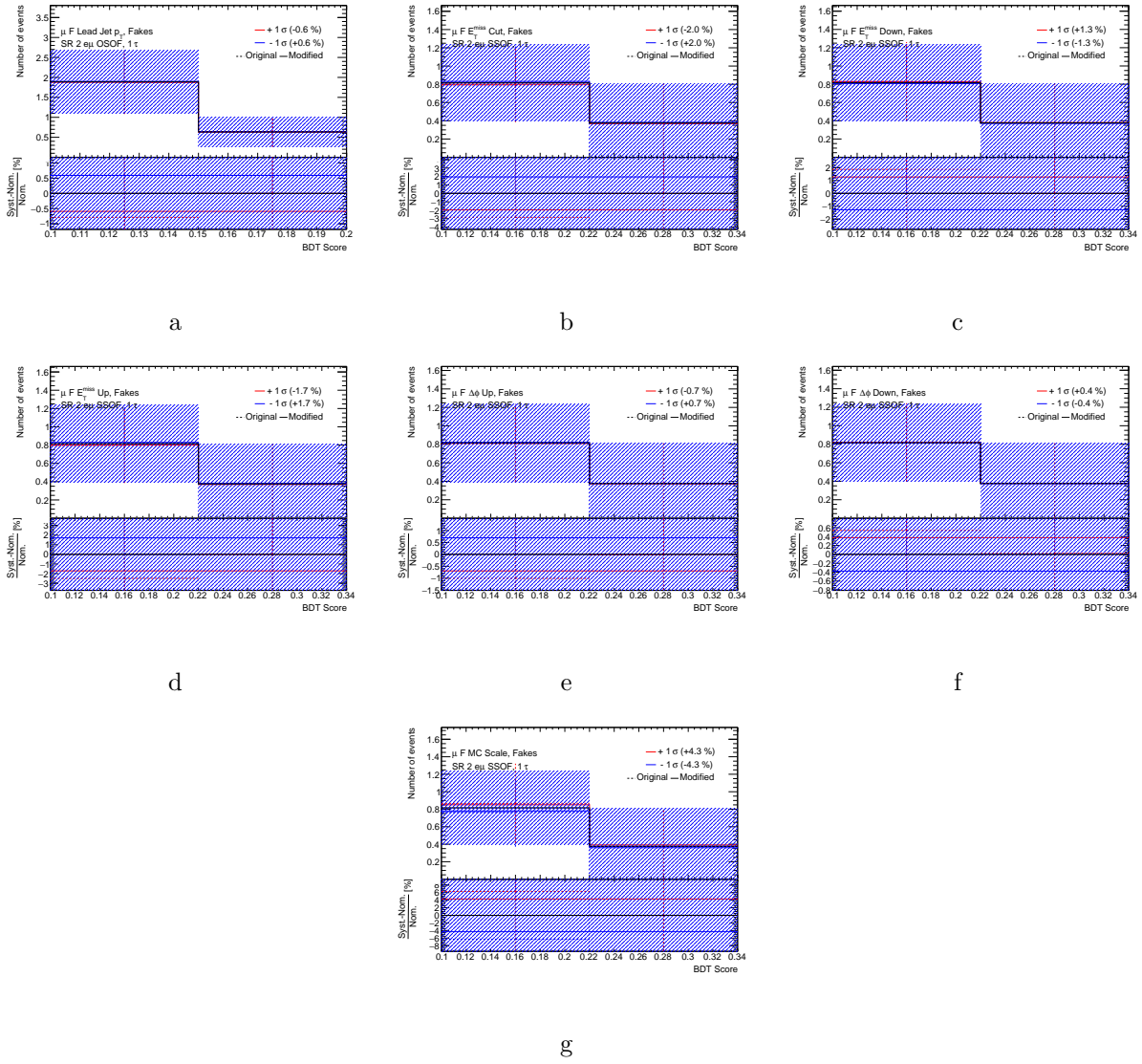
Figure 8.2: μ fake factor uncertainties. (a) Leading jet $p_T > 40$ GeV. (b) Removed E_T^{miss} requirement. (c) $E_T^{\mathrm{miss}} < 30$ GeV. (d) $E_T^{\mathrm{miss}} < 50$ GeV. (e) $\Delta\phi(\mu, \mathrm{jet}_{\mathrm{leading}}) > 2.8$. (f) $\Delta\phi(\mu, \mathrm{jet}_{\mathrm{leading}}) > 2.6$. (g) MC scaled up and down by 10%. The dashed line denotes the uncertainty before smoothing is applied, while the solid line shows the uncertainty after smoothing.

153

between zero and one, statistical variation in the LF and HF fake factor measurement, and the contribution of gluon and pile-up fakes for τ_{had} $p_T < 40$ GeV. The uncertainty on the LF and HF fraction, and the statistical uncertainty components are both split according to τ_{had} $p_T < 40$ GeV and τ_{had} $p_T > 40$ GeV.

Figure 8.3 shows the SRs where these systematics have the largest effect for τ_{had} $p_T < 40$. These uncertainties have the largest effect in the 3ℓ SR, where the variation is 24.3%. Figure 8.4 shows the SRs where these systematics have the largest effect for τ_{had} $p_T > 40$. These uncertainties have the largest effect in the 2ℓ-OSOF SR, where the variation is 21.4%.

8.3   Theory/Modeling Uncertainties

MC simulation allows variations of models in order to quantify the uncertainty in theoretical prediction. μ_R and μ_F scale variation uncertainties, α_s uncertainties and PDF uncertainties are evaluated for the largest backgrounds in this thesis: WZ, ZZ and $t\bar{t} + Z$. Additionally, matrix element and parton shower uncertainties are evaluated for $t\bar{t} + Z$ by using an alternate MC generator for comparison.

Variation of μ_R and μ_F is performed in order to estimate the contribution of missing higher orders in perturbative expansion of the production cross-section (Equation 1.29). An asymmetric envelope of seven variations is taken to estimate this certainty. Variations are taken as factors of two in each, excluding the case where one is varied up and the other is varied down. Table 8.2 shows the variation scheme.

There are multiple sources of uncertainty associated with choice of PDF, specifically experimental uncertainties in PDF fits and uncertainties in the functional form used in the
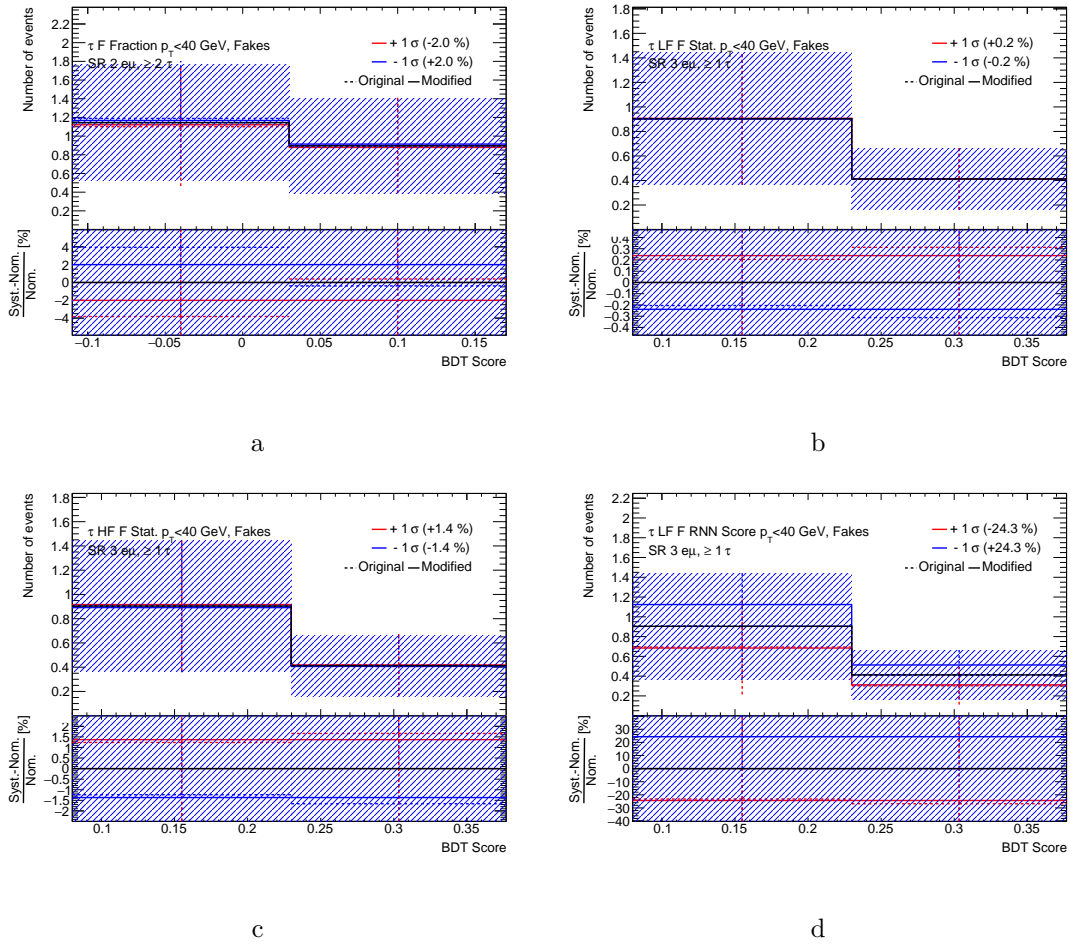
Figure 8.3: τ fake factor uncertainties for τ_{had} $p_T < 40$. (a) LF and HF fake factor fraction. (b) Statistical uncertainty in the LF fake factor measurement. (c) Statistical uncertainty in the LF fake factor measurement. (d) Gluon and pile-up fake contribution. The dashed line denotes the uncertainty before smoothing is applied, while the solid line shows the uncertainty after smoothing.

a

b

c
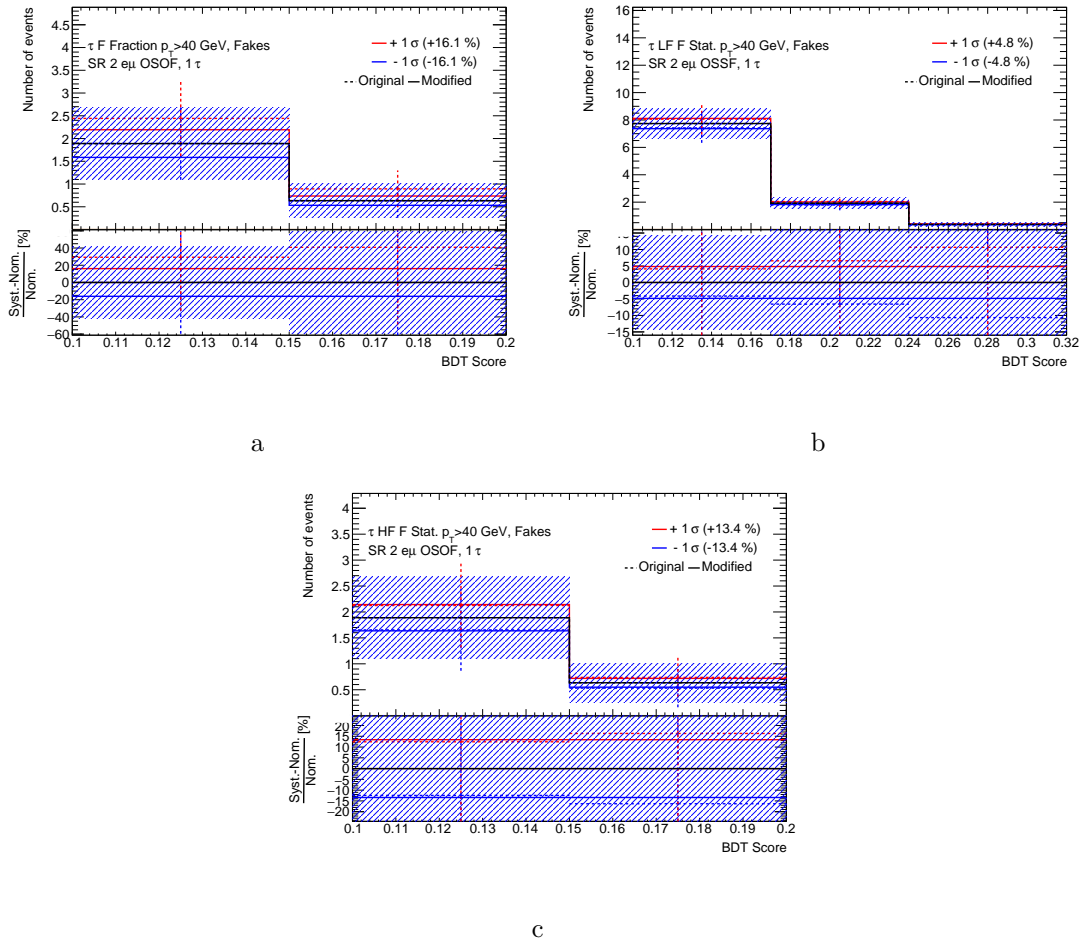
Figure 8.4: τ fake factor uncertainties for τ_{had} $p_T > 40$. (a) LF and HF fake factor fraction. (b) Statistical uncertainty in the LF fake factor measurement. (c) Statistical uncertainty in the LF fake factor measurement. The dashed line denotes the uncertainty before smoothing is applied, while the solid line shows the uncertainty after smoothing.

	μ_F		
	0.5	1	2
μ_R 0.5	✓	✓	
μ_R 1	✓	✓	✓
μ_R 2		✓	✓

Table 8.2: Variations of μ_R and μ_F used to build an asymmetric envelope of seven variations.

PDF fit. PDF uncertainties are calculated using the `LHAPDF6` toolkit [114].

The value of α_s is determined empirically from various experimental datasets. Uncertainties arise from experimental uncertainties with its measurement and truncation from higher order perturbative terms. The nominal value is $\alpha_s = 0.118$ which is quoted at the Z mass. Variations are performed such that the value of α_s varies by ± 0.001.

The PDF and α_s uncertainties are combined such that:

$$\delta^{\alpha_s + \text{PDF}}\sigma = \sqrt{(\delta^{\text{PDF}}\sigma)^2 + (\delta^{\alpha_s}\sigma)^2} \tag{8.1}$$

The background which are not normalized in dedicated CRs, namely Other Top, triboson and Z+jets are assigned 10% uncertainties on their production cross section.

8.3.1 Uncertainty in WZ Re-weighting

An uncertainty associated with WZ re-weighting (Section 7.2) was derived. This uncertainty was calculated by varying the re-weighting factors up and down according to statistical uncertainty in the fake lepton sample.

This uncertainty was found to have a negligible effect in the CRs and SRs, where a maximum variation of 0.1% was observed. Figure 8.5 shows the variation in the WZ CR and

the 2ℓ-SSOF SR.
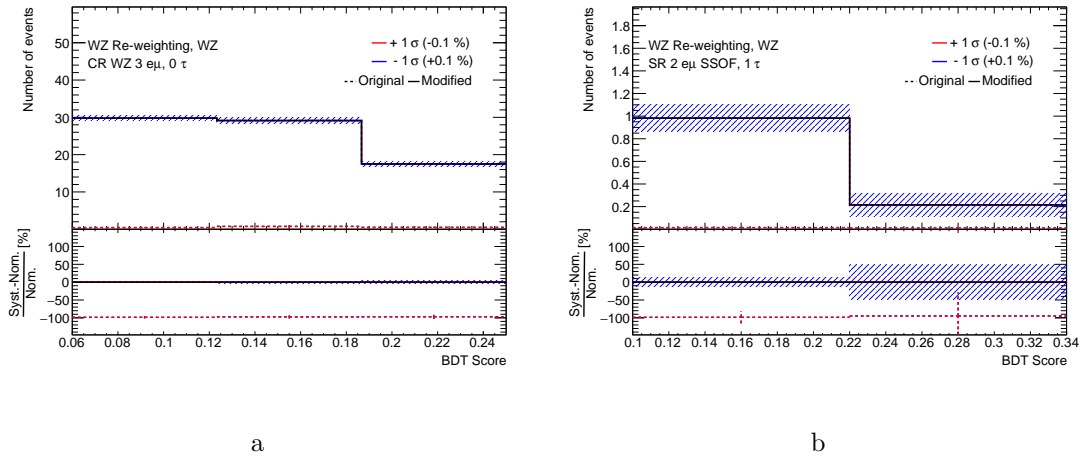
Figure 8.5: WZ re-weighting uncertainties. (a) WZ CR. (b) 2ℓ-SSOF SR. The dashed line denotes the uncertainty before smoothing is applied, while the solid line shows the uncertainty after smoothing.

8.4 Treatment of Systematics

Systematics are treated as nuisance parameters in the statistical analysis, as is described in Chapter 9. In this procedure, the minimization of the fit is performed with systematics as Gaussian distributions and their effect is treated as simultaneously along with the parameter of interest. In order to minimize both fit convergence problems as well as computation time, systematics are subject to *symmetrization*, *smoothing* and *pruning*.

Symmetrization Systematics are implemented as 1 σ variations across all bins and analysis regions. A coefficient is introduced to the systematic variation which is found by the fitting procedure and quantifies the overall effect of the uncertainty. The fitted coefficient is singular for the systematic, which means that the variation from each bin and analysis region are

taken as fully correlated and are compacted into a single quantity. Since up and down 1 σ

variations are used for some systematics, their effect is symmetrized into a single quantity

such that:

$$\sigma_i = \frac{(\sigma_{i+} + \sigma_{i-})}{2} \tag{8.2}$$

where i is for each bin.

Smoothing   Many systematics are prone to non-negligible statistical fluctuations, which

can lead to unrealistic shape variations. A smoothing procedure is performed where the

distribution is varied by averaging adjacent bin yields and associated uncertainties. This

effectively removes the statistical fluctuation on a per-bin level.

Pruning   In order to reduce computation time and simplify the fit, a pruning procedure is

performed for both the shape and normalization contribution of systematics. The threshold

used for this thesis is 1%, where systematics that contribute less than this value in terms of

impact on the fitted result, are removed from the procedure. A similar procedure is performed

for per-bin statistical uncertainty, where the threshold is taken as 0.1%.

Chapter 9

Statistical Analysis and Results

A search for the presence of VLLs was evaluated by comparing background and signal expectation with the observed data. The *signal plus background* (S+B) and *background-only* (B) hypotheses were tested to quantify the significance of the VLL signal. If a statistically significant signal is not observed, an upper bound on possible production cross sections is calculated.

The `TRexFitter` [115] framework is used to perform a binned likelihood fit. This framework combines the functionality of `RooFit` [116] and `RooStats` [117]. The fitting procedure is such that all SRs and CRs are simultaneously fit. Both statistical and systematic uncertainties are included as a parameterization in signal and background.

9.1   The Likelihood Function

The *probability density function* (PDF) for a set of data that depends on external parameters can be expressed generically as $p(\boldsymbol{x}|\boldsymbol{\mu})$, where $\boldsymbol{x}$ are variables in the dataset and $\boldsymbol{\mu}$ are external parameters. Typically one does not have the ability to probe the entire phase space of $\boldsymbol{x}$ due to regions of varying sensitivity. Further, $\boldsymbol{\mu}$ may occupy a large parameter space with many sources of constraints or uncertainties. The *likelihood function* $(\mathcal{L} = p(\boldsymbol{\mu}|\boldsymbol{x}))$ [99] can be used instead, such that external parameters are inferred given the available dataset.

In the case of a counting experiment, the likelihood can be interpreted as the probability of observing n events given the number of predicted signal and background events. The parameter of interest (POI) is the *signal strength* μ, where $\mu = 0$ corresponds to the B

hypothesis and $\mu = 1$ corresponds to the full S+B hypothesis.

The total number of entires in a particular bin can be expressed as $n_i = \mu s_i + \beta b_i$ where $s(b)_i$ is the number of expected signal (background) events in the ith bin and β is a normalization factor measured in a control region. Assuming the bins follow a Poisson distribution, the likelihood can be written as:

$$\mathcal{L}(\mu) = \prod_{i=1}^{N} \frac{(\mu s_i + \beta b_i)^{n_i}}{n_i!} e^{-(\mu s_i + \beta b_i)} \tag{9.1}$$

Systematic uncertainties (Chapter 8) can be incorporated into the likelihood as *nuisance parameters* (NP), such that:

$$s \rightarrow s(\boldsymbol{\theta}) = s \prod_k (1 + \theta_k \sigma_k^s) \tag{9.2}$$

$$b \rightarrow b(\boldsymbol{\theta}) = b \prod_k (1 + \theta_k \sigma_k^b) \tag{9.3}$$

where $\sigma_k^{s/b}$ is the relative uncertainty on the signal or background expectation for the kth systematic uncertainty. θ_k is the NP for the kth systematic uncertainty, which is constrained according to a unit-width Gaussian PDF centered at zero:

$$p_{\text{syst}}(\boldsymbol{\theta}) = \prod_k \frac{1}{\sqrt{2\pi}} e^{-\frac{\theta_k^2}{2}} \tag{9.4}$$

This term is then included in the definition of the likelihood as:

$$\mathcal{L}(\mu, \boldsymbol{\theta}) = \prod_{i=1}^{N} \frac{(\mu s_i + \beta b_i)^{n_i}}{n_i!} e^{-(\mu s_i + \beta b_i)} \times p_{\text{syst}}(\boldsymbol{\theta}) \tag{9.5}$$

9.2 Hypothesis Testing

The *profile-likelihood ratio* $\lambda(\mu)$ is used to define the test statistic needed for hypothesis testing:

$$\lambda(\mu) = \frac{\mathcal{L}(\mu, \hat{\hat{\boldsymbol{\theta}}}_{\boldsymbol{\mu}})}{\mathcal{L}(\hat{\mu}, \hat{\boldsymbol{\theta}})} \tag{9.6}$$

where $\hat{\hat{\boldsymbol{\theta}}}_{\boldsymbol{\mu}}$ is the set of NPs that maximize the likelihood for a specified μ, and where $\hat{\mu}$ and $\hat{\boldsymbol{\theta}}$ are the signal strength and NP set that maximize that likelihood unconditionally. For computational convenience, the test statistic is taken as:

$$t_\mu = -2 \ln \lambda(\mu) \tag{9.7}$$

which is the *profile-likelihood ratio test statistic*. This test statistic is used to calculate the *p-value* of the hypothesis under test. The p-value is defined as:

$$p_\mu = \int_{t_\mu^{\text{obs}}}^{\infty} f(t_\mu | \mu) dt_\mu \tag{9.8}$$

where t_μ^{obs} is the observed value of the test-statistic in data and $f(t_\mu | \mu)$ is the PDF of t_μ at signal strength μ. The functional form of this PDF is estimated by using a set of pseudo-data built from MC simulation. This dataset can be approximated by using the signal and background expectation for the hypothesis under test and is known as the *Asimov* dataset [99].

The presence of signal is tested by assessing the B hypothesis, where $\mu = 0$. In this test, the p_0-value represents the probability for the background expectation to fluctuate to the observed data. A lower p_0-value corresponds to more significant deviations from the background-only expectation. The significance is typically quoted to quantify the presence of

signal, given by:

$$Z_0 = \Phi^{-1}(1 - p_0) \tag{9.9}$$

where Φ^{-1} is the inverse of the cumulative distribution of the normal distribution. Positive significances correspond to $p_0 < 0.5$ with positive signal yields and negative significances correspond to $p_0 > 0.5$ with negative signal yields. Significance thresholds for "evidence" and "discovery" of the tested signal are conventionally set to 3σ ($p_0 = 1.35 \times 10^{-3}$) and 5σ ($p_0 = 2.87 \times 10^{-7}$) respectively.

When the B hypothesis is not rejected, upper limits on signal production cross-section can be calculated. The S+B hypothesis is tested for multiple values of μ in this case. The profile-likelihood ratio is designed such that it increases monotonically for increasingly signal-like experiments. Therefore, p_{B} is defined as the probability for t_μ to be as small as t_μ^{obs} under the B hypothesis and $p_{\mathrm{S+B}}$ is the probability for t_μ to be as large as t_μ^{obs} under the S+B hypothesis:

$$p_{\mathrm{B}} = p(t_\mu < t_\mu^{\mathrm{obs}}|\mathrm{B}) = \int_{-\infty}^{t_\mu^{\mathrm{obs}}} f(t_\mu|0, \hat{\boldsymbol{\theta}}_0) dt_\mu \tag{9.10}$$

$$p_{\mathrm{S+B}} = p(t_\mu > t_\mu^{\mathrm{obs}}|\mathrm{S+B}) = \int_{t_\mu^{\mathrm{obs}}}^{\infty} f(t_\mu|\mu, \hat{\boldsymbol{\theta}}_\mu)) dt_\mu \tag{9.11}$$

The CL_s method [118] is used to place upper bounds on signal production at the 95% confidence level when the following condition is satisfied:

$$\mathrm{CL}_{\mathrm{s}} \equiv \frac{p_{\mathrm{S+B}}}{1 - p_{\mathrm{B}}} < 0.05$$

$p_{\mathrm{S+B}}$ approaching 0 indicates poor compatibility with the S+B hypothesis and p_{B} approaching 1 indicates poor compatibility with the B hypothesis. The CL_s method ensures

that both conditions are satisfied in order to protect against exclusion in regions with poor sensitivity.

9.3 Results

A likelihood fit was performed to assess the presence of VLL signal. The SRs and CRs introduced in Chapter 6 are fit simultaneously. Performing the fit in this manner provides four free parameters: the signal strength and the normalization factors for the ZZ, WZ and $t\bar{t} + Z$ backgrounds. Additional free parameters associated with systematic uncertainties ($\boldsymbol{\theta}$) are also included in the fitting procedure. The post-fit values for the free parameters are propagated to all analysis regions, including VRs, which do not enter the fit but are used to assess the results. Free parameters associated with per-bin statistical uncertainty are also added in a similar manner as Equation 9.4 and are denoted as γ factors to distinguish from systematic uncertainties labeled with θ_k. Statistical uncertainty NPs are not propagated between analysis regions or bins.

Post-fit normalization factors for the ZZ, WZ and $t\bar{t} + Z$ backgrounds are provided in Table 9.1. The fitted normalization scales are compatible with SM prediction. Post-fit results for the CRs and background normalization VRs with all fitted free parameters propagated are shown in Figure 9.1 and Figure 9.2, where good agreement between data and background expectation is observed.

Statistical and systematic uncertainties are assessed by comparing the nominal predicted value and the value as determined by the fitting procedure. Optimal uncertainties should not deviate significantly from predicted values by the fit, where those that deviate are referred to
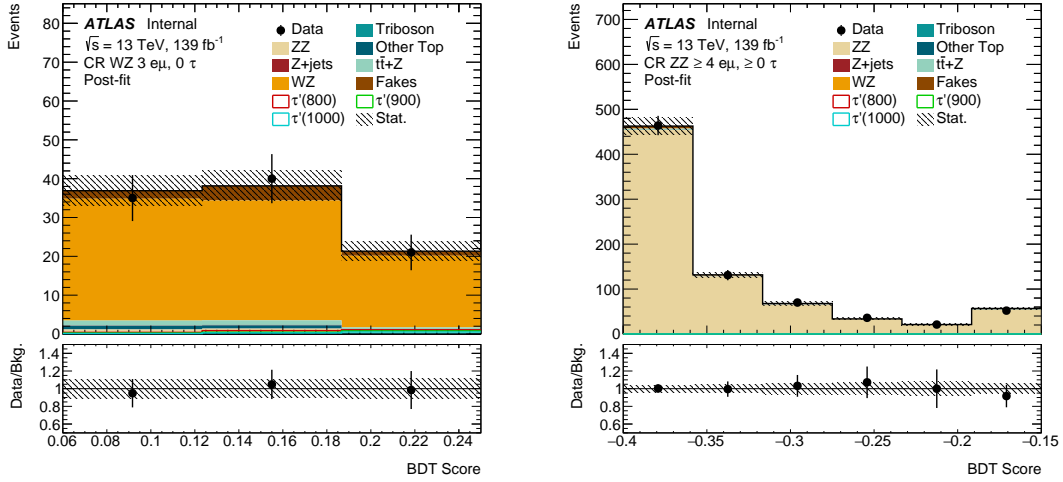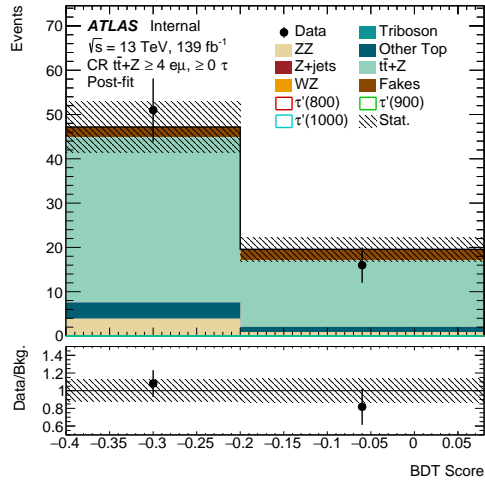
Figure 9.1: Post-fit distributions of BDT score in the (a) WZ CR (b) ZZ CR and (c) $t\bar{t} + Z$ CR. The uncertainty contains statistical and systematic error.
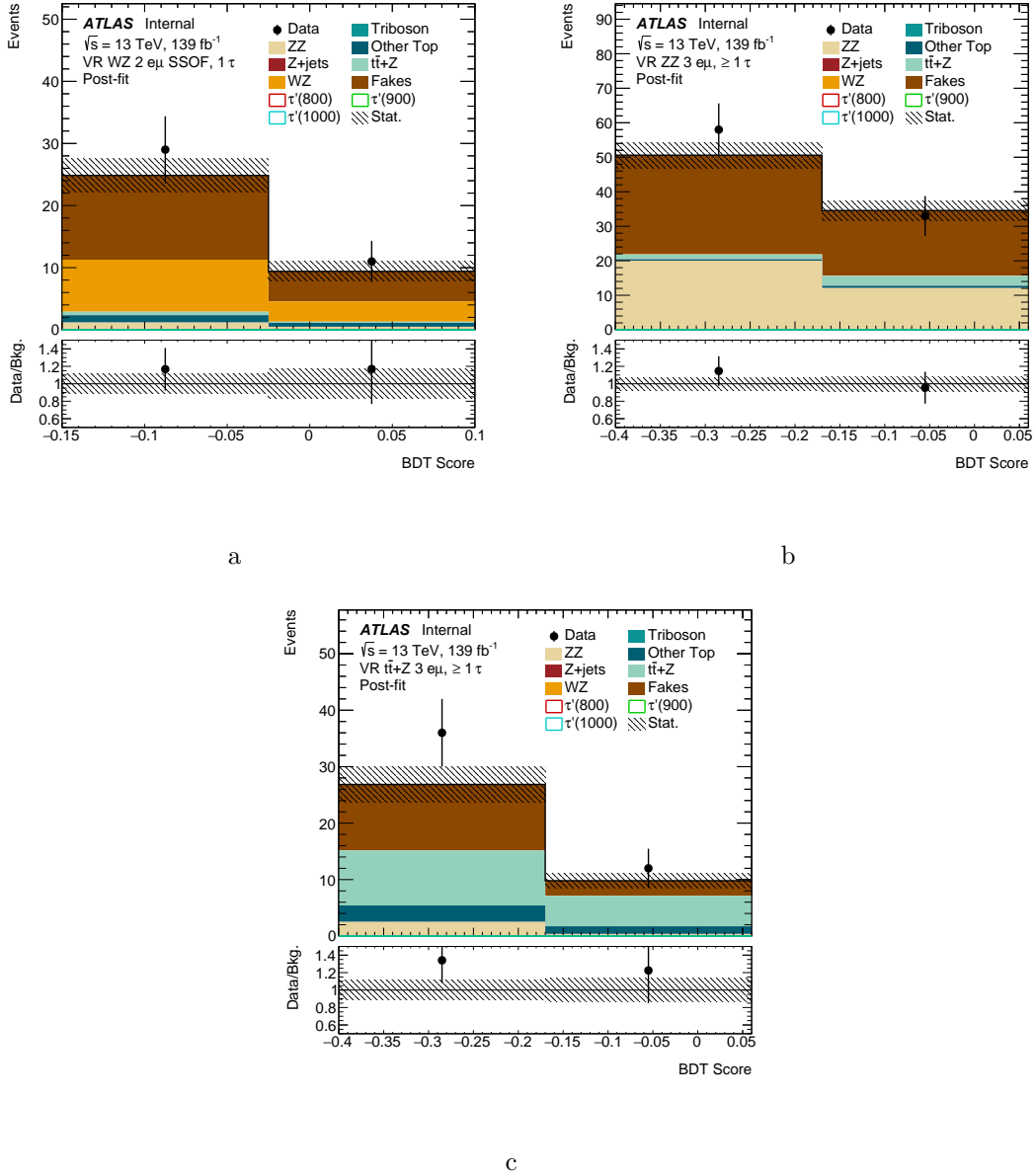
Figure 9.2: Post-fit distributions of BDT score in the (a) WZ VR (b) ZZ VR and (c) $t\bar{t} + Z$ VR. The uncertainty contains statistical and systematic error.

Background	Normalization Factor
WZ	1.06 ± 0.13
ZZ	1.02 ± 0.07
$t\bar{t} + Z$	1.17 ± 0.20

Table 9.1: Normalization factors derived from the simultaneous likelihood fit in CRs and SRs for ZZ, WZ and $t\bar{t} + Z$ backgrounds.

as "pulled". Uncertainties on fitted NPs are calculated by varying the fitted value until the likelihood function doubles. An uncertainty is well-behaved if it doubles the likelihood at its 1σ value and is considered "constrained" otherwise.

The difference between the nominal (θ_0) and fitted ($\tilde{\theta}$) NPs are given in Figure 9.3a. The difference is centered at 0 for the majority of NPs, indicating the fitted values are compatible with nominal prediction. The "τ F Fraction" uncertainties are slightly off-center, indicating the fitted fraction of fake hadronic taus initiated by LF and HF quarks is influenced by the composition in the VRs (Section 7.6.3). The systematic associated with the gluon and pile-up composition in fake hadronic taus ("τ_{had} LF F RNN Score $p_T < 40$ GeV") is both pulled and constrained, however, this NP was constrained by design using the fake τ_{had} CR (Section 7.6.4). Figure 9.3b shows the same as Figure 9.3a, but for statistical uncertainty γ factors. The γ factors are slightly off-center in bins with large statistical uncertainty.

Another useful assessment of the result is the effect of each free parameter on the fitted value of μ. Figure 9.4 shows the 20 parameters with the largest effect on μ, calculated by varying the parameters within their uncertainty by $\pm 1\sigma$. The parameter with the largest
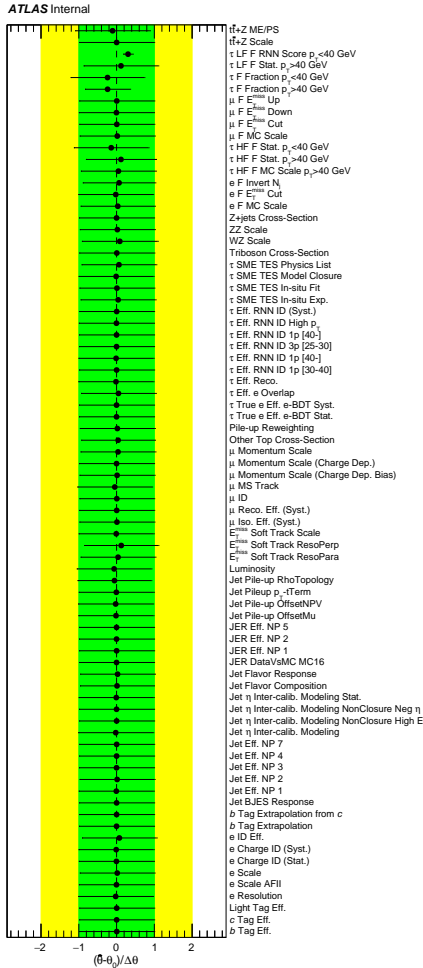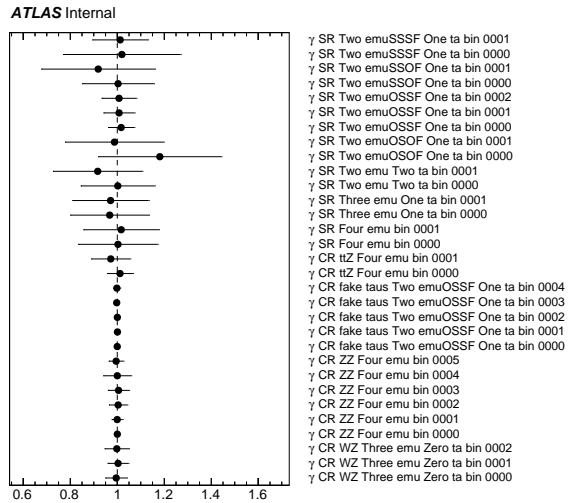
Figure 9.3: (a) Comparison of nominal and fitted systematic uncertainty NPs. The black line is found by varying the fitted NP value until the likelihood doubles. (b) Comparison of nominal and fitted statistical uncertainty NPs.

effect are is the WZ normalization factor. Further, Table 9.2 gives the positive impact $(+1\sigma)$ of each NP source on μ.
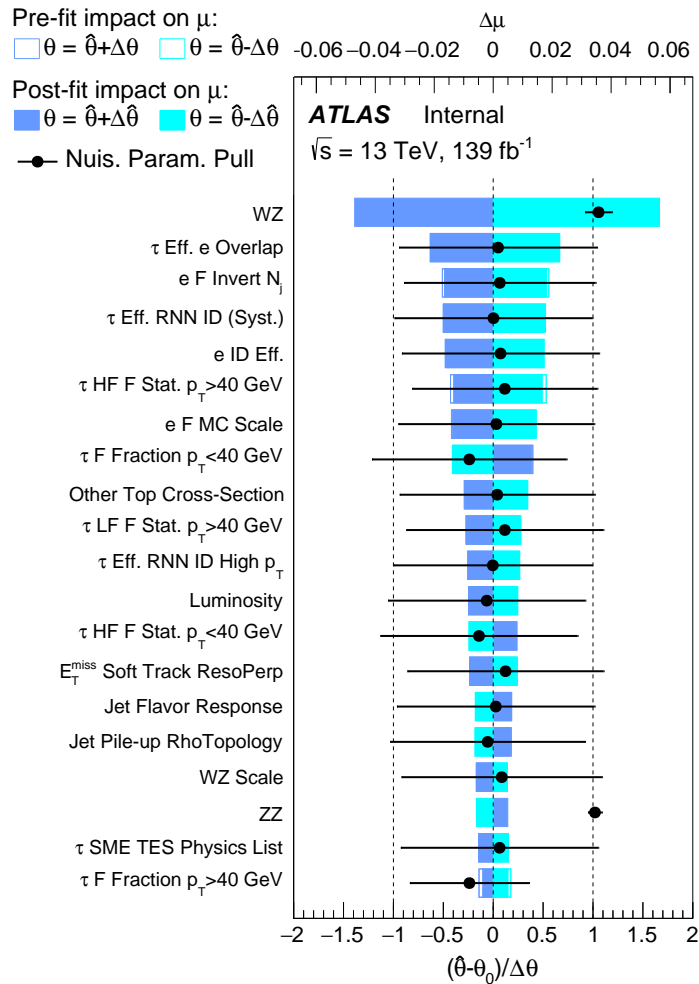
Figure 9.4: The 20 parameters with the largest effect on μ. The WZ normalization factor has the largest effect on μ. This is shown in the colored bars (axis on the top of the plot) and the black points (axis on the bottom of the plot) are analogous to Figure 9.3a.

Figure 9.5 shows the post-fit BDT score distributions and with all parameters propagated as determined by the fit. The arrows indicate the regions along the BDT score defined as SRs (Section 6.2) and the inverted BDT score VRs (Section 6.4). The 2ℓ OSOF, 1τ region

Uncertainty	$\Delta\mu$
Fakes	0.115
Tau Energy Scale	0.015
Tau ID and Reco	0.036
Light Lepton ID, Reco, Energy Scale and Momentum Resolution	0.0212
Jet Energy Scale and Resolution, JVT, PRW	0.020
Flavor Tagging	0.0004
E_T^{miss}	0.004
Norm Factors	0.068
Other Theory	0.003
Luminosity	0.006
Statistical Uncertainty	0.132
Total Uncertainty	0.209

Table 9.2: Positive impact $(+1\sigma)$ of each systematic source on μ fitting procedure.

also contains the fake τ_{had} CR (Section 6.3). Good agreement between data and background expectation is shown in the VRs and CR post-fit.

To assess whether the VLL signal is significant relative to background expectation, the p_0-value is calculated. Table 9.3 gives the expected and observed p_0-values, and corresponding significance for each VLL mass point tested. Figure 9.6 shows the observed and expected significance, where the dashed lines at 3 and 5 σ indicate typical criteria for evidence and discovery, respectively. The expected significance is such that the analysis had potential for 5 σ discovery in the mass range $M_{\tau'} < 700$ GeV. The observed significance for the mass range $M_{\tau'} < 300$ GeV is negative, indicating a downward fluctuation of data relative to the signal plus background prediction. For each mass point tested, the observed significance is compatible with the B hypothesis.

The upper limit on VLL production cross-section as a function of VLL mass is calculated using the CL_S method. The expected 95% CL exclusion limit with 1 and 2 σ uncertainty is shown in Figure 9.7. The observed 95% CL exclusion limit is shown in the solid black line. All production cross-section values larger than the observed limit are excluded by this analysis. Table 9.4 gives the expected and observed upper limits for each VLL production cross-section as a function of VLL mass. The expected VLL mass limit is calculated as 967 GeV. The observed VLL mass limit is 898 GeV.

Numerical yields for the post-fit SRs and CRs are given in Table 9.5 and Table 9.6, respectively.
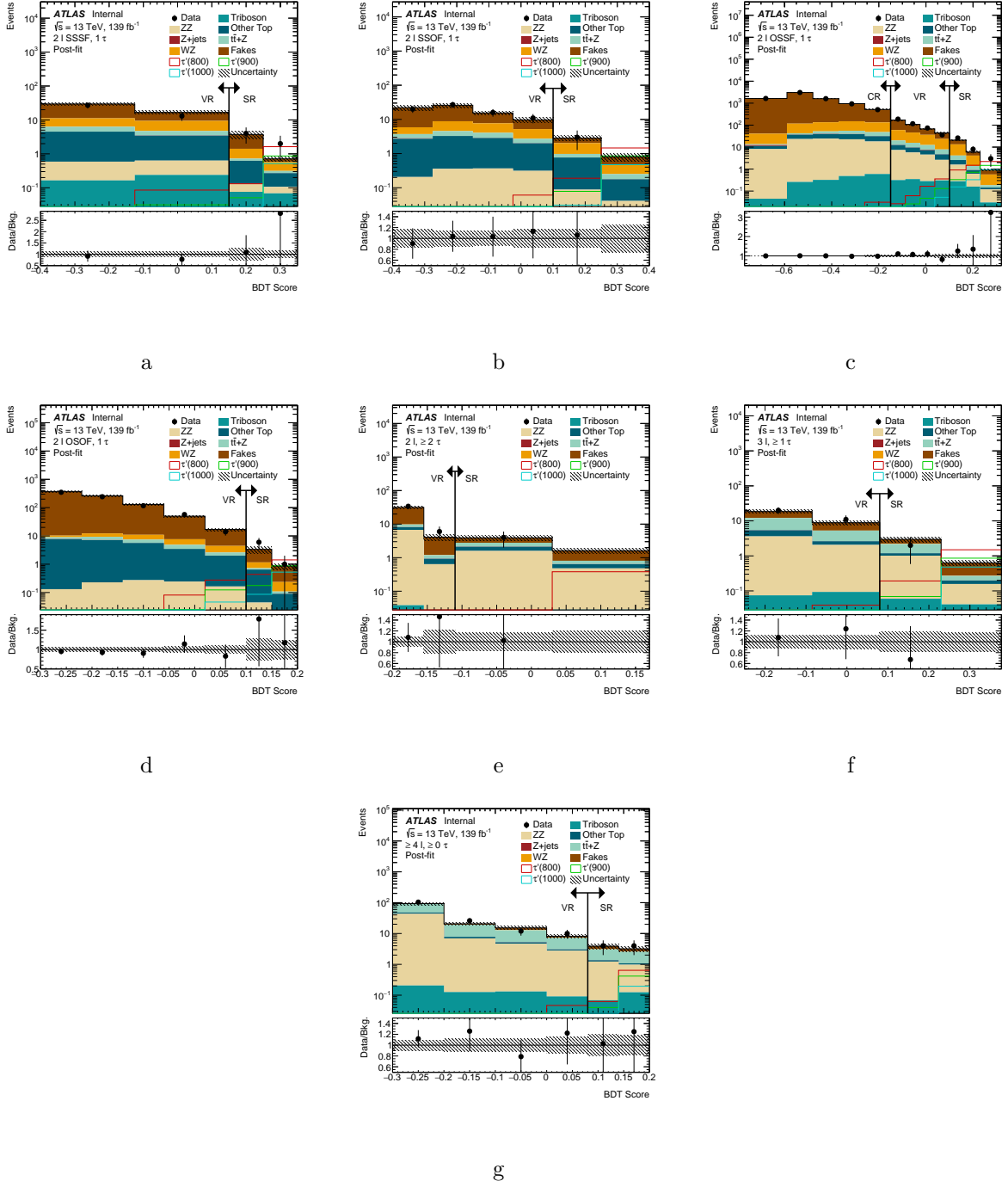
Figure 9.5: Post-fit distributions of the BDT score. SRs and inverse BDT score VRs are differentiated by the arrow. (a) 2ℓ SSSF, 1τ (b) 2ℓ SSOF, 1τ (c) 2ℓ OSSF, 1τ including the fake τ_{had} CR (d) 2ℓ OSOF, 1τ (e) $2\ell, \geq 2\tau$ (f) $3\ell, \geq 1\tau$ (g) $\geq 4\ell, \geq 0\tau$. The uncertainty contains statistical and systematic error.

$M_{\tau'}$ [GeV]	Exp. p_0	Exp. Z_0	Obs. p_0	Obs. Z_0
130	1.98×10^{-09}	5.89	0.67	-0.44
200	0	12.18	0.66	-0.41
300	0	15.02	0.46	0.09
400	0	12.07	0.38	0.31
500	0	10.09	0.24	0.69
600	1.92×10^{-14}	7.57	0.18	0.91
700	2.04×10^{-7}	5.06	0.17	0.96
800	3.93×10^{-4}	3.35	0.13	1.10
900	0.02	2.14	0.13	1.11
1000	0.09	1.34	0.12	1.19

Table 9.3: Expected and observed p-values, p_0, and corresponding significance, Z_0. These values are given for each $M_{\tau'}$ mass tested.
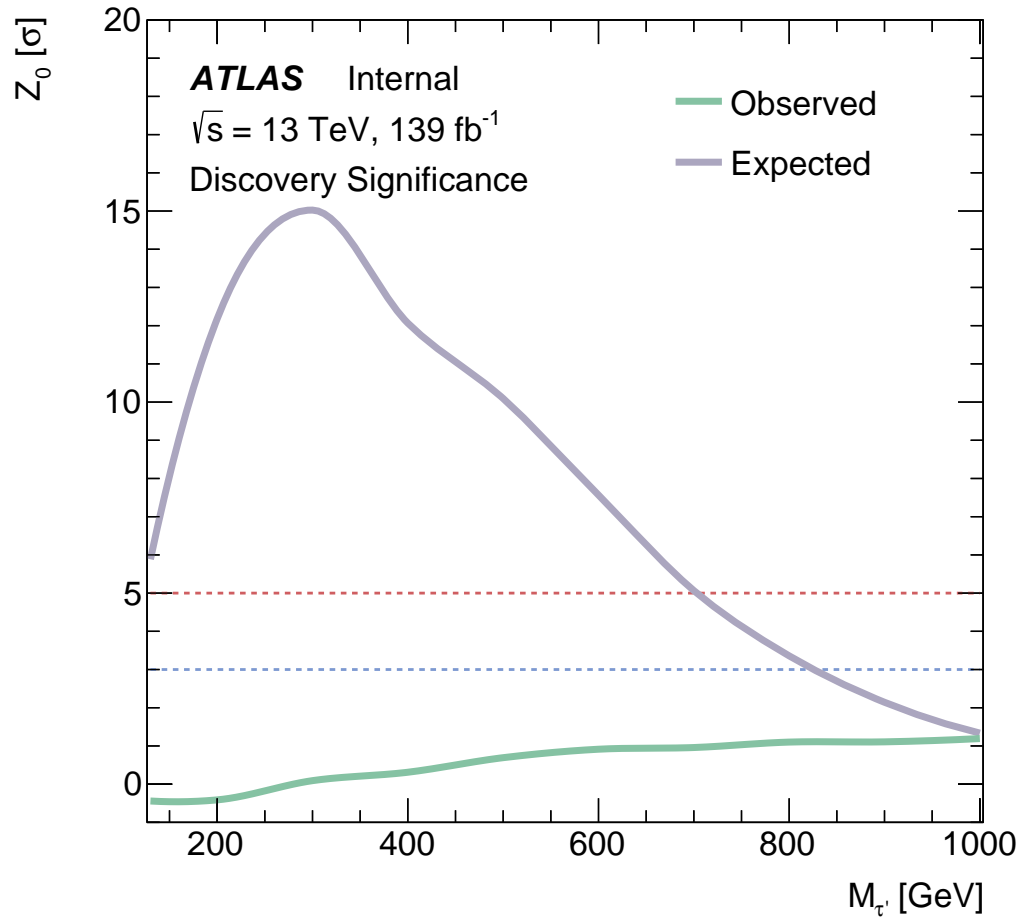
Figure 9.6: Observed and expected significance (Z_0), where the dashed lines at 3 and 5 σ indicate typical criteria for evidence and discovery, respectively. The significance is given as a function of τ' mass.
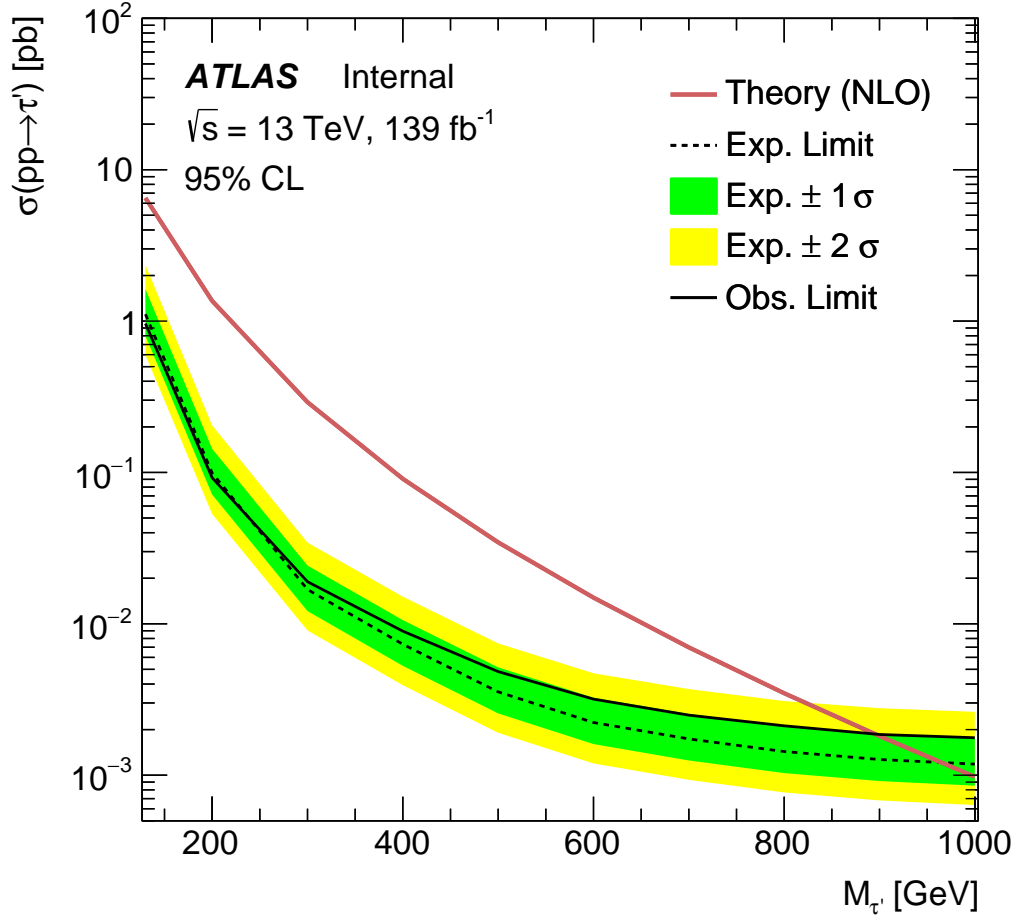
Figure 9.7: Upper limit on VLL production cross-section calculated with the CL$_S$ method. The shaded bands correspond 1 and 2 σ uncertainty around the central expected value (dashed black line). The solid black line is the observed limit as a function of τ' mass. The expected VLL mass limit is calculated as 967 GeV. The observed VLL mass limit is 898 GeV

$M_{\tau'}$ [GeV]	Exp. [pb]	Exp. $+1\sigma$	Exp. $+2\sigma$	Exp. -1σ	Exp. -2σ	Obs.
130	1.1	1.6	2.4	0.8	0.6	0.96
200	0.099	0.14	0.2	0.071	0.053	0.092
300	0.017	0.024	0.034	0.012	0.009	0.019
400	0.0073	0.011	0.015	0.0053	0.0039	0.0089
500	0.0036	0.0052	0.0074	0.0026	0.0019	0.0048
600	0.0022	0.0032	0.0047	0.0016	0.0012	0.0032
700	0.0017	0.0025	0.0037	0.0013	0.00093	0.0025
800	0.0014	0.0021	0.0031	0.001	0.00077	0.0021
900	0.0013	0.0019	0.0028	0.00091	0.00068	0.0019
1000	0.0012	0.0018	0.0026	0.00085	0.00064	0.0018

Table 9.4: Expected and observed upper limits for each τ' production cross section as a function of mass analyzed. The expected limit also includes ± 1 and ± 2 σ values.

	SR 2 ℓ SSSF, 1 τ	SR 2 ℓ SSOF, 1 τ	SR 2 ℓ OSSF, 1 τ	SR 2 ℓ OSOF, 1 τ	SR 2 ℓ, ≥ 2 τ	SR 3 ℓ, ≥ 1 τ	SR ≥ 4 ℓ, ≥ 0 τ
Z+jets	$0.00000203 \pm 0.00000028$	$0.00000192 \pm 0.00000027$	$0.00000303 \pm 0.00000011$	0.0000022 ± 0.0000004	$0.00000192 \pm 0.00000024$	$0.00000194 \pm 0.00000023$	$0.00000202 \pm 0.00000024$
Other Top	0.65 ± 0.18	0.81 ± 0.19	1.31 ± 0.30	0.68 ± 0.21	0.70 ± 0.16	0.22 ± 0.05	0.24 ± 0.05
$t\bar{t} + Z$	0.15 ± 0.04	0.28 ± 0.07	2.1 ± 0.4	0.10 ± 0.06	0.82 ± 0.18	1.06 ± 0.24	3.2 ± 0.6
ZZ	0.094 ± 0.028	0.129 ± 0.022	1.85 ± 0.15	0.054 ± 0.018	2.0 ± 0.4	1.07 ± 0.19	2.01 ± 0.32
WZ	0.95 ± 0.23	1.25 ± 0.24	12.3 ± 1.7	0.56 ± 0.15	0.0000020 ± 0.0000004	$0.00000205 \pm 0.00000035$	0.06 ± 0.04
Triboson	0.145 ± 0.030	$0.00000192 \pm 0.00000027$	0.47 ± 0.04	0.0000022 ± 0.0000004	0.050 ± 0.008	0.101 ± 0.015	0.193 ± 0.030
Fakes	2.5 ± 0.7	1.15 ± 0.21	9.6 ± 1.5	2.8 ± 0.7	1.95 ± 0.28	1.16 ± 0.18	1.4 ± 0.4
$\tau'(130)$	1.2 ± 0.6	2.8 ± 1.1	4.0 ± 1.2	2.3 ± 0.5	8.4 ± 1.6	4.2 ± 1.0	1.8 ± 0.9
$\tau'(200)$	3.6 ± 0.7	5.4 ± 0.8	13.3 ± 1.1	4.7 ± 1.5	19.9 ± 2.8	9.4 ± 1.4	3.6 ± 0.5
$\tau'(300)$	7.0 ± 1.1	8.6 ± 1.2	18.6 ± 1.0	6.5 ± 1.3	17.8 ± 2.4	11.4 ± 1.5	3.8 ± 0.5
$\tau'(400)$	5.0 ± 0.7	6.1 ± 0.9	13.0 ± 0.7	5.2 ± 0.9	9.0 ± 1.3	7.3 ± 0.9	2.37 ± 0.31
$\tau'(500)$	4.4 ± 0.5	4.5 ± 0.7	10.3 ± 0.5	3.9 ± 0.7	4.4 ± 0.7	4.6 ± 0.6	1.64 ± 0.22
$\tau'(600)$	2.65 ± 0.30	2.5 ± 0.4	6.51 ± 0.34	2.7 ± 0.5	2.3 ± 0.4	2.53 ± 0.33	0.97 ± 0.13
$\tau'(700)$	1.35 ± 0.15	1.33 ± 0.27	3.74 ± 0.21	1.56 ± 0.26	1.09 ± 0.21	1.46 ± 0.21	0.57 ± 0.08
$\tau'(800)$	0.82 ± 0.10	0.71 ± 0.15	2.14 ± 0.12	0.88 ± 0.15	0.55 ± 0.11	0.76 ± 0.11	0.33 ± 0.05
$\tau'(900)$	0.43 ± 0.05	0.40 ± 0.09	1.17 ± 0.07	0.50 ± 0.09	0.31 ± 0.06	0.42 ± 0.07	0.214 ± 0.033
$\tau'(1000)$	0.254 ± 0.031	0.21 ± 0.05	0.66 ± 0.04	0.29 ± 0.05	0.162 ± 0.033	0.23 ± 0.04	0.100 ± 0.016
Total background	4.4 ± 1.0	3.6 ± 0.5	27.7 ± 2.1	4.2 ± 1.0	5.5 ± 0.8	3.6 ± 0.6	7.1 ± 1.0
Data	6	3	37	7	4	2	8

Table 9.5: Post-fit yields for SRs.

	CR $t\bar{t}+Z \geq 4\,\ell,\, \geq 0\,\tau$	CR WZ $3\,\ell,\, 0\,\tau$	CR ZZ $\geq 4\,\ell,\, \geq 0\,\tau$	CR Fake $\tau_{\mathrm{had}}\, 2\,\ell$ OSSF, $1\,\tau$
Z+jets	$0.00000198 \pm 0.00000010$	0.13 ± 0.06	$0.00000600 \pm 0.00000009$	2.55 ± 0.32
Other Top	4.8 ± 1.0	2.2 ± 0.4	0.48 ± 0.10	61 ± 12
$t\bar{t}+Z$	52 ± 8	3.0 ± 0.5	6.7 ± 1.2	51 ± 9
ZZ	4.8 ± 0.5	2.48 ± 0.22	753 ± 28	95 ± 5
WZ	0.0139 ± 0.0025	81 ± 10	0.174 ± 0.026	360 ± 50
Triboson	0.032 ± 0.004	0.89 ± 0.09	0.44 ± 0.04	1.71 ± 0.15
Fakes	4.8 ± 0.8	7.0 ± 0.7	12.4 ± 1.2	7180 ± 100
$\tau'(130)$	3.8 ± 0.9	4.3 ± 0.8	97 ± 5	470 ± 29
$\tau'(200)$	4.0 ± 0.6	4.8 ± 0.6	26.5 ± 1.1	262 ± 8
$\tau'(300)$	1.57 ± 0.18	4.30 ± 0.33	4.31 ± 0.24	56.4 ± 1.5
$\tau'(400)$	0.57 ± 0.06	3.03 ± 0.16	0.80 ± 0.05	8.02 ± 0.30
$\tau'(500)$	0.229 ± 0.022	2.55 ± 0.12	0.220 ± 0.022	1.27 ± 0.05
$\tau'(600)$	0.097 ± 0.012	2.14 ± 0.11	0.083 ± 0.012	0.260 ± 0.015
$\tau'(700)$	0.037 ± 0.005	1.65 ± 0.07	0.032 ± 0.004	0.052 ± 0.007
$\tau'(800)$	0.010 ± 0.004	1.08 ± 0.05	0.0102 ± 0.0016	0.020 ± 0.007
$\tau'(900)$	0.0041 ± 0.0005	0.682 ± 0.034	0.0042 ± 0.0005	0.0079 ± 0.0015
$\tau'(1000)$	0.0017 ± 0.0007	0.419 ± 0.022	0.0014 ± 0.0004	0.00186 ± 0.00027
Total background	67 ± 8	96 ± 9	774 ± 28	7750 ± 90
Data	67	96	774	7743

Table 9.6: Post-fit yields for CRs.

Chapter 10

Conclusion

The Standard Model is an extremely successful description of the fundamental nature of our universe. It falls short, however, in explaining perplexing anomalies and is regarded as incomplete. Vector-like leptons are a viable extension to the model. They can help to explain inconsistencies with the SM and also provide an avenue to new Beyond the Standard Model theories.

This thesis presented a search for vector-like leptons using data collected by the ATLAS detector. The data was collected during 2015-2018 using proton-proton collisions at the LHC. The full LHC Run 2 luminosity of 139 fb^{-1} provided a sufficiently large dataset to probe masses on the order of 1 TeV. A final state with multiple leptons was examined to increase signal sensitivity. This thesis set upper limits on vector-like lepton production cross sections up to masses of 898 GeV.

Multivariate analyses are becoming more popular in high energy physics. Their use in simulation, reconstruction and in physics analysis is a powerful tool. This thesis utilized a Boosted Decision Tree in order to maximize signal and background separation.

As the LHC continues to provide large statistics datasets, especially after it upgrades to the HL-LHC, searches for vector-like leptons will become more sensitive to mass ranges not considered in this thesis. While not explicitly observed in this work, their presence should be probed in future analyses. Their mere existence can guide fundamental physics for generations to come.

References

[1] ATLAS Collaboration, G. e. a. Aad, *Observation of a new particle in the search for the Standard Model Higgs boson with the ATLAS detector at the LHC*, Physics Letters B **716** (2012) 129, http://dx.doi.org/10.1016/j.physletb.2012.08.020. 1

[2] CMS Collaboration, S. e. a. Chatrchyan, *Observation of a new boson at a mass of 125 GeV with the CMS experiment at the LHC*, Physics Letters B **716** (2012) 3061, http://dx.doi.org/10.1016/j.physletb.2012.08.021. 1

[3] E. Noether, *Invariant variation problems*, Transport Theory and Statistical Physics **1** (1971) 186207, http://dx.doi.org/10.1080/00411457108231446. 1.1

[4] M. E. Peskin and D. V. Schroeder, *An Introduction to quantum field theory.* Addison-Wesley, Reading, USA, 1995. 1.1

[5] M. D. Schwartz, *Quantum Field Theory and the Standard Model.* Cambridge University Press, 3, 2014. 1.1

[6] Particle Data Group Collaboration, P. A. Zyla et al., *Review of Particle Physics*, PTEP **2020** (2020) 083C01. (document), 1.1.1, 1.1, 1.2, 1.3, 3.6

[7] M. Gell-Mann, *The interpretation of the new particles as displaced charge multiplets*, Nuovo Cim. **4** (1956) 848–866. 1.1.2

[8] K. Nishijima, *Charge Independence Theory of V Particles*, Prog. Theor. Phys. **13** (1955) 285–304. 1.1.2

[9] M. Kobayashi and T. Maskawa, *CP Violation in the Renormalizable Theory of Weak Interaction*, Prog. Theor. Phys. **49** (1973) 652–657. 1.1.2

[10] N. Cabibbo, *Unitary Symmetry and Leptonic Decays*, Phys. Rev. Lett. **10** (1963) 531–533. 1.1.2

[11] F. Englert and R. Brout, *Broken Symmetry and the Mass of Gauge Vector Mesons*, Phys. Rev. Lett. **13** (1964) 321–323, https://link.aps.org/doi/10.1103/PhysRevLett.13.321. 1.1.3

[12] P. W. Higgs, *Broken Symmetries and the Masses of Gauge Bosons*, Phys. Rev. Lett. **13** (1964) 508–509, https://link.aps.org/doi/10.1103/PhysRevLett.13.508. 1.1.3

[13] G. S. Guralnik, C. R. Hagen, and T. W. B. Kibble, *Global Conservation Laws and Massless Particles*, Phys. Rev. Lett. **13** (1964) 585–587, https://link.aps.org/doi/10.1103/PhysRevLett.13.585. 1.1.3

[14] J. Goldstone, A. Salam, and S. Weinberg, *Broken Symmetries*, Phys. Rev. **127** (1962) 965–970, https://link.aps.org/doi/10.1103/PhysRev.127.965. 1.1.3

[15] G. J. Gounaris, R. Kögerler, and H. Neufeld, *Relationship between longitudinally polarized vector bosons and their unphysical scalar partners*, Phys. Rev. D **34** (1986) 3257–3259, https://link.aps.org/doi/10.1103/PhysRevD.34.3257. 1.1.3

[16] G. Altarelli and G. Parisi, *Asymptotic Freedom in Parton Language*, Nucl. Phys. B **126** (1977) 298–318. 1.1.5

[17] K. Jakobs, *Physics at the LHC - From Standard Model measurements to Searches for New Physics*, arXiv:1206.7024, https://cds.cern.ch/record/1459024, Comments: 53 pages, 42 figures, to be published in the proceedings of ESHEP 2011. (document), 1.3

[18] Z. Poh and S. Raby, *Vectorlike leptons: Muon g-2 anomaly, lepton flavor violation, Higgs boson decays, and lepton non-universality*, Physical Review D **96** (2017), http://dx.doi.org/10.1103/PhysRevD.96.015032. 1.2

[19] N. Kumar and S. P. Martin, *Vectorlike leptons at the Large Hadron Collider*, Physical Review D **92** (2015), http://dx.doi.org/10.1103/PhysRevD.92.115018. 1.2, 1.2

[20] P. N. Bhattiprolu and S. P. Martin, *Prospects for vectorlike leptons at future proton-proton colliders*, Physical Review D **100** (2019), http://dx.doi.org/10.1103/PhysRevD.100.015033. 1.2, 1.2

[21] Z. Maki, M. Nakagawa, and S. Sakata, *Remarks on the unified model of elementary particles*, pp. , 663–666. 1962. 1.2

[22] LHCb Collaboration,, *Test of lepton universality in beauty-quark decays*, 2021. 1.2

[23] LHCb Collaboration, R. e. a. Aaij, *Measurement of the Ratio of Branching Fractions*, Physical Review Letters **115** (2015), http://dx.doi.org/10.1103/PhysRevLett.115.111803. 1.2

[24] Muon $g - 2$ Collaboration,, *Measurement of the anomalous precession frequency of the muon in the Fermilab Muon $g - 2$ Experiment*, Phys. Rev. D **103** (2021) 072002, https://link.aps.org/doi/10.1103/PhysRevD.103.072002. 1.2

[25] ATLAS Collaboration, A. e. a. Sirunyan, *Search for vectorlike leptons in multilepton final states in proton-proton collisions at $\sqrt{s}$=13 TeV*, Physical Review D **100** (2019), http://dx.doi.org/10.1103/PhysRevD.100.052003. 1.2

[26] CMS Collaboration, A. Tumasyan et al., *Inclusive nonresonant multilepton probes of new phenomena at $\sqrt{s}$ = 13 TeV*, arXiv:2202.08676 [hep-ex]. 1.2

[27] L. Evans and P. Bryant, *LHC Machine*, Journal of Instrumentation **3** (2008) S08001–S08001, https://doi.org/10.1088/1748-0221/3/08/s08001. 2.1

[28] ATLAS Collaboration,, *The ATLAS Experiment at the CERN Large Hadron Collider*, Journal of Instrumentation **3** (2008) S08003–S08003, https://doi.org/10.1088/1748-0221/3/08/s08003. (document), 2.1, 2.2, 2.4, 2.6, 2.7

[29] CMS Collaboration,, *The CMS experiment at the CERN LHC*, Journal of Instrumentation **3** (2008) S08004–S08004, https://doi.org/10.1088/1748-0221/3/08/s08004. 2.1

[30] ALICE Collaboration,, *The ALICE experiment at the CERN LHC*, Journal of Instrumentation **3** (2008) S08002–S08002, https://doi.org/10.1088/1748-0221/3/08/s08002. 2.1

[31] LHCb Collaboration,, *The LHCb Detector at the LHC*, Journal of Instrumentation **3** (2008) S08005–S08005, https://doi.org/10.1088/1748-0221/3/08/s08005. 2.1

[32] E. Mobs, *The CERN accelerator complex - August 2018. Complexe des acclrateurs du CERN - Aot 2018*, https://cds.cern.ch/record/2636343, General Photo. (document), 2.1

[33] j. . J. G. Avoni et al.), title = The new LUCID-2 detector for luminosity measurement and monitoring in ATLAS https://doi.org/10.1088/1748-0221/13/07/p07017. 2.1.2, 8.1.1

[34] ATLAS Collaboration,, *LuminosityPublicResultsRun2*, https://twiki.cern.ch/twiki/bin/view/AtlasPublic/LuminosityPublicResultsRun2. Accessed: 2022-01-03. (document), 2.2, 2.1.2, 2.3

[35] ATLAS Collaboration,, *Track Reconstruction Performance of the ATLAS Inner Detector at $\sqrt{s} = 13$ TeV*, tech. rep., CERN, Geneva, Jul, 2015. https://cds.cern.ch/record/2037683. 2.2.1

[36] ATLAS Collaboration, M. e. a. Capeans, *ATLAS Insertable B-Layer Technical Design Report*, tech. rep., Sep, 2010. https://cds.cern.ch/record/1291633. (document), 2.5, 2.2.1

[37] ATLAS Collaboration,, *ATLAS magnet system: Technical Design Report, 1.* Technical design report. ATLAS. CERN, Geneva, 1997. https://cds.cern.ch/record/338080. 2.2.1, 2.2.3

[38] ATLAS Collaboration, G. Aad and et al., *Studies of the performance of the ATLAS detector using cosmic-ray muons*, Eur. Phys. J. C **71** (2011) 1593, arXiv:1011.6665 [physics.ins-det]. 2.2.1

184

[39] Y. Takubo, *ATLAS IBL operational experience*, PoS **Vertex 2016** (2017) 004. 2.2.1, 2.2.1

[40] ATLAS Collaboration,, *ATLAS liquid-argon calorimeter: Technical Design Report.* Technical design report. ATLAS. CERN, Geneva, 1996. https://cds.cern.ch/record/331061. 2.2.2

[41] ATLAS Collaboration, M. Aaboud et al., *Electron and photon energy calibration with the ATLAS detector using 2015–2016 LHC proton-proton collision data*, JINST **14** (2019) P03017, arXiv:1812.03848 [hep-ex]. 2.2.2

[42] ATLAS Collaboration,, *ATLAS tile calorimeter: Technical design report,*. 2.2.2

[43] A. A. et al., *The ATLAS Forward Calorimeter*, Journal of Instrumentation **3** (2008) P02010–P02010, https://doi.org/10.1088/1748-0221/3/02/p02010. 2.2.2

[44] P. A. et al, *Testbeam studies of production modules of the ATLAS Tile Calorimeter*, Nuclear Instruments and Methods in Physics Research Section A: Accelerators, Spectrometers, Detectors and Associated Equipment **606** (2009) 362–394, https://www.sciencedirect.com/science/article/pii/S016890020900792X. 2.2.2

[45] ATLAS Collaboration,, *ATLAS muon spectrometer: Technical Design Report.* Technical design report. ATLAS. CERN, Geneva, 1997. https://cds.cern.ch/record/331068. 2.2.3

[46] A. R. M. and, *The Run-2 ATLAS Trigger System*, Journal of Physics: Conference Series **762** (2016) 012003, https://doi.org/10.1088/1742-6596/762/1/012003. (document), 2.2.4, 2.8

[47] ATLAS Collaboration, M. Aaboud et al., *Performance of the ATLAS Track Reconstruction Algorithms in Dense Environments in LHC Run 2*, Eur. Phys. J. C **77** (2017) 673, arXiv:1704.07983 [hep-ex]. 3.1

[48] R. Frhwirth, *Application of Kalman filtering to track and vertex fitting*, Nuclear Instruments and Methods in Physics Research Section A: Accelerators, Spectrometers, Detectors and Associated Equipment **262** (1987) 444–450, https://www.sciencedirect.com/science/article/pii/0168900287908874. 3.1

[49] ATLAS Collaboration, M. Aaboud et al., *Reconstruction of primary vertices at the ATLAS experiment in Run 1 proton–proton collisions at the LHC*, Eur. Phys. J. C **77** (2017) 332, arXiv:1611.10235 [physics.ins-det]. 3.1

[50] ATLAS Collaboration, G. Aad et al., *Topological cell clustering in the ATLAS calorimeters and its performance in LHC Run 1*, Eur. Phys. J. C **77** (2017) 490, arXiv:1603.02934 [hep-ex]. (document), 3.2, 3.2

[51] ATLAS Collaboration, G. Aad et al., *Electron and photon performance measurements with the ATLAS detector using the 2015–2017 LHC proton-proton collision data*, JINST **14** (2019) P12006, arXiv:1908.00005 [hep-ex]. (document), 3.3, 3.3, 8.1.3

[52] ATLAS Collaboration,, *Improved electron reconstruction in ATLAS using the Gaussian Sum Filter-based model for bremsstrahlung*, tech. rep., CERN, Geneva, May, 2012. https://cds.cern.ch/record/1449796. 3.3

[53] ATLAS Collaboration, G. Aad et al., *Muon reconstruction and identification efficiency in ATLAS using the full Run 2 pp collision data set at $\sqrt{s} = 13$ TeV*, Eur. Phys. J. C **81** (2021) 578, arXiv:2012.00578 [hep-ex]. (document), 3.4, 3.4, 8.1.3

[54] ATLAS Collaboration, M. Aaboud et al., *Jet reconstruction and performance using particle flow with the ATLAS Detector*, Eur. Phys. J. C **77** (2017) 466, arXiv:1703.10485 [hep-ex]. (document), 3.5, 3.5

[55] M. Cacciari, G. P. Salam, and G. Soyez, *The anti-k_t jet clustering algorithm*, JHEP **04** (2008) 063, arXiv:0802.1189 [hep-ph]. 3.5

[56] ATLAS Collaboration, M. Aaboud et al., *Jet energy scale measurements and their systematic uncertainties in proton-proton collisions at $\sqrt{s} = 13$ TeV with the ATLAS detector*, Phys. Rev. D **96** (2017) 072002, arXiv:1703.09665 [hep-ex]. 3.5, 8.1.5

[57] ATLAS Collaboration, G. Aad et al., *Performance of pile-up mitigation techniques for jets in pp collisions at $\sqrt{s} = 8$ TeV using the ATLAS detector*, Eur. Phys. J. C **76** (2016) 581, arXiv:1510.03823 [hep-ex]. 3.5

[58] ATLAS Collaboration, G. Aad et al., *ATLAS b-jet identification performance and efficiency measurement with $t\bar{t}$ events in pp collisions at $\sqrt{s} = 13$ TeV*, Eur. Phys. J. C **79** (2019) 970, arXiv:1907.05120 [hep-ex]. (document), 3.5, 3.6

[59] ATLAS Collaboration,, *Measurement of the tau lepton reconstruction and identification performance in the ATLAS experiment using pp collisions at $\sqrt{s} = 13$ TeV*, tech. rep., CERN, Geneva, May, 2017. http://cds.cern.ch/record/2261772. 3.6, 8.1.4, 8.1.4

[60] ATLAS Collaboration,, *Identification of hadronic tau lepton decays using neural networks in the ATLAS experiment*, tech. rep., CERN, Geneva, Aug, 2019. http://cds.cern.ch/record/2688062. (document), 3.6, 3.8

[61] ATLAS Collaboration, M. Aaboud et al., *Performance of missing transverse momentum reconstruction with the ATLAS detector using proton-proton collisions at $\sqrt{s} = 13$ TeV*, Eur. Phys. J. C **78** (2018) 903, arXiv:1802.08168 [hep-ex]. 3.7

[62] ATLAS Collaboration,, *E_T^{miss} performance in the ATLAS detector using 2015-2016 LHC p-p collisions*, tech. rep., CERN, Geneva, Jun, 2018. https://cds.cern.ch/record/2625233. 3.7, 8.1.5

[63] ATLAS Collaboration, G. Aad et al., *The ATLAS Simulation Infrastructure*, Eur. Phys. J. C **70** (2010) 823–874, arXiv:1005.4568 [physics.ins-det]. 4

[64] GEANT4 Collaboration, S. Agostinelli, et al., GEANT4 – *a simulation toolkit*, Nucl. Instrum. Meth. A **506** (2003) 250. 4

[65] ATLAS Collaboration,, *The simulation principle and performance of the ATLAS fast calorimeter simulation FastCaloSim*, tech. rep., CERN, Geneva, Oct, 2010. https://cds.cern.ch/record/1300517. 4

[66] T. Sjöstrand, S. Mrenna, and P. Skands, *A brief introduction to PYTHIA 8.1*, Comput. Phys. Commun. **178** (2008) 852–867, arXiv:0710.3820 [hep-ph]. 4

[67] ATLAS Collaboration,, *Further ATLAS tunes of* Pythia *6 and Pythia 8*,
ATL-PHYS-PUB-2011-014, 2011, https://cds.cern.ch/record/1400677. 4

[68] ATLAS Collaboration,, *Luminosity determination in pp collisions at* $\sqrt{s} = 13\,TeV$
using the ATLAS detector at the LHC, ATLAS-CONF-2019-021, 2019,
https://cds.cern.ch/record/2677054. 4.1, 8.1.1

[69] Avoni, G. and others, *The new LUCID-2 detector for luminosity measurement and*
monitoring in ATLAS, JINST **13** (2018) P07017. 4.1

[70] ATLAS Collaboration, G. Aad et al., *ATLAS data quality operations and performance*
for 2015–2018 data-taking, JINST **15** (2020) P04003, arXiv:1911.04632
[physics.ins-det]. 4.1

[71] Alwall, J. et al., *The automated computation of tree-level and next-to-leading order*
differential cross sections, and their matching to parton shower simulations, JHEP **07**
(2014) 079, arXiv:1405.0301 [hep-ph]. 4.1.1

[72] Sjöstrand, Torbjörn et al., *An introduction to PYTHIA 8.2*, Comput. Phys. Commun.
191 (2015) 159, arXiv:1410.3012 [hep-ph]. 4.1.1, 4.2.4

[73] *ATLAS Pythia 8 tunes to 7 TeV data*, tech. rep., CERN, Geneva, Nov, 2014.
https://cds.cern.ch/record/1966419. 4.1.1, 4.2.4

[74] NNPDF Collaboration, R. D. Ball et al., *Parton distributions for the LHC run II*,
JHEP **04** (2015) 040, arXiv:1410.8849 [hep-ph]. 4.1.1

[75] C. Anastopoulos and et al., *Electron identification and efficiency measurements in 2017 data*, tech. rep., CERN, Geneva, Jan, 2019. https://cds.cern.ch/record/2652163. 4.2

[76] E. Bothmann et al., *Event generation with Sherpa 2.2*, SciPost Phys. **7** (2019) 034, arXiv:1905.09127 [hep-ph]. 4.2.1

[77] T. Gleisberg and S. Höche, *Comix, a new matrix element generator*, JHEP **12** (2008) 039, arXiv:0808.3674 [hep-ph]. 4.2.1

[78] F. e. a. Buccioni, *OpenLoops 2*, Eur. Phys. J. C **79** (2019) 866, arXiv:1907.13071 [hep-ph]. 4.2.1

[79] F. Cascioli, P. Maierhöfer, and S. Pozzorini, *Scattering Amplitudes with Open Loops*, Phys. Rev. Lett. **108** (2012) 111601, arXiv:1111.5206 [hep-ph]. 4.2.1

[80] A. Denner, S. Dittmaier, and L. Hofer, COLLIER*: A fortran-based complex one-loop library in extended regularizations*, Comput. Phys. Commun. **212** (2017) 220–238, arXiv:1604.06792 [hep-ph]. 4.2.1

[81] S. Schumann and F. Krauss, *A parton shower algorithm based on Catani–Seymour dipole factorisation*, JHEP **03** (2008) 038, arXiv:0709.1027 [hep-ph]. 4.2.1

[82] J.-C. Winter, F. Krauss, and G. Soff, *A modified cluster-hadronization model*, Eur. Phys. J. C **36** (2004) 381–395, arXiv:hep-ph/0311085. 4.2.1

[83] NNPDF Collaboration, R. D. Ball et al., *Parton distributions for the LHC Run II*, JHEP **04** (2015) 040, arXiv:1410.8849 [hep-ph]. 4.2.1

[84] S. Höche, F. Krauss, M. Schönherr, and F. Siegert, *A critical appraisal of NLO+PS matching methods*, JHEP **09** (2012) 049, `arXiv:1111.1220 [hep-ph]`. 4.2.1

[85] S. Catani, F. Krauss, B. R. Webber, and R. Kuhn, *QCD Matrix Elements + Parton Showers*, JHEP **11** (2001) 063, `arXiv:hep-ph/0109231`. 4.2.1

[86] S. Höche, F. Krauss, S. Schumann, and F. Siegert, *QCD matrix elements and truncated showers*, JHEP **05** (2009) 053, `arXiv:0903.1219 [hep-ph]`. 4.2.1

[87] S. Höche, F. Krauss, M. Schönherr, and F. Siegert, *QCD matrix elements + parton showers. The NLO case*, JHEP **04** (2013) 027, `arXiv:1207.5030 [hep-ph]`. 4.2.1

[88] E. Bothmann, M. Schönherr, and S. Schumann, *Reweighting QCD matrix-element and parton-shower calculations*, Eur. Phys. J. C **76** (2016) 590, `arXiv:1606.08753 [hep-ph]`. 4.2.2

[89] S. e. a. Dulat, *New parton distribution functions from a global analysis of quantum chromodynamics*, Phys. Rev. D **93** (2016) 033006, `arXiv:1506.07443 [hep-ph]`. 4.2.2

[90] L. Harland-Lang, A. Martin, P. Motylinski, and R. Thorne, *Parton distributions in the LHC era: MMHT 2014 PDFs*, Eur. Phys. J. C **75** (2015) 204, `arXiv:1412.3989 [hep-ph]`. 4.2.2

[91] S. Alioli, P. Nason, C. Oleari, and E. Re, *A general framework for implementing NLO calculations in shower Monte Carlo programs: the POWHEG BOX*, JHEP **06** (2010) 043, `arXiv:1002.2581 [hep-ph]`. 4.2.4

[92] P. Nason, *A new method for combining NLO QCD with shower Monte Carlo algorithms*, JHEP **11** (2004) 040, arXiv:hep-ph/0409146. 4.2.4

[93] S. Frixione, P. Nason, and C. Oleari, *Matching NLO QCD computations with parton shower simulations: the POWHEG method*, JHEP **11** (2007) 070, arXiv:0709.2092 [hep-ph]. 4.2.4

[94] ATLAS Collaboration,, *Studies on top-quark Monte Carlo modelling for Top2016*, ATL-PHYS-PUB-2016-020, 2016, https://cds.cern.ch/record/2216168. 4.2.4

[95] D. J. Lange, *The EvtGen particle decay simulation package*, Nucl. Instrum. Meth. A **462** (2001) 152. 4.2.4

[96] S. Frixione, E. Laenen, P. Motylinski, and B. R. Webber, *Angular correlations of lepton pairs from vector boson and top quark decays in Monte Carlo simulations*, JHEP **04** (2007) 081, arXiv:hep-ph/0702198. 4.2.4

[97] P. Artoisenet, R. Frederix, O. Mattelaer, and R. Rietkerk, *Automatic spin-entangled decays of heavy resonances in Monte Carlo simulations*, JHEP **03** (2013) 015, arXiv:1212.3460 [hep-ph]. 4.2.4

[98] P. K. Sinervo, *Signal significance in particle physics*, pp. , 64–76. 6, 2002. arXiv:hep-ex/0208005. 5

[99] G. Cowan, K. Cranmer, E. Gross, and O. Vitells, *Asymptotic formulae for likelihood-based tests of new physics*, Eur. Phys. J. C **71** (2011) 1554, arXiv:1007.1727 [physics.data-an], [Erratum: Eur.Phys.J.C 73, 2501 (2013)]. 5, 9.1, 9.2

[100] P. C. Bhat, *Multivariate Analysis Methods in Particle Physics*, Annual Review of Nuclear and Particle Science **61** (2011) 281–309, https://doi.org/10.1146/annurev.nucl.012809.104427, https://doi.org/10.1146/annurev.nucl.012809.104427. (document), 5.2, 5.6

[101] B. P. Roe, H.-J. Yang, J. Zhu, Y. Liu, I. Stancu, and G. McGregor, *Boosted decision trees, an alternative to artificial neural networks*, Nucl. Instrum. Meth. A **543** (2005) 577–584, arXiv:physics/0408124. 5.2

[102] Coadou, Yann, *Boosted Decision Trees and Applications*, EPJ Web of Conferences **55** (2013) 02004, https://doi.org/10.1051/epjconf/20135502004. 5.2

[103] Y. Freund and R. E. Schapire, *A Decision-Theoretic Generalization of on-Line Learning and an Application to Boosting* ,. 5.2

[104] J. Zhu, H. Zou, S. Rosset, and T. Hastie, *Multi-class AdaBoost*, Statistics and Its Interface **2** (2009) 349–360. 5.2

[105] F. e. a. Pedregosa, *Scikit-learn: Machine Learning in Python*, Journal of Machine Learning Research **12** (2011) 2825–2830. (document), 5.2.1, 5.7, 5.2.3

[106] ATLAS Collaboration, M. Aaboud et al., *Search for doubly charged Higgs boson production in multi-lepton final states with the ATLAS detector using proton–proton collisions at $\sqrt{s} = 13\,TeV$*, Eur. Phys. J. C **78** (2018) 199, arXiv:1710.09748 [hep-ex]. 7.3

[107] ROOT Collaboration Collaboration, K. e. a. Cranmer, *HistFactory: A tool for creating statistical models for use with RooFit and RooStats*, tech. rep., New York U., New York, Jan, 2012. https://cds.cern.ch/record/1456844. 7.6.3

[108] ATLAS Collaboration, Z. Marshall, *Simulation of Pile-up in the ATLAS Experiment*, J. Phys. Conf. Ser. **513** (2014) 022024. 8.1.2

[109] ATLAS Collaboration, G. Aad et al., *Muon reconstruction performance of the ATLAS detector in proton–proton collision data at $\sqrt{s}$ =13 TeV*, Eur. Phys. J. C **76** (2016) 292, arXiv:1603.05598 [hep-ex]. 8.1.3

[110] ATLAS Collaboration, G. Aad et al., *Electron and photon energy calibration with the ATLAS detector using LHC Run 1 data*, Eur. Phys. J. C **74** (2014) 3071, arXiv:1407.5063 [hep-ex]. 8.1.3

[111] ATLAS Collaboration, G. Aad et al., *Jet energy resolution in proton-proton collisions at $\sqrt{s} = 7$ TeV recorded in 2010 with the ATLAS detector*, Eur. Phys. J. C **73** (2013) 2306, arXiv:1210.6210 [hep-ex]. 8.1.5

[112] ATLAS Collaboration,, *Calibration of b-tagging using dileptonic top pair events in a combinatorial likelihood approach with the ATLAS experiment*, tech. rep., CERN, Geneva, Feb, 2014. https://cds.cern.ch/record/1664335. 8.1.5

[113] ATLAS Collaboration,, *Calibration of the performance of b-tagging for c and light-flavour jets in the 2012 ATLAS data*, tech. rep., CERN, Geneva, Jul, 2014. https://cds.cern.ch/record/1741020. 8.1.5

[114] A. e. a. Buckley, *LHAPDF6: parton density access in the LHC precision era*, Eur. Phys. J. C **75** (2015) 132, `arXiv:1412.7420 [hep-ph]`. 8.3

[115] *TRexFitter*, 2525. `https://twiki.cern.ch/twiki/bin/viewauth/AtlasProtected/TtHFitter`. 9

[116] W. Verkerke and D. Kirkby, *The RooFit toolkit for data modeling*, arXiv e-prints (2003) physics/0306116, `arXiv:physics/0306116 [physics.data-an]`. 9

[117] L. Moneta, K. Cranmer, G. Schott, and W. Verkerke, *The RooStats project*, p. , 57. Jan., 2010. `arXiv:1009.1003 [physics.data-an]`. 9

[118] A. L. Read, *Presentation of search results: The CL(s) technique*, J. Phys. G **28** (2002) 2693–2704. 9.2

[119]

[120] R. D. Ball et al., *Parton distributions with LHC data*, Nucl. Phys. B **867** (2013) 244, `arXiv:1207.1303 [hep-ph]`.

[121] T. e. a. Gleisberg, *Event generation with SHERPA 1.1*, JHEP **02** (2009) 007, `arXiv:0811.4622 [hep-ph]`.

[122] Sherpa Collaboration, E. Bothmann et al., *Event Generation with Sherpa 2.2*, SciPost Phys. **7** (2019) 034, `arXiv:1905.09127 [hep-ph]`.

[123] ATLAS Collaboration, G. Aad et al., *Search for doubly and singly charged Higgs bosons decaying into vector bosons in multi-lepton final states with the ATLAS detector*

using proton-proton collisions at $\sqrt{s} = 13$ TeV, JHEP **06** (2021) 146,
arXiv:2101.11961 [hep-ex].

[124] C. Anastasiou, L. J. Dixon, K. Melnikov, and F. Petriello, *High precision QCD at hadron colliders: Electroweak gauge boson rapidity distributions at next-to-next-to leading order*, Phys. Rev. D **69** (2004) 094008, arXiv:hep-ph/0312266.

Appendix A

Number of Variables in the BDT Training

The number of included variables for training a BDT can affect the training performance and subsequently the calculated upper limit. In general, variables which are less separated in terms of signal and background distributions are ignored by the algorithm and do not deteriorate performance. However, issues related to the number of variables in regards to the dimensionality of the BDT can lead to overtraining and degraded performance. Therefore, a study was performed to assess whether the BDTs used in this analysis can be made less complex by reducing the number of variables.

The analysis was performed using 8, 12 and 16 variables as a comparison between the nominal case. Table A.1 shows the nominal number of variables included for each BDT.

SR	Number of Variables
2ℓ-SSSF- Lep	29
2ℓ-SSOF- Lep	31
2ℓ-OSSF- 2 Lep	28
2ℓ-OSOF- 2 Lep	29
2ℓ-Inc- 2 Lep	31
3ℓ	25
4ℓ-	23

Table A.1: Number of variables used for each BDT training procedure, split by region.

For each iteration, the BDTs are provided the same number of variables, however, the

variables are chosen based on ranking which is in general not the same for each region. The BDT training procedure was performed as for the nominal case, where hyperparameters were optimized. Figure A.1 shows the different cases superimposed on the nominal case.
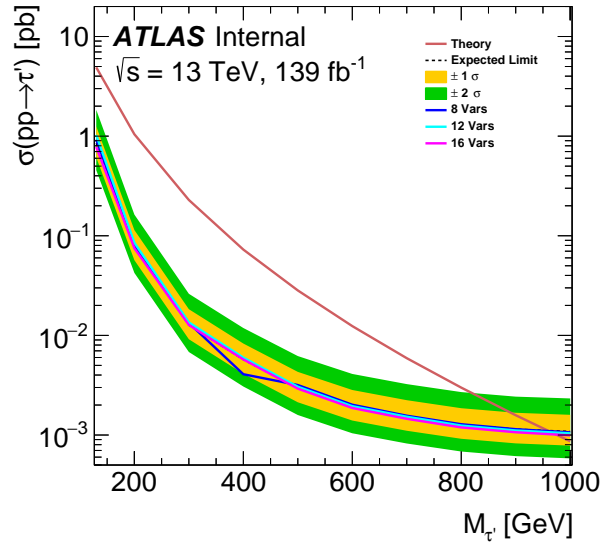

Figure A.1: Expected limit for the nominal analysis and for retrained BDTs with 8,12,16 variables.

The results from this study in terms of expected exclusion limit are:

- Nominal: 967 GeV

- 16 vars: 965 GeV

- 12 vars: 958 GeV

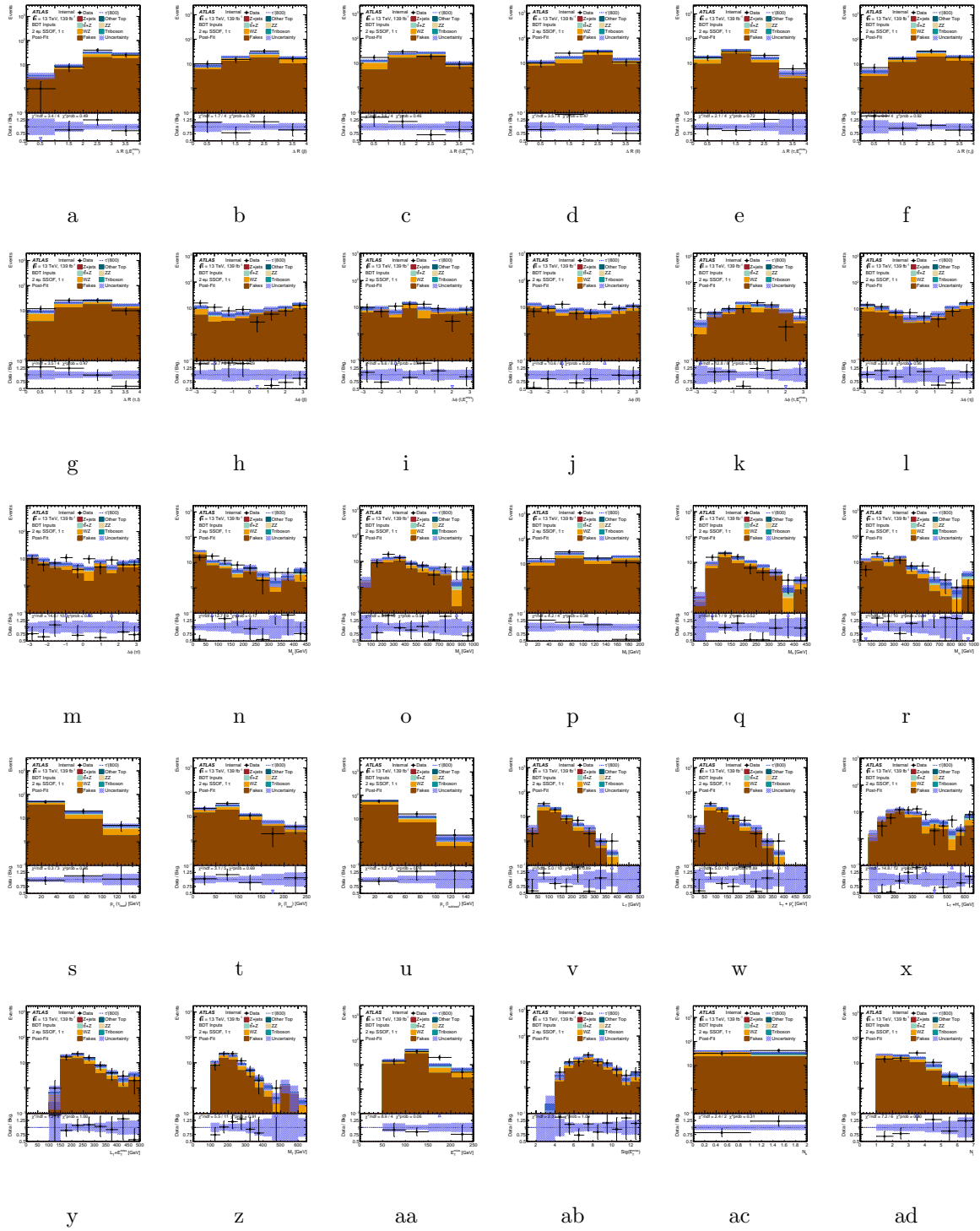- 8 vars: 951 GeV

Appendix B

BDT Input Variable Distributions

Figure B.1: Input variable distributions for BDT training for the 2ℓ-SSSF region. Variables were included in the BDT training if the χ^2 probability was greater than 5%. Normalization factors (Chapter 9) are applied.
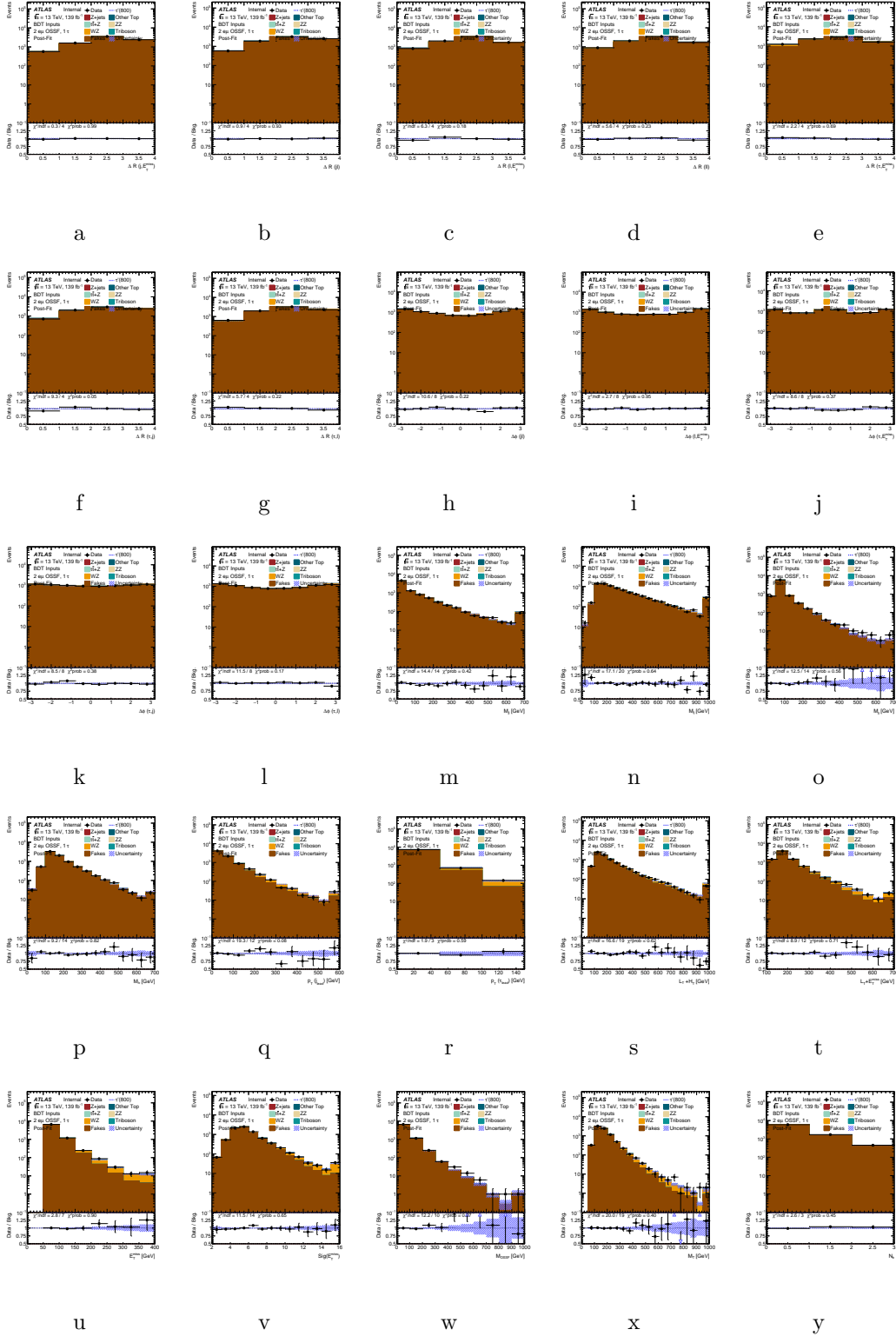
Figure B.2: Input variable distributions for BDT training for the 2ℓ-SSOF region. Variables were included in the BDT training if the χ^2 probability was greater than 5%. Normalization factors (Chapter 9) are applied.
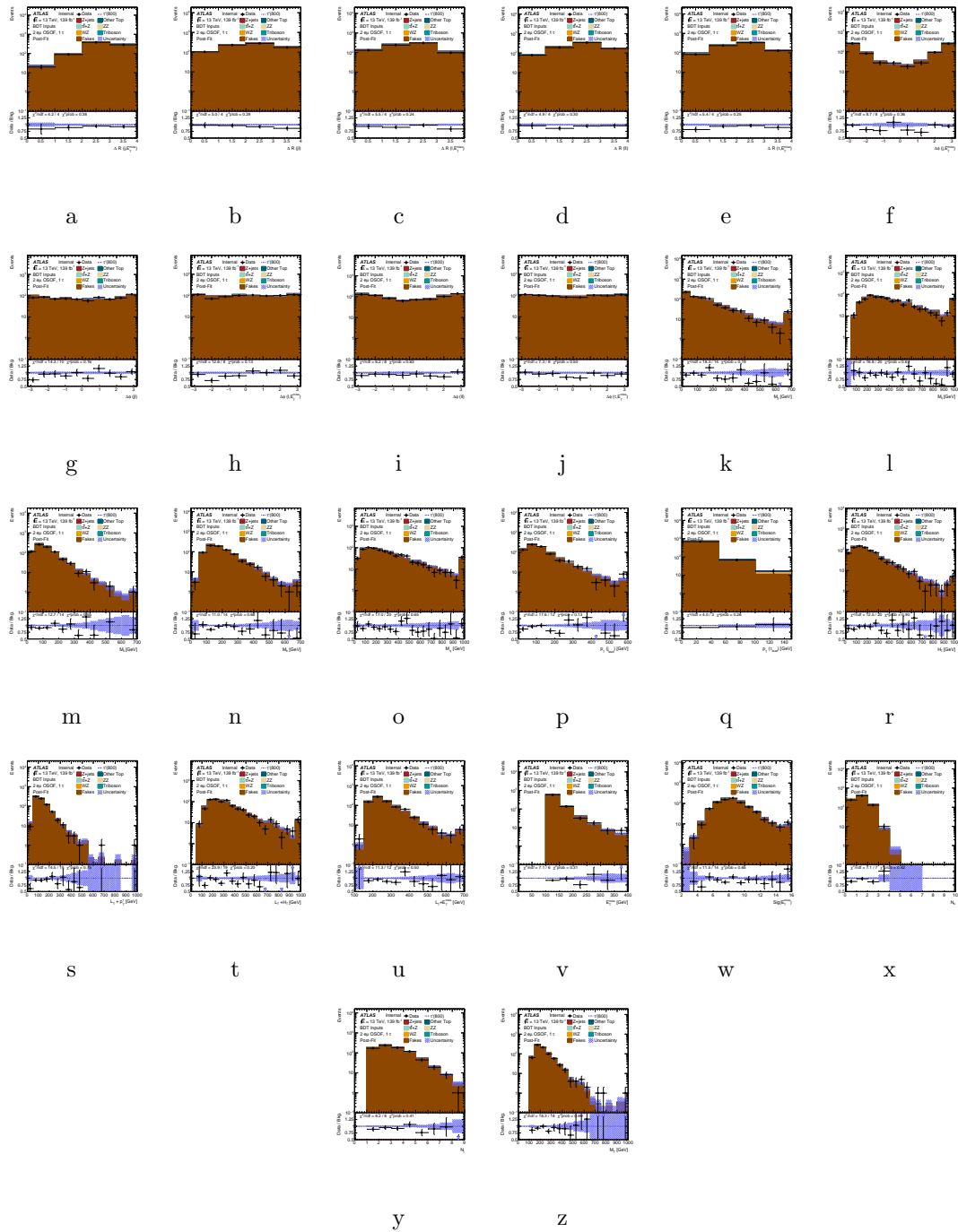
Figure B.3: Input variable distributions for BDT training for the 2ℓ-OSSF region. Variables were included in the BDT training if the χ^2 probability was greater than 5%. Normalization factors (Chapter 9) are applied.

Figure B.4: Input variable distributions for BDT training for the 2ℓ-OSOF region. Variables were included in the BDT training if the χ^2 probability was greater than 5%. Normalization factors (Chapter 9) are applied.
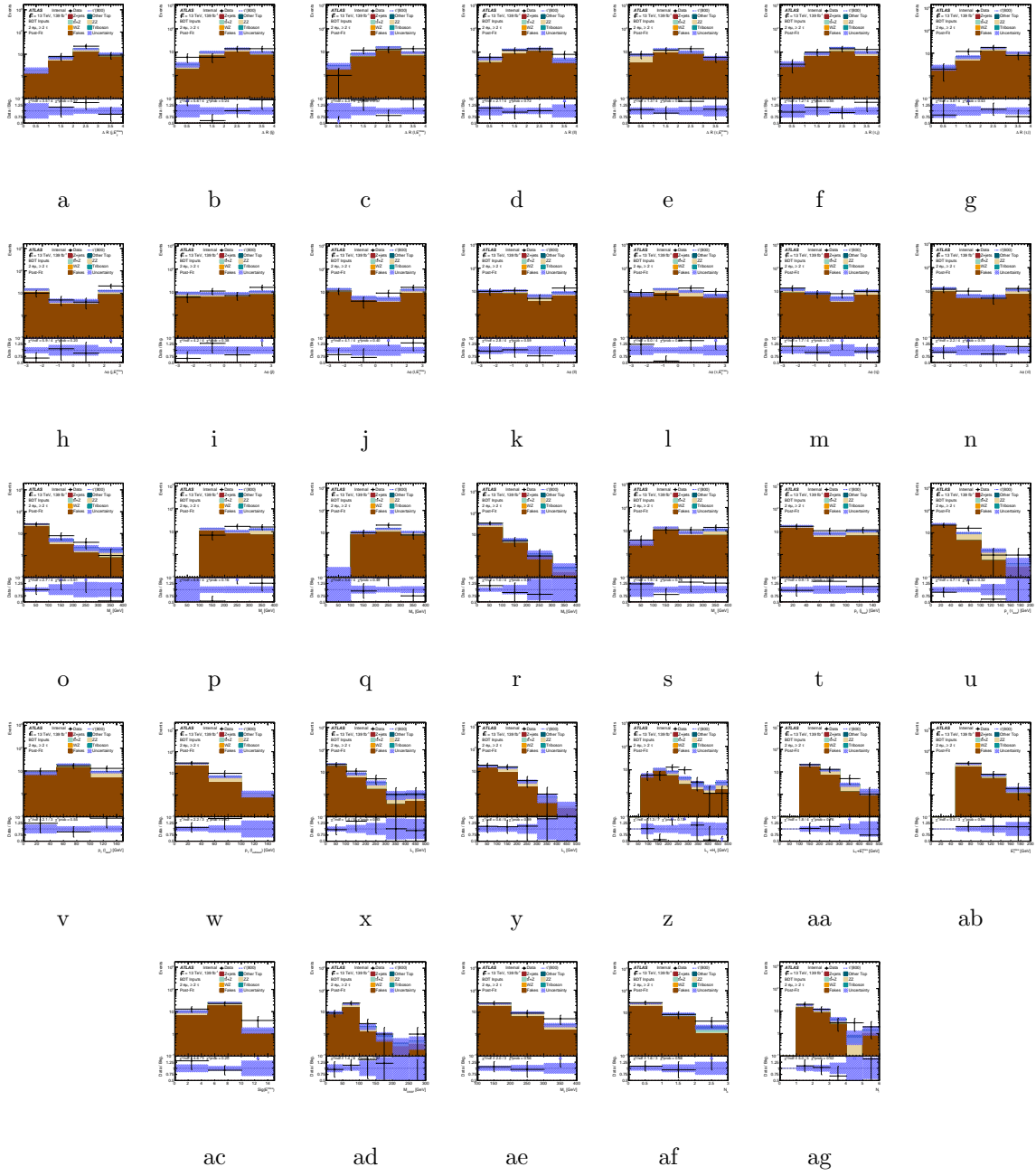
Figure B.5: Input variable distributions for BDT training for the 2ℓ-inc region. Variables were included in the BDT training if the χ^2 probability was greater than 5%. Normalization factors (Chapter 9) are applied.
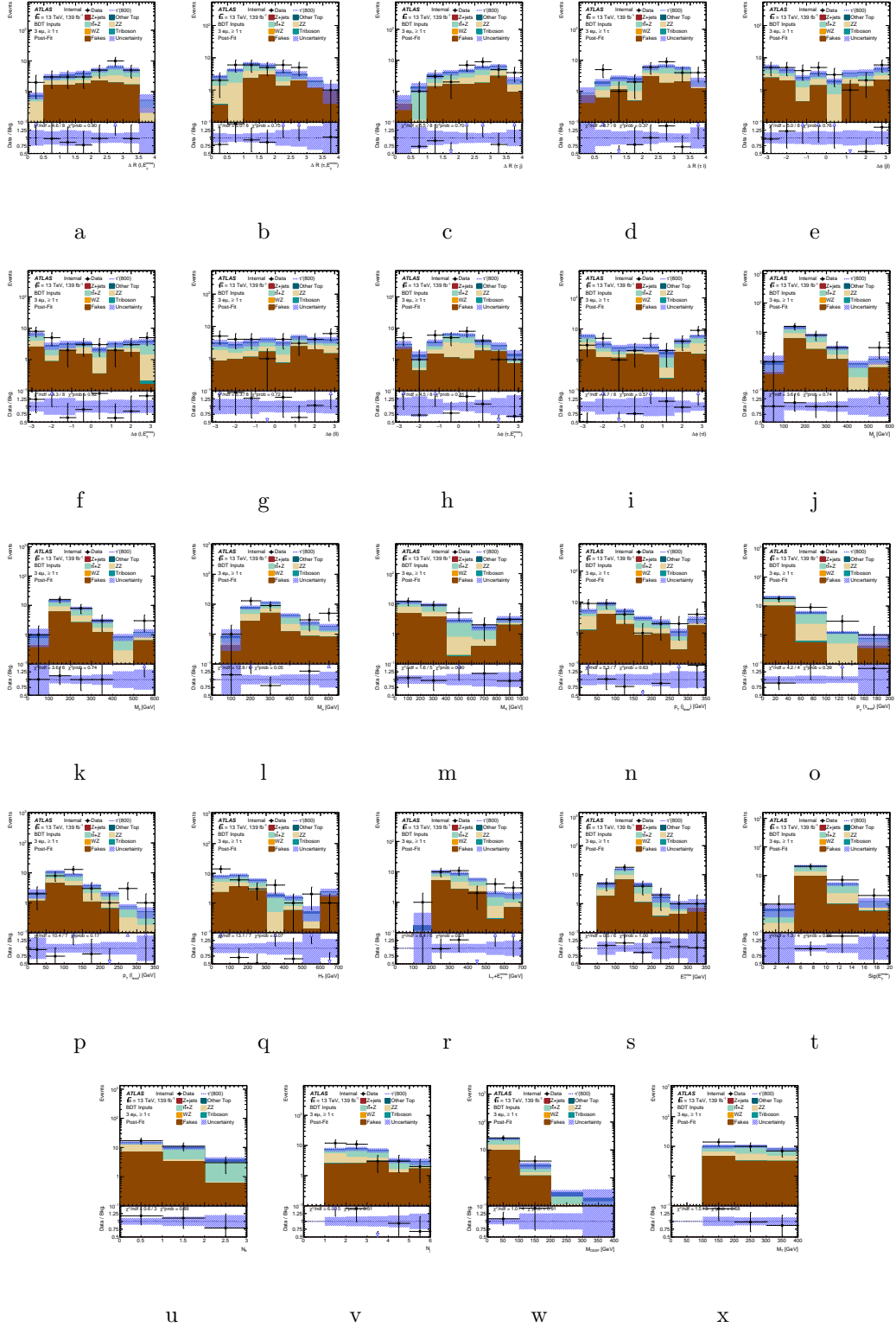
Figure B.6: Input variable distributions for BDT training for the 3ℓ region. Variables were included in the BDT training if the χ^2 probability was greater than 5%. Normalization factors (Chapter 9) are applied.

205

Figure B.7: Input variable distributions for BDT training for the 4ℓ region. Variables were included in the BDT training if the χ^2 probability was greater than 5%. Normalization factors (Chapter 9) are applied.
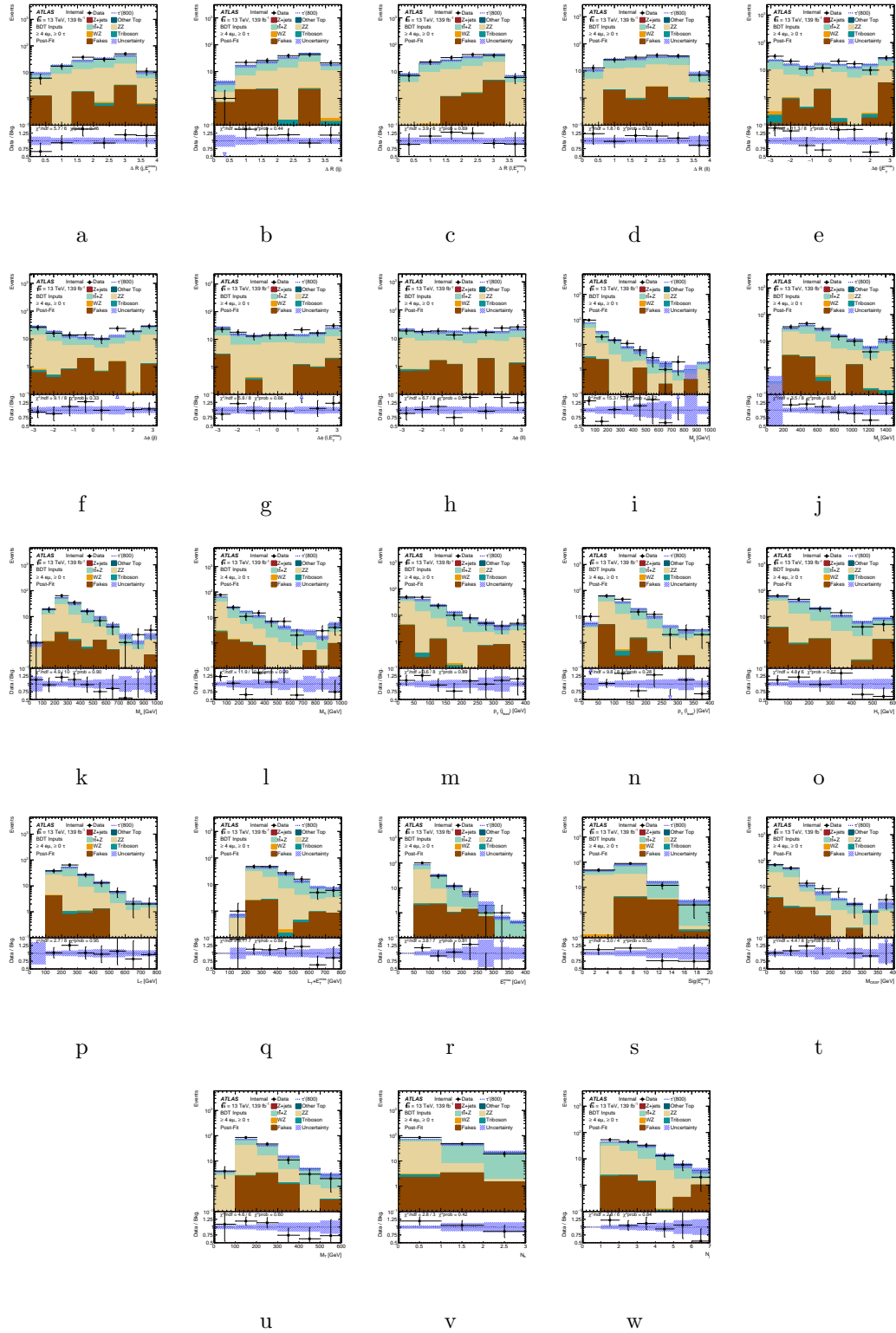
Appendix C

Composition of Fakes

The composition of fakes from electrons, muon and hadronic taus were investigated. Table C.1 shows the relative number of fakes from each source for each SR. Figure C.1 shows the various SRs with this decomposition. The plots in Figure C.1 are just an approximation and do not account for final states with more than one fake object. Not accounting for final states with more than one fake object neglects the possibility of doubling counting.

SR	Muons (%)	Electrons	Hadronic Taus	Total Number of Fakes
2ℓ-SSSF	7	72	21	2.18
2ℓ-SSOF	50	20	30	1.03
2ℓ-OSSF	0	10	90	9.82
2ℓ-OSOF	10	40	50	2.44
2ℓ-Inc	0	23	77	1.91
3ℓ	0	1	90	1.29
4ℓ	4	92	4	1.26

Table C.1: Relative composition of fakes from electrons muons and taus. The last column shows the total number of expected fakes in a given SR.
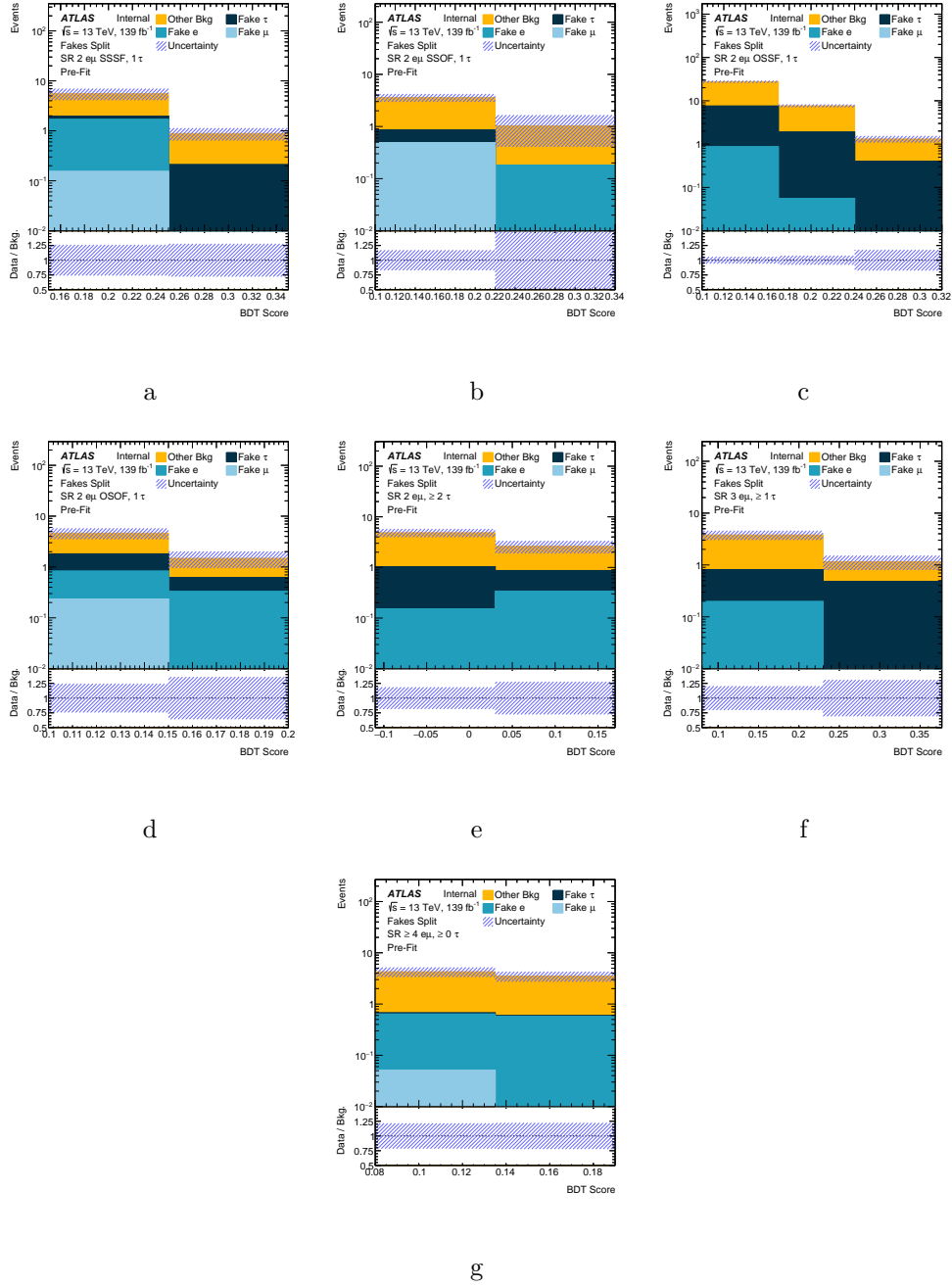
Figure C.1: BDT score distributions for the SRs split into various fake sources. The uncertainty is statistical only. This plot is an approximation as it only counts final states with one fake object and the possibility of double counting is neglected. (a) 2ℓ SSSF, 1τ (b) 2ℓ SSOF, 1τ (c) 2ℓ OSSF, 1τ (d) 2ℓ OSOF, 1τ (e) $2\ell, \geq 2\tau$ (f) $3\ell, \geq 1\tau$ (g) $\geq 4\ell, \geq 0\tau$

Appendix D

Composition of Fake Hadronic Taus

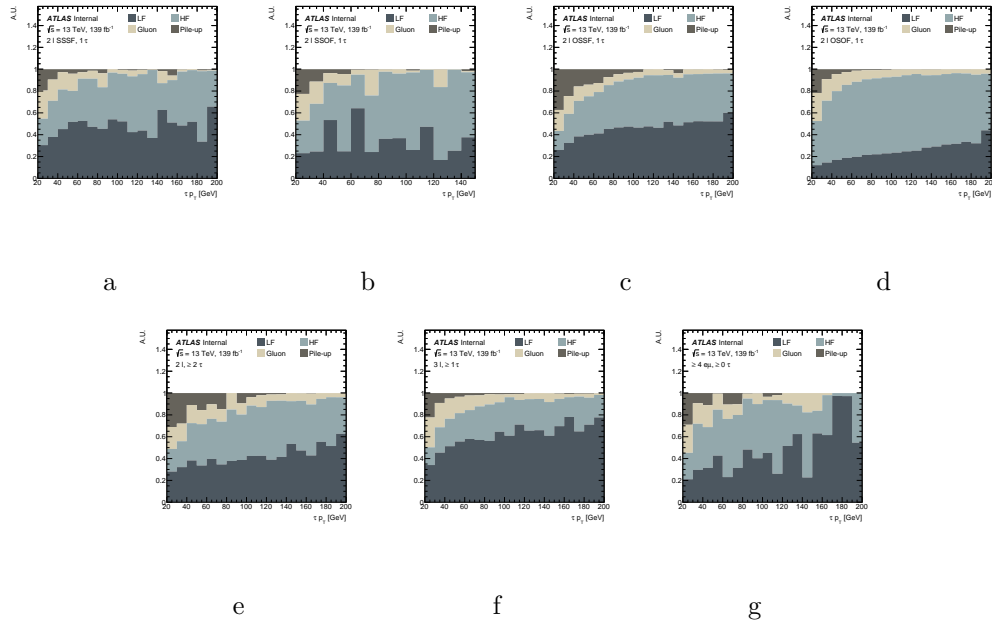The fake τ_{had} composition as a function of p_T for all lepton multiplicity final states in given in Figure D.1.

Figure D.1: Relative contribution from LF, HF gluon and pile-up initiated fake τ_{had} as a function of p_T. (a) 2ℓ SSSF, 1τ (b) 2ℓ SSOF, 1τ (c) 2ℓ OSSF, 1τ (d) 2ℓ OSOF, 1τ (e) $2\ell, \geq 2\tau$ (f) $3\ell, \geq 1\tau$ (g) $\geq 4\ell, \geq 0\tau$